ABSTRACT

THE INITIATION, DEVELOPMENT, AND DECAY
OF THE SECONDARY FLOW IN AN
INCOMPRESSIBLE TURBULENT BOUNDED JET

By

James Donald Holdeman

A comprehensive explanation of the initiation, development, and decay of the secondary flow in an incompressible turbulent bounded jet is presented and supported by experimental data.

The planar vortex ring near the nozzle exit is stretched and reoriented resulting in the development of a large scale secondary flow. As the streamwise vorticity is diffused, the secondary motion decays. This explanation is supported by the vorticity and velocity data of this investigation.

A measure of the vorticity near the nozzle exit was obtained with a four-blade vorticity meter. Isotachs and mass, momentum, and energy flux ratios were calculated from mean velocity measurements made at various elevations in a direction perpendicular to the streamwise direction of the flow.

THE INITIATION, DEVELOPMENT, AND DECAY OF THE SECONDARY FLOW IN AN INCOMPRESSIBLE TURBULENT BOUNDED JET

By

James Donald Holdeman

A THESIS

Submitted to
Michigan State University
in partial fulfillment of the requirements
for the degree of

DOCTOR OF PHILOSOPHY

Department of Mechanical Engineering

1970

G - 65432
1-18-71

To my Father

ACKNOWLEDGEMENTS

The author wishes to thank his Major Professor, Dr. John F. Foss, for his guidance and interest throughout this study. His active participation in the project and his willingness to discuss problems as they arose made working with him a rewarding experience. Thanks are also due to Dr. J. V. Beck, Dr. D. Fisher, Dr. D. H. Y. Yen, and Dr. J. B. Harrington for serving as members of the Doctoral Guidance Committee.

The author appreciates the assistance of Mr. Robert L. Walton who developed the programming necessary for the "on-line" data acquisition. Without Mr. Walton's ability to convert the author's unrealistic requests into programming realities, and his tireless efforts during the data acquisition period, this study could not have been completed in its present form.

Thanks are also due to Mr. Stanley J. Kleis for many thought provoking conversations and his assistance in laboratory troubleshooting, and to Mr. Loren Simons for his superb craftsmanship in the construction of the vorticity meters.

The financial support which the author received from NASA, NSF, and Michigan State University made the continuation of graduate study possible.

To his wife, Joann, the author expresses the sincerest thank you for her encouragement, cooperation and patience throughout the thesis effort.

TABLE OF CONTENTS

LIST OF TABLES

LIST OF FIGURES

NOMENCLATURE

a	nozzle width (= 1 inch)
aspect ratio	nozzle height/nozzle width
b	momentum flux thickness = $\frac{1}{2}\int_{-\infty}^{\infty}(\frac{U}{U_c})^2 dy$
centerline	line y = 0; z = 0
centerplane	plane y = 0
midplane	plane z = 0
SD	turbulence intensity for vertical wire
u_i'	fluctuating velocity components
U, V, W	streamwise, lateral, and vertical mean velocity components
V_E	magnitude of entrainment velocity
x, y, z	coordinate directions; see Figure 1
X	x/a
Y	y/a
Z	z/a

Flux Ratios:

M/M_0	mass flux ratio	$= \int_{-\infty}^{\infty}(\frac{U}{U_o})\frac{dy}{a}$
IM/M_0	integrated mass flux ratio	$= \int_{Z}^{2}(M/M_0)\frac{dz}{(2-Z)}$
AM/M_0	average mass flux ratio	$= \int_{o}^{Z}(M/M_0)\frac{dz}{Z}$
J/J_0	momentum flux ratio	$= \int_{-\infty}^{\infty}(\frac{U}{U_o})^2\frac{dy}{a}$
IJ/J_0	integrated momentum flux ratio	$= \int_{Z}^{2}(\frac{J}{J_o})\frac{dz}{(2-Z)}$

AJ/J_0	average momentum flux ratio	$= \int_o^Z (\frac{J}{J_o}) \frac{dz}{Z}$
E/E_0	energy flux ratio	$= \int_{-\infty}^{\infty} (\frac{U}{U_o})^3 \frac{dy}{a}$
IE/E_0	integrated energy flux ratio	$= \int_Z^2 (\frac{E}{E_o}) \frac{dz}{(2-Z)}$
AE/E_0	average energy flux ratio	$= \int_o^Z (\frac{E}{E_o}) \frac{dz}{Z}$
TKE/E_0	turbulence kinetic energy flux ratio	$= \int_{-\infty}^{\infty} (\frac{SD}{U_o})^2 (\frac{U}{U_o}) \frac{dy}{a}$
$ITKE/E_0$	integrated turbulence kinetic energy flux ratio	$= \int_Z^2 (\frac{TKE}{E_o}) \frac{dz}{(2-Z)}$
$ATKE/E_0$	average turbulence kinetic flux ratio	$= \int_o^Z (\frac{TKE}{E_o}) \frac{dz}{Z}$
Λ	net vertical mass flux	$= \int_o^X \int_{-\infty}^{\infty} \frac{W}{U_o} \frac{dy}{a} dx$
Ξ	net vertical momentum flux	$= \int_o^X \int_{-\infty}^{\infty} [\frac{UW}{U_o^2} + \frac{\overline{u_1'u_3'}}{U_o^2}] \frac{dy}{a} dx$

Subscripts:

c	pertaining to the centerplane
m	pertaining to the centerline
0	pertaining to the nozzle exit plane
$]_e$	experimental flux ratios
$]_{zsf}$	calculated flux ratios for zero secondary flow
$]_X$	evaluated from a X traverse
$]_Y$	evaluated from a Y traverse
$]_Z$	evaluated from a Z traverse

CHAPTER 1

PROBLEM DESCRIPTION

This study of the developing secondary flow in an incompressible turbulent bounded jet is a part of the research effort on bounded and intersecting jets being conducted at Michigan State University. The bounded jet flow field is formed when a jet issues from a rectangular orfice into quiescent ambient fluid where it is free to expand laterally but is confined vertically by the presence of bounding walls extending downstream from the upper and lower nozzle surfaces. This flow field is shown schematically in Figure 1. In the present study the working fluid is air issuing from a nozzle of aspect ratio (height/width) of four.

Studies of bounded jets of modest aspect ratio are of interest for three principal reasons. First, this flow field can be viewed as a generalization of the two-dimensional plane jet. That is, a two-dimensional jet is approached as the aspect ratio of a bounded jet is increased. Secondly, the bounded jet is a three-dimensional turbulent shear flow in which a secondary flow is created by the production of streamwise vorticity. In addition, the bounded jet is of technological importance to the understanding of fluid amplifiers. Contrary to the apparent design simplicity of many amplifiers, the flow pattern is a very complex phenomenon, combining effects due to aspect ratio, jet-jet interaction, and jet-wall interaction. Therefore, it is desirable to study the single bounded jet separately, with the hope that greater knowledge about this three-dimensional flow field will contribute to an increased understanding of the more complex phenomena which occur within fluidic devices.

A characteristic of all three-dimensional turbulent shear flows is an incomplete system of governing equations. The continuity and momentum equations form a set of four equations for ten unknowns, namely, the three mean velocity components, the static pressure, and the six independent components of the Reynolds stress tensor, $-\rho\,\overline{u_i'u_j'}$. It is possible to formally effect a closure of these equations by the introduction of artificial constitutive equations based on some phenomenological theory; the mixing length and eddy viscosity are defined in these theories. However, these relationships are only useful after their general "validity" has been established by comparison with experimental data for a particular flow condition. Consequently the study of the bounded jet must be predicated on experimental observations.

For the bounded jet it would seem plausible to expect the flow to be a combination of the jet flow from a nozzle of infinite aspect ratio and a boundary layer flow near the bounding plates. The velocity distribution would then be Gaussian in the y-direction and uniform in the z-direction except near the plates where the boundary layers merge into the jet flow.

The expected isotachs, lines of constant streamwise mean velocity in the y,z plane, would appear as shown in Figure 2a.

The initial study of a modest aspect ratio bounded jet by Foss (1965) revealed a three-dimensional flow behavior significantly different from the combination of the plane jet and boundary layer flow fields described above. In contrast to the expected form, the maximum velocity of the (non-center-plane) vertical velocity profiles occurred near the bounding plates rather than at the midplane. The corresponding isotach contours were wider near the plate than at the midplane. This pattern and the secondary flow it suggests are shown in Figure 2b. The vortex stretching hypothesis was presented by Foss and Jones (1968) to explain the experimental observations. In the present study, sufficient data has been acquired to document and to support a comprehensive explanation of the initiation, development, and decay of the secondary flow in the turbulent bounded jet.

CHAPTER 2

HISTORICAL PERSPECTIVE

The existence of a secondary flow pattern in the bounded jet suggests an examination of related flow fields in which secondary flow and velocity irregularities have been observed. A well documented secondary flow caused by the production of streamwise vorticity occurs in the fully developed turbulent flow in rectangular ducts. Irregularities in the mean velocity profile have been observed in duct flow, as well as in three-dimensional free and wall jets. Since the initial study on the bounded jet, additional documentation of the secondary flow has been presented. The literature relating to the flow fields mentioned is discussed below.

2.1 Secondary Flow in Rectangular Ducts

Recent and comprehensive studies by Brundrett and Baines (1964) and Gessner and Jones (1965) have explored the secondary motion which occurs in fully developed turbulent flow in rectangular ducts. Brundrett and Baines have shown the importance of the vorticity equation in describing the secondary motion. Since the fully developed flow denies the possibility of creating streamwise vorticity by the stretching of mean flow stream tubes, the secondary flow is a consequence of the production of vorticity by the turbulence structure.

Brundrett and Baines found the streamwise vorticity to be greatest near the corner in the region bounded by the wall and the corner bisector. The production and diffusion of vorticity are also most intense in the corner region with the greatest production near the corner bisector and the greatest diffusion near the wall. Convection of vorticity occurs from the zones of production to zones of diffusion resulting in the secondary flow into the corner along the corner bisector and then outward along the wall. The study of Gessner and Jones (1965) approaches the secondary flow in straight ducts by a consideration of the unequal turbulence intensities along the isotachs. Their data also support the secondary flow pattern noted above by suggesting acceleration of fluid particles into the corner along the bisectors, and deceleration away from the corner along the wall.

2.2 Velocity Irregularities in Three-Dimensional Trubulent Shear Flows

A description of the evidence of velocity irregularities in three-dimensional flow problems has recently been presented by Sforza and Trentacoste (1969). They cite references to irregularities found in studies of "two-dimensional" jets dating back to Forthmann (1934). Observations of saddle shaped velocity profiles parallel to the long direction of the orfice have also been mentioned by Van der Hegge Zijnen (1957), Bradbury (1965), and Heskestad (1965). The recent investigations by Sforza, Steiner and Trentacoste (1966) and Sforza and Trentacoste (1967) were the first to specifically study the three-dimensional flow behavior in free jets. The latter study, which was concerned with turbulent free jets, revealed the saddle shaped velocity profiles in the direction of the major axis of the orfice. Their explanation of the irregularities is an extension of that originally suggested by Van der Hegge Zijnen (1957); "The saddle shaped distributions can be explained by assuming a system of closed vortex rings surrounding the jet. The velocity induced by these vortex rings, when superimposed upon a uniform axial velocity, yields in the plane of symmetry parallel to the slit a saddle shape velocity distribution".

Trentacoste and Sforza (1967) defined three regions for the three-dimensional free jet; the potential core (PC) region, the characteristic decay (CD) region, and the axi-symmetric decay (AD) region. In the AD region the flow behavior tends to the axisymmetric configuration; the flow is independent of the shape of the nozzle, and no velocity irregularities are observed. Within the CD region, velocity profiles in the direction parallel to the minor axis of the orfice are found to be similar, but those in the direction of the major axis are non-similar where the saddle shape profiles occur. Isotachs presented for the CD region of the three-dimensional free jet show an elliptical shape with major axis initially aligned with the major axis of the orfice. Then near the end of the CD region the isotachs are nearly circular. Farther downstream they are again elliptical but with the major axis of the ellipse parallel to the minor axis of the orfice. Far downstream the flow becomes axisymmetric. This pattern illustrates an important aspect of the dynamics of eccentric vortex rings, namely that they form aligned with the orfice, tend toward an axisymmetric shape, over-shoot this circular configuration to become elliptical but aligned crosswise to the orfice, and finally decay to the stable circular shape. A recent report by Viets and Sforza (1969) on the "Dynamics of Bilaterally Symmetric Vortex Rings" shows photographic evidence of this deformation. The report also contains computer solutions for vortex deformation and will be referred to later in connection with the vortex structure in the bounded jet.

Trentacoste and Sforza (1969) also cite references to velocity irregularities in other three-dimensional turbulent shear flows. These are wall jets, "free" wakes, and bounded wakes.

2.3 Secondary Flow Effects in Bounded Jets

The major contributions of the initial work by Foss (1965) were the documentations of a three-dimensional flow behavior contrary to expectations, and the presentation of the vortex stretching hypothesis to explain the results.

For a bounded jet with an aspect ratio of six, the dimensionless midplane mean velocity profiles at several downstream distances show good similarity to each other and to the Gaussian solution for a plane jet. The non-dimensionalizing parameters used were analyzed to determine the differences between the bounded and two-dimensional jet. The centerline velocity was observed to be greater for the bounded than for a plane jet at the same downstream location. A comparison of the jet width scale, the momentum flux thickness, for the two flows showed that the bounded jet spreads less rapidly than the plane jet.

The isotachs for fifteen nozzle widths downstream displayed an outward curvature near the plates. This suggested the presence of a secondary flow pattern with an outflow near the bounding plates and a return flow distributed over the middle two thirds of the distance between the plates. The isotachs were straight in the mid-region, as would occur in a two-dimensional flow; however, the width of the bounded jet at the midplane was less than the width of the plane jet.

Foss explained the secondary flow with the following vortex stretching hypothesis. A vortex ring is formed downstream of the nozzle which has vertical filaments formed in the free mixing layer at the sides of the jet. Since the vortex ring is formed from a given collection of fluid particles, it will be convected downstream by the mean flow. As the upper and lower sections of the ring are in the relatively slow moving boundary layer fluid*, and since the side filaments are not so constrained, the sides will be convected ahead of the

---

* The original hypothesis argued that the vertical vortex filaments ended at the plates, with stretching caused because the ends of the filaments were held on the wall by the no slip condition. The modification here was suggested by Heskestad (1968) in his comments on the paper by Foss and Jones (1968). It acknowledges the fact that vorticity must appear in closed loops.

horizontal sections. The result of this stretching and reorientation of the vertical filaments is the production of streamwise vorticity and the creation of the secondary flow.

The appearance of maxima in the vertical velocity profiles illustrates the convective action of this secondary flow in transporting high velocity fluid from the center of the jet outward near the plates. Foss' measurements of yaw angles and static pressure values in the jet flow substantiate the hypothesis. Also calculations of mass, momentum, and energy flux ratios from the velocity profiles of this study show characteristic differences between the midplane behavior of the bounded jet and the behavior of the plane jet.

A recent thesis by Bettoli (1968) has added to the available data on bounded jet flows. His experiments were performed with aspect ratios of 1, 2, and 4 and substantiate the spreading and centerline velocity decay pattern mentioned above.

The vertical velocity traverses from this study (at centerplane and near the jet edge) show an interesting aspect of the bounded jet flow field not perceptible from previous data, namely that for small aspect ratios the secondary flow seems to develop and decay within a relatively short distance from the nozzle. For an aspect ratio of 2 the centerplane velocity profile is initially flat, begins to develop a parabolic shape, and then returns to a uniform profile. Near the edge of the jet, the profile is initially saddle shaped in each half-plane, changes to the single saddle shape found by

Foss, and then decays to a uniform profile. As the aspect ratio is decreased, these phenomena occur in a shorter distance from the nozzle exit.

The effects of upstream turbulence intensity on the spreading of bounded jets have been studied by Gray (1969). For an aspect ratio of 4, he found that increasing the exit intensity level of the jet created a saddle profile on the centerplane, whereas for the Foss (1965) and Bettoli (1968) studies this phenomenon was observed only off the centerplane. Gray has presented vertical centerplane isotachs for two exit intensity levels showing the decay of the saddle profiles for the lower intensity and the persistence of a double saddle shape for the higher intensity jet. The accompanying y, z, plane isotach $(X = 15)$ for the low intensity case was similar to that in Foss' study. For the higher intensity case, the saddle profiles on the centerplane and the increased isotach curvature suggested a stronger secondary flow.

CHAPTER 3

EXPERIMENTAL FACILITY AND DATA ACQUISITION PROCEDURE

3.1 The Flow System

A sketch of the total flow system is shown in Figure 3. The plenum chamber is pressurized by a model 37V Buffalo Forge volume fan driven by a 15 h.p., ± 1% feedback speed controlled motor. The wide angle diffuser following the blower has been fitted with 30 mesh screens for separation control. The contraction sections from the plenum follow the "free beam deflection" contour (Appendix A of Foss, 1965), and are designed to allow the internal geometry to be free of steps or sharp contractions. The nozzle blocks were machined from four-inch plate stock to insure a uniform nozzle height (± .002 in.) and to insure that the nozzle walls were perpendicular to the bounding plate. The nozzle width was one inch for this study. The 3/4 inch Formica-faced composition board plates are supported by a grid of adjustable screws as shown in Figure 4. With this system a plate spacing of four inches ± .005 was achieved where the spacing was determined with a capacitance gage (gage sensitivity ± .001 in.).

3.2 Data Acquistion System

A schematic of the x, y, z traverse device and its position control and sensing system is shown in Figure 5. A cable drive provides the lateral movement (much like the movable horizontal member of a drawing board). Two rubber rollers drive the entire unit in the streamwise direction. The vertical motion at the traverse head is accomplished with a lateral splined shaft and the appropriate gearing. The traverse head is shown with the vorticity sensor in Figure 6. The control system allows positioning accuracies of: $x = \pm 0.1$ inch, $y = \pm .04$ inch, $z = \pm 0.005$ inch. An auxiliary read-out system using an unbalanced bridge provides additional discrimination in the y position to ± 0.001 inch.

A Decker Model 308 pressure transducer (3 in. H_2O max.) was used for measuring the static pressure in the plenum. From this reading the nozzle exit velocity was determined. In this study the nozzle exit velocity was set at 100 $\pm$ 2 ft/sec. The Decker pressure transducer was used with the Disa 55A60 calibration tunnel for calibration of the hot wire probes.

Velocity magnitude readings were made using a Disa 55A25 hot-wire probe with the wire positioned vertically. Most of the velocity measurements in this study were made with a Disa 55D05 battery-operated anemometer, and a Disa 55D15 linearizer. Standard deviation measurements were made with a Disa 55D35 RMS Voltmeter. Initially a TSI Model 1054A linearized anemometer was used in conjunction with a TSI Model 1060 RMS Voltmeter. A change was made to the Disa equipment when it was discovered that the TSI Voltmeter provided incorrect readings. The Y traverses in which the standard deviations were measured with the TSI RMS Voltmeter are so designated. The standard deviation curves from these traverses have the same character as the standard deviation curves from the traverses repeated at the same X,Z location with the Disa equipment. This suggests that the trends shown by standard deviations obtained with the TSI meter are correct when compared to other standard deviations similarly obtained. Since the turbulence intensity values were not of fundamental importance to the major results of this study, only selected traverses containing the quantitatively innaccurate data were repeated.

Crossed vane vorticity meters, constructed by milling two perpendicular vanes from an aluminum bar, were used to examine the nature of the vorticity field near the nozzle exit. Four of these meters were used in three sizes: 1/4 inch, 3/8 inch, and 1/2 inch. All flow field data was obtained with the 3/8 inch meter. A second, nominally identical, 3/8 inch meter was checked against the first with similar responses observed.

A photograph of the 1/2 inch meter and the hot wire sensor appears in Figure 6. The hot wire probe measures the passage of the blade wake. In regions of low turbulence intensity, the wake is observable in the hot wire signal. However, in regions of high intensity, the wake is obscured by the fluctuating turbulent velocity. By auto-correlating the hot wire signal using a Princeton Applied Research Model 101 Correlation Function Computor, the desired rotational speed of the meter can be recovered. Since the PAR unit averages over a 20 second period, the measured meter speed is an average for such a period. This method of speed measurement was adopted because (1) it satisfied the requirements that the speed measuring device should not have any retarding effect on meter rotation and that it should move with the vorticity meter as the meter is traversed in the three coordinate directions, (2) the hot wire system and the PAR 101 were available, and (3) a quantitative indication of meter speed was necessary to evaluate relative vortex strength and flow field symmetry.

The PAR 101 was also used with the velocity survey to obtain Eulerian time correlation functions at selected locations in the flow field. From these the micro and macroscales of the turbulence were determined. Because the data obtained was too fragmentary to contribute to the explanation of the flow behavior in the bounded jet, it is not reported herein.

3.3 Data Processing

The analog data generated in the laboratory was processed on-line with the IBM 1800 computer. A typical experimental run included the following:

1. At least two calibration runs of hot wire voltage versus velocity* using the Disa calibration tunnel were made each time experimental data was acquired. The calibration runs, in which the hot-wire anemometer and pressure transducer analog voltages were

---

* The measured pressures at the upstream and probe locations in the nozzle provide a measure of the velocity at the probe using the Bernoulli equation.

simultaneously sampled as the speed was increased, were averaged and corrected for scatter to form a calibration table for the velocity data.

2. The plenum pressure was recorded to obtain a record of the nozzle exit velocity.
3. Control voltages were recorded specifying the type and x, y, z location of the data.
4. The hot wire data was recorded in digitized form for 10 seconds from which the mean voltage was calculated. The average wire voltage was compared with the calibration table to obtain an interpolated value of the mean velocity.
5. The standard deviations were measured on the RMS voltmeter using a 10 second time constant. The data record, which ran simultaneously with the mean velocity sampling, was begun when the RMS reading appeared to be stable. The digitized RMS signal was averaged for 10 seconds and the mean RMS value, the mean velocity, and the probe position were recorded.
6. The correlation functions were input to the IBM 1800 using the slow readout rate (50 sec/correlation function) on the correlator. The 100 voltage steps in the correlation function were sampled and the normalized (first step = 1.0) autocorrelation function was recorded. Where required, the autocorrelation function was formed from the normalized

autocorrelation function by multiplying by the square of the turbulence intensity obtained from the RMS voltmeter.

For the velocity field data the positions, mean velocity, and RMS voltages were punched on cards for additional processing on the CDC 6500. The correlation functions were also punched for further processing. A schematic of the data acquisition and processing system is shown in Figure 7.

CHAPTER 4

RESULTS OF THE BOUNDED JET STUDY

4.1 Velocity Field Data

4.1.1 X, Y, and Z Traverse Data

A typical calibration of hot-wire voltage versus velocity is shown in Figure 8. Data similar to this was obtained each time the system was readied for the acquisition of velocity data.

The velocity field survey contained X, Y, and Z traverse hot-wire anemometer data for evaluation of mean velocity and turbulence intensity (standard deviation). The X traverse data at the jet centerline is shown in Figures 9 and 10.

Z traverses at the centerplane were made at X = 2, 5, 10, 15, 20, 30, and 40. Figures 11a-11c show the velocity profiles for these traverses. The velocities were normalized* to make the centerline velocity for each Z traverse equivalent to that obtained from the X traverse. That is, $U_c/U_0 = [U_c/U_m]_Z[U_m/U_0]_X$. The turbulence intensities for the

* Normalization schemes for the data were required because the accuracy of the data points in a given traverse with respect to other data in the same traverse was much better than the precision with which a given U_c/U_0 value could be repeated during the 8 month period of data acquisition.

Z traverses appear in Figures 12a-12c. The following normalization was used on these: $SD_c/U_0 = [SD_c/U_m]_Z[U_m/U_0]_X$.

The number of Y traverses at each X-Z location is shown in Table 1. The Y traverse data was normalized by the following procedure:

$$U/U_0 = [U/U_c]_Y[U_c/U_m]_Z[U_m/U_0]_X \ .$$

For X = 2, and X = 5,

$$SD/U_0 = [SD/U_c]_Y[U_c/U_m]_Z[U_m/U_0]_X \ .$$

For X = 10, 15, 20, and 40,

$$SD/U_0 = [SD/SD_c]_Y[SD_c/U_m]_Z[U_m/U_0]_X \ .$$

The normalization used for the intensity at the downstream location was not used at X = 2 and X = 5 because of the low turbulence intensity levels at the upstream centerplane locations. Use of the $[SD_c/U_m]_Z$ normalization in the near field to make small corrections at the centerplane resulted in large magnitude changes at the peaks. The intensity values were thus distorted rather than corrected; the alternate method of normalization was adopted in the near field with good results.

To facilitate the numerical integration of the Y traverse data, a gridding scheme was used to generate data by linear interpolation at equal increments in the y-coordinate direction. For the calculation of isotachs and contours of constant turbulence intensity, the several Y traverses at a given X location were also gridded by a linear interpolation

TABLE 1. Location of Y traverses for evaluation of velocity and turbulence intensity.

Y \ X	0	2	5	10	15	20	30	40
-.5								1
0	1	1	2	1	2	2	1	1
.2					1			
.5		1	1	1	1	1		1
1.0	1	1	1	1	1	1		1
1.2			1					1
1.3		2	1	1	1	1		1
1.4					1	1		
1.5		2	1	1	1	1		1
1.6		1	1	1				
1.7	1	1	1	1	1	1		1
1.8	1	2	2	1	2	1		1
1.9	1	1	1	1	1	1		1

scheme for equal increments in the z-direction. The isotachs and turbulence intensity contours are shown in Figures 13-24.

4.1.2 Scaling Parameters and Dimensionless Profiles

The discussion by Townsend (1956) concerning self-preservation of developing flows is relevant to the selection of scaling parameters in the bounded jet problem. From page 90 of this reference:

> In a developing flow, the transverse distributions of the mean velocity and other mean quantities change with position in the downstream direction, but the distributions are subject to various restrictions, e.g. the momentum condition, and it is often assumed that they retain the same functional forms, merely changing in scale. It is always necessary to bear in mind that there may be features about any particular flow that prevent it having a self-preserving form, and that, even if such a form is possible, it may only exist as an asymptotic condition not valid over the range of observation. For a particular flow to be self-preserving, it is necessary that the variation of any mean quantity over any plane, x = constant, should be expressible non-dimensionally through suitable scales of length and velocity, u_0 and l_0, as a universal function of y/l_0.

For a two-dimensional jet, with zero pressure gradient, the conservation of momentum relation can be written as

$$U_0^2 a = \int_{-\infty}^{\infty} U^2 dy = U_c^2 \int_{-\infty}^{\infty} \left(\frac{U}{U_c}\right)^2 dy .$$

The momentum flux thickness, b, is defined by

$$b = \frac{1}{2} \int_{-\infty}^{\infty} \left(\frac{U}{U_c}\right)^2 dy \; .$$

Thus the conservation of momentum equation for $\partial p/\partial x = 0$ can be expressed as

$$\left(\frac{U_c}{U_0}\right)^2\left(\frac{2b}{a}\right) = 1.$$

For the selection of U_c as the velocity scaling parameter, b is seen to be a "natural" choice as the width scale. Because of the relationship of the bounded jet to the plane jet, U_c and b will be used as the scaling parameters for this study. The momentum flux thickness values for the bounded jet are shown in Figures 25 and 26. The use of the momentum flux thickness does not bias the dimensionless profiles by forcing the curve to pass through a specified point as does the more commonly used half-velocity width, $y_{\frac{1}{2}}$.

As shown by Townsend (1956), the conditions for self-preservation of $\bar{u}\ (y/l_0)$ are

$$\frac{l_0}{u_0}\frac{du_0}{dx} = \text{constant, and } \frac{dl_0}{dx} = \text{constant} .$$

For the scaling parameters U_c and b, the requirements for self-preservation in the two-dimensional jet are:

$$b\ \alpha(x - x_0) \quad ; \quad u_0\ \alpha(x - x_0)^{-\frac{1}{2}} .$$

These relations will be considered in Chapter 6 where the plane jet is compared to the bounded jet.

The tendency toward self-preservation of the dimensionless midplane mean velocity profiles for the bounded jet is evident in Figure 27a. These curves also appear in Figures 27b and 27c where the streamwise changes in the profiles are discernable. The streamwise changes in the dimensionless midplane turbulence intensity distributions are shown in

Figures 28a and 28b.

The dimensionless mean velocity and turbulence intensity distributions are shown with the midplane curves in Figures 29-42. Several Y traverses in this study were repeated as a check on the measurement accuracy; the locations of the repeated traverses are shown in Table 1. The turbulence intensity distributions for $X = 15$ and $X = 20$ in Figures 37 and 40 show quantitatively inaccurate data (see Chapter 3). The trends evident in these figures are substantiated by the correct standard deviation values for several traverses which were repeated; see Figures 36 and 39.

In the course of the experimental investigation a gap was discovered between the upper bounding plate and the nozzle block on the positive y side of the jet. This was initially observed in a y-traverse for $Z = 1.8$ at the nozzle exit. The shear layer at $y = -a/2$, $Z = 1.8$ contained high frequency fluctuations while the shear layer at $y = +a/2$, $Z = 1.8$ was characterized by low frequency, high amplitude fluctuations. The affect of the bleeding-off of the boundary layer at $y = +a/2$ and $Z = 2$ is seen in Figures 29c and 30c. The curves for $Z = 1.7$, 1.9, and one of the curves for $Z = 1.8$ show data obtained with the gap and resulting boundary-layer bleed present; the data shown in the second curve at $Z = 1.8$ were obtained after the plate and the nozzle were made contiguous. The differences in the curves at $Z = 1.8$ occur near the tail of the profiles for $y < 0$ (the opposite side from the gap). These differences are magnified by the dimensionless presentation of the data; they have no significant effect on the basic shape of the isotachs at $X = 2$. The two traverses at $X = 5$, $Z = 1.8$ provide a check on the downstream influence of the boundary layer bleed at the nozzle exit since one of these traverses preceeded the correction of this misalignment. Figures 31b and 32b show that the gap at $z = 0$, $y = \pm a/2$ had no effect downstream on either the mean velocity or turbulence intensity distributions.

4.1.3 Entrainment Data

Three X traverses were made on the midplane in the entrainment region of the jet for $y = -5b$, $-6b$, and $-13a$; the y locations where data was obtained are shown in Figure 43. For these traverses, the hot-wire anemometer was linearized and calibrated for flow velocities from zero to twenty ft/sec. In the calibration the velocity vector was parallel to the axis of the probe, whereas in the flow field the entrainment mean velocity vector was perpendicular to the probe axis. For the type of sensor used, the transverse orientation of the probe results in indicated velocity values which are 10-15 percent too large. The entrainment traverses were made to determine the thickness of the entrainment boundary layer and to determine if the midplane entrainment velocity varied in the streamwise direction. Therefore, the relative magnitude of the velocities was more pertinent than the absolute magnitude of the velocities. The midplane entrainment data is shown in Figure 44. The Z traverse data ($X = 1$, $Y = -2.5$) appears in Figure 45.

4.2 Integrated Velocity Field Data

4.2.1 Limits for the Y Integrations

Y-integration of the first, second and third powers of U/U_0 were required for the mass, momentum, and energy flux ratios respectively. In most of the flow field, $V << U$ and the mean velocities measured with the vertical hot-wire can be considered to be the x-component mean velocity U. Foss (1965) shows measured yaw angles in the bounded jet which are less than ten degrees except in the entrainment region. Because the tails of the mean velocity curves represent the entrainment velocity V, they were eliminated from the flux integrals by integrating only in the region where U/U_0 was greater than a preset cutoff velocity ratio U_{cut}/U_0. For each Y traverse, the integration was performed for $U_{cut}/U_0 = 0$, $.1(U_c/U_0)$, and 0.06. The flux ratio figures presented are for $U_{cut}/U_0 = 0.06$ except at $X = 40$ where the entrainment data, Figure 44, suggested that $U_{cut}/U_0 = .1\ (U_c/U_o)$ was more appropriate.

4.2.2 Derivation and Significance of Mass Flux Ratios

Consider a control volume of height Δz which extends from the nozzle exit plane to X and from $y = -\infty$ to $y = +\infty$. With the flow through the plane of the nozzle exit into the control volume approximated by $U_0 a\Delta z$, the continuity relation requires that,

$$\Delta z \int_{-\infty}^{\infty} U\, dy = U_0 a\Delta z + 2\Delta z \int_0^X V_E dx$$
$$- \int_0^X\int_{-\infty}^{\infty} W\, dydx\Big|_{Z+\Delta z} + \int_0^X\int_{-\infty}^{\infty} W\, dydx\Big|_Z \,.$$

The mass flux ratio is defined as the ratio of the mass efflux through the $y - \Delta z$ face at X to the mass influx through the $y - \Delta z$ face at the nozzle exit. Dividing the equation above by $U_0 a \Delta z$ and taking the limit as $\Delta z \to 0$ gives the relation for the mass flux ratio, M/M_0, at any Z,

$$\frac{M}{M_0} = \int_{-\infty}^{\infty} \frac{U}{U_0} \frac{dy}{a} = 1 + \frac{2}{a} \int_0^X \frac{V_E}{U_0} dx - \frac{d}{dz} \int_0^X \int_{-\infty}^{\infty} \frac{W}{U_0} \frac{dy}{a} dx. \quad (1)$$

Integrating M/M_0 (Equation 1) from Z to 2 and dividing by $(2-Z)$ gives IM/M_0 at any Z; that is,

$$IM/M_0 = \int_Z^2 \frac{M}{M_0} \frac{dz}{(2-Z)} = 1 + \frac{2}{a} \int_Z^2 \int_0^X \frac{V_E}{U_0} dx \frac{dz}{(2-Z)}$$

$$+ \frac{1}{(2-Z)} \int_0^X \int_{-\infty}^{\infty} \frac{W}{U_0} \frac{dy}{a} dx. \quad (2)$$

If M/M_0 (Equation 1) is integrated from $z = 0$ to Z and divided by Z, the average mass flux ratio from the midplane to Z is obtained;

$$AM/M_0 = \int_0^Z \frac{M}{M_0} \frac{dz}{Z} = 1 + \frac{2}{a} \int_0^Z \int_0^X \frac{V_E}{U_0} dx \frac{dz}{Z}$$

$$- \frac{1}{Z} \int_0^X \int_{-\infty}^{\infty} \frac{W}{U_0} \frac{dy}{a} dx . \quad (3)$$

The velocity profiles from each Y traverse were integrated as noted in 4.2.1 to obtain the experimental mass flux ratios, $M/M_0]_e$. The values of $IM/M_0]_e$ and $AM/M_0]_e$ were obtained by integrating $M/M_0]_e$ in Z by the following parabolic integration technique.

A parabola was fitted to each set of three $M/M_0]_e$ values. Two parabolic sections were thus determined for each interval between the $M/M_0]_e$ data points except the first and last intervals where only one parabolic section was determined for each region. For the end intervals the integral of $M/M_0]_e$ was approximated by the area under the parabolic section in each region. The integral of $M/M_0]_e$ for all intermediate intervals was approximated by the average of the areas under the two parabolic sections in each interval.

The integrated mass flux ratio (Equation 2) for any Z is influenced by the amount of fluid entering the control volume through the X-Z faces, the entrainment, and the amount of fluid entering the control volume through the X-Y face at Z (i.e., the net vertical mass flux). The net vertical mass flux, Λ, is defined as,

$$\Lambda \equiv \int_0^X \int_{-\infty}^{\infty} \frac{W}{U_0} \frac{dy}{a} \, dx \ .^* \tag{4}$$

To separate the effects of secondary flow and entrainment on the mass flux ratios, calculations of IM/M_0 were made with the net vertical mass flux set equal to zero for all Z. For these calculations the entrainment velocity was assumed to be constant in Z for $0 \le Z \le 1.5$ and to follow a 1/7 power relationship in terms of the distance from the wall for $1.5 \le Z \le 2$. That is

$$\begin{aligned} \frac{V_E}{U_0} &= \frac{\overline{V}_E}{U_0} = \text{constant} && \text{for} \quad 0 \le Z \le 1.5 \\ \frac{V_E}{U_0} &= \frac{\overline{V}_E}{U_0} \left(\frac{2-Z}{.5}\right)^{1/7} && \text{for} \quad 1.5 \le Z \le 2 \end{aligned} \tag{5}$$

---

* As defined, Λ is the net vertical dimensionless mass flux per nozzle width. Consequently Λ has the units of length.

This model is compared with the available experimental Z traverse data in Figure 45.

At $Z = 0$, $W = 0$ $(\Lambda = 0)$ and $IM/M_0]_e$ is determined entirely by the entrainment. Thus the $IM/M_0]_e$ value and the IM/M_0 for the zero secondary flow model, $IM/M_0]_{zsf}$, must be equal for $Z = 0$, where

$$IM/M_0]_{zsf} = 1 + \frac{2}{a} \int_Z^2 \int_0^X \frac{V_E}{U_0}\, dx \, \frac{dz}{(2-Z)} \; . \tag{6}$$

Substituting the entrainment velocity model into this expression and evaluating it at $Z = 0$ gives the appropriate value of $\overline{V_e}/U_0$ for each X location. Using the $\overline{V_e}/U_0$ value, $IM/M_0]_{zsf}$ can be evaluated for any Z.

The difference between $IM/M_0]_e$ and $IM/M_0]_{zsf}$ is a measure of the net vertical mass flux at any Z. That is,

$$IM/M_0]_e - IM/M_0]_{zsf} = \frac{1}{(2-Z)} \int_0^X \int_{-\infty}^{\infty} \frac{W}{U_0} \frac{dy}{a}\, dx = \frac{\Lambda}{(2-Z)} . \tag{7}$$

Consequently, where $IM/M_0]_e < IM/M_0]_{zsf}$ the net vertical mass flux is directed toward the midplane, and where $IM/M_0]_e > IM/M_0]_{zsf}$ the net vertical mass flux is directed away from the midplane.

Using the same entrainment model with the values of $\overline{V}_e/U_0$ found above, a zero secondary flow mass flux ratio was calculated;

$$M/M_0]_{zsf} = 1 + \frac{2}{a} \int_0^X \frac{V_E}{U_0}\, dx \; . \tag{8}$$

Thus,

$$M/M_0]_e - M/M_0]_{zsf} = -\frac{d}{dz}\int_0^X \int_{-\infty}^{\infty} \frac{W}{U_0}\frac{dy}{a}\,dx = -\frac{d\Lambda}{dz} . \tag{9}$$

Z locations where $-d\Lambda/dz = 0$ are thus maxima or minima of the net vertical mass flux. This information complements the discrimination of positive and negative regions of net vertical mass flux made from the IM/M_0 comparison.

Two typical $-d\Lambda/dz$ curves are shown schematically in Figures 46a and 46b. In Figure 46a, a maximum or minimum must occur at $Z = 1.2$ because $-d\Lambda/dz = 0$. Since $-d^2\Lambda/dz^2 < 0$, $-\Lambda$ is a maximum at $Z = 1.2$. Because $-d\Lambda/dz = 0$ for only one Z value, $-\Lambda$ is everywhere greater than zero.

In Figure 46b, maxima or minima occur at $Z = 1.0$ and $Z = 1.8$. At $Z = 1.0$, $-d^2\Lambda/dz^2 > 0$ and $-\Lambda$ is a minimum; at $Z = 1.8$, $-d^2\Lambda/dz^2 < 0$, and $-\Lambda$ is a maximum.

The experimental and zero secondary flow values of M/M_0 and IM/M_0 are shown in Figures 47 and 48. The average mass flux ratios, $AM/M_0]_e$, are shown in Figure 49.

4.2.3 Derivation and Significance of Momentum Flux Ratios

For a control volume of height Δz which extends from the nozzle exit plane to X and from $y = -\infty$ to $y = +\infty$, conservation of momentum requires that, for $\partial p/\partial x = 0$,

$$\Delta z \int_{-\infty}^{\infty} U^2 dy = \Delta z\, U_0^2 a - \int_0^X \int_{-\infty}^{\infty} (UW + \overline{u_1' u_3'})\,dy\,dx\Big|_{Z+\Delta z}$$

$$+ \int_0^X \int_{-\infty}^{\infty} (UW + \overline{u_1' u_3'})\,dy\,dx\Big|_Z$$

The momentum flux ratio is defined as the ratio of the momentum efflux through the $y - \Delta z$ face at X to the momentum influx through the $y - \Delta z$ face at the nozzle exit. Dividing the equation above by $U_0^2 a \Delta z$ and taking the limit as $\Delta z \to 0$ gives for any Z,

$$J/J_0 = \int_{-\infty}^{\infty} (\frac{U}{U_0})^2 \frac{dy}{a} = 1 - \frac{d}{dz} \int_0^X \int_{-\infty}^{\infty} (\frac{UW}{U_0^2} + \frac{\overline{u_1' u_3'}}{U_0^2}) \frac{dy}{a}\, dx \tag{10}$$

Integrating J/J_0 (Equation 10) from Z to 2 and dividing by $(2-Z)$ gives IJ/J_0.

$$IJ/J_0 = \int_Z^2 \frac{J}{J_0} \frac{dz}{(2-Z)} = 1 - \frac{1}{(2-Z)} \int_0^X \int_{-\infty}^{\infty} \frac{\tau_w}{\rho U_0^2} \frac{dy}{a}\, dx$$
$$+ \frac{1}{(2-Z)} \int_0^X \int_{-\infty}^{\infty} (\frac{UW}{U_0^2} + \frac{\overline{u_1' u_3'}}{U_0^2}) \frac{dy}{a}\, dx \ . \tag{11}$$

The second term on the right in Equation 11 is due to the viscous shear on the upper plate.

If J/J_0 (Equation 10) is integrated from $z = 0$ to Z and divided by Z, the average momentum flux ratio from the midplane to Z is obtained;

$$AJ/J_0 = \int_0^Z \frac{J}{J_0} \frac{dz}{Z} = 1 - \frac{1}{Z} \int_0^X \int_{-\infty}^{\infty} (\frac{UW}{U_0^2} + \frac{\overline{u_1' u_3'}}{U_0^2}) \frac{dy}{a}\, dx \ . \tag{12}$$

The experimental momentum flux ratios, $J/J_0]_e$, were obtained by integrating $(U/U_0)^2$ from each Y traverse. The parabolic integration technique was used to obtain values of $IJ/J_0]_e$ and $AJ/J_0]_e$.

The integrated momentum flux ratio (Equation 11) for any Z, is influenced by the integrated shear stress values over the upper plate, and the flux of momentum through the X-Y plane at Z. The net vertical momentum flux, Ξ, is defined as

$$\Xi = \int_0^X \int_{-\infty}^{\infty} \left(\frac{UW}{U_0^2} + \frac{\overline{u_1'u_3'}}{U_0^2}\right)\frac{dy}{a}\, dx \tag{13}$$

To evaluate the effect of the secondary flow on the momentum flux ratios, calculations of IJ/J_0 were made with the net vertical momentum flux, Ξ, set equal to zero. This requires the assumption that the secondary flow and the Reynolds stress are both identically zero. Thus

$$IJ/J_0]_{zsf} = 1 - \frac{1}{(2-Z)} \int_0^X \int_{-\infty}^{\infty} \frac{\tau_w}{\rho U_0^2} \frac{dy}{a}\, dx \ . \tag{14}$$

At $Z = 0$, $IJ/J_0]_e = IJ/J_0]_{zsf}$ due to the symmetry in Z at the midplane. Consequently,

$$IJ/J_0]_{zsf} = 1 + \frac{2}{(2-Z)}\{IJ/J_0]_e|_{z=0} - 1\}. \tag{15}$$

The difference between $IJ/J_0]_e$ and $IJ/J_0]_{zsf}$ gives the sense of the net vertical momentum flux at any Z. That is

$$IJ/J_0]_e - IJ/J_0]_{zsf} = \frac{1}{(2-Z)} \int_0^X \int_{-\infty}^{\infty} \left(\frac{UW}{U_0^2} + \frac{\overline{u_1'u_3'}}{U_0^2}\right)\frac{dy}{a} dx = \frac{\Xi}{(2-Z)}. \tag{16}$$

Where $IJ/J_0]_e < IJ/J_0]_{zsf}$ the net vertical momentum flux is negative; where $IJ/J_0]_e > IJ/J_0]_{zsf}$ the net vertical momentum flux is positive. Because of the non-linearity of the momentum transport, the net vertical momentum flux contains both mean flow and turbulence contributions. The UW product in the net vertical momentum flux causes Ξ to be more sensitive to secondary flow velocities near the center-plane than is the net vertical mass flux. Since data for $\overline{u_1'u_3'}$ are not available, the sign of this Reynolds stress term must be inferred from the magnitude of the $U(z)$ gradient, namely, $\partial U/\partial z$.

The values of $J/J_0]_e$ and $AJ/J_0]_e$ are shown in Figures 50 and 52. Values of $IJ/J_0]_e$ and $IJ/J_0]_{zsf}$ appear in Figure 51.

4.2.4 Energy and Turbulence Energy Flux Ratios

The energy flux ratio, E/E_0, is defined as the ratio of the mean flow kinetic energy efflux through the $y - \Delta z$ face at X, to the mean flow kinetic energy influx through the $y - \Delta z$ face at $X = 0$;

$$E/E_0 = \int_{-\infty}^{\infty} \left(\frac{U}{U_0}\right)^3 dy \cdot \tag{17}$$

The integrated energy flux ratio, IE/E_0, is

$$IE/E_0 = \int_Z^2 \frac{E}{E_0} \frac{dz}{(2-Z)} \quad . \tag{18}$$

The average energy flux ratio, AE/E_0, is

$$AE/E_0 = \int_0^Z \frac{E}{E_0} \frac{dz}{Z} \ . \tag{19}$$

The energy flux ratios are influenced by the dissipation of mean flow kinetic energy through viscosity, the conversion of mean flow kinetic energy to turbulence kinetic energy, and the flux of mean flow kinetic energy out of the control volume due to the secondary flow. Because these effects can not be evaluated from the data in the present study, no zero secondary flow calculations were attempted for energy fluxes.

The values of $E/E_0]_e$, $IE/E_0]_e$, and $AE/E_0]_e$ are shown in Figures 53-55. Midplane and average values of the mass, momentum and energy flux ratios appear in Figure 59.

The turbulence kinetic energy flux ratio is defined as the ratio of the turbulence kinetic energy efflux through the $y - \Delta z$ face of the control volume at X to the mean flow kinetic energy influx through the $y - \Delta z$ face at $X = 0$. The turbulence kinetic energy flux ratios are:

$$TKE/E_0 = \int_{-\infty}^{\infty} \left(\frac{SD}{U_0}\right)^2 \frac{U}{U_0} \frac{dy}{a} \tag{20}$$

$$ITKE/E_0 = \int_{Z}^{2} \frac{TKE}{E_0} \frac{dz}{(2-Z)} \tag{21}$$

$$ATKE/E_0 = \int_{0}^{Z} \frac{TKE}{E_0} \frac{dz}{Z} \tag{22}$$

The values of $TKE/E_0]_e$, $ITKE/E_0]_e$, and $ATKE/E_0]_e$ are shown in Figures 56-58.

4.3 Vorticity Field Data

4.3.1 Determination of Meter Speed

As described in Chapter 3, the voltage signal from the hot-wire probe behind the vorticity meter, Figure 6, was autocorrelated to obtain the average meter speed. Because a blade of the meter passes the wire four times per meter revolution, the time at which the first positive peak occurs in the correlation represents one-quarter of a revolution; see Figure 60. The meter speed can then be calculated directly. Because, in some correlations, the occurrence of a broad positive peak made the direct determination of the meter speed arbitrary, a numerical Fourier cosine transform of the correlation was obtained. The meter speed was then interpreted to be the frequency at which the transformed correlation function attained its maximum value. This method takes advantage of the required periodicity of the correlation function and bases the meter speed on an integral value rather than a single point of the correlation function.

The numerical transform was obtained by generating 201 values of the correlation function by linear interpolation of the 100 values of the function output from the PAR 101 correlator. These 201 values were multiplied by $\cos(8\pi Ft)$ and summed over t to form the transform for a given frequency, F. By repeating the procedure for several frequencies, the maximum of the transform can be defined and the meter speed determined. For the correlation function shown in Figure 60, the directly measured speed was 21.01 rev/sec whereas the transform determined speed was 20.66 rev/sec. Meter speeds were determined by both methods for all correlation functions; in many cases the two calculated speeds were identical. All meter speed values shown in this study are transform determined.

4.3.2 Vortex Meter Response to a Wing-Tip Vortex

The vorticity meter described in Chapter 3 was traversed in the bounded jet flow field to determine the strength and location of zones of concentrated vorticity. To aid in the interpretation of the flow field data, the response of the meter to a wing-tip vortex generated by a flat plate at various angles of incidence was determined. The flat plate airfoil, with a thickness of 1/8 inch, a chord of 1 inch, and a leading edge with 60^{o} included angle, was positioned in the flow field with the trailing edge at $x = 1.5$, $y = z = 0$. X traverses were made in the trailing vortex ($y = 0$) for pitch angles of +10, +20, +30, and -10 with the 3/8 inch vorticity meter. The streamwise response of the meter for $\alpha = 10$ is shown in Figure 61a. For $\alpha = +10$, z traverses were made at two and four inches downstream from the trailing edge of the wing; see Figure 61b. The principal observations from this trailing vortex response determination were as follows:

1. Measurable meter rotation occurred for $z \leq \pm 1/4$ inch from the vortex core.
2. No reversal of the direction of rotation was observed as the meter was traversed out of the strong vortex core.
3. For distances greater than six inches from the trailing edge of the wing the meter rotation was too intermittent to be measurable.
4. The response of the 1/2 inch vorticity meter was similar to the response of the 3/8 inch meter.

4.3.3 Flow Field Vorticity Data

Y traverses were made with the 3/8 inch vorticity meter for the X, Z locations shown in Table 2. These traverse locations were selected as a result of a preliminary visual survey with the vorticity meter to determine approximately the strength and extent of the vorticity in the flow.

TABLE 2. Vorticity data traverse locations

Z \ X	1	2	3	4	5
1.75				x	x
1.7		x	x	x	x
1.6	x	x	x		x
1.5	x		x	x	x
1.4		x	x		x
1.3	x				
1.0		x			

The location of the changes in the sense of the vorticity and the location of the maximum meter rotation are shown in Figures 62, 64, 66, 68, and 70. Where the meter rotation was sufficiently strong and constant to cause a recognizable peak in the correlation function, the correlation was recorded for calculation of the meter speed. The meter speed distributions for the Y traverses are shown in Figures 63, 65, 67, 69, and 71. The excellent symmetry in these data confirms that the vorticity meter was not biased to either positive or negative rotation.

For distances greater than five inches from the nozzle exit plane, the vorticity was too intermittent for successful correlation. The observation that the concentrated wing-tip vortex was also not measurable for distances greater than six inches downstream suggests that the flow field vorticity is initially concentrated. The similarity between the Z traverse data for the wing-tip vortex, Figure 61b, and the lateral speed distributions in the flow field, Figures 63, 65, 67, 69 and 71, also suggests that the flow field vorticity is the result of concentrated vortex filaments formed near the nozzle exit plane.

CHAPTER 5

THE INITIATION, DEVELOPMENT AND DECAY OF THE SECONDARY FLOW

5.1 General Characteristics of Turbulent Jets

Turbulent jet flows exhibit several characteristics which are independent of the geometric configuration of the nozzle. Slightly downstream of the nozzle exit plane, the peripheral fluid of the jet is strongly sheared by ambient fluid. This intense shearing action initially occurs over a small lateral region; the fluid near the axis remains in an unsheared (or inviscid) condition. In this inviscid core the velocity remains nearly equal to the jet exit velocity. The result of the shearing action is the production of turbulence energy and the entrainment of ambient fluid into the main jet flow.

A few nozzle widths from the exit plane the shearing action permeates the entire lateral extent of the flow and the inviscid core disappears. The mean velocity gradients at the outside of the jet remain high even after the two shear layers merge. Increasing values of the turbulence kinetic energy result from the continued dominance of turbulence production over turbulence dissipation; a short distance downstream from the core the turbulence kinetic energy attains its maximum value.

The entrainment of ambient fluid causes the width of the jet to increase, with an associated increase in the mass transported across planes parallel to the plane of the nozzle exit. As the entrained fluid has no x-momentum, the conservation of momentum requires that, as streamwise momentum is imparted to the entrained fluid, the x-momentum of the fluid previously in the jet must decrease. The result is a decay of the centerline velocity and a general flattening of the velocity profiles.

The reduced velocity gradient and the reduced Reynolds stress needed to support the gradient cause a decrease in the production of turbulence kinetic energy. Since the dissipation of turbulence kinetic energy is dependent on the turbulence structure, rather than the mean velocity gradient, the dissipation will remain relatively large. This results in a decrease in the turbulence kinetic energy in the jet.

The behavior of the secondary flow in an incompressible turbulent bounded jet can be conveniently discussed by considering the flow in three downstream regions: the near field, middle field, and far field. The secondary flow is initiated in the near field by the reorientation of the planar vortex ring which forms a short distance downstream from the nozzle exit. A larger scale secondary flow, which increases in extent in the middle field, develops from the initially concentrated streamwise vorticity in the near field. The secondary flow decays in the far field as the streamwise vorticity is diffused.

5.2 The Extended Vortex Stretching Model

Immediately downstream of the nozzle exit plane the vortex sheets which separate the jet and ambient fluid become unstable. The distributed vortex filaments in these shear layers interact to form a planar rectangular vortex ring; see Figure 72. Since the vortex ring is formed from a given collection of fluid particles, it will be convected downstream by the mean flow. Because the short upper and lower sections of the ring are in the relatively slow moving boundary layer fluid, and since the long sides are not so constrained, the long sides will be convected ahead of the short sides. This results in the stretching of the long side filaments near the plate and a reorientation of the net vorticity vector. By this action, negative streamwise vorticity (in the $+y$, $+z$ quadrant) is produced near the bounding plates.

As shown by Hama (1962), Hama and Arms (1965), and Viets and Sforza (1969), an unconstrained eccentric vortex ring progressively deforms toward a circular shape. Near the midplane between the plates the long sides of the vortex ring move away from the centerplane (and each other) into a region of lower mean velocity as indicated schematically in Figure 72. Because this outward motion of the ring is greatest near the midplane, segments of the long sides at increasing distances from the midplane are subject to larger convection velocities. This causes stretching of the vortex filaments with an associated production of positive streamwise vorticity (in the $+y$, $+z$ quadrant).

The segments of the long side filaments just outside the boundary layer are neither slowed by the boundary layer nor pulled farther away from the centerplane by the expansion of the midsection of the vortex ring. Because these segments are subject to the greatest streamwise convection velocity, they become the leading sections of the deformed vortex ring.

In a free jet of rectangular cross-section, the leading short sides of the vortex ring move toward the jet midplane as the long sides move away from the jet centerplane. The effect of the plates in a bounded jet is to inhibit this motion of the short sides. With reference to Figure 72 for the bounded jet, it can be seen that the expansion of the midsection and the continuity of the vortex ring require that the leading segments on the long sides move toward the midplane.

The result of the stretching and reorientation of the initially planar vortex ring is the creation of zones of positive and negative streamwise vorticity with associated secondary flow velocities.

5.3 The Secondary Flow in the Near Field*

No distortion of the mean flow occurred at $X = 0.1$ as can be seen from the momentum flux thickness, mass flux ratio, and energy flux ratio data in Figures 25, 47, 53. The centerplane mean velocity distribution at the nozzle exit was uniform to within $\pm$ 0.5% for $0 \leq Z \leq 1.9$. Weak streamwise

---

* In this section, all references to positive and negative vorticity apply to the +y, +z quadrant.

vorticity was observed near the nozzle exit with the 1/4 inch meter. The Z location and sense of this vorticity was the same as observed near the plate at X = 1; see Figure 62. No consistant rotation of the 3/8 inch meter occurred near the jet exit plane.

5.3.1 Results at X = 1

The regions of positive and negative vorticity are shown in Figure 62 with the associated meter speed curves appearing in Figures 63a-63d. The outside positive zone caused by the stretching of the expanded segment of the ring is the dominant vorticity at this location. Because of its proximity to the plate, the upper region of negative vorticity was discernable only with the small 1/4 inch meter; hence no speed measurements were made. The location of this vorticity which is caused by the stretching near the plate is consistant with the very thin boundary layer observed at the nozzle exit. The presently unexplained zones of positive and negative vorticity in the center region do not appear to contribute to the large scale secondary flow farther downstream. It should be noted that the lateral dimensions of these four central zones are small with respect to the diameter of the meter (3/8 inch). Consequently, the measured and observed rotation of the meter is difficult to interpret in these regions.

5.3.2 Results at X = 2

As the expanded segment of the vortex ring approaches a circular shape (front view) the stretching of the filament produces a strong positive vorticity over an increasing vertical span as seen in Figure 64. The extent of the negative vorticity created by the stretching near the plate has also increased; negative rotation of the 3/8 inch meter is now observable. The weakening of the innermost positive region now precludes measurement of meter speed in that zone.

As shown in Figure 11a, the centerplane velocity is constant to within $\pm$ .5% for $0 < Z < 1.8$. The narrow section of the isotachs, Figure 13, around $Z = 1.7$ is the result of the inward secondary flow induced by the positive vorticity. The vortex stretching near the wall causes an outflow which is shown by the increasing width of the isotachs at $Z = 1.9$.

The centerplane intensity is slightly saddle shaped as shown in Figure 12a. The minimum value at $Z = 1.3$ results from the outflow induced by the inner positive vortex. This outflow, which counteracts the diffusion of turbulence energy to the centerplane, is also evident in the increased width of the center of the intensity contours near $Z = 1.3$; see Figure 14.

The double saddle shaped vertical velocity profiles in the near field for an aspect ratio of 2 and an aspect ratio of 4 shown by Bettoli (1968) are in agreement with the isotachs of the present study and are caused by the vortex stretching cited above.

For $X = 2$ the mass flux ratio integrated from Z to 2, IM/M_0, is everywhere less for the experimental data than for the zero secondary flow model;* see Figure 48. That is,

$$IM/M_0]_e - IM/M_0]_{zsf} = \frac{1}{(2-Z)} \int_0^X \int_{-\infty}^{\infty} \frac{W}{U_0} \frac{dy}{a} dx = \frac{\Lambda}{(2-Z)} < 0.$$

The net vertical mass flux, Λ, must therefore be negative (directed toward the midplane) for $0 < Z < 2$.

The experimentally determined mass flux ratio, $M/M_0]_e$, and the mass flux ratio calculated from the entrainment approximation with zero secondary flow, $M/M_0]_{zsf}$, appear in Figure 47. As shown in Chapter 4,

$$M/M_0]_e - M/M_0]_{zsf} = - \frac{d}{dz} \int_0^X \int_{-\infty}^{\infty} \frac{W}{U_0} \frac{dy}{a} dx = - \frac{d\Lambda}{dz} .$$

The net vertical mass flux, Λ, is a maximum or minimum when $-d\Lambda/dz = 0$. For $X = 2$, $-d\Lambda/dz = 0$ at $Z = 1.3$. Since $-d^2\Lambda/dz^2 < 0$ at $Z = 1.3$, $-\Lambda$ is a maximum at this Z location.

Therefore, the net vertical mass flux is negative for $0 < Z < 2$ and attains its maximum negative value at $Z = 1.3$. This corresponds to the region of the largest negative secondary flow velocity on the centerplane caused by the inner positive vortex.

For $X = 2$ the momentum flux ratio integrated from Z to 2, IJ/J_0, is also everywhere less for the experimental data than for the zero secondary flow model; see Figure 51.

---

* A detailed derivation and explanation of the several flux ratios and the entrainment velocity approximation used in this study appear in Chapter 4.

That is,

$$IJ/J_0]_e - IJ/J_0]_{zsf} = \frac{1}{(2-Z)} \int_0^X \int_{-\infty}^{\infty} \left(\frac{UW}{U_0^2} + \frac{\overline{u_1'u_3'}}{U_0^2}\right) \frac{dy}{a}\, dx$$

$$= \frac{\Xi}{(2-Z)} < 0 \quad \text{for} \quad 0 < Z < 2.$$

The net vertical momentum flux, Ξ, must therefore be negative through every X, Y plane for X = 2. It should be noted that the zero secondary flow model assumes that both the secondary flow velocity W, and the Reynolds stress term, $\overline{u_1'u_3'}$, are zero. Because of the UW/U_0^2 product, Ξ is more dependent on the secondary flow velocities near the centerplane than is Λ. For X = 2, the inner positive vortex causes negative secondary flow velocities near the centerplane. UW/U_0^2 is therefore strongly negative. The isotachs suggest that $\partial U/\partial z$ is large only in the boundary layer; thus $(\overline{u_1'u_3'})/U_0^2$ is small over most of the field. Consequently the primary contribution to the negative net momentum flux at X = 2 is made by the UW/U_0^2 term.

5.3.3 Results at X = 3

At three nozzle widths downstream from the exit plane the region of weak negative vorticity between the two positive regions is no longer discernable; see Figure 66. The vertical extent of the strong positive region has decreased to 1.2 < Z < 1.8. As the strength and extent of the positive vorticity have decreased, the strength and extent of the negative vorticity due to stretching near the plate have increased.

5.3.4 Results at X = 4

The roll-up of the positive streamwise vortex zone suggested at X = 3 is strongly apparent in Figure 68 for X = 4. The negative zone is expanding concurrently with the diffusion of vorticity in the positive region. The maximum vortex strength is nearly equal in the positive and negative zones, as shown in Figures 69a-69c.

5.3.5 Results at X = 5

The trend toward increasing size and strength of the region of negative vorticity caused by the stretching near the plate continues at five nozzle widths downstream from the exit. The location of the maximum positive vorticity has moved toward the centerplane; see Figure 70. This movement is suggested by the photographs of the deformation of a vortex ring generated by a rectangular orfice in Viets and Sforza (1969). After expanding from its initial eccentric shape toward an eccentric shape with major and minor axis reversed, the vortex ring deformation changes and the ring deforms toward its original shape. The observed weakening of the positive vorticity near Z = 1.5 would result from a similar behavior in the bounded jet. As the midsection of the long side filaments moves toward the faster moving fluid near the centerplane the vortex stretching in this region is weakened and the strength of the positive streamwise vorticity decreases.

The isotachs for X = 5 are shown in Figure 15. The height of the narrowest part of the isotachs moves from Z = 1.6

near the outside of the jet to $Z = 1.7$ near the centerplane of the jet. This region of strong inflow is the separation of the positive and negative vorticity zones as shown in Figure 70. The centerplane velocity, Figure 11a, is flat for $1.6 < Z < 1.8$. For $1.3 < Z < 1.6$, the increasing centerplane velocity is a result of the negative secondary flow near the centerplane caused by the positive vortex. The outflow in the vicinity of $Z = 1.3$ induced by the positive vorticity causes the observed widening of the isotachs near the centerplane.

This outflow from a region of low turbulence intensity inhibits the diffusion of high intensity fluid toward the centerplane. The result is the increased width of the low intensity contours near $Z = 1.3$ in Figure 16. The narrow low intensity region in the intensity contour for $1.5 < Z < 1.7$ is similarly due to the positive vortex inflow. The strong inflow between the positive and negative vorticity regions results in narrow intensity contours near the outside of the jet for $Z = 1.6$.

At $X = 5$, $IM/M_0]_e$ is everywhere greater than $IM/M_0]_{zsf}$; see Figure 48. Therefore the net vertical mass flux, Λ, is negative for $0 < Z < 2$ as it was at $X = 2$. The equality of $M/M_0]_e$ and $M/M_0]_{zsf}$ at $Z = 1.3$ in Figure 47 implies that the maximum negative value of Λ occurs at $Z = 1.3$. The location of the maximum is due primarily to the negative centerplane W caused by the positive vortex.

The relative minimum in $M/M_0]_e$ at $Z = 1.6$ and the relative maximum at $Z = 1.8$ cause a plateau in the net vertical mass flux at $Z = 1.7$; see Figure 46a. The negative z-component velocities in the boundary layer and the negative W velocities caused by the vortex structure are therefore interpreted to represent separate physical effects.

The IJ/J_0 curves, Figure 51, also show a net vertical momentum flux toward the midplane for $0 < Z < 2$. For $1.0 < Z < 1.7$, the $IJ/J_0]_e$ curve exhibits a constant Z-gradient caused by the strong negative secondary flow velocities near the centerplane. Because Ξ is more dependent on secondary flow velocities near the centerplane than is Λ, the constant gradient section is more pronounced in $IJ/J_0]_e$ than in $IM/M_0]_e$.

The energy flux ratio curves for $X = 2$ and $X = 5$, Figure 53, are approximately parallel except for $1.0 < Z < 1.2$. The general decrease in the energy flux ratio occurs as turbulence kinetic energy is produced at the expense of the mean flow kinetic energy. The high energy flux ratio at $X = 5$ for $1.0 < Z < 1.2$ reflects a build-up of high energy fluid in the center region caused by the convective action of the positive vortex.

5.4 The Large Scale Secondary Flow in the Middle Field

In the middle field the vortex stretching and re-orientation near the plate has become the dominant feature of the flow field, with the result that a large scale secondary flow exists in each of the four quadrants of the bounded jet. The secondary flow causes spreading of the isotachs and distinct shape differences in the dimensionless mean velocity profiles.

The dimensionless mean velocity profiles for $Z \neq 0$, compared with the midplane profiles at each downstream location show two characteristic types of distortion. Above the center of rotation of the secondary flow the profiles are typically of the crossover type shown in Figure 73. Near the midplane the dimensionless profiles are similar. Between the similar and crossover profiles, corresponding to the region below the center of rotation of the secondary flow, the profiles are of the tail-excess type also shown in Figure 73.

The relation of these distortions to the secondary flow can be seen by considering a large scale circulating motion as shown in Figure 74. For a narrow control volume of height Δz there will be differences in the net secondary flow into the control volume in the various parts of the circulating zone. The dashed line through the center of the circulating flow region represents a constant times the scale width of the jet, cb.

For $Z > Zc$ and $y < cb$ the secondary flow influx is greater than the efflux. This is balanced by an increased efflux from the control volume in the x-direction; $U(X, < cb, > Zc) > U(X, < cb, 0)$. For $Z > Zc$ and $y > cb$ the secondary flow efflux is greater than the influx. This causes a decreased efflux from the control volume in the streamwise direction; $U(X, > cb, > Zc) < U(X, > cb, 0)$. When compared to the midplane profile, the dimensionless profile for $Z > Zc$ is distorted by the local excess and deficit into the crossover shape.

For $Z < Zc$ and $y > cb$ the secondary flow influx is greater than the efflux creating an increase in the streamwise efflux from the control volume; $U(X, > cb, < Zc) > U(X, > cb, 0)$. This causes a tail-excess profile compared to the midplane curve.

Because of the tendency toward similarity in the profiles, it can be assumed, for a given y/b, that V remains in the same proportion to U for all Z. Thus the profile distortion can be attributed to the excess and deficit in the streamwise velocity.

As will be evident from the isotach contours in the middle field, the jet is considerably wider near the bounding plates than at the midplane. Without a dimensionless presentation of the data, the profile shape differences would not be discrenable. The observation that the dimensionless mean velocity profiles are similar except for the relatively small characteristic distortions is also significant. It can be inferred that the tendency toward a "self-preserving" structure is quite strong.

5.5 Discussion of Results for the Middle Field

5.5.1 Results at $X = 10$

One effect of the vortex structure, from the nozzle exit to ten nozzle widths downstream, has been to accelerate the normal boundary layer growth at the centerplane. This is apparent in the centerplane velocity profile shown in Figure 11a. A constant maximum value of the centerplane intensity occurs for $0.8 < Z < 1.8$; see Figure 12a. This region is caused by the convection of the very high intensity fluid in the boundary layer at $X = 5$ away from the wall for $5 < X < 10$. The development of positive secondary flow velocities on the centerplane near the midplane retards the diffusion of this high intensity fluid to the midplane.

The isotachs for $X = 10$ are straight for $0 < Z < 1.0$, see Figure 17. In the upper half plane the width of the isotachs increases significantly suggesting that the primary influence on the secondary flow is in that region.

The dimensionless mean velocity profiles, Figures 33a and 33b, are similar for $0 < Z < 1.0$. Crossover profiles occur for $Z > 1.7$. Between $Z = 1.0$ and $Z = 1.7$ the profiles are the tail-excess type. Therefore, the center of the circulating zone is considered to be at $Z = 1.7$.

No net vertical mass flux occurs for $0 < Z < 0.7$ as can be seen from the IM/M_0 curves in Figure 48. At $X = 5$ the net vertical mass flux in this region is negative. Therefore, in order to have a net zero Λ at $X = 10$, there must be local positive secondary flow velocities, $W > 0$, in the vicinity of $X = 10$.

The M/M_0 and IM/M_0 curves show a negative net vertical mass flux for $1.6 < Z < 2$ with the maximum negative value occurring at $Z = 1.9$. The shift of the negative maximum from $Z = 1.3$ at $X = 5$ to $Z = 1.9$ at $X = 10$ reflects the development of positive secondary flow velocities in the center region as the large scale secondary flow increases.

For $X = 10$ the net vertical momentum flux remains negative for all $Z > 0$, see Figure 51. As can be inferred from the vorticity contour at $X = 5$, Figure 70, the positive vertical secondary flow velocities are greatest away from the centerplane. Thus the UW term in $IJ/J_0]_e$ is increased less than the W term in $IM/M_0]_e$. The spreading isotachs at $X = 10$ suggest that $\overline{u_1'u_3'} < 0$. This effect combined with the net negative UW effect causes the negative Ξ value at $X = 10$.

The energy flux ratio, Figure 53, at ten nozzle widths downstream decreases monotonically as Z increases.

5.5.2 Results at $X = 15$

In Figure 11b, the centerplane velocity profile at $X = 15$ is flat for $0 < Z < 1.2$ and decreases for $Z > 1.2$. The isotachs show the increasing scale of the secondary flow as the spreading begins at $Z = 0.5$, compared to $Z = 1.0$ for $X = 10$, see Figure 19.

The center of rotation has also moved toward the midplane as can be seen in the dimensionless mean velocity profiles, Figures 35 and 35b. These are similar for $0 < Z < 1.0$, tail-excess for $1.0 < Z < 1.4$, and crossover for $Z > 1.4$. The center of rotation of the secondary flow is therefore considered to be located near $Z = 1.4$.

The maximum value of the centerplane intensity occurs at $Z = 0$; this corresponds to the narrowest region of the jet. See Figure 12b. As the secondary flow away from the centerplane causes the jet to become wider, the diffusion of high intensity fluid to the centerplane is inhibited. This results in a decreasing intensity level as Z increases. The local maximum in the intensity at $Z = 1.7$ occurs in the boundary layer flow near the upper plate.

As the secondary flow causes the jet to become wider, the decreased mean velocity gradients cause a decrease in the production of turbulence energy. Although the peak value of the intensity is less in this region than on the midplane, the turbulence kinetic energy flux ratio increases slightly due to the increased width of the high intensity region caused by the secondary flow. See Figures 20 and 56.

The M/M_0 and IM/M_0 curves, Figures 47 and 48, show a positive net vertical mass flux for $0 < Z < 1.7$ and a negative net vertical mass flux near the wall. The maximum positive value occurs at $Z = 1.0$ with the negative maximum at $Z = 1.9$. The difference between the location of the local center of rotation and the location of maximum positive Λ is due to the negative secondary flow in the near field.

For $0 < Z < 1.3$, $IJ/J_0]_e$ is slightly greater than $IJ/J_0]_{zsf}$; see Figure 51. The momentum transport to the control volume is less than the mass transport due to the center weighting of the secondary flow velocity, W, in the momentum integral and the occurance of the negative Reynolds stress, $\overline{u_1'u_3'} < 0$, caused by the spreading isotachs ($\partial U/\partial z > 0$). This also causes the net vertical momentum flux to become negative before the sense of the net vertical mass flux changes.

The energy flux ratio, Figure 53, for $X = 15$ is less than for $X = 10$ in the range $0 < Z < 1.5$ since the mean flow kinetic energy is decreased by dissipation and the production of turbulence kinetic energy. The energy flux ratio for these two downstream locations are approximately equal for $Z > 1.5$. This shows that the mean flow energy transferred into the upper regions, causing the isotachs to become wider in the center, is sufficient to compensate for the effect of the downstream decay of the centerplane velocities.

5.5.3 Results at $X = 20$

The secondary flow circulating zone influences the entire span between the plates at $X = 20$. This is shown by the isotachs which begin to spread at the midplane in Figure 21. The dimensionless midplane mean velocity profile for $X = 20$ is distorted to the tail-excess shape with respect to the midplane profile at $X = 15$; see Figure 27c. The dimensionless mean velocity profiles at $X = 20$, Figures 38a and 38b, are similar for $0 < Z < 1.0$ and crossover for $1.0 < Z < 2$ when compared to the midplane profile. The center of the circulating zone is thus at $Z = 1.0$.

The increasing secondary flow causes a flow toward the wall near the centerplane which decreases the thickness of the boundary layer at $X = 20$ compared with $X = 15$. This flattened centerplane velocity profile is shown in Figure 11b.

The net vertical mass flux is positive for $0 < Z < 1.7$ with the maximum value occurring at $Z = 1.0$ as shown by the IM/M_0 and M/M_0 curves in Figures 48 and 47.

For $X = 20$ the net vertical momentum flux is positive everywhere. Since the net vertical **mass flux is negative for** $1.7 < Z < 2$ the dominant contribution to the net vertical momentum flux must come from $\overline{u_1'u_3'}$ which is greater than zero due to the negative $\partial U/\partial z$ in the boundary layer.

The decreasing turbulence kinetic energy ratios from $X = 15$ to $X = 20$, Figure 56, reflect the dominance of dissipation over production.

5.6 <u>The Secondary Flow Decay in the Far Field</u>

The trend toward a flattening of the centerplane mean velocity profiles, which was first apparent at twenty nozzle widths downstream of the nozzle exit, continues in the far field. The profiles for $X = 30$ and $X = 40$ are shown in Figure 11c.

Downstream from the region of maximum observed influence of the large scale secondary flow, i.e., $X = 20$, the secondary flow strength decreases as the vorticity is diffused. At $X = 40$, the isotachs, Figure 23, show none of the curvature or widening effects caused by the secondary flow in the middle field. As was true in the near field, the constant intensity contours appear to be more sensitive to small secondary flow distortion than are the isotachs. At $X = 40$, the intensity contours suggest that a weak secondary flow may still be present, see Figure 24. The distinct shape differences in the dimensionless mean velocity profiles which were characteristic of the middle field are not present at $X = 40$. The profiles for various Z locations are similar to the centerplane profile except at $Z = 1.8$ and 1.9, see Figures 41a and 41b.

From the M/M_0 curve, Figure 47, the net secondary flow from the nozzle exit to $X = 40$ is slightly positive with the maximum occurring at $Z = 0.5$. Even for a zero secondary flow condition at $X = 40$ this number would be expected to be positive as a result of the strong positive secondary flow in the middle field.

At $X = 40$, the energy flux ratio is small and exceptionally constant for all Z; see Figure 53. This reflects the dominance of the energy dissipation phenomena in the far field.

CHAPTER 6

SUMMARY AND COMPARISON WITH THE PLANE JET

The momentum flux thickness variations, Figure 25, and the average and midplane flux ratios, Figure 59, illustrate the important characteristics of the three regions of the bounded jet. In the near field, the jet is narrower at $Z \approx 1.7$ than at the midplane as a result of the strong inflow caused by the double stretching of the initially planar vortex ring. The resultant secondary flow toward the midplane causes the midplane flux ratios to be greater than the average values. The average width of the jet increases only slightly from the width of the nozzle in the near field.

The large scale secondary flow in the middle field causes the increasing jet width as Z increases; see Figure 25. For greater distances downstream, the secondary flow effects are observed in an increasing percentage of the Y, Z plane. The secondary flow velocities directed away from the midplane cause a net transport of mass, momentum, and energy away from the midplane region; therefore, the midplane flux ratios are less than the average flux ratios in the middle field.

In the far field, the decay of the secondary flow is reflected in smaller percentage changes in the jet width as Z increases; see Figure 25. This decay is also evident from the tendency of the midplane and average flux ratios to approach equality; see Figure 59.

Because a plane jet flow is approached as the aspect ratio of a bounded jet becomes large, the plane jet flow provides a natural reference for concluding the discussion of the flow behavior in a modest aspect ratio bounded jet.

The centerline velocity of the bounded jet is consistantly greater than the centerline velocity given by Albertson, et. al. (1948) for a plane jet; see Figure 10. Following the closing of the inviscid core, the bounded jet centerline velocity decays more slowly than the centerline velocity in the plane jet. Farther downstream in the middle field, the centerline velocity in the bounded jet decays faster than the centerline velocity of the plane jet. For increasing distances from the nozzle exit in the far field, the decay rates of the centerline velocity for the two flows approach each other.

The midplane and average momentum flux thickness values for the bounded jet are shown in Figure 26 along with the corresponding curve for a plane jet from Miller and Comings (1957). In the near field where the net vertical mass flux in the bounded jet is negative for $0 < Z < 2$, the midplane width of the bounded jet is greater than the width of the plane jet. In the middle field the net vertical mass flux in the bounded jet is away from the midplane; consequently the midplane width of the bounded jet is less than the width of the plane jet. As the secondary flow in the bounded jet decays in the far field, the midplane width of the bounded jet approaches the width of the plane jet. An additional affect may be expected in the far field. The wall shear will act to retard the fluid near the wall; the resulting "displacement thickness effect" will cause the jet to be relatively wider than a plane jet at the same X location.

The (approximate) equivalence of the average width of the bounded jet and the width of the plane jet supports the interpretation of the bounded jet flow as a plane jet flow with a superimposed secondary motion. Also, the good agreement between the bounded jet average width and the plane jet width given by Miller and Comings (1957) lends credulity to the overall measurement accuracy of the present study.

BIBLIOGRAPHY

BIBLIOGRAPHY

Albertson, M. J., et. al., "Diffusion of Submerged Jets," Proceedings, ASCE, Vol. 74, (1948).

Bettoli, R., "Experimental Study of Spreading of Semi-Confined Jets," M. S. Thesis, Department of Mechanical Engineering, The Pennsylvania State University, (1968).

Bradbury, L. J. S., "The Structure of a Self-Preserving Turbulent Plane Jet," Journal of Fluid Mechanics, Vol. 23, Part 1, (1967).

Brundrett, E., and Baines, W. D., "The Production and Diffusion of Vorticity in Duct Flow," Journal of Fluid Mechanics, Vol. 19, Part 3, (1964).

Forthmann, E., "Turbulent Jet Expansion," NACA TM 789, (1934).

Foss, J. F., "A Study of Incompressible Turbulent Bounded Jets," Ph.D. Thesis, School of Mechanical Engineering, Purdue University, (1965).

Foss, J. F., and Jones, J. B., "Secondary Flow Effects in a Bounded Rectangular Jet," Trans. ASME, Journal of Basic Engineering, Vol. 90, Series D., No. 2, (1968).

Foss, J. F., "A Study of an Incompressible Turbulent Bounded Jet," Final Report, NSF GK-340, Division of Engineering Research, Michigan State University, (1969).

Gessner, F. B., and Jones, J. B., "On Some Aspects of Fully-Developed Turbulent Flow in Rectangular Channels," Journal of Fluid Mechanics, Vol. 23, Part 4, (1965).

Gray, R. W., "Effects of Upstream Disturbance Intensity on the Spreading of a Semi-Confined Jet," Department of Mechanical Engineering, The Pennsylvania State University, (1969).

Hama, F. R., "Progressive Deformation of a Curved Vortex Filament by its Own Induction," Physics of Fluids, Vol. 10, No. 5, (1962).

Hama, F. R., and Arms, R. J., "Localized Induction Concept on a Curved Vortex and Motion of an Elliptic Vortex Ring," Physics of Fluids, Vol. 8, No. 4, (1965).

Heskestad, G., "Hot-Wire Measurements in a Plane Turbulent Jet," Trans. ASME, Journal of Applied Mechanics, Vol. 32, Series E, No. 4, (1965).

Heskestad, G., Discussion of "Secondary Flow Effects in a Bounded Rectangular Jet," Trans. ASME, Journal of Basic Engineering, Vol. 90, Series D, No. 4, (1968).

Miller, D. R., and Comings, E. W., "Static Pressure Distribution in the Free Turbulent Jet," Journal of Fluid Mechanics, Vol. 3, Part 1, (1957).

Sforza, P. M., Steiger, M. H., and Trentacoste, N., "Studies on Three-Dimensional Viscous Jets," AIAA Journal, Vol. 4, No. 5, (1966).

Sforza, P. M., and Trentacoste, N., "Mean Flow Non-Uniformities in Three-Dimensional Turbulent Shear Flows," Polytechnic Institute of Brooklyn, PIBAL Report (1969).

Townsend, A. A., The Structure of Turbulent Shear Flow, Cambridge University Press, (1956).

Trentacoste, N., and Sforza, P. M., "An Experimental Investigation of Three-Dimensional Free Mixing of Incompressible, Turbulent, Free Jets," Polytechnic Institute of Brooklyn, PIBAL Report 871, (1966).

Van der Hegge Zijnen, B. G., "Measurements of the Velocity Distributions in a Plane Turbulent Jet of Air," Applied Scientific Research, Section A, Vol. 7, No. 4, (1958).

Viets, H., and Sforza, R. M., "Dynamics of Bilaterally Symmetric Vortex Rings," Polytechnic Institute of Brooklyn, PIBAL Report 69-37, (1969).

ILLUSTRATIONS

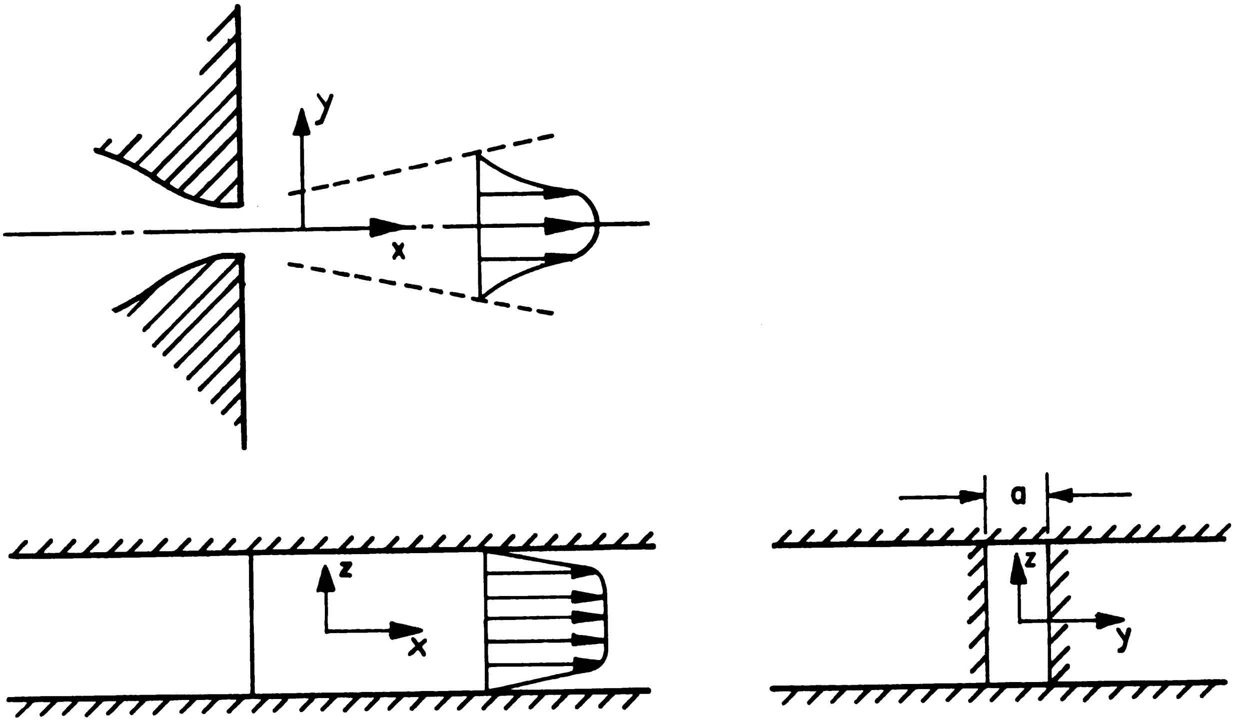

Figure 1. Schematic representation of bounded jet flow field.

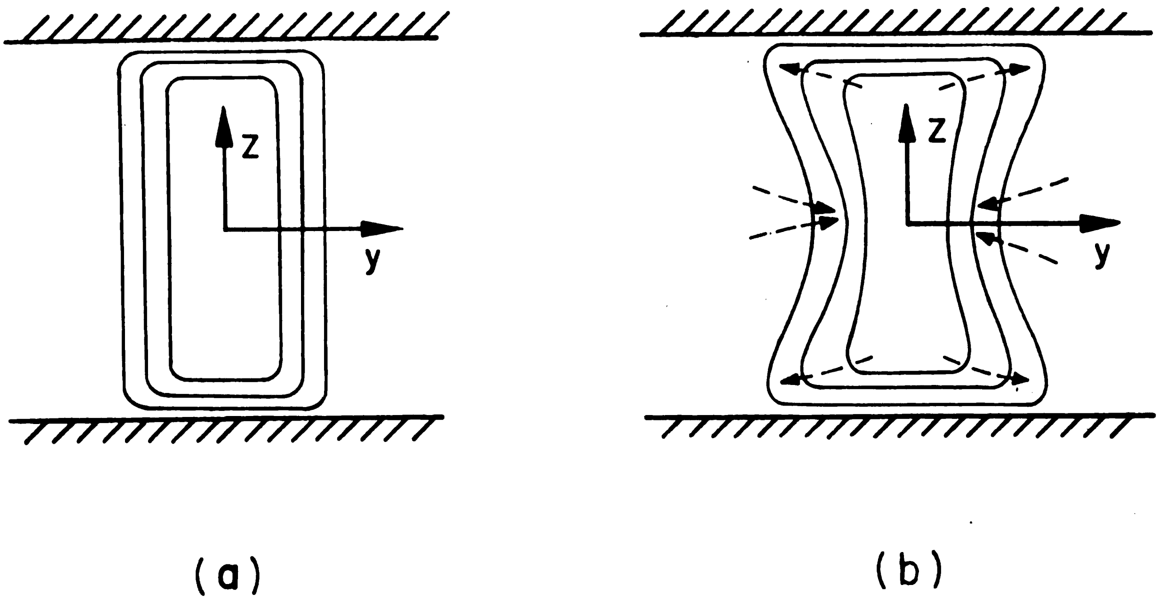

Figure 2. Schematic representation of bounded jet isotachs.

Figure 3.

Schematic drawing of the air flow system.

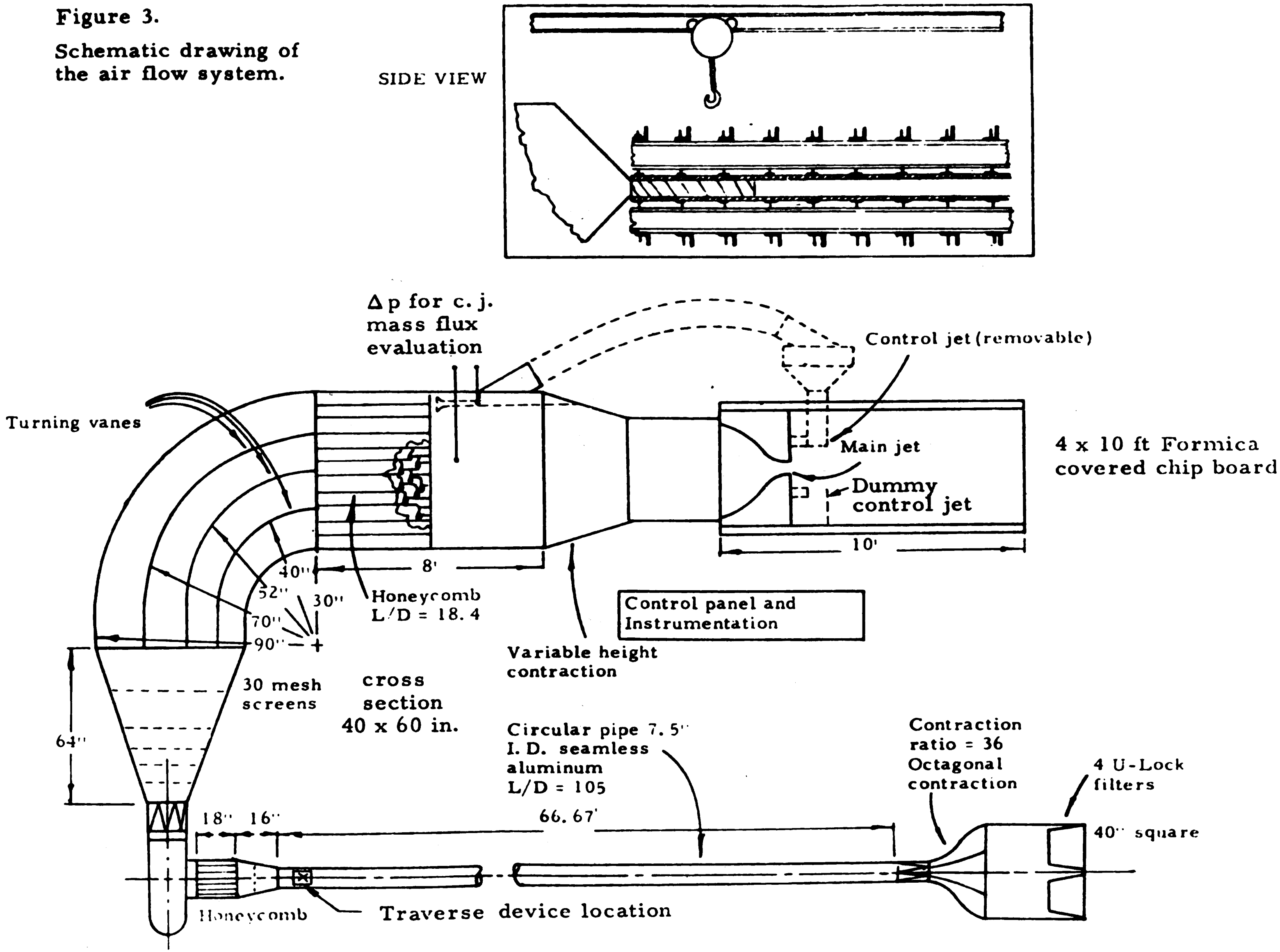

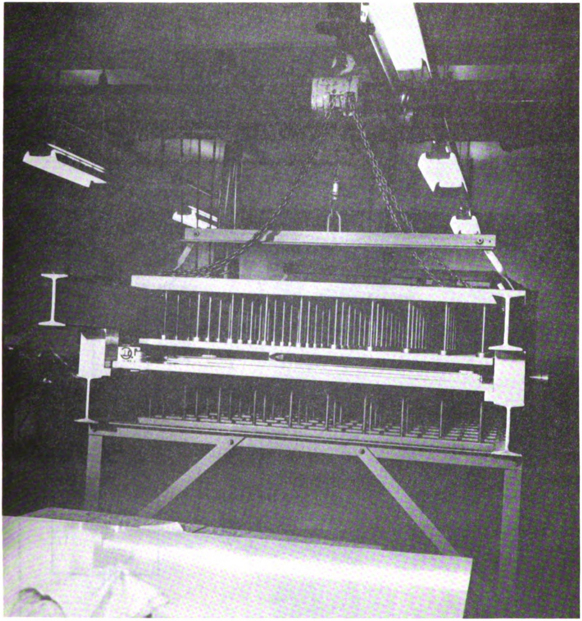

Figure 4. End view of the parallel plates showing the support bolts.

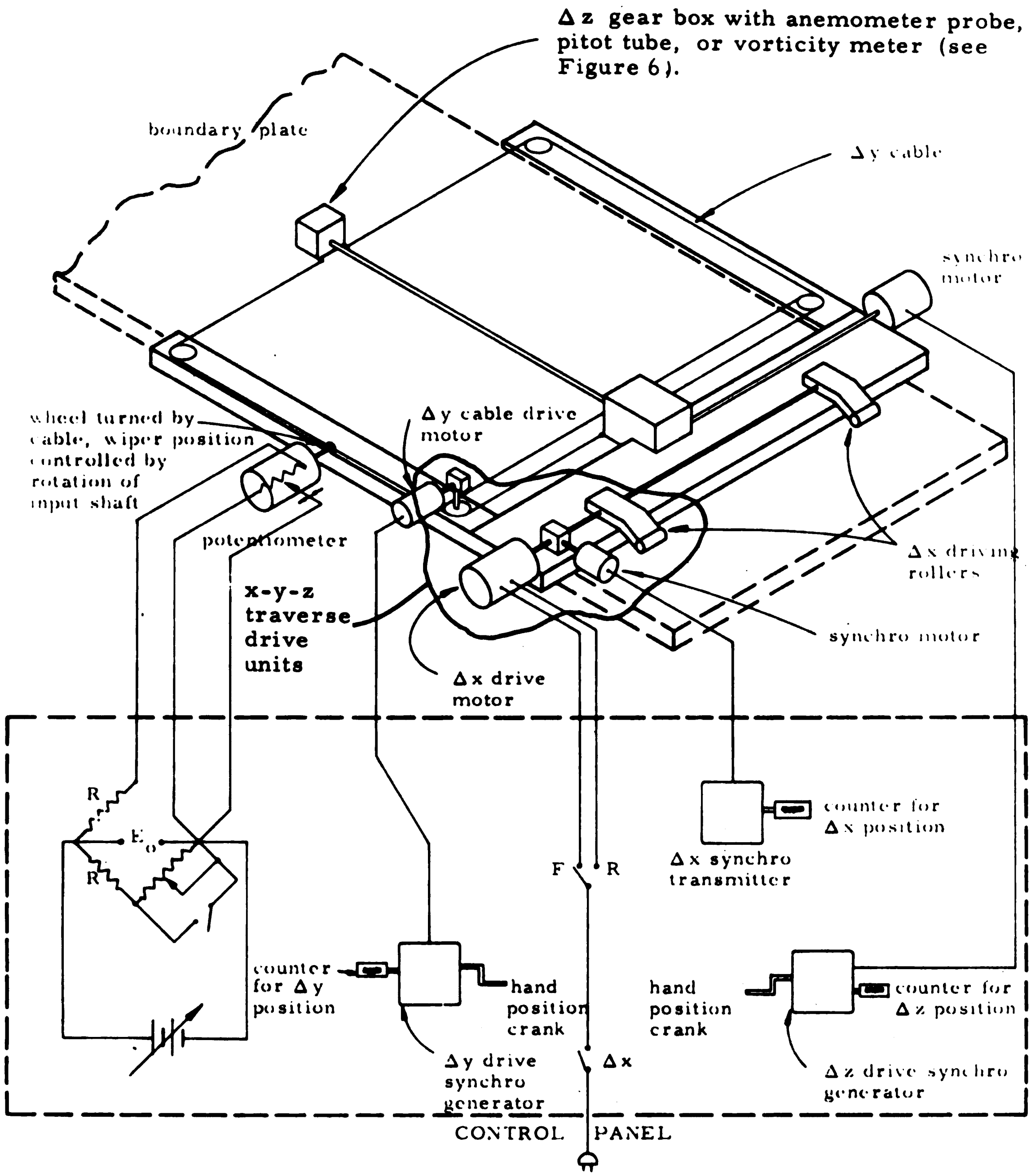

Modes of operation: With shorting switch closed, resistence across the 40 turn pot on the traverse is sensed. With shorting switch open, may set control panel helipot for null at "y = 0", set sensitivity of read-out with the power supply.

Figure 5. Schematic drawing of the x-y-z traverse system.

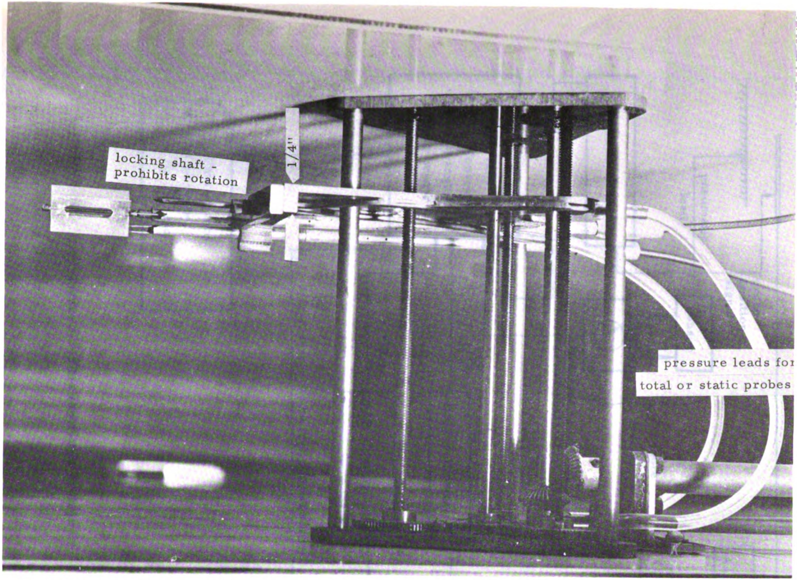

Figure 6. Vorticity meter and 4-inch z-traverse unit.

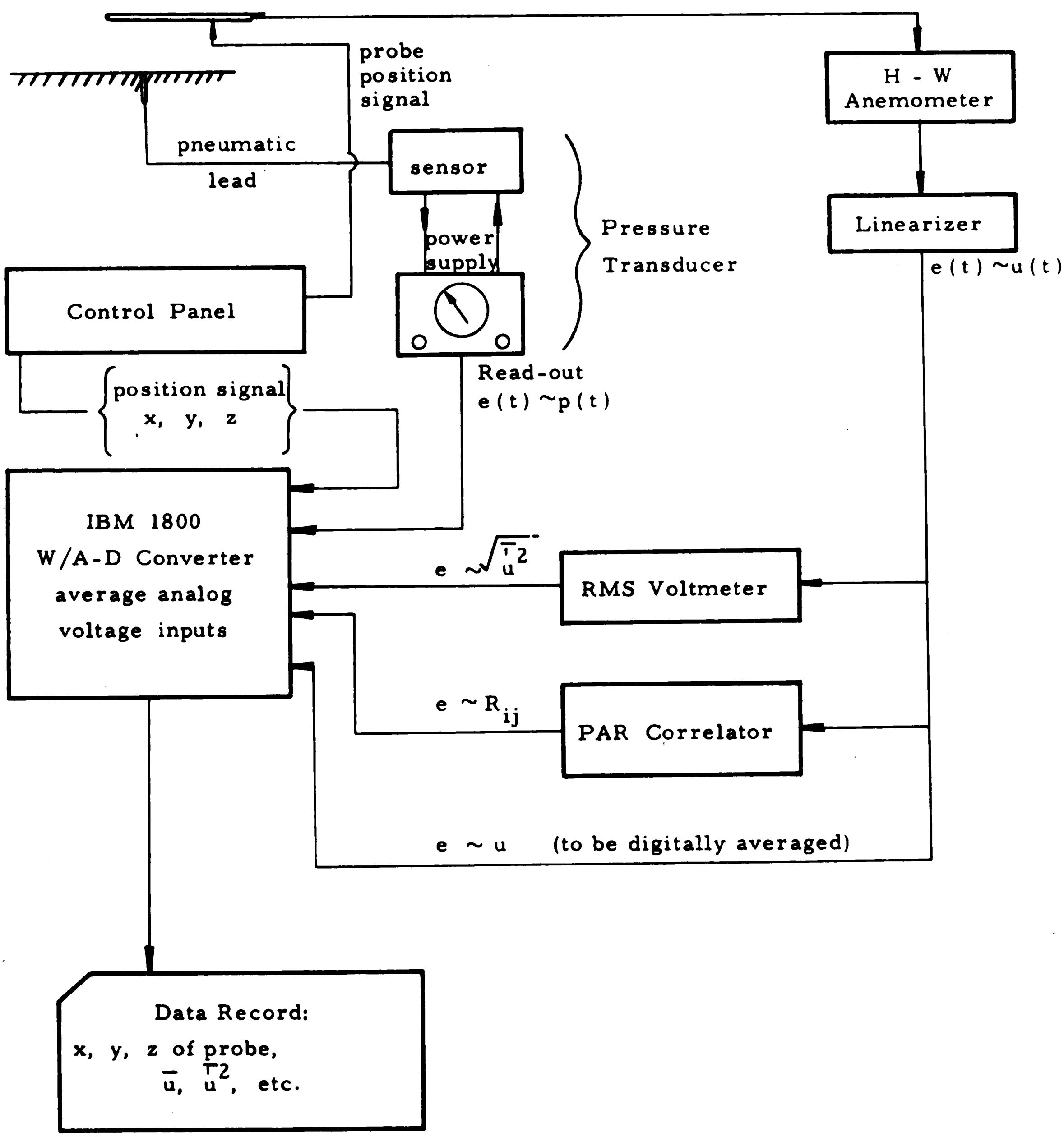

Figure 7. Data acquisition system.

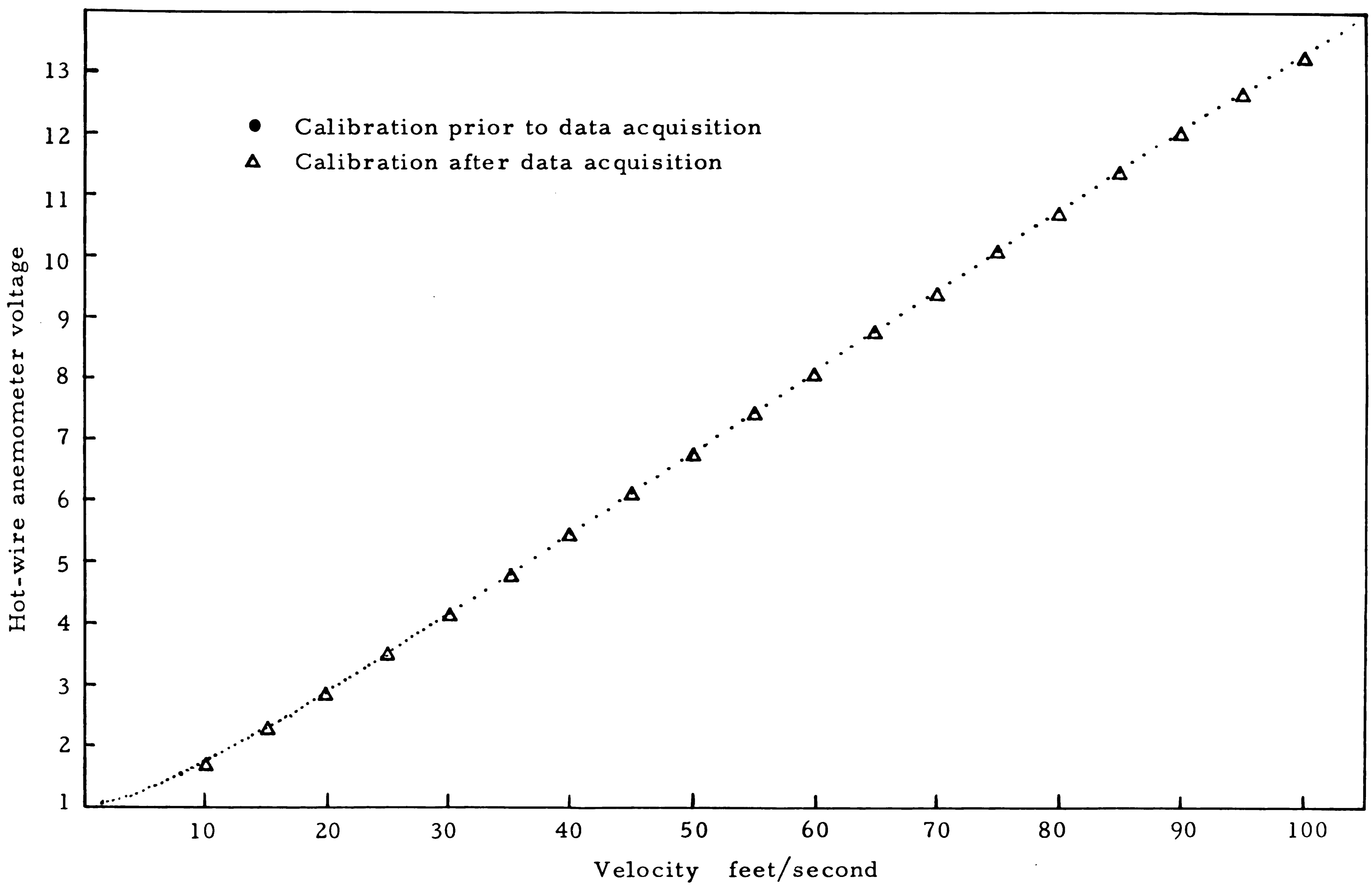

Figure 8. Hot-wire anemometer calibration curve

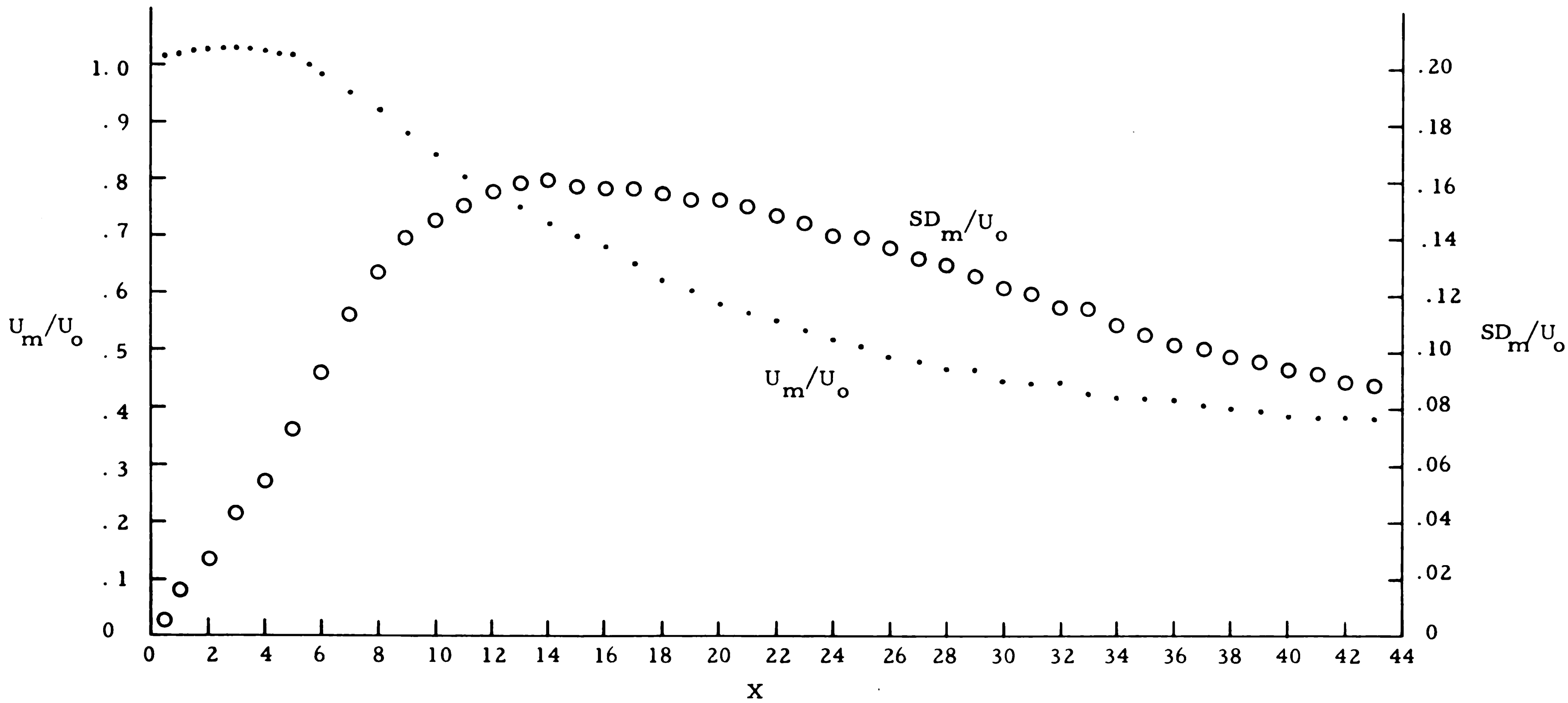

Figure 9. Centerline mean velocity and turbulence intensity

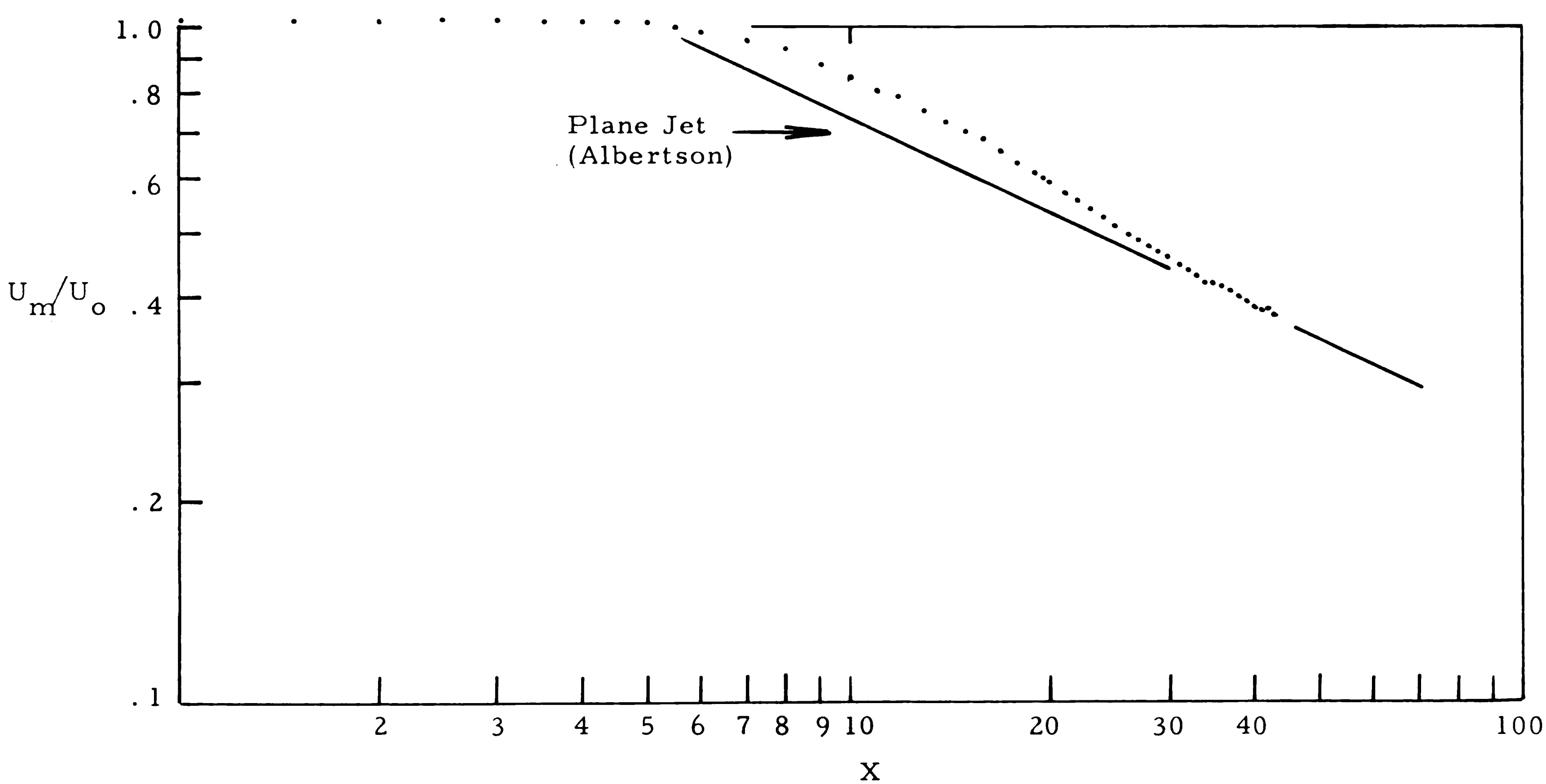

Figure 10. Centerline mean velocity for bounded jet and plane jet

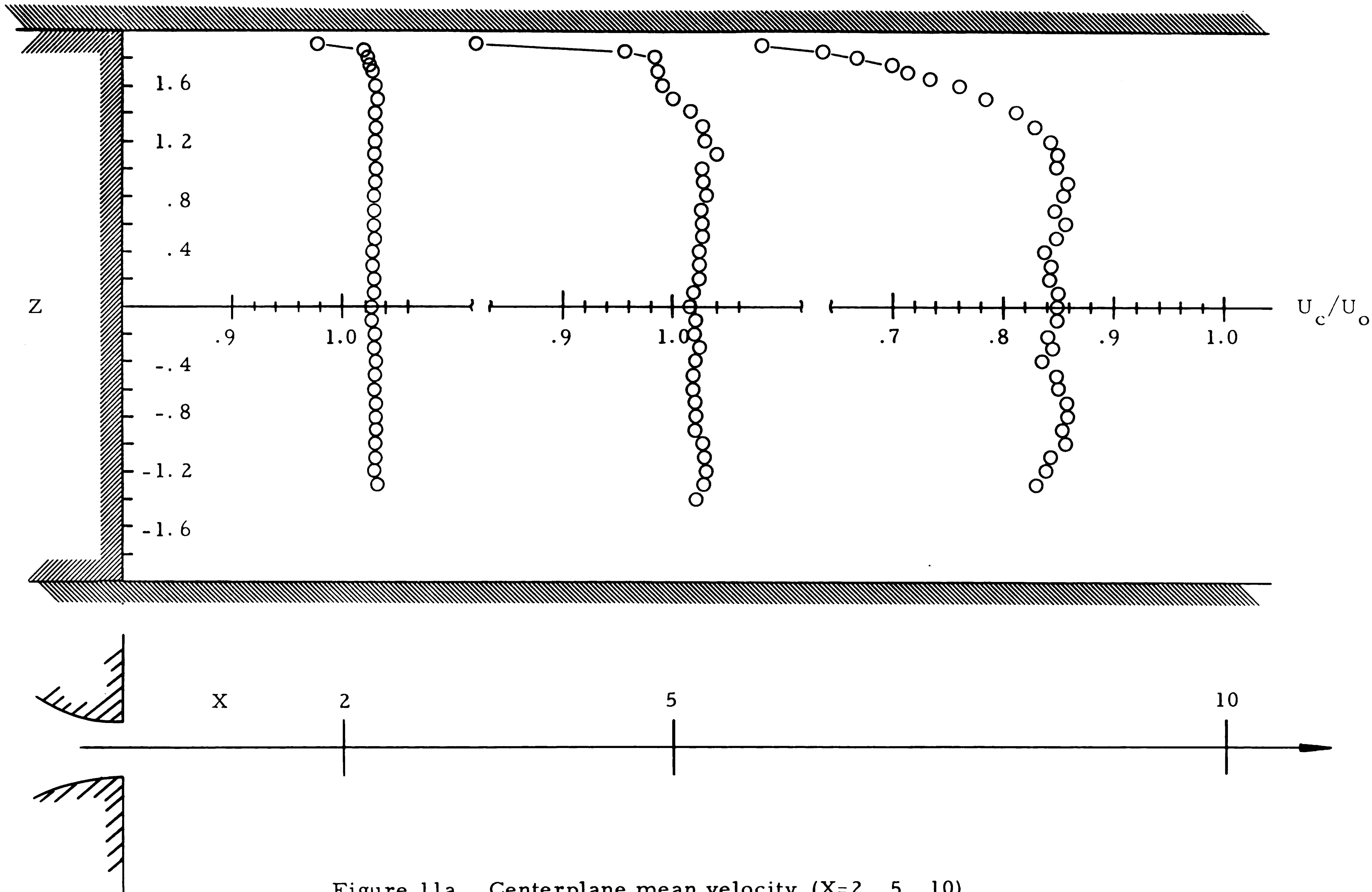

Figure 11a. Centerplane mean velocity (X=2, 5, 10)

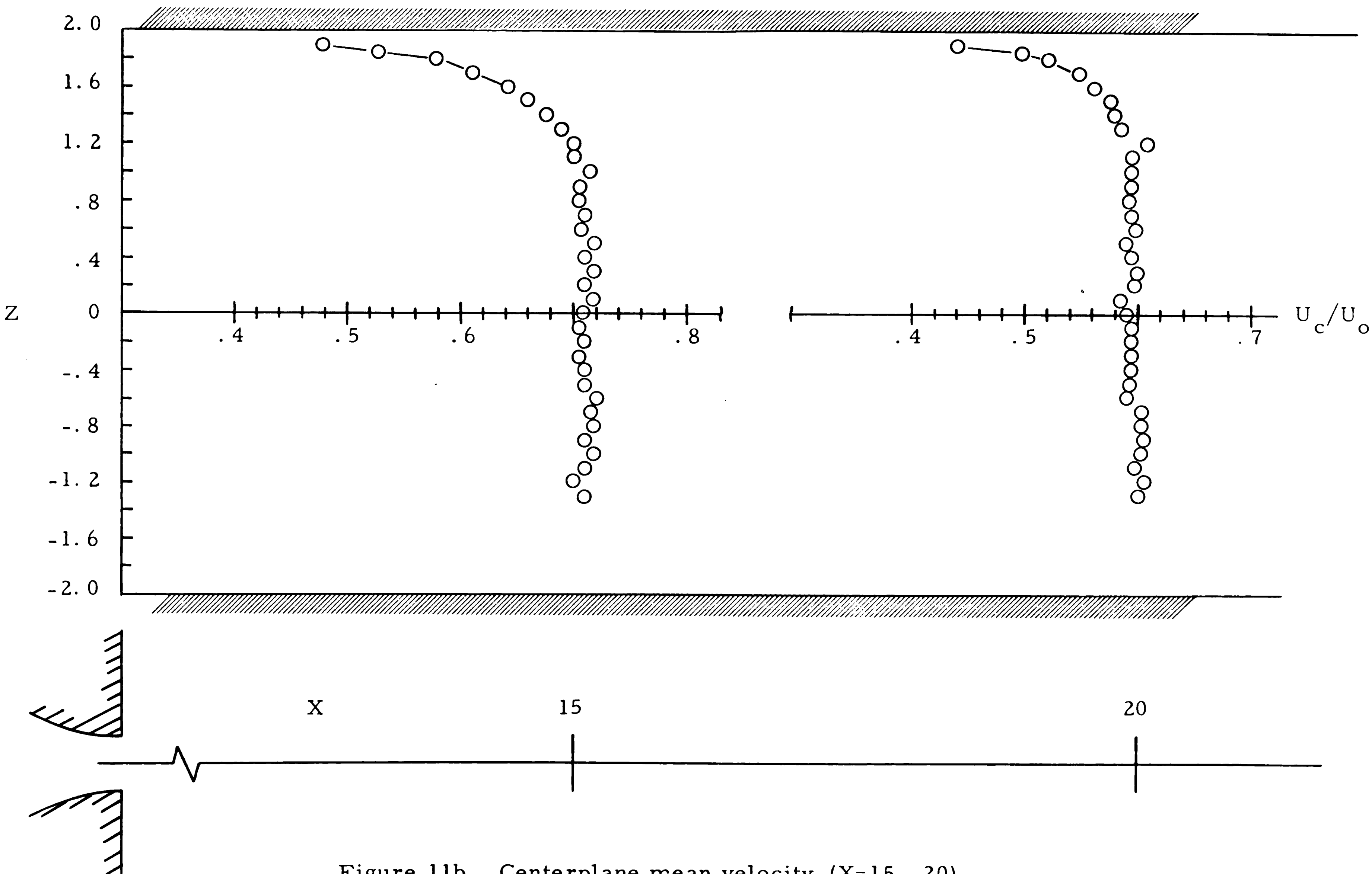

Figure 11b. Centerplane mean velocity (X=15, 20)

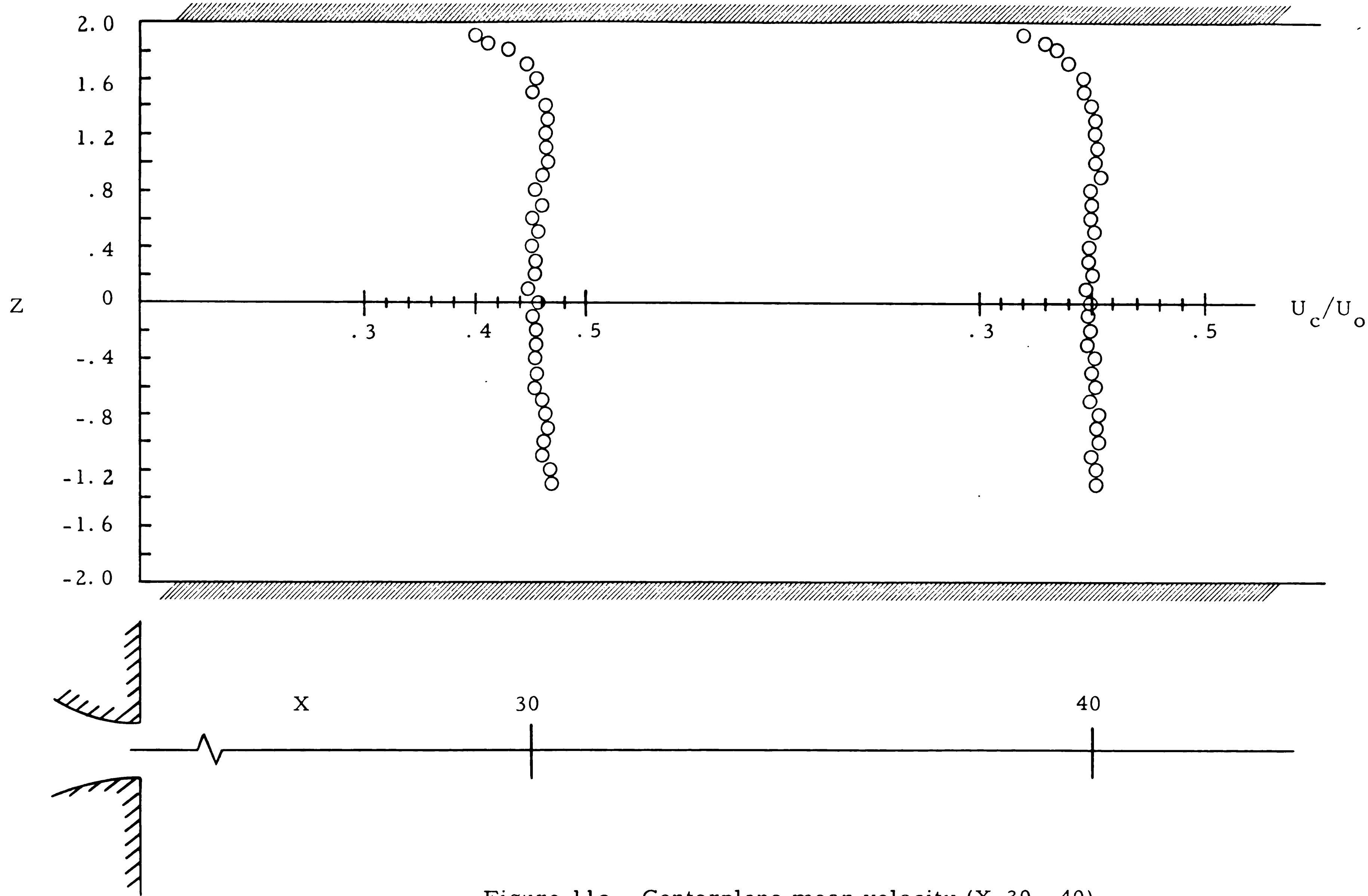

Figure 11c. Centerplane mean velocity (X=30, 40)

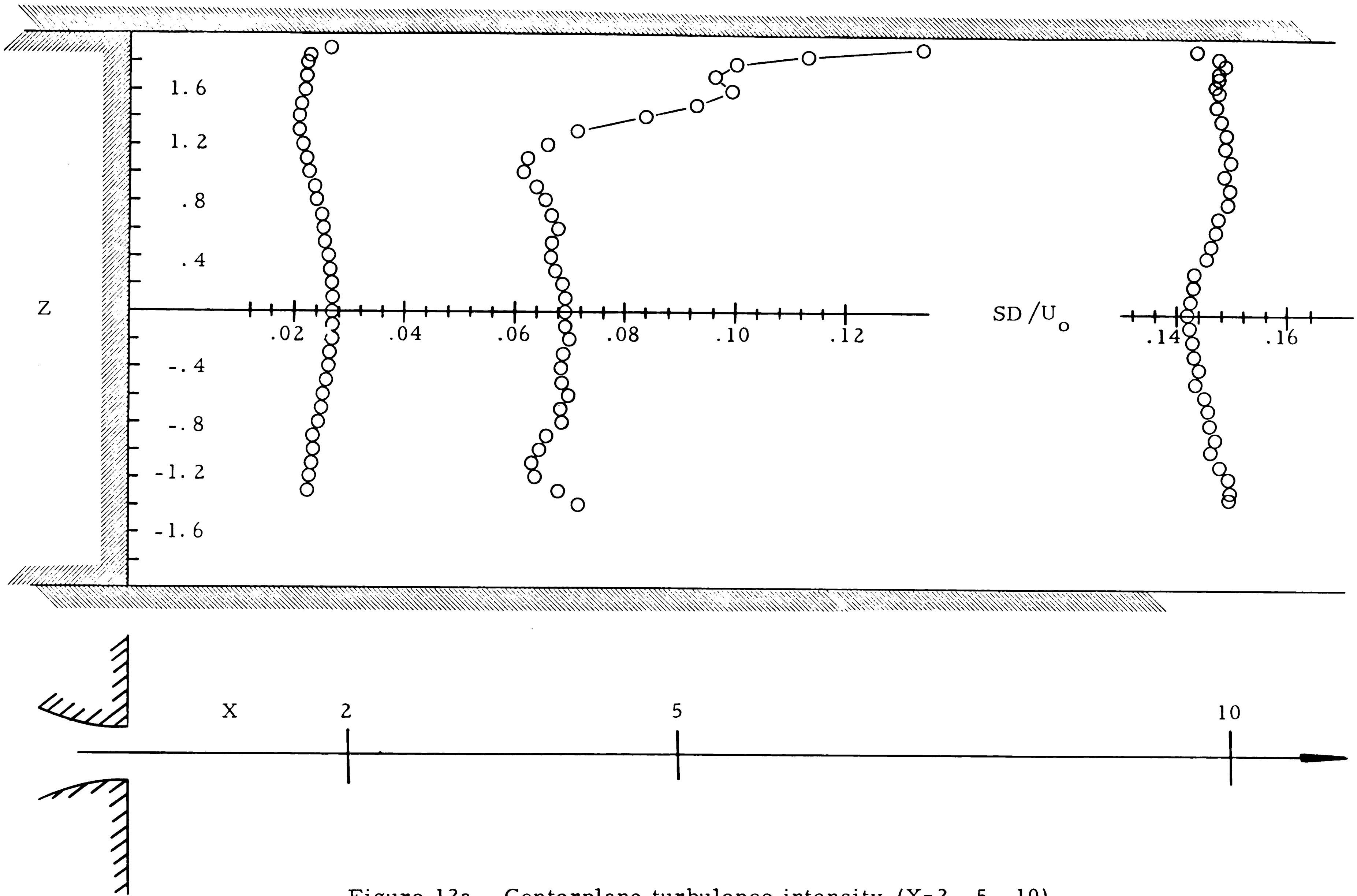

Figure 12a. Centerplane turbulence intensity (X=2, 5, 10)

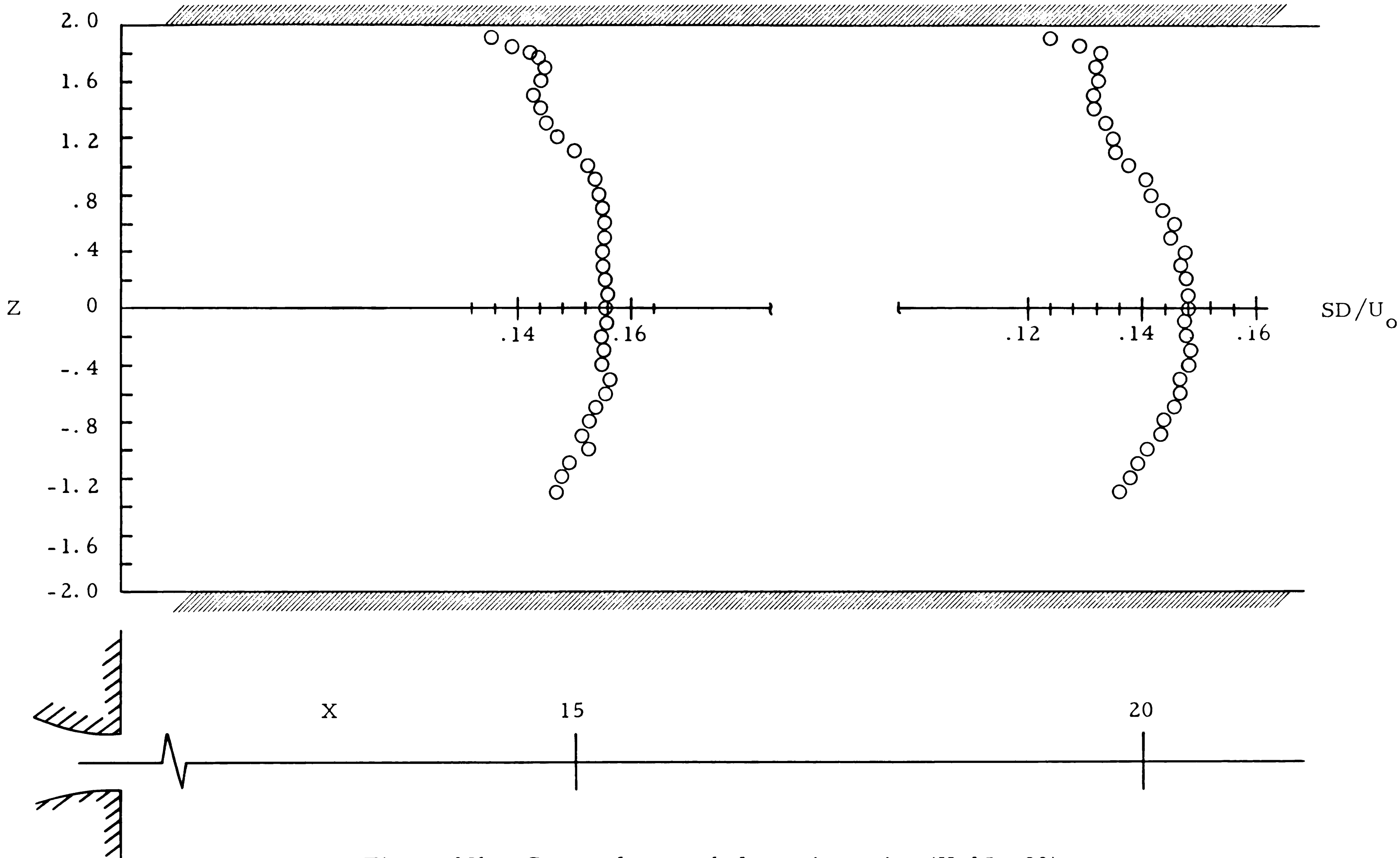

Figure 12b. Centerplane turbulence intensity (X=15, 20)

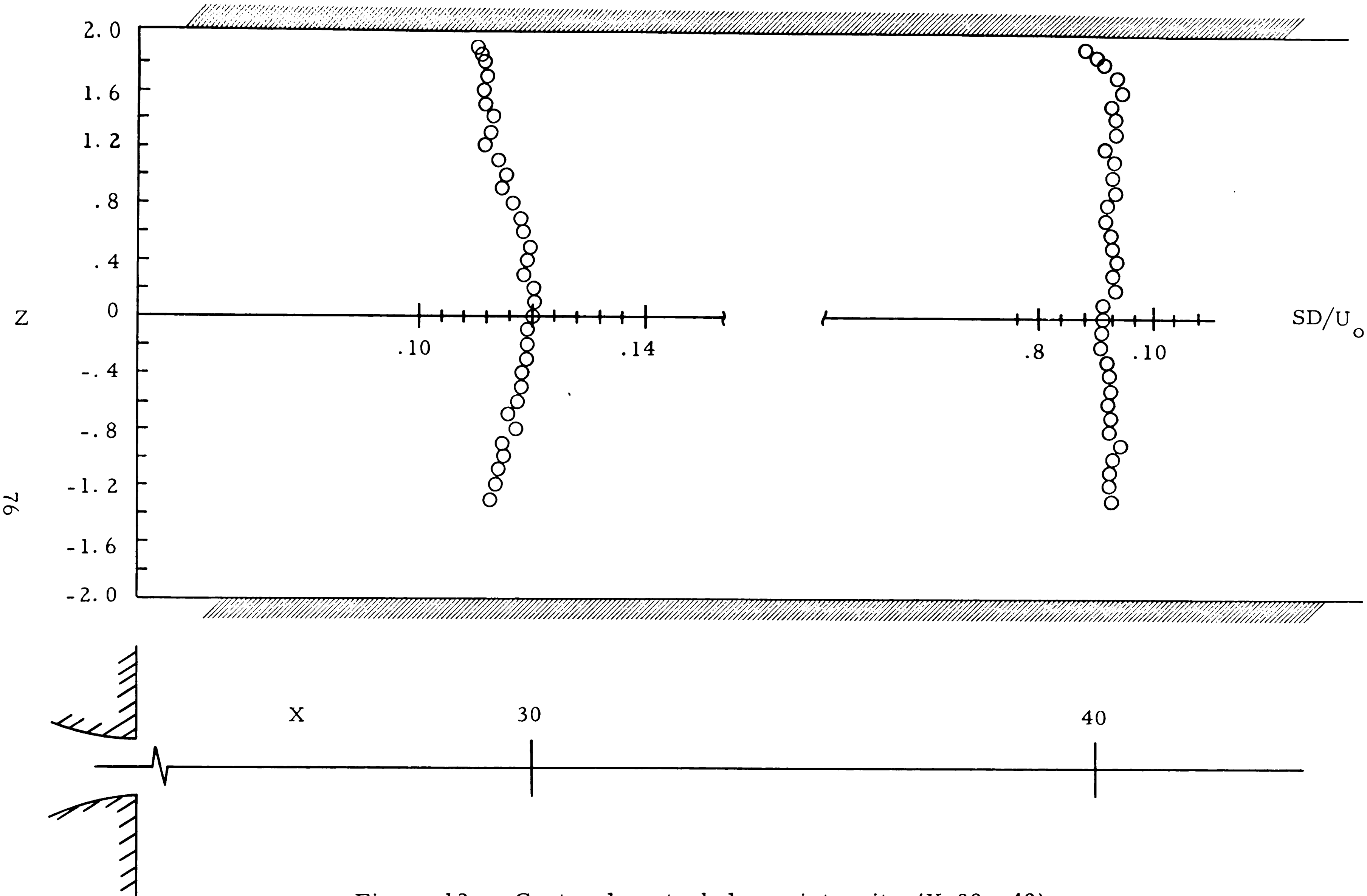

Figure 12c. Centerplane turbulence intensity (X=30, 40)

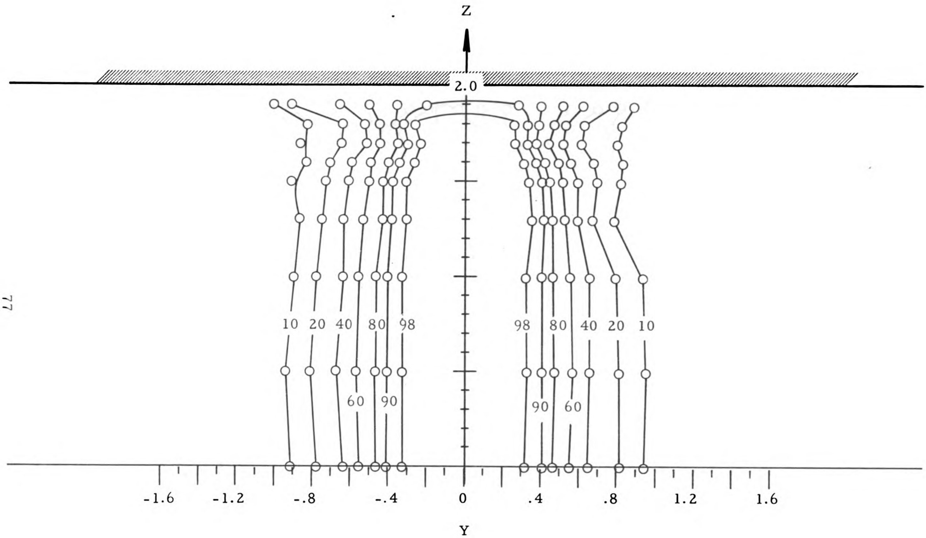

Figure 13. Isotachs at X=2

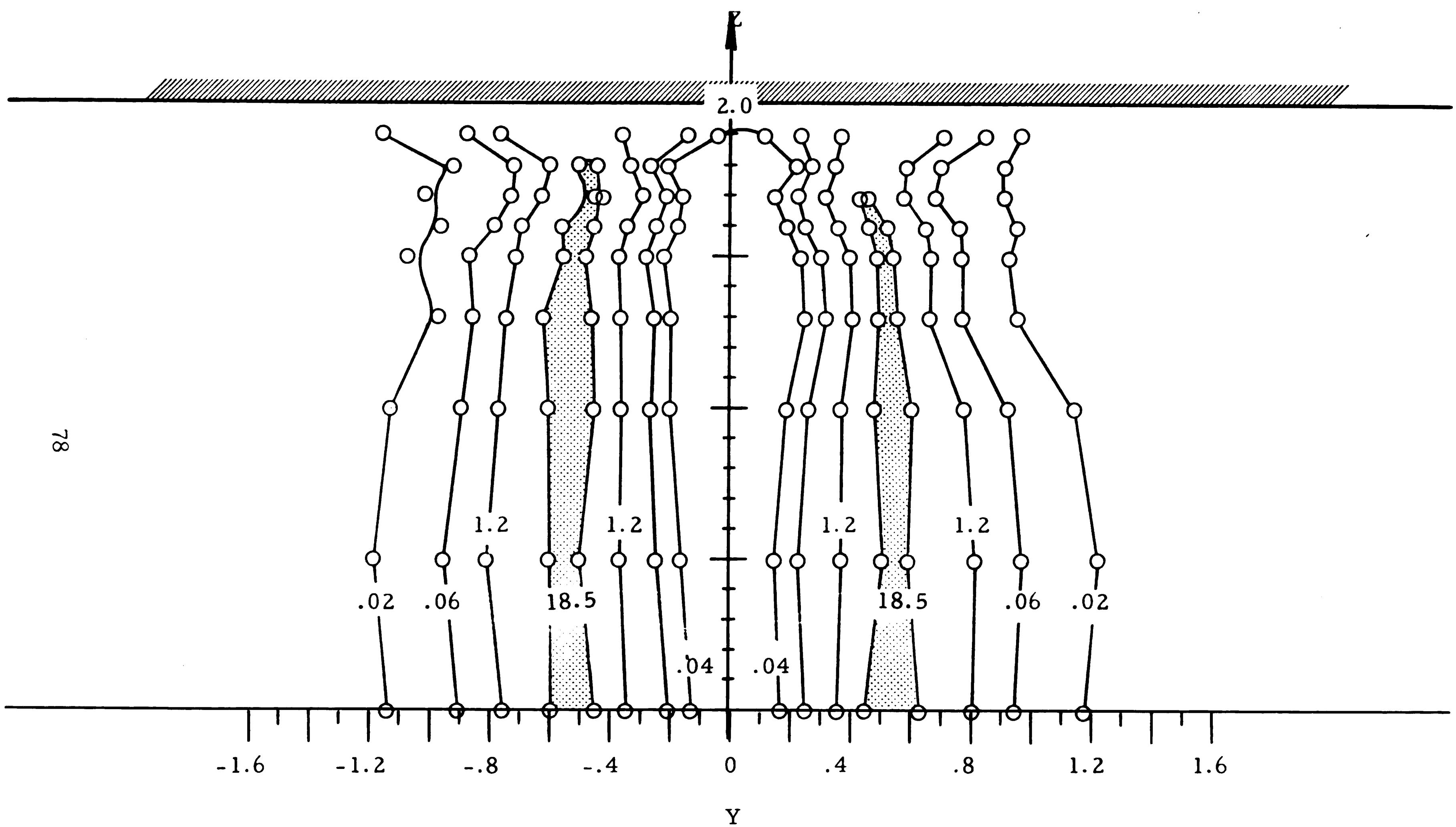

Figure 14. Contours of constant turbulence intensity at X=2

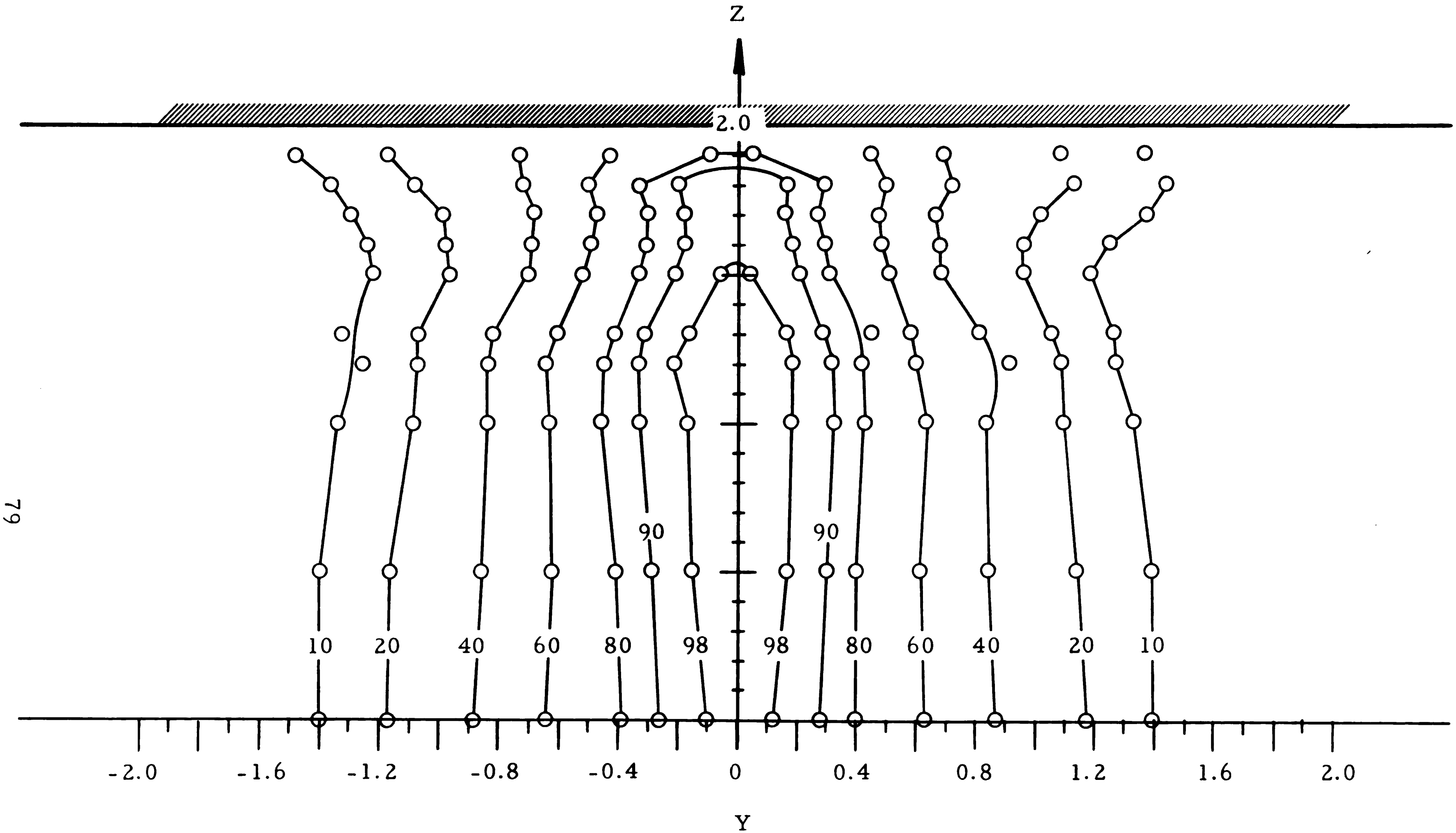

Figure 15. Isotachs at X=5

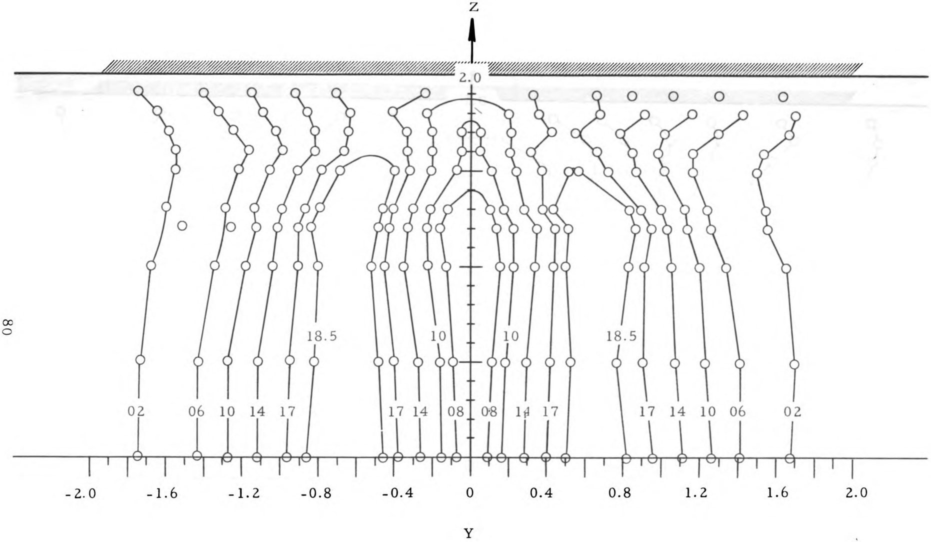

Figure 16. Contours of constant turbulence intensity at X=5

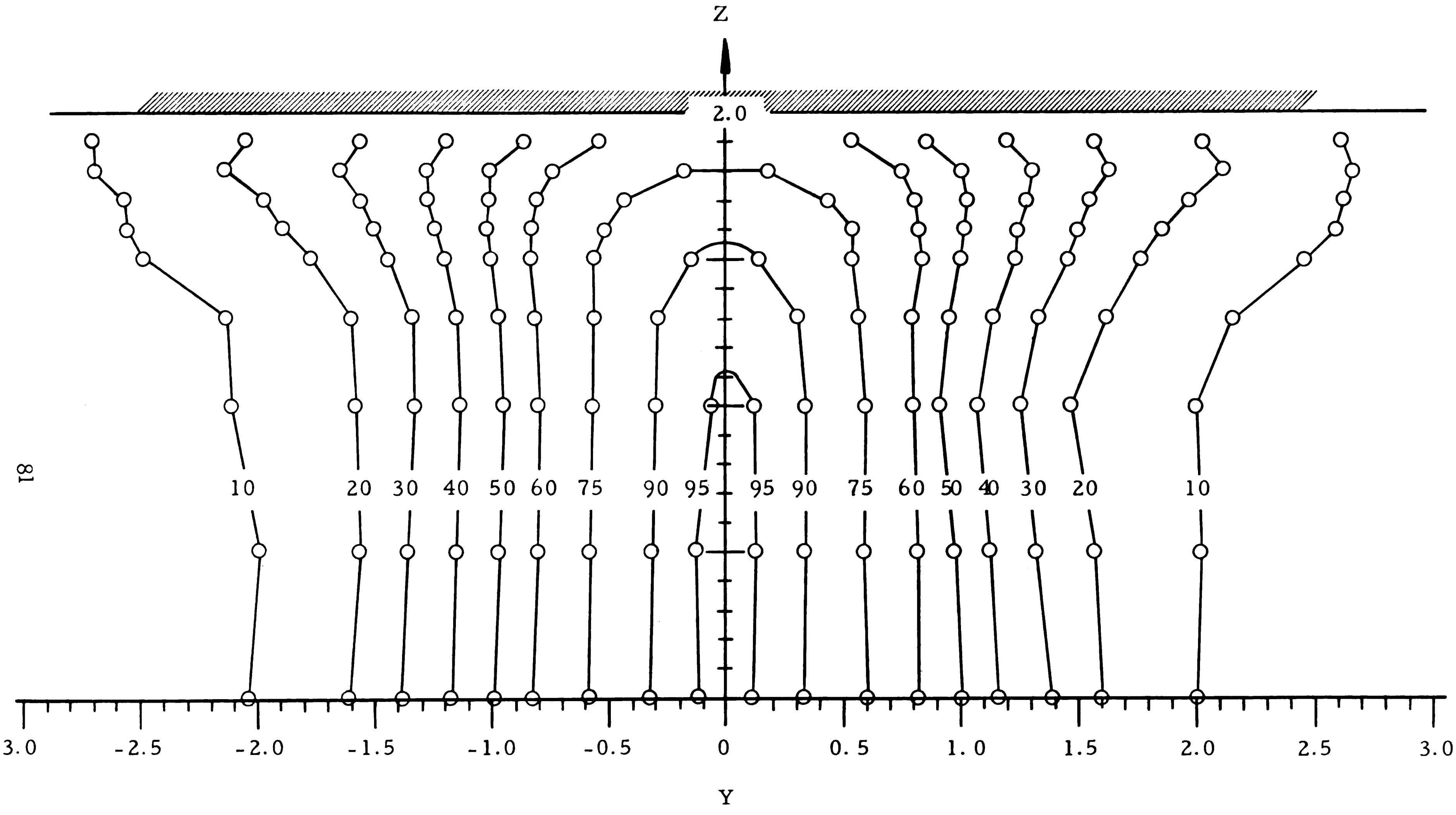

Figure 17. Isotachs at X=10

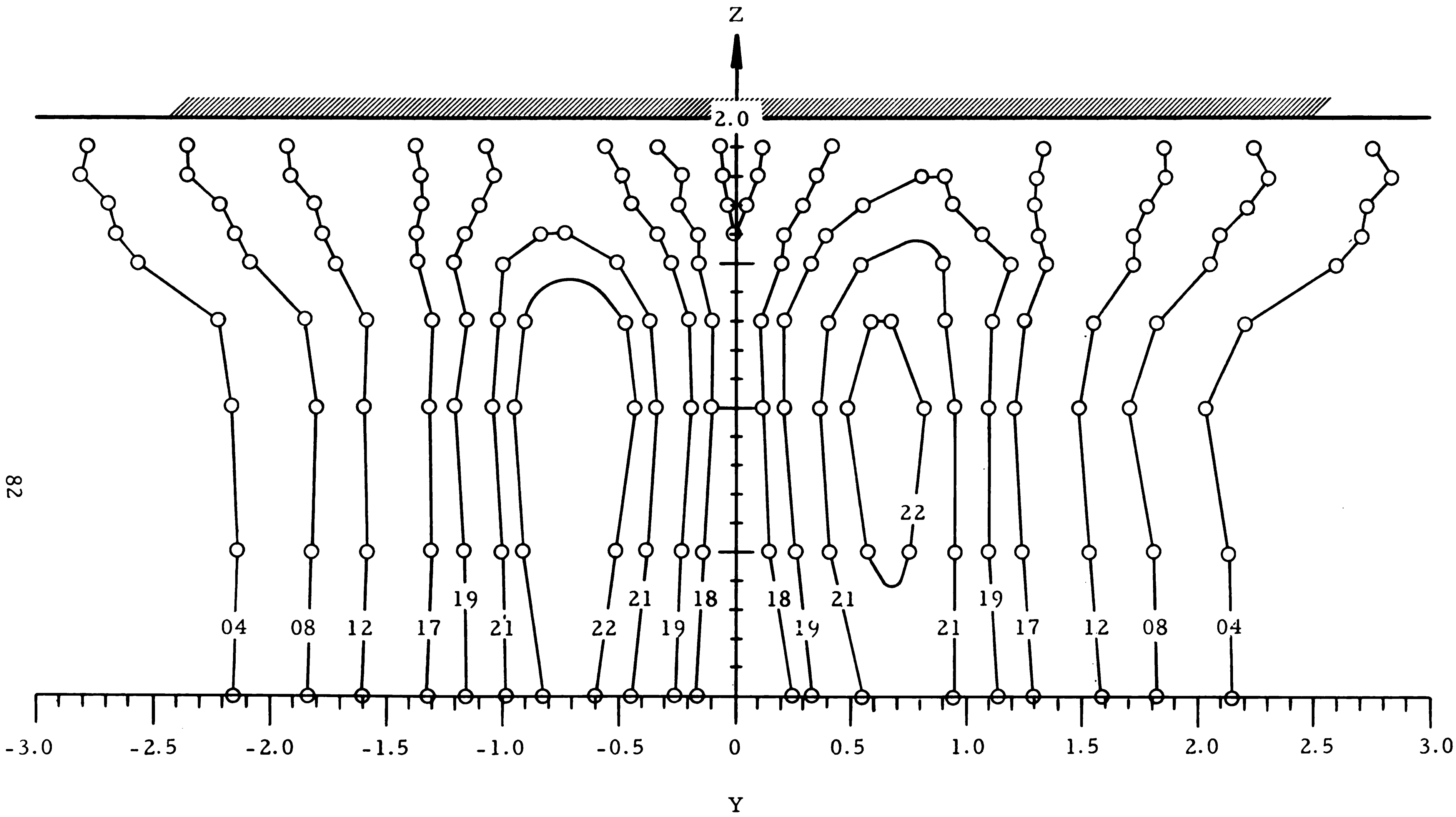

Figure 18. Contours of constant turbulence intensity at X=10

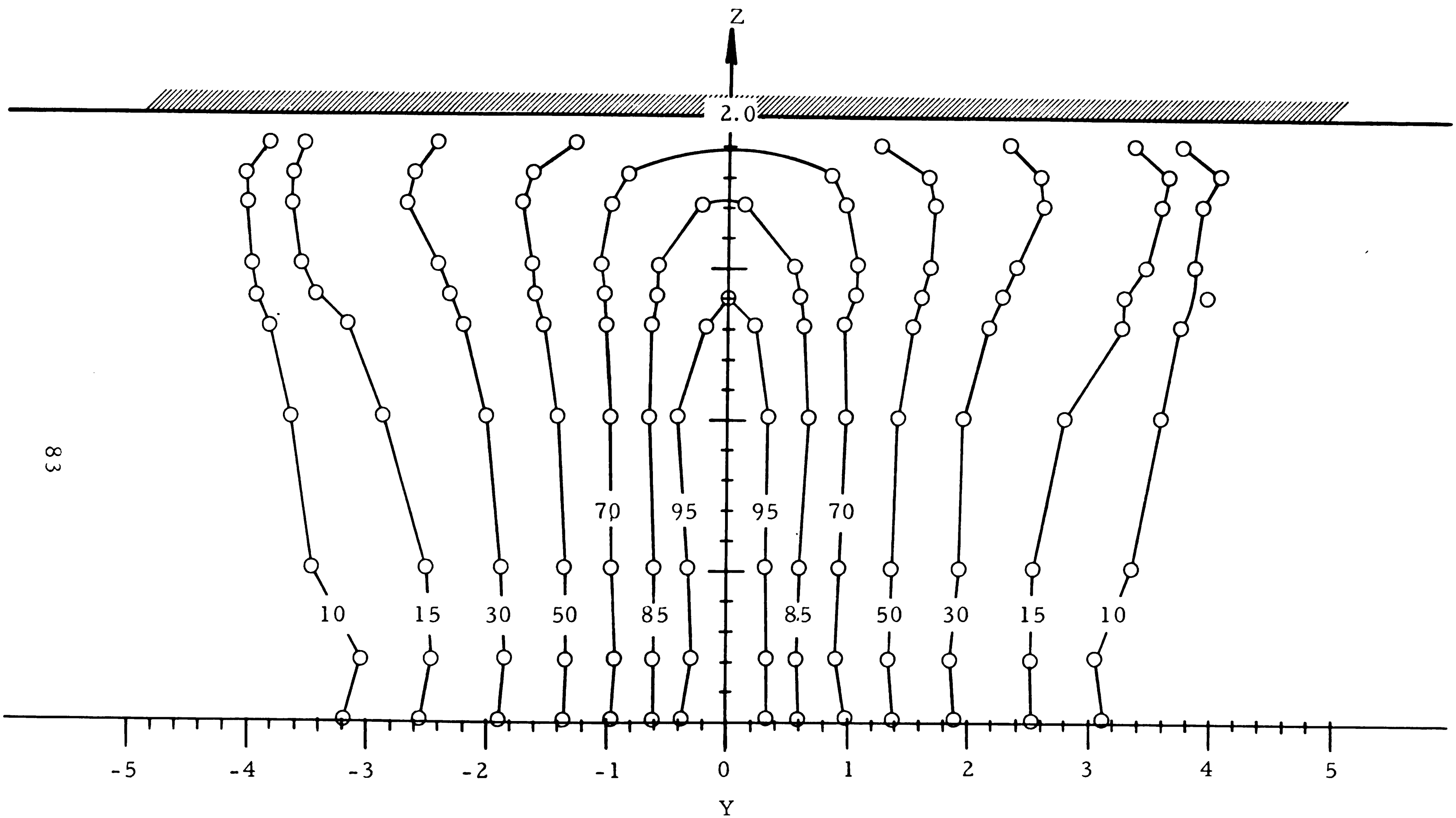

Figure 19. Isotachs at X=15

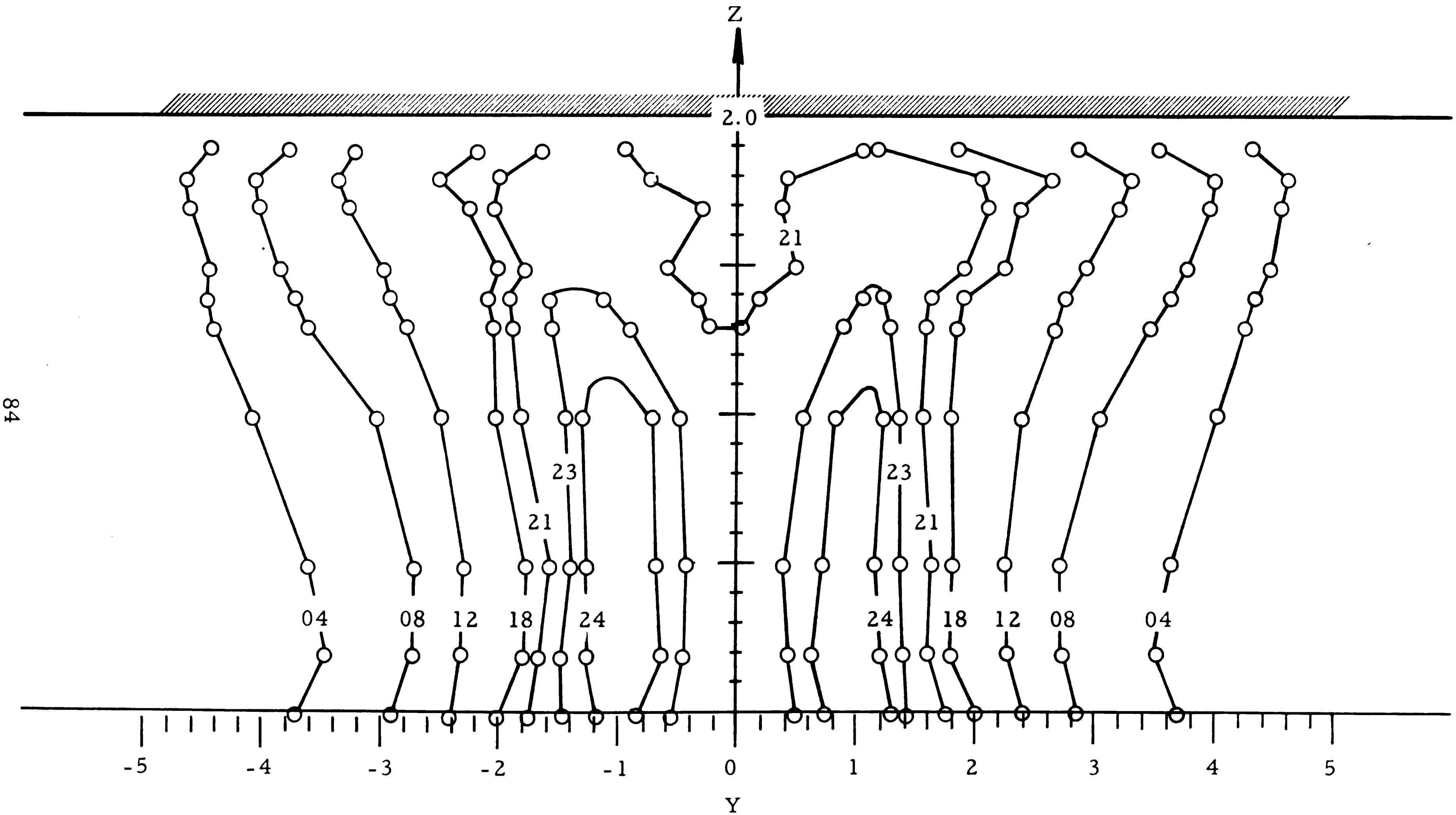

Figure 20. Contours of constant turbulence intensity at X=15

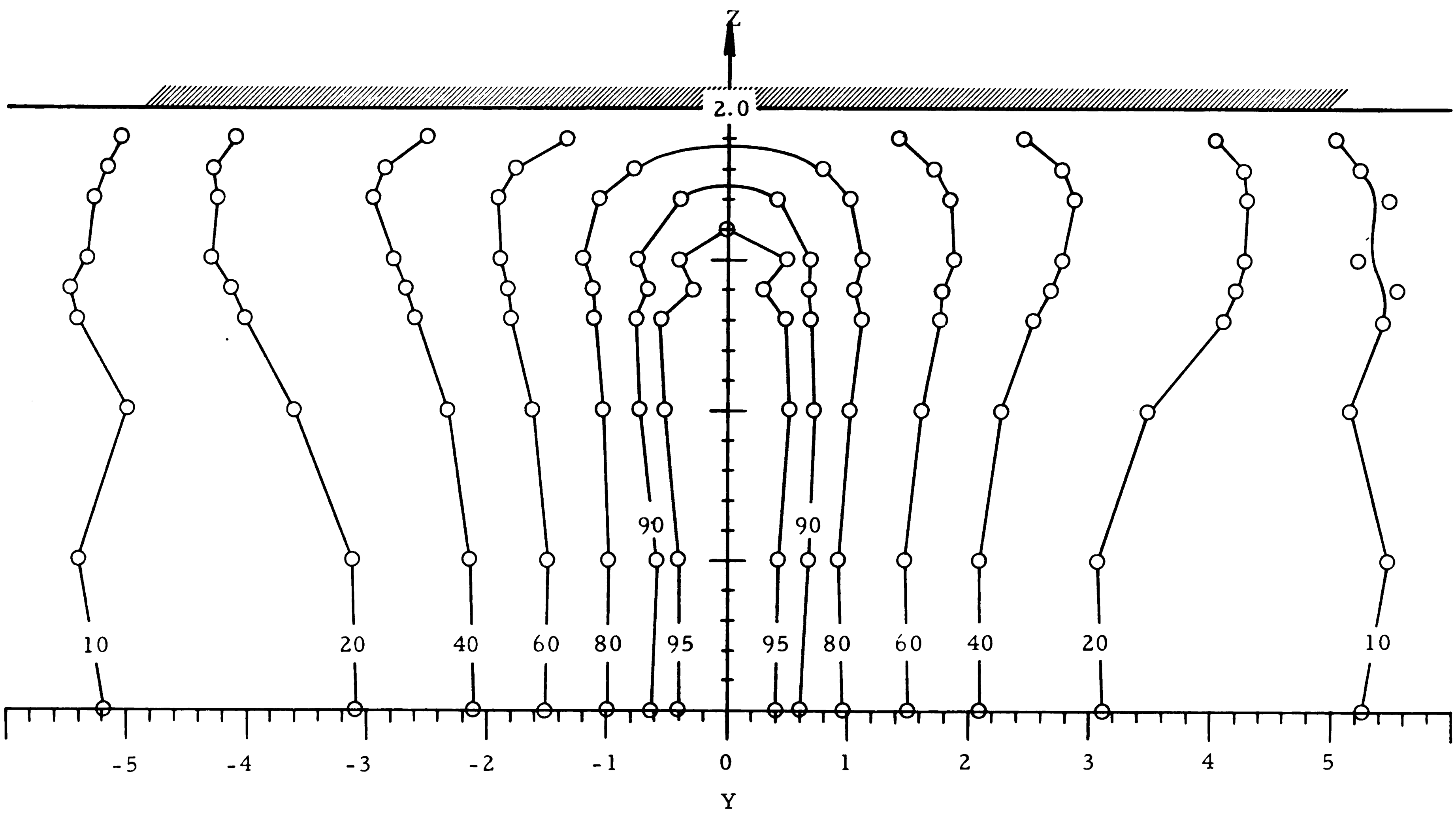

Figure 21. Isotachs at X=20

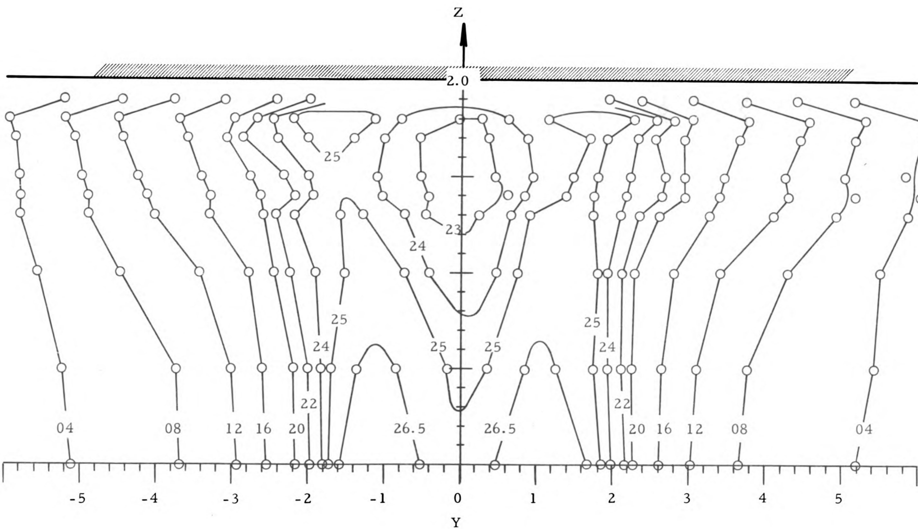

Figure 22. Contours of constant turbulence intensity at X=40

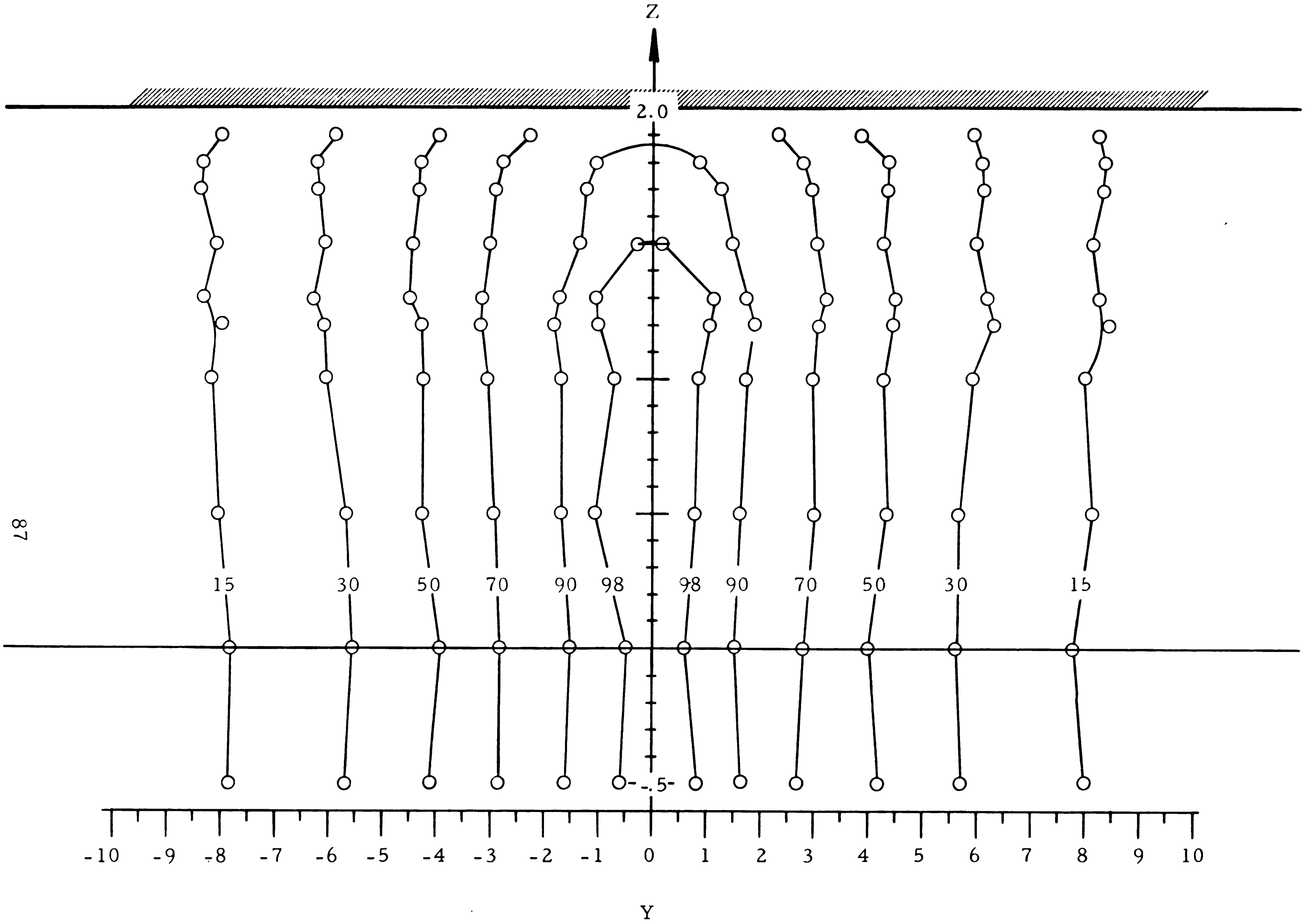

Figure 23. Isotachs at X=40

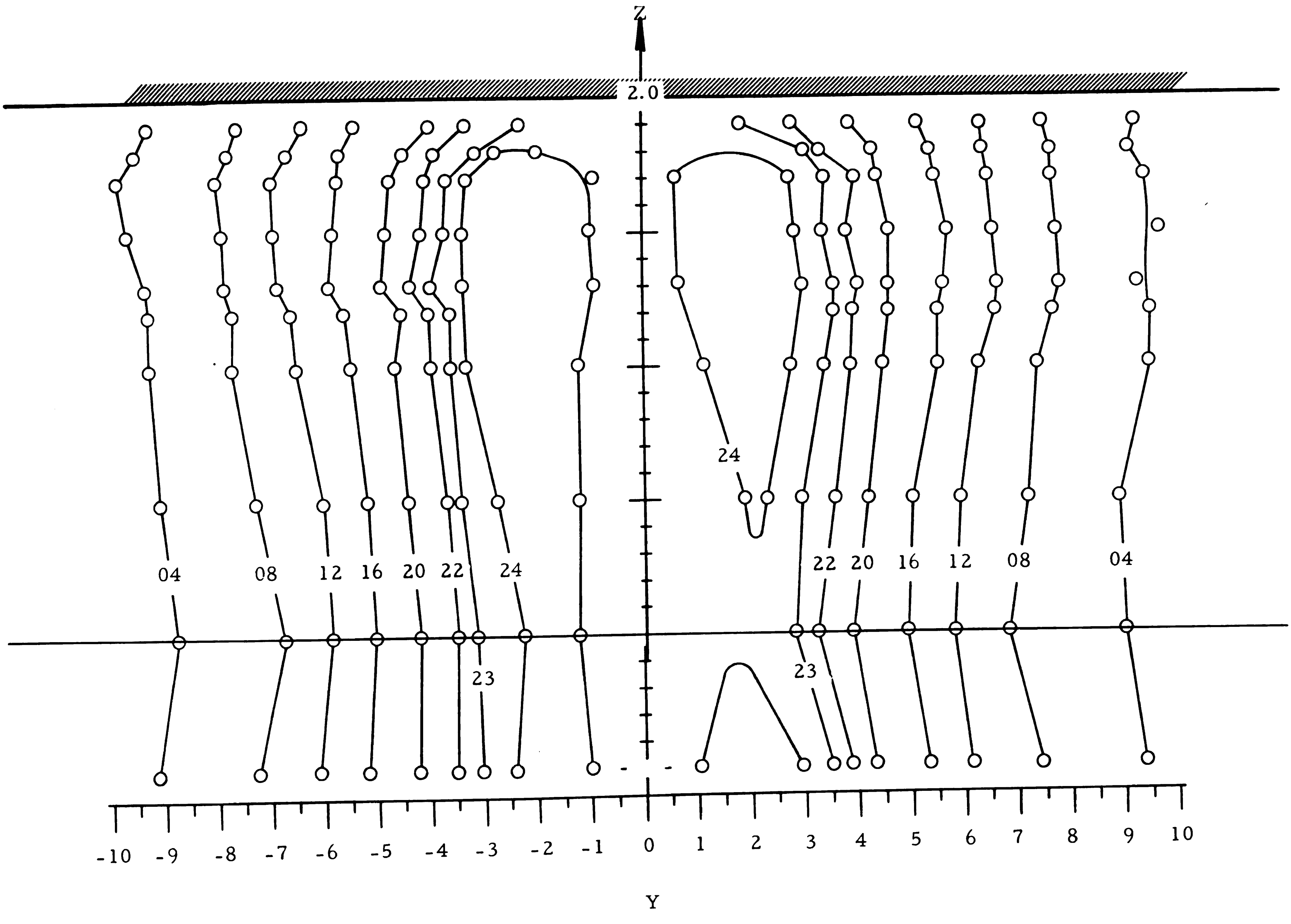

Figure 24. Contours of constant turbulence intensity at X=40

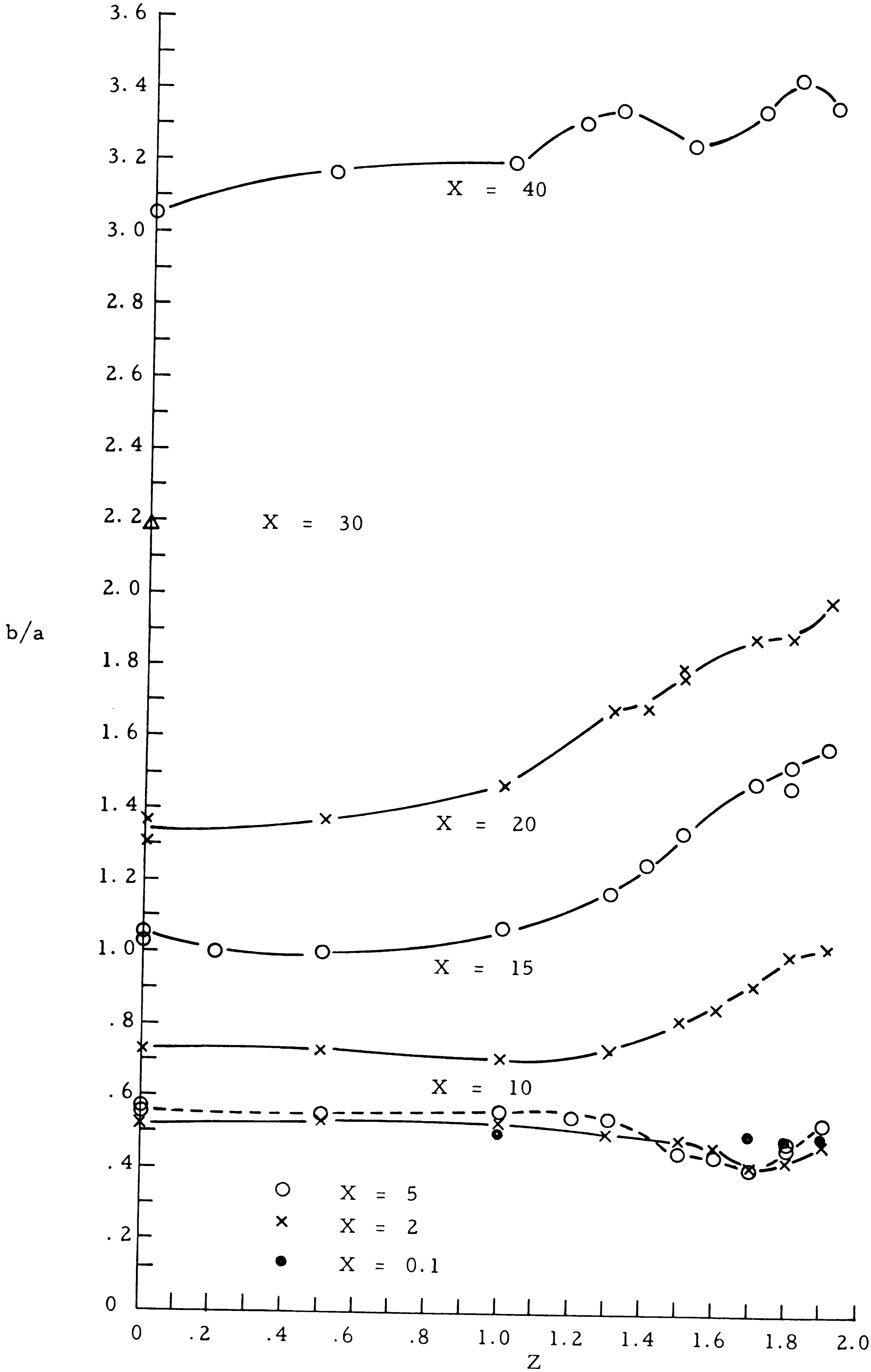

Figure 25. Momentum flux thickness values

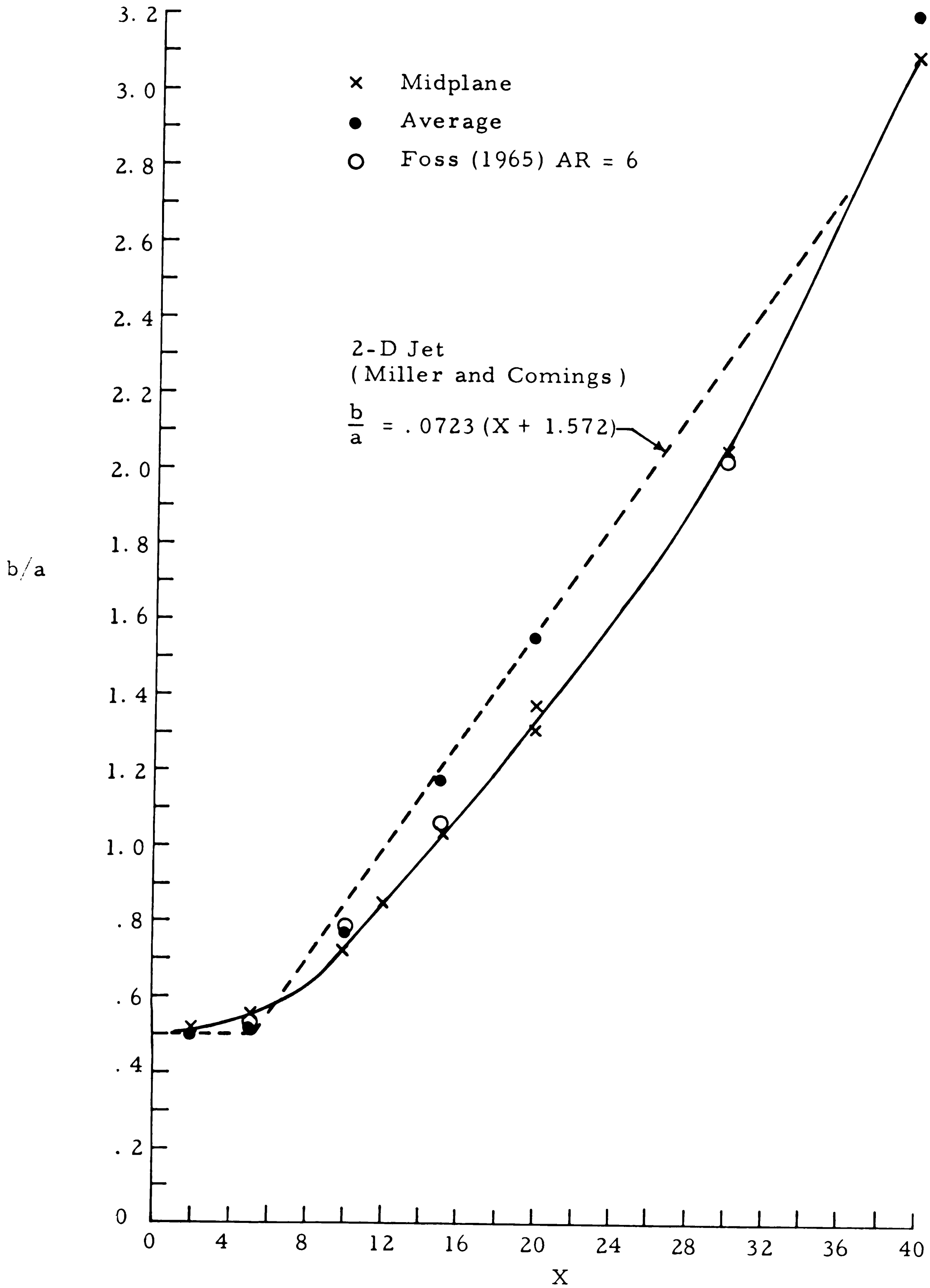

Figure 26. Midplane and average momentum flux thickness values

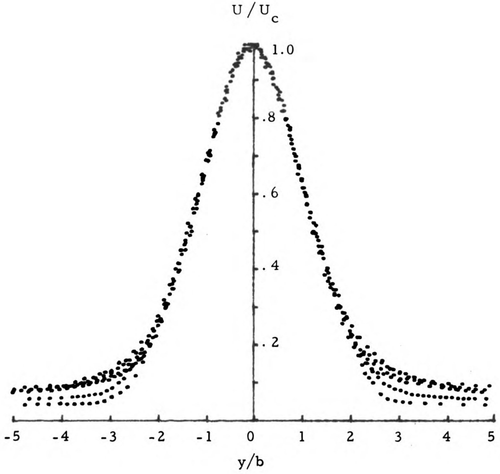

Figure 27a. Dimensionless midplane mean velocity distributions

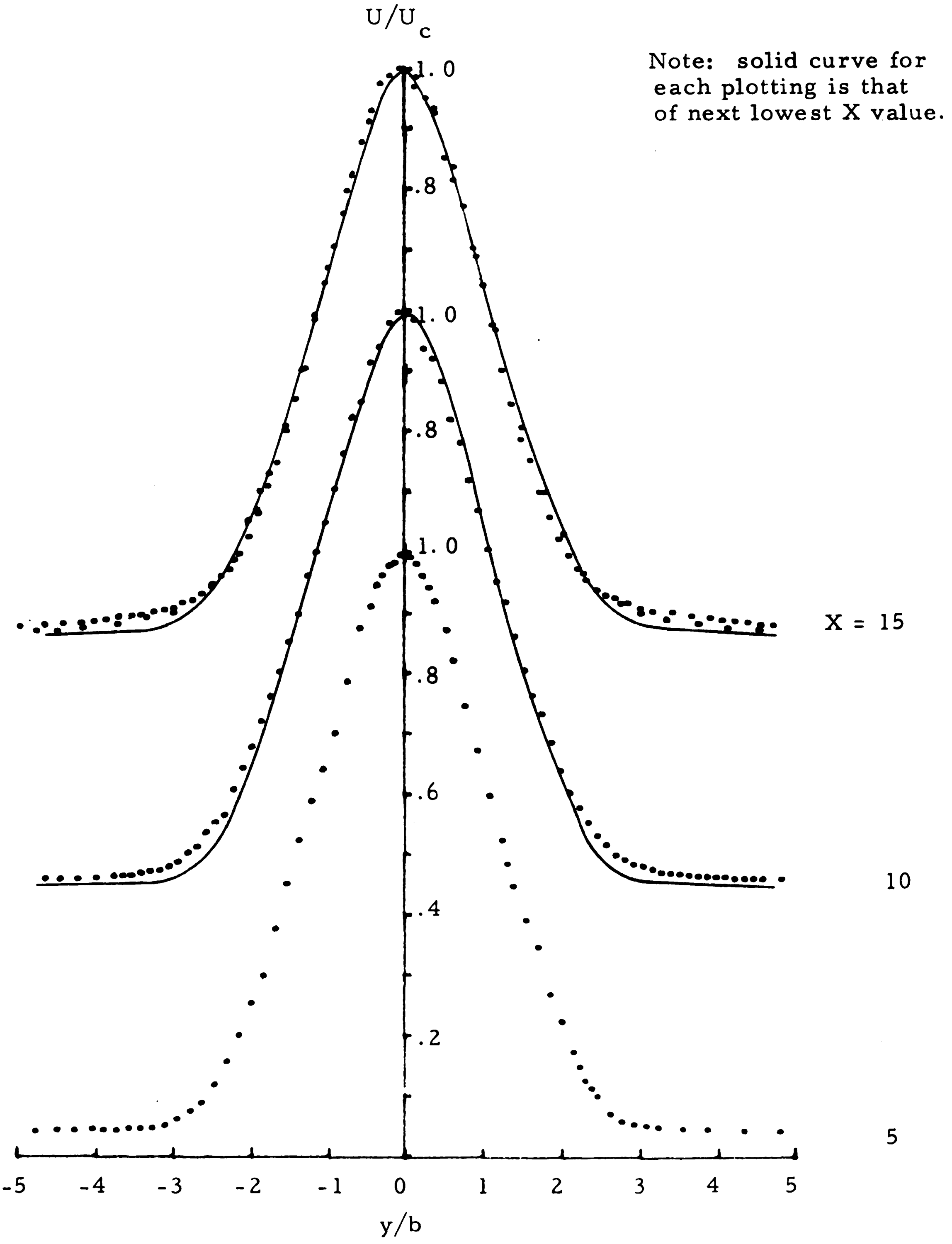

Figure 27b. Dimensionless midplane mean velocity distributions (X = 5, 10, 15)

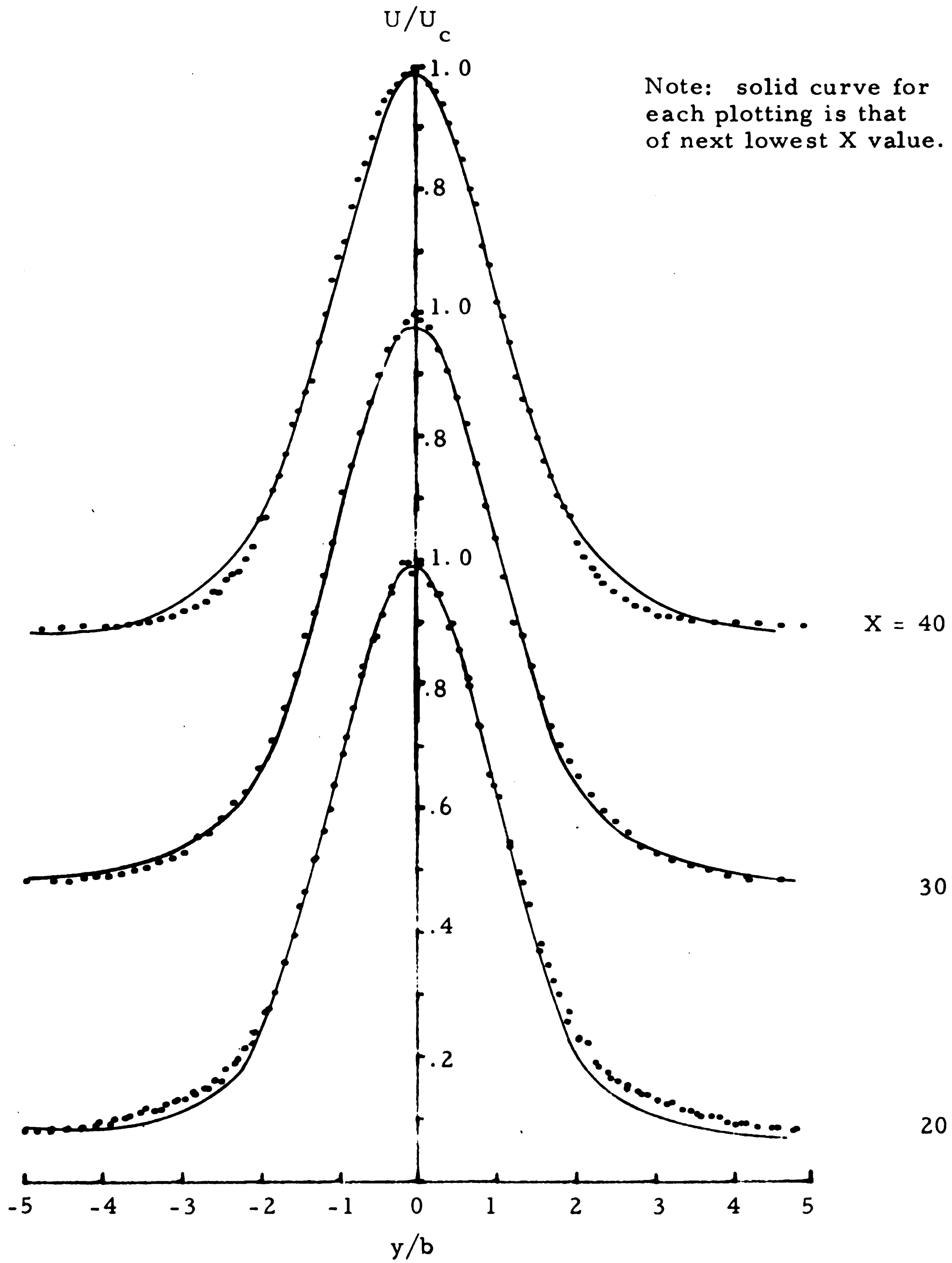

Figure 27c. Dimensionless midplane mean velocity distributions (X = 20, 30, 40)

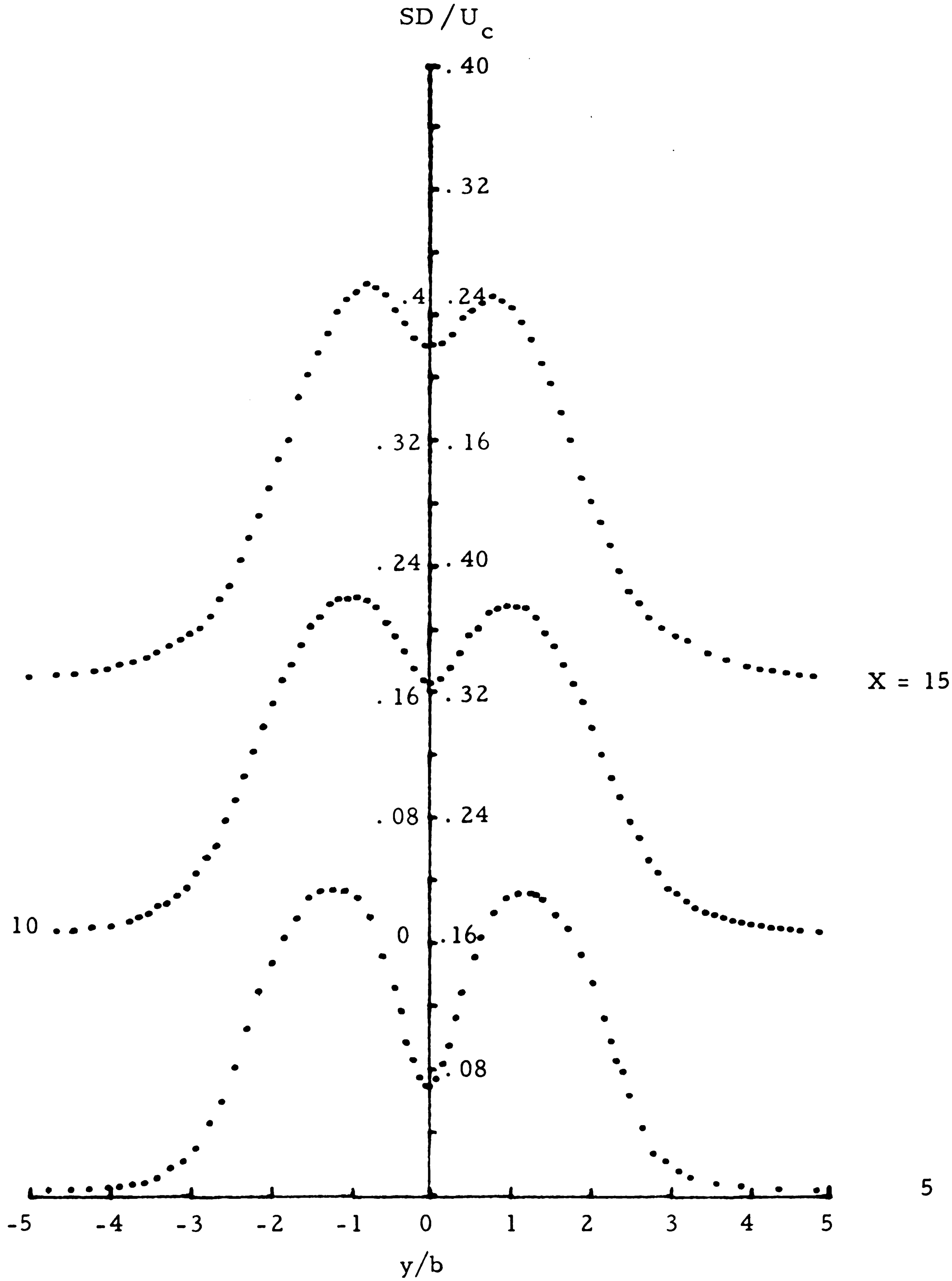

Figure 28a. Dimensionless midplane turbulence intensity distributions (X = 5, 10, 15)

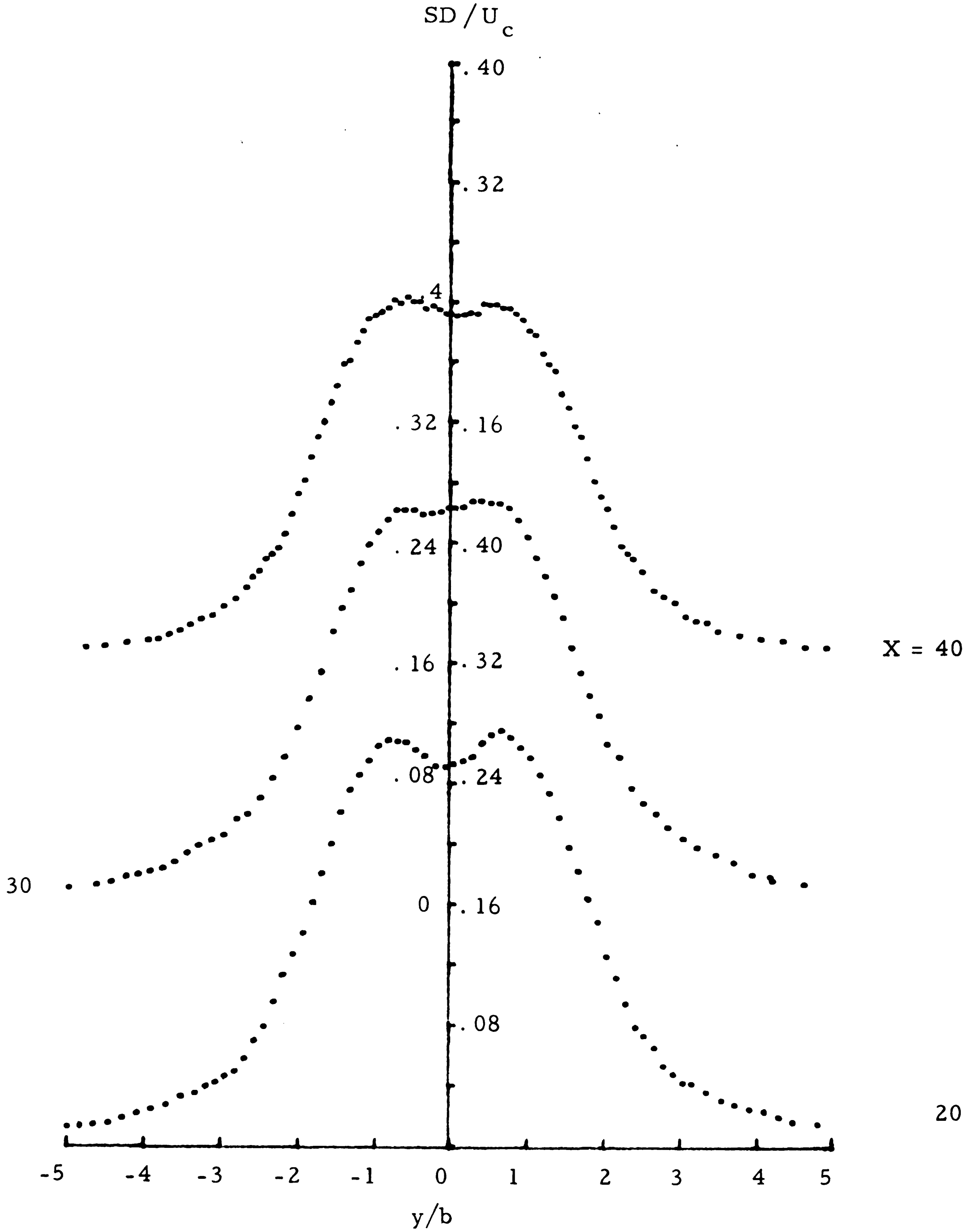

Figure 28b. Dimensionless midplane turbulence intensity distributions (X = 20, 30, 40)

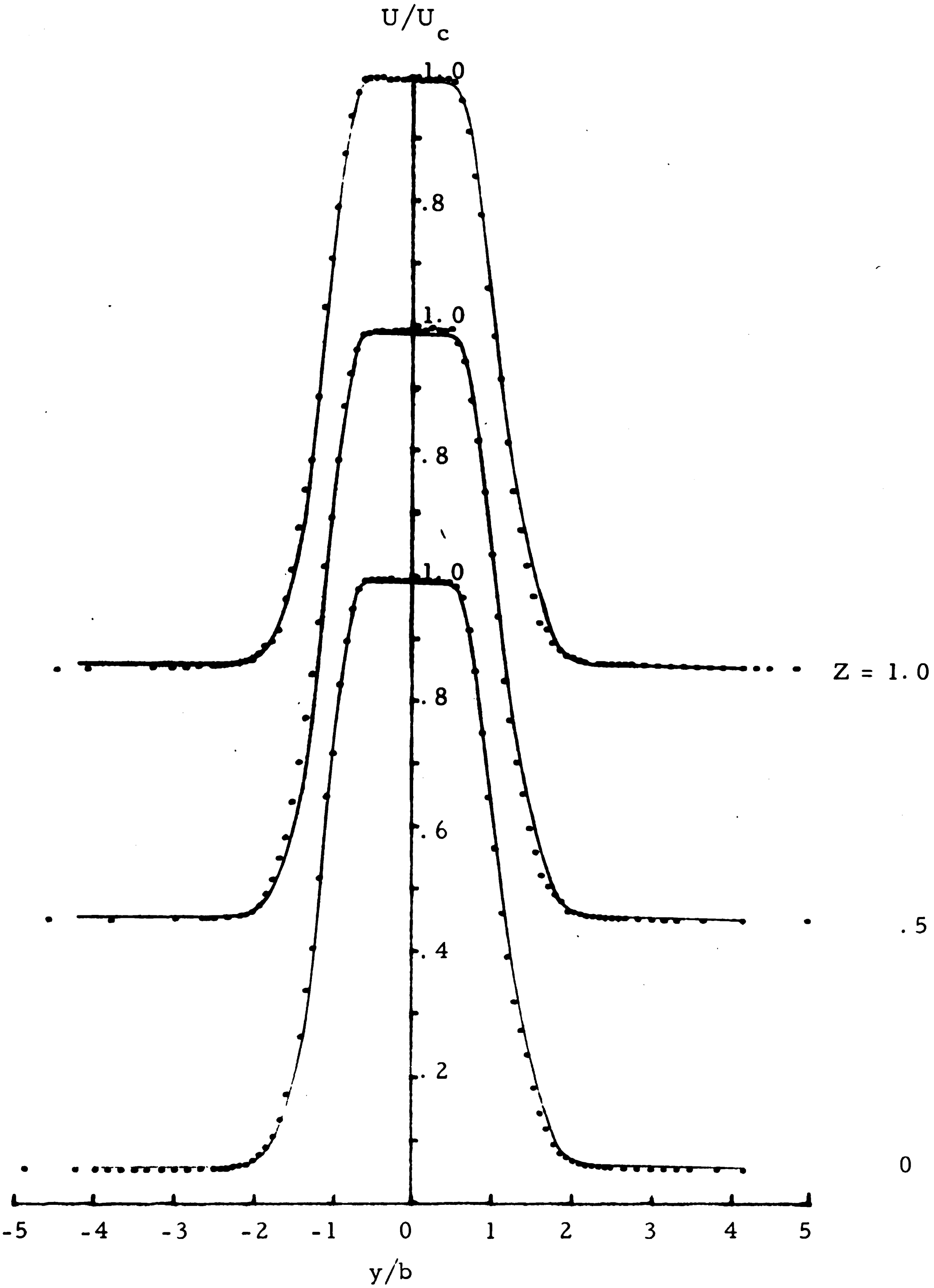

Figure 29a. Dimensionless mean velocity distributions at X=2 (Z= 0, 0.5, 1.0)

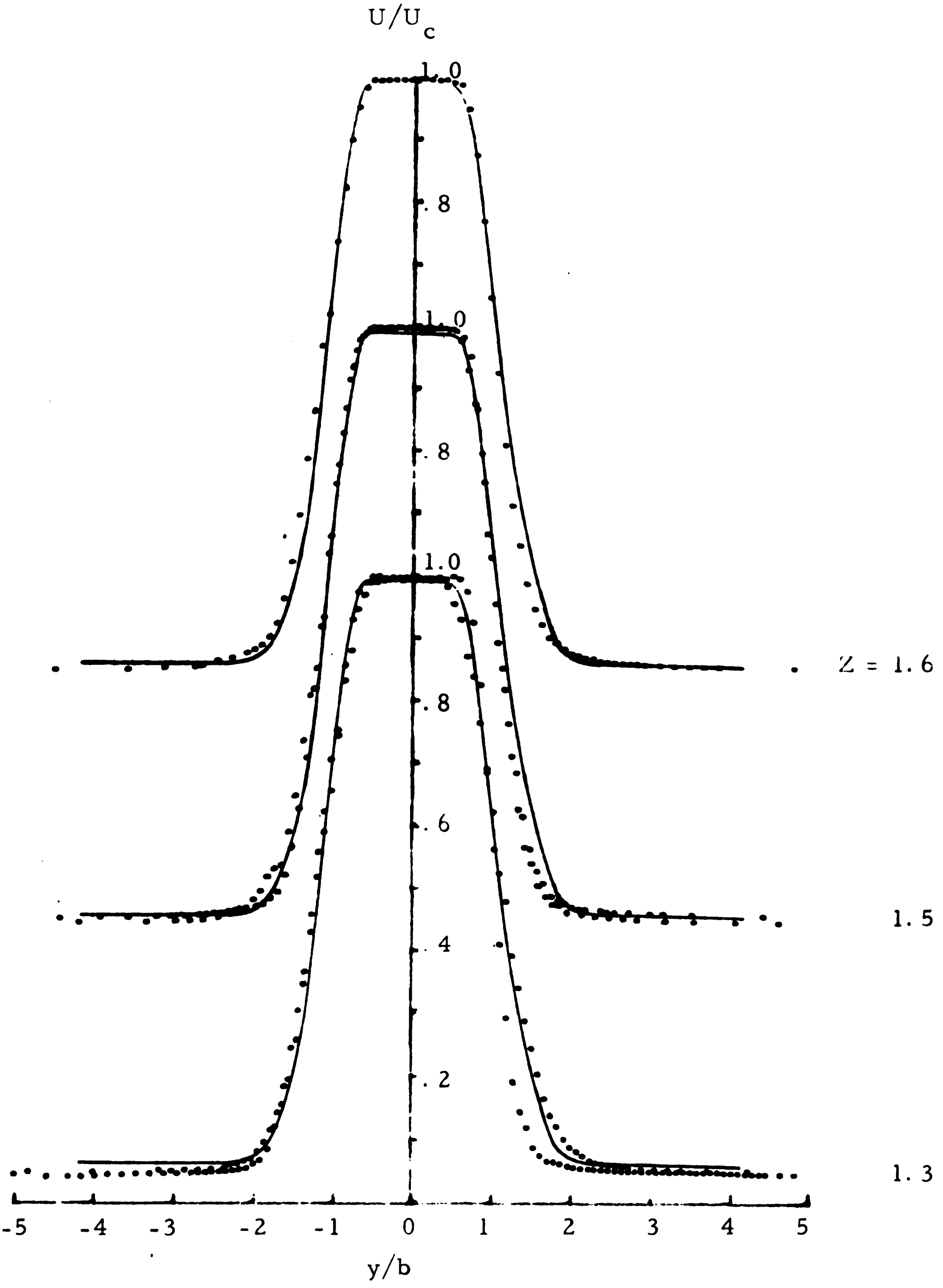

Figure 29b. Dimensionless mean velocity distributions at X= 2 (Z= 1.3, 1.5, 1.6)

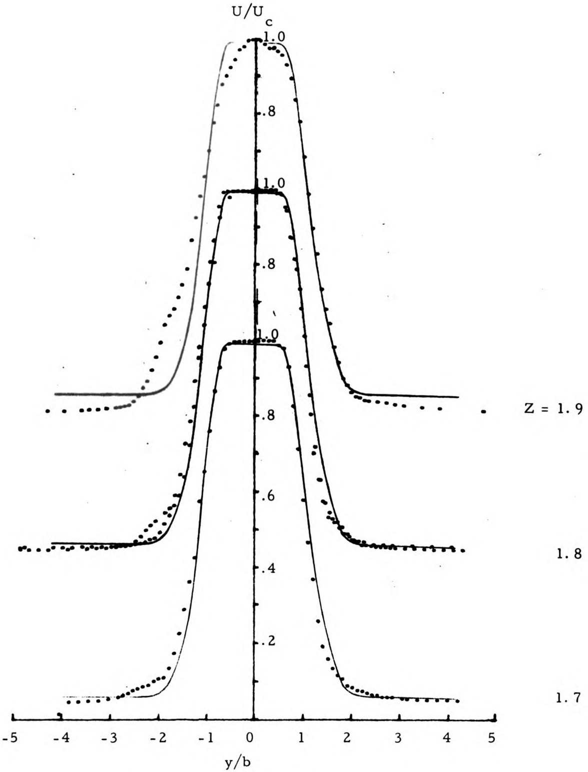

Figure 29c. Dimensionless mean velocity distributions at X=2 (Z= 1.7, 1.8, 1.9)

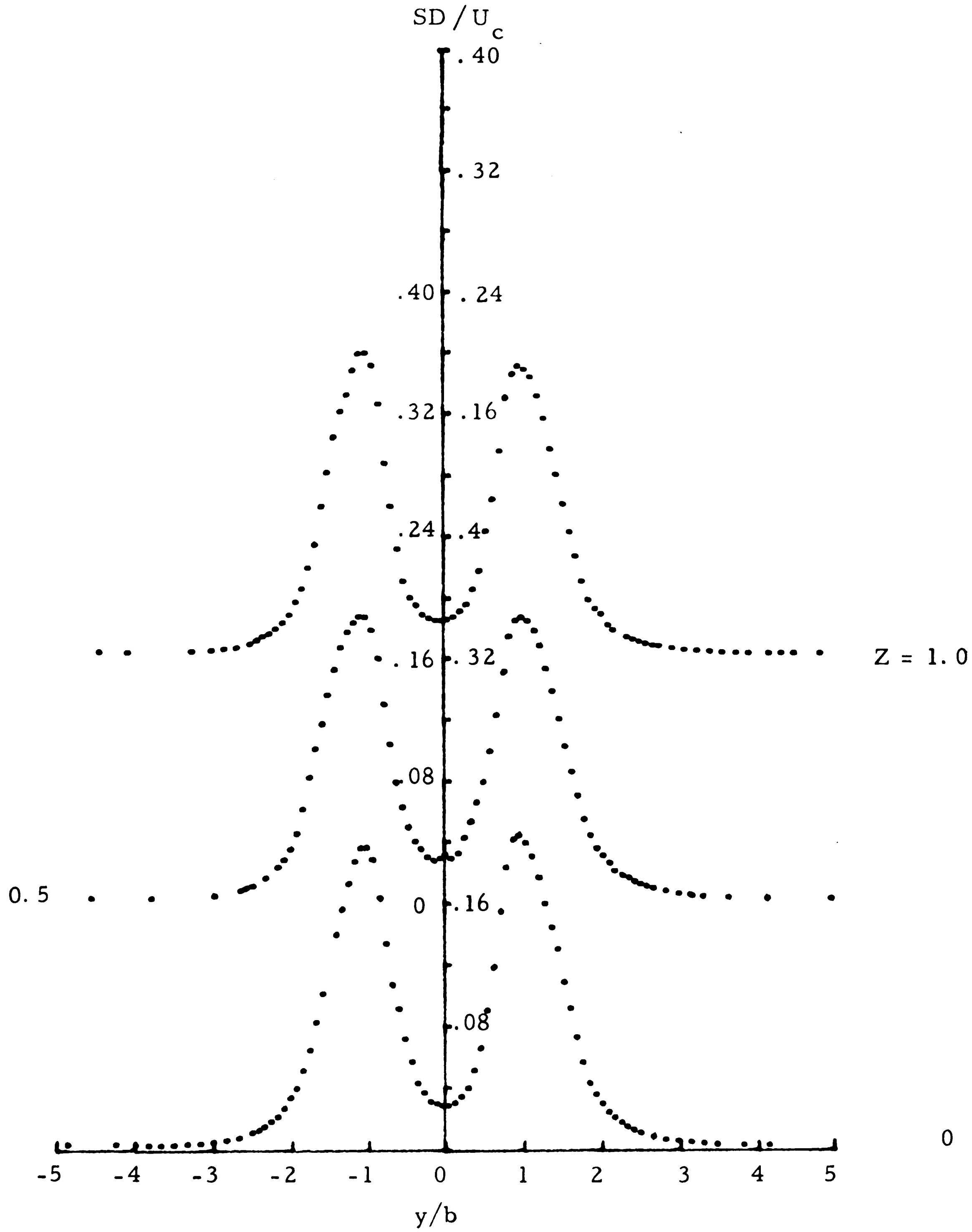

Figure 30a. Dimensionless turbulence intensity distributions at X=2 (Z= 0, .5, 1.0)

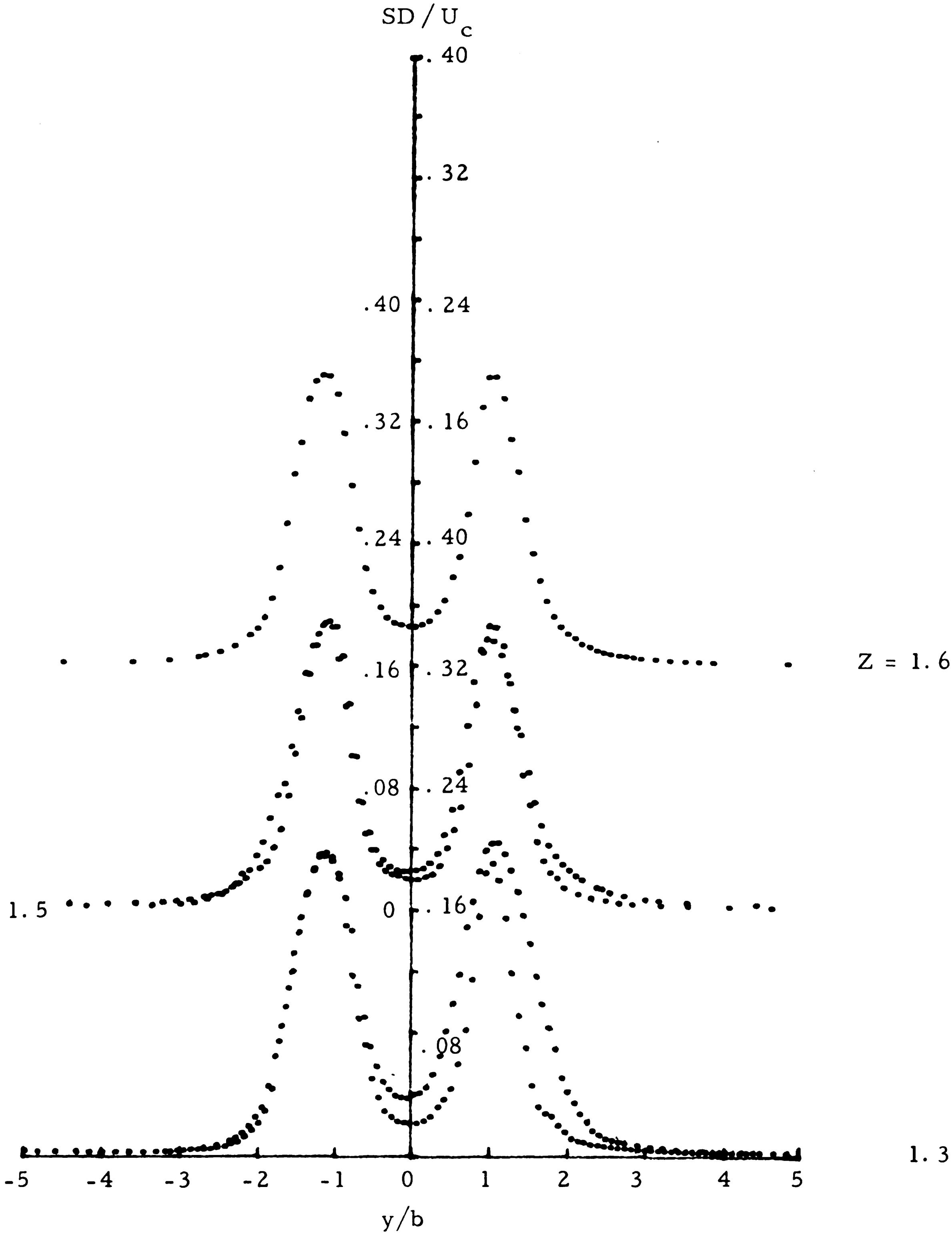

Figure 30b. Dimensionless turbulence intensity distributions at X=2 (Z=1.3, 1.5, 1.6)

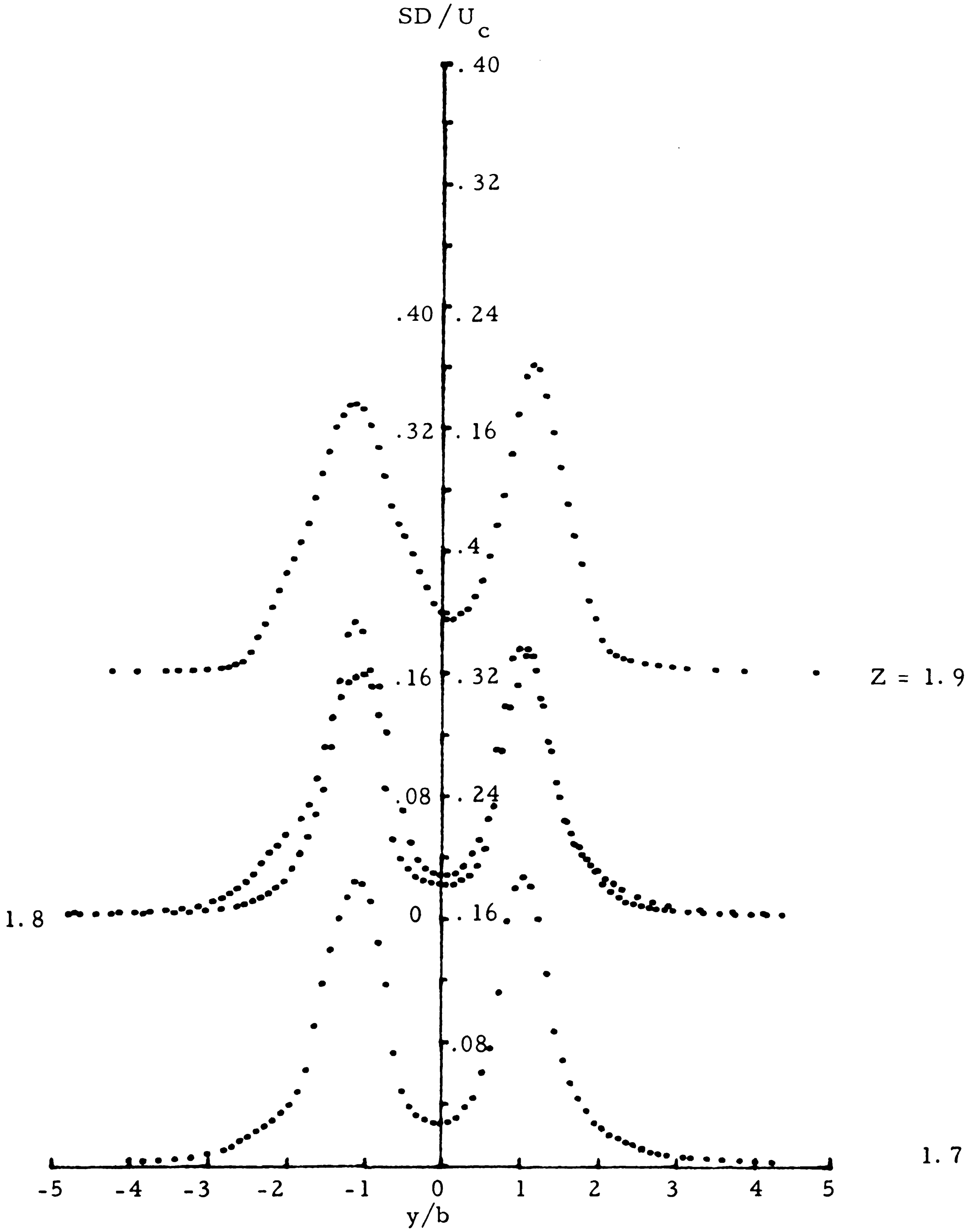

Figure 30c. Dimensionless turbulence intensity distributions at X=2 (Z= 1.7, 1.8, 1.9)

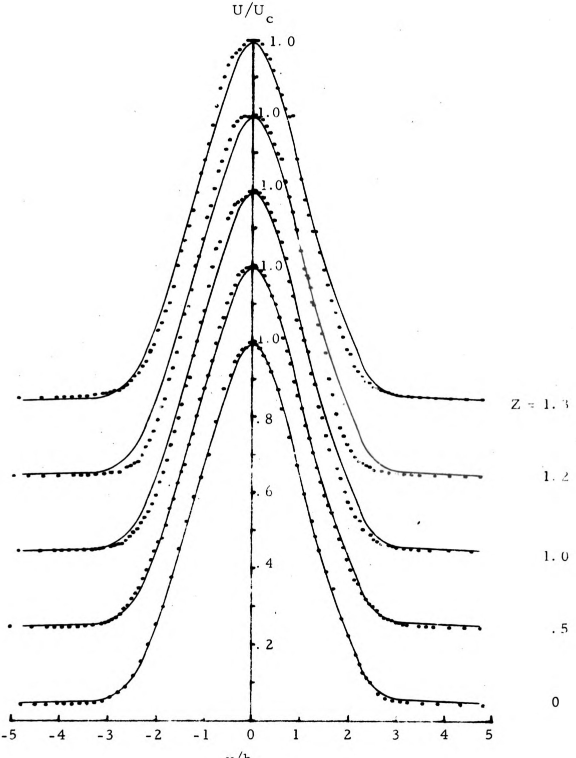

Figure 31a. Dimensionless mean velocity distributions at X=5 (Z=0, 0.5, 1.0, 1.2, 1.3)

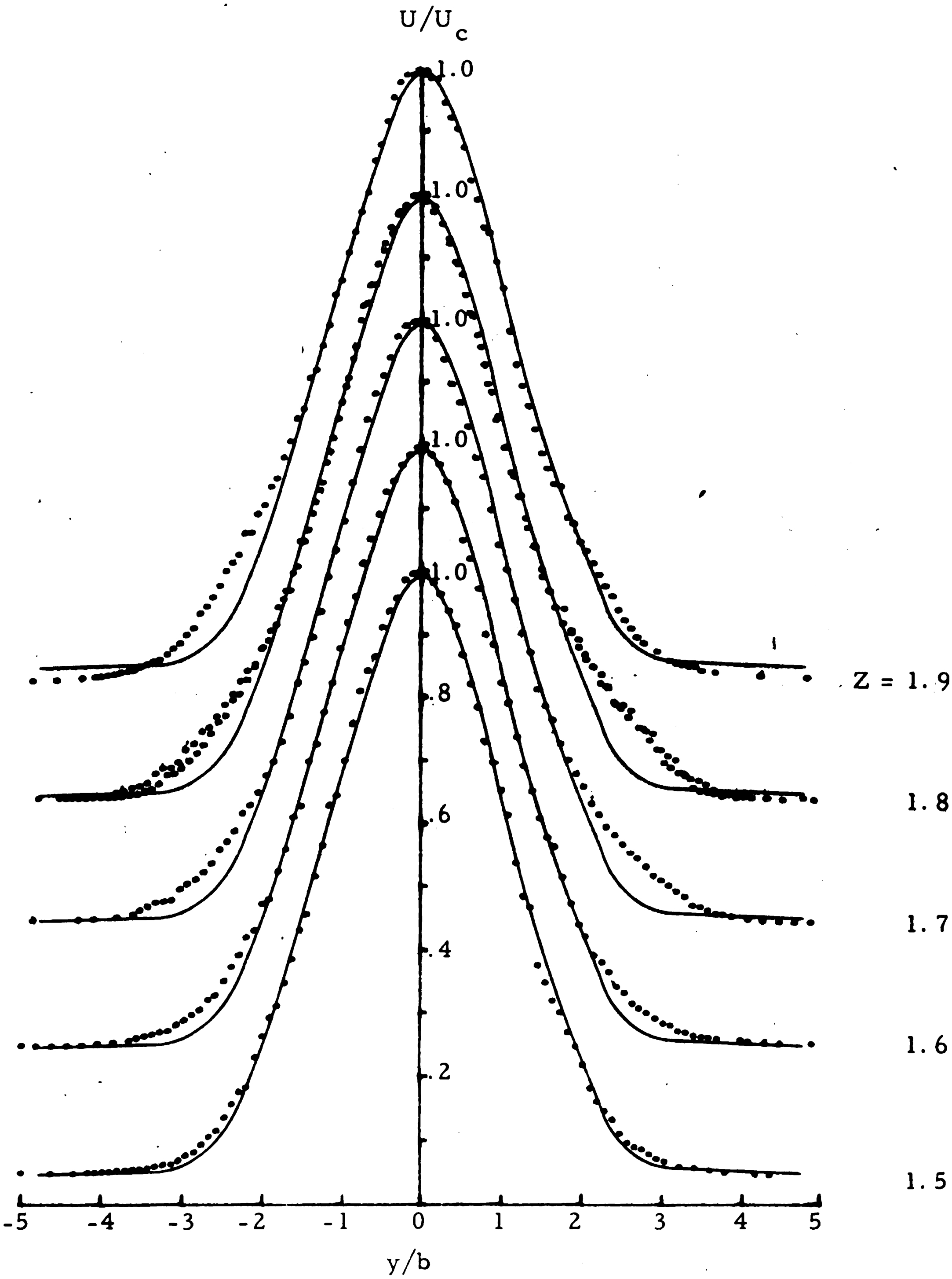

Figure 31b. Dimensionless mean velocity distributions at X=5 (Z=1.5, 1.6, 1.7, 1.8, 1.9)

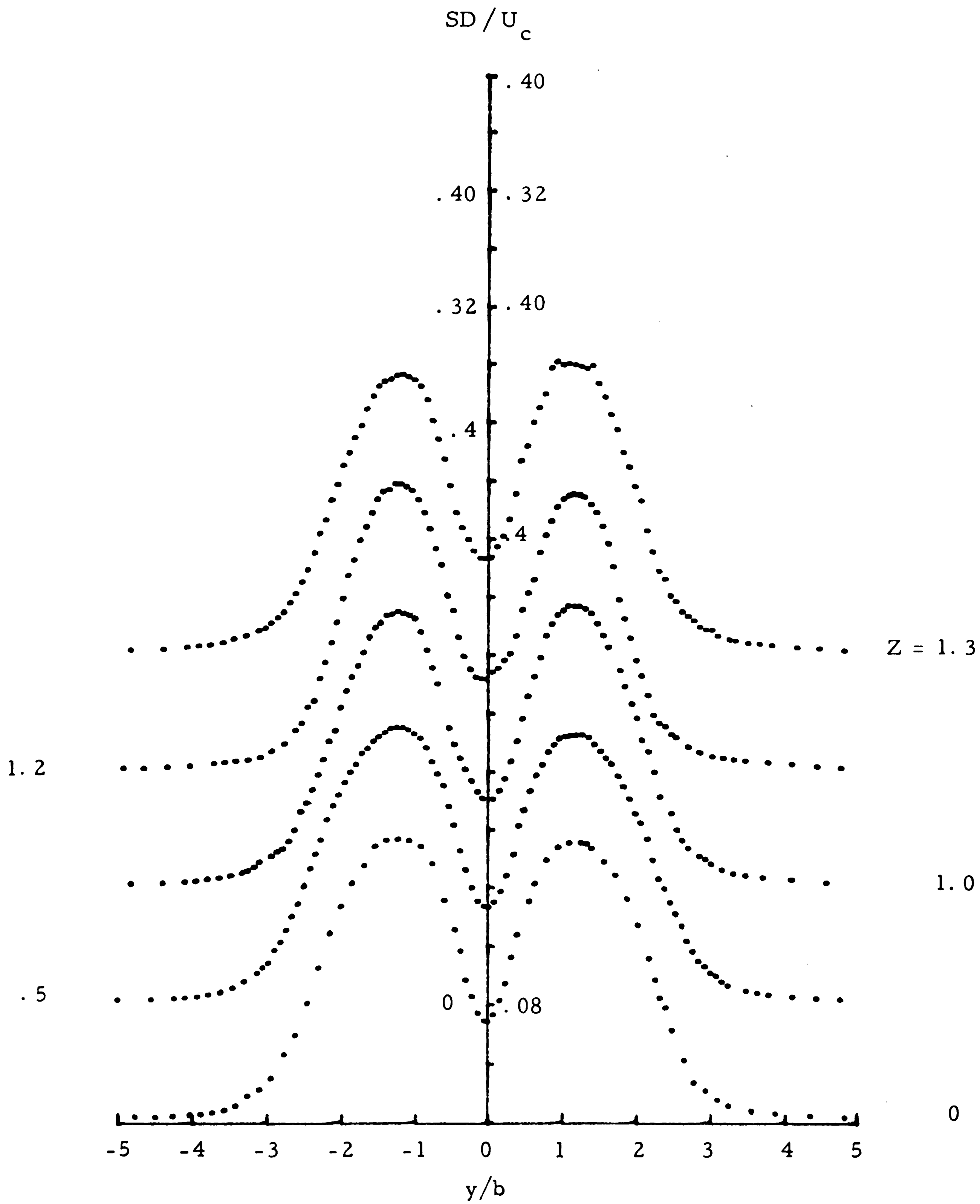

Figure 32a. Dimensionless turbulence intensity distributions at X=5 (Z= 0, . 5, 1. 0, 1. 2, 1. 3)

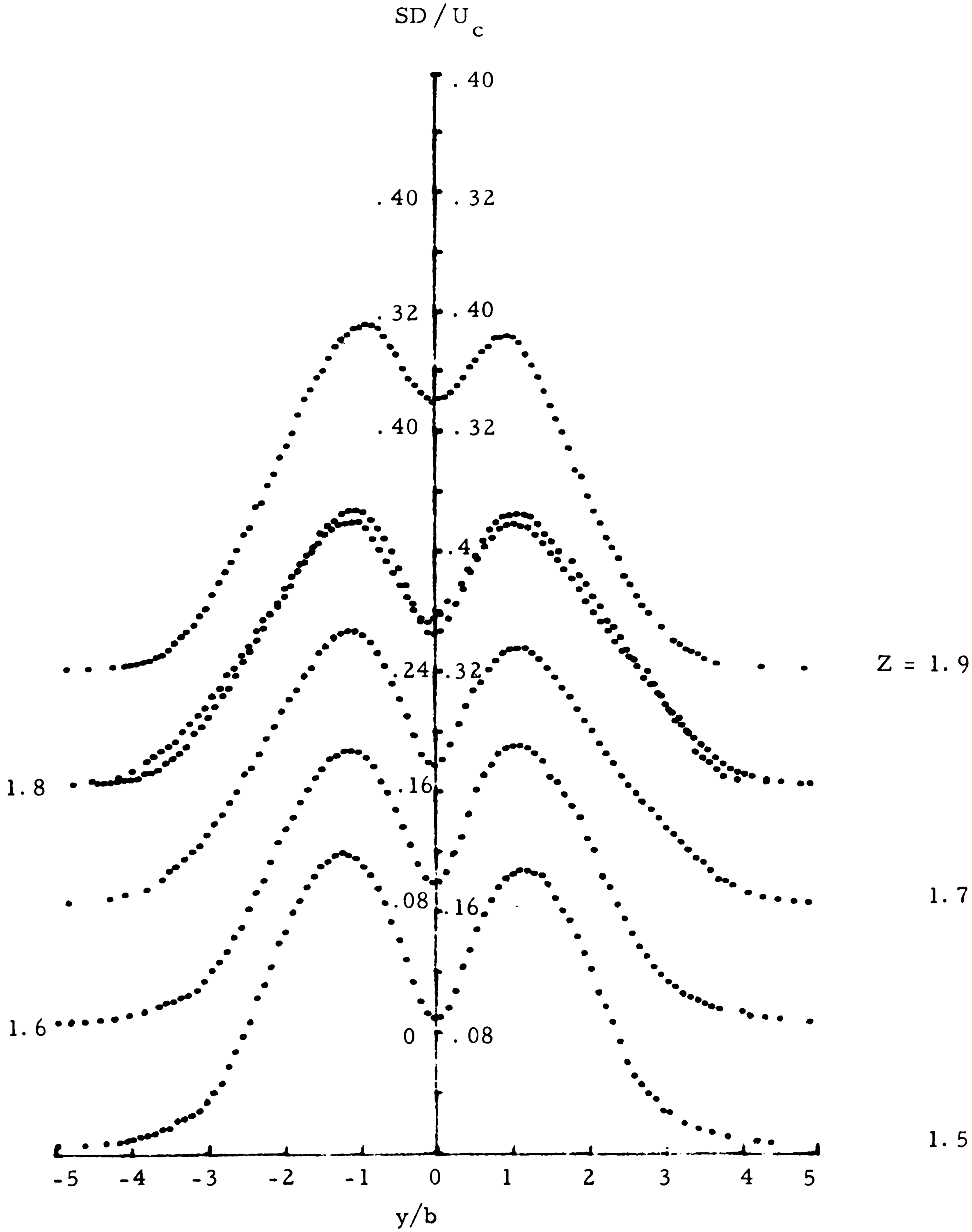

Figure 32b. Dimensionless turbulence intensity distributions at X=5 (Z= 1.5, 1.6, 1.7, 1.8, 1.9)

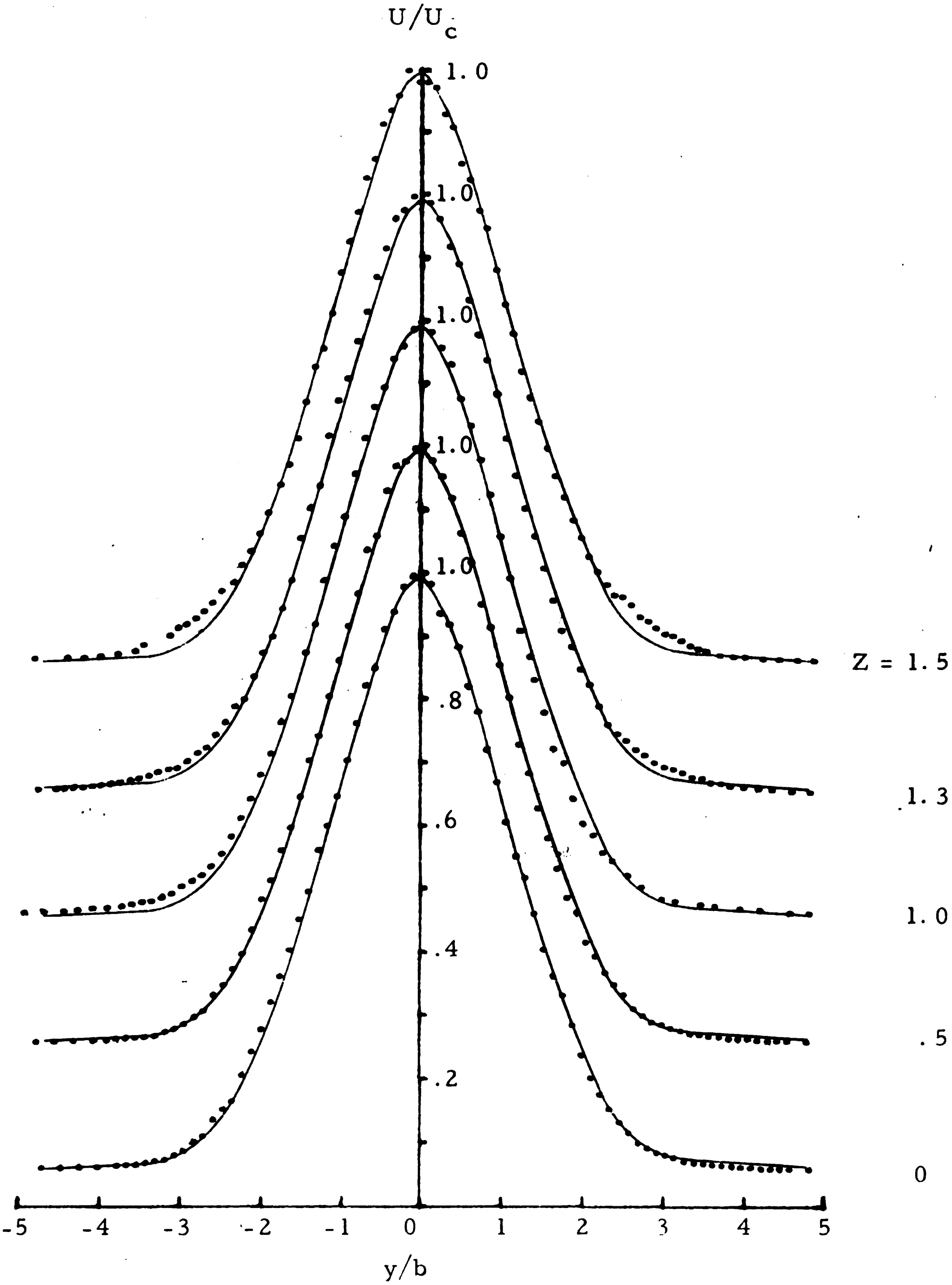

Figure 33a. Dimensionless mean velocity distributions at X=10 (Z= 0, 0.5, 1.0, 1.3, 1.5)

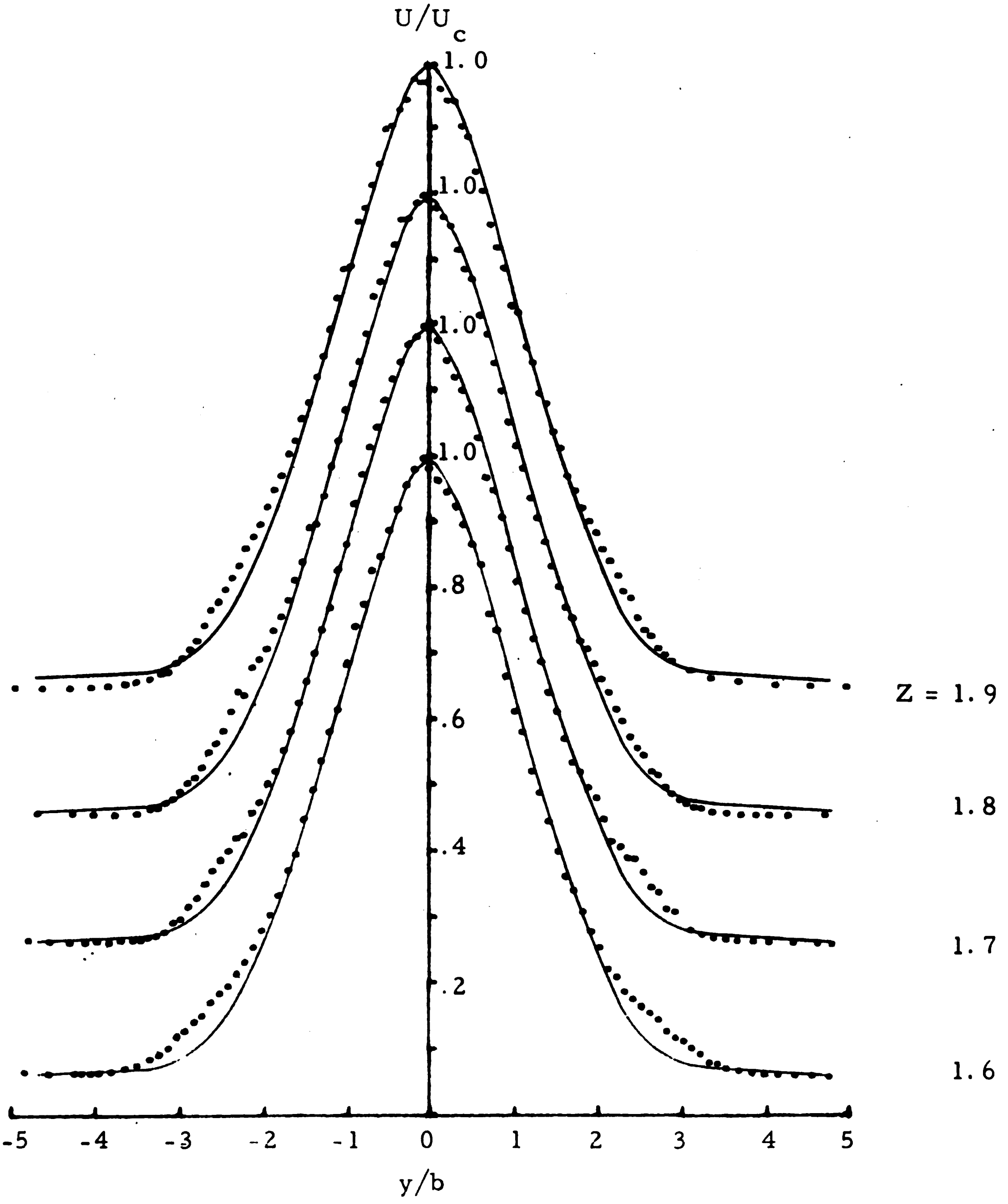

Figure 33b. Dimensionless mean velocity distributions at X=10 (Z= 1.6, 1.7, 1.8, 1.9)

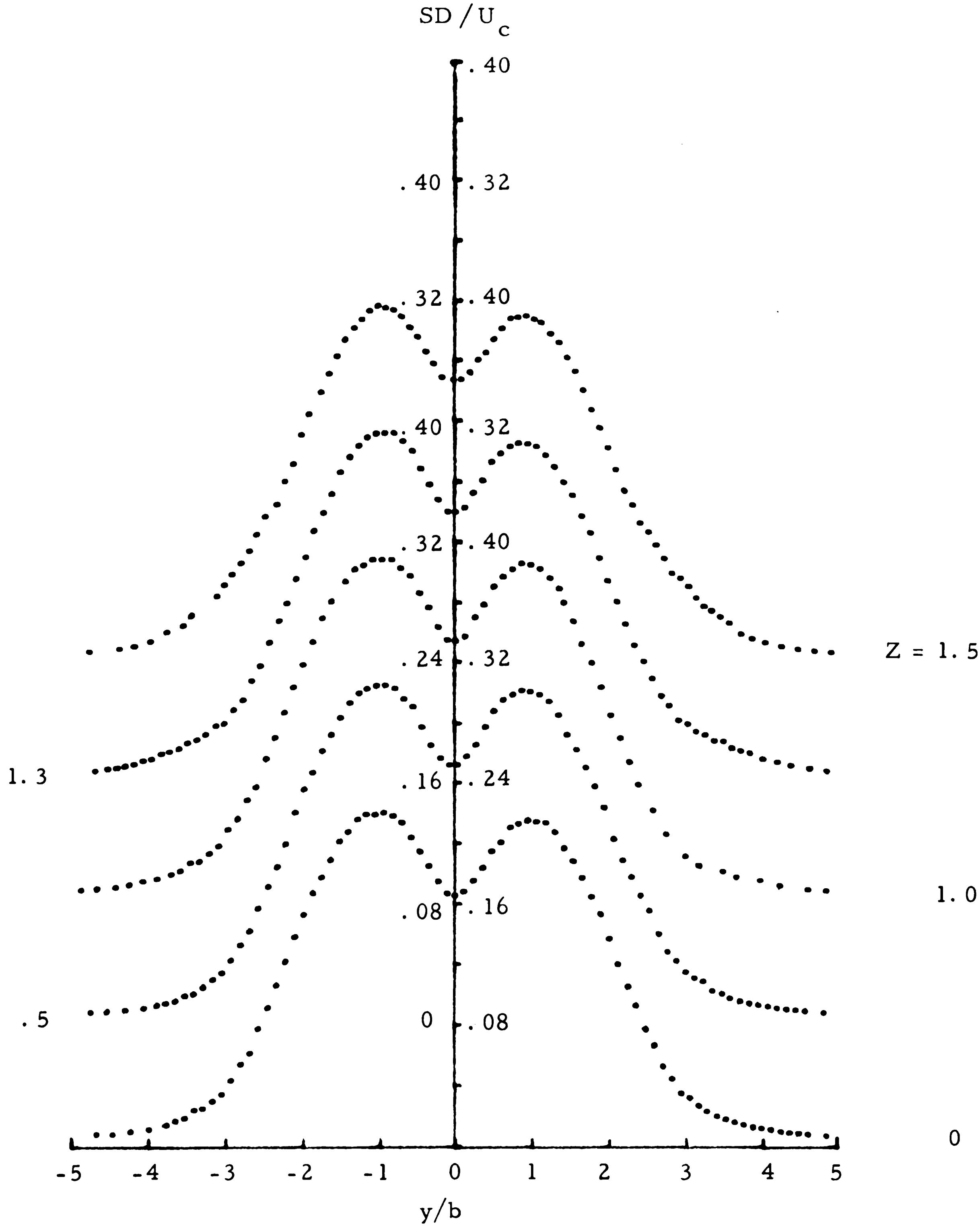

Figure 34a. Dimensionless turbulence intensity distributions at X=10 (Z= 0, .5, 1.0, 1.3, 1.5)

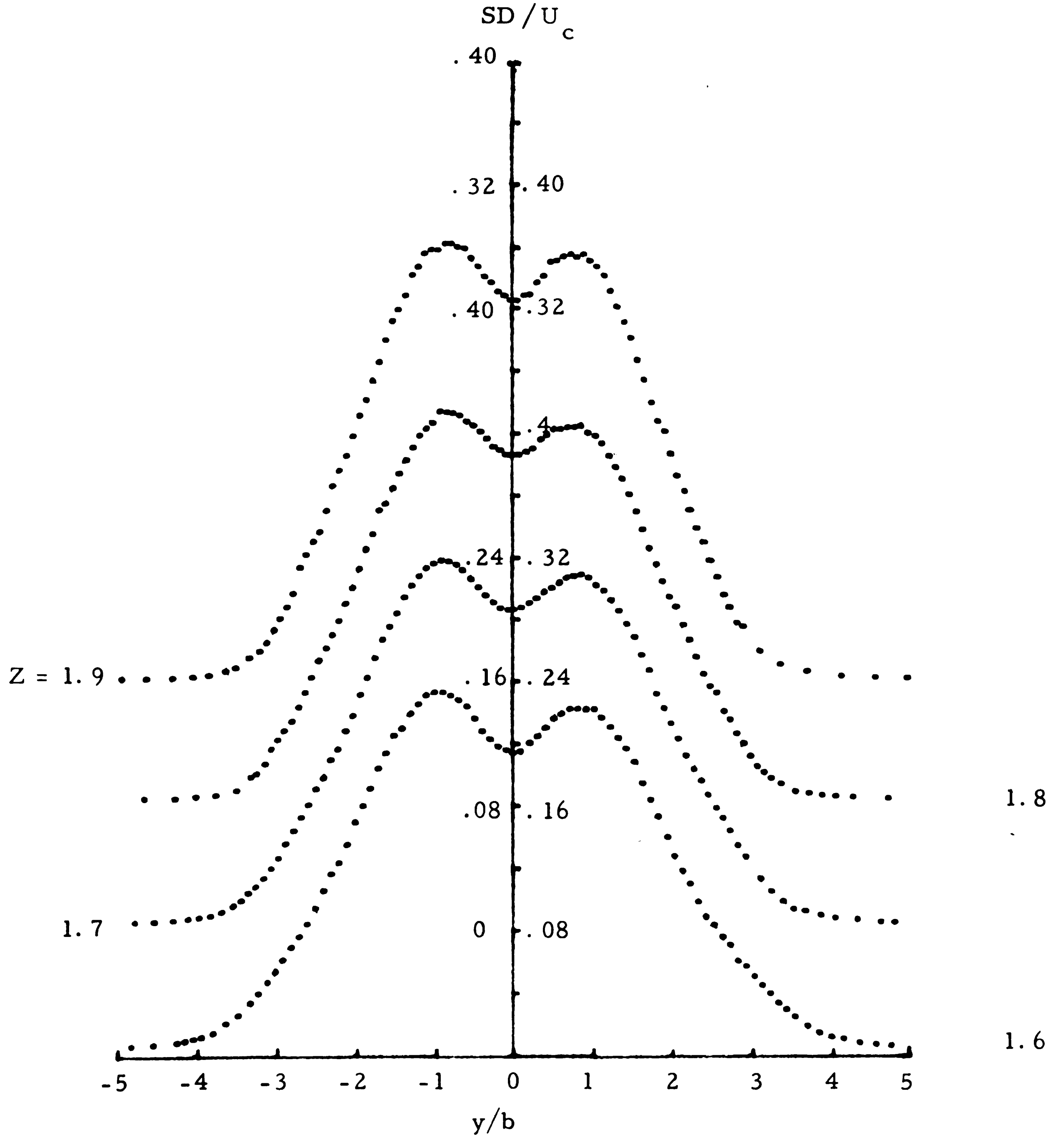

Figure 34b. Dimensionless turbulence intensity distributions at X=10 (Z= 1.6, 1.7, 1.8, 1.9)

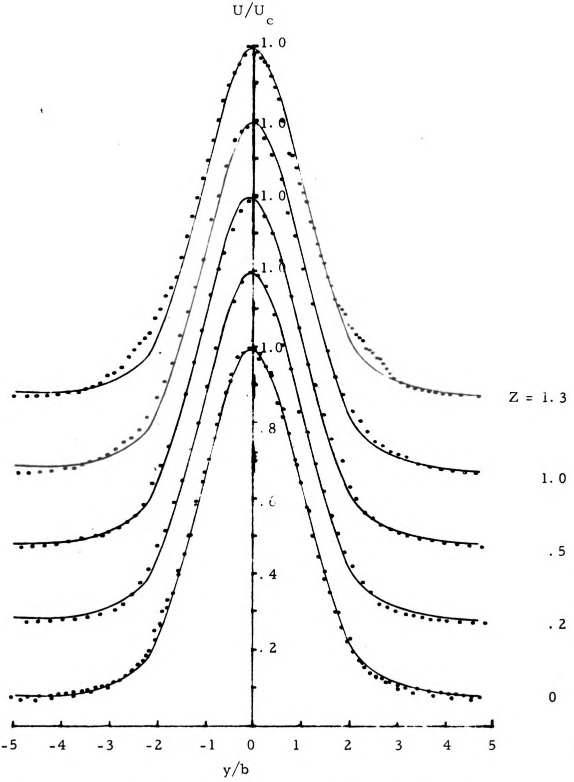

Figure 35a. Dimensionless mean velocity distributions at X=15 (Z= 0, 0.2, 0.5, 1.0, 1.3)

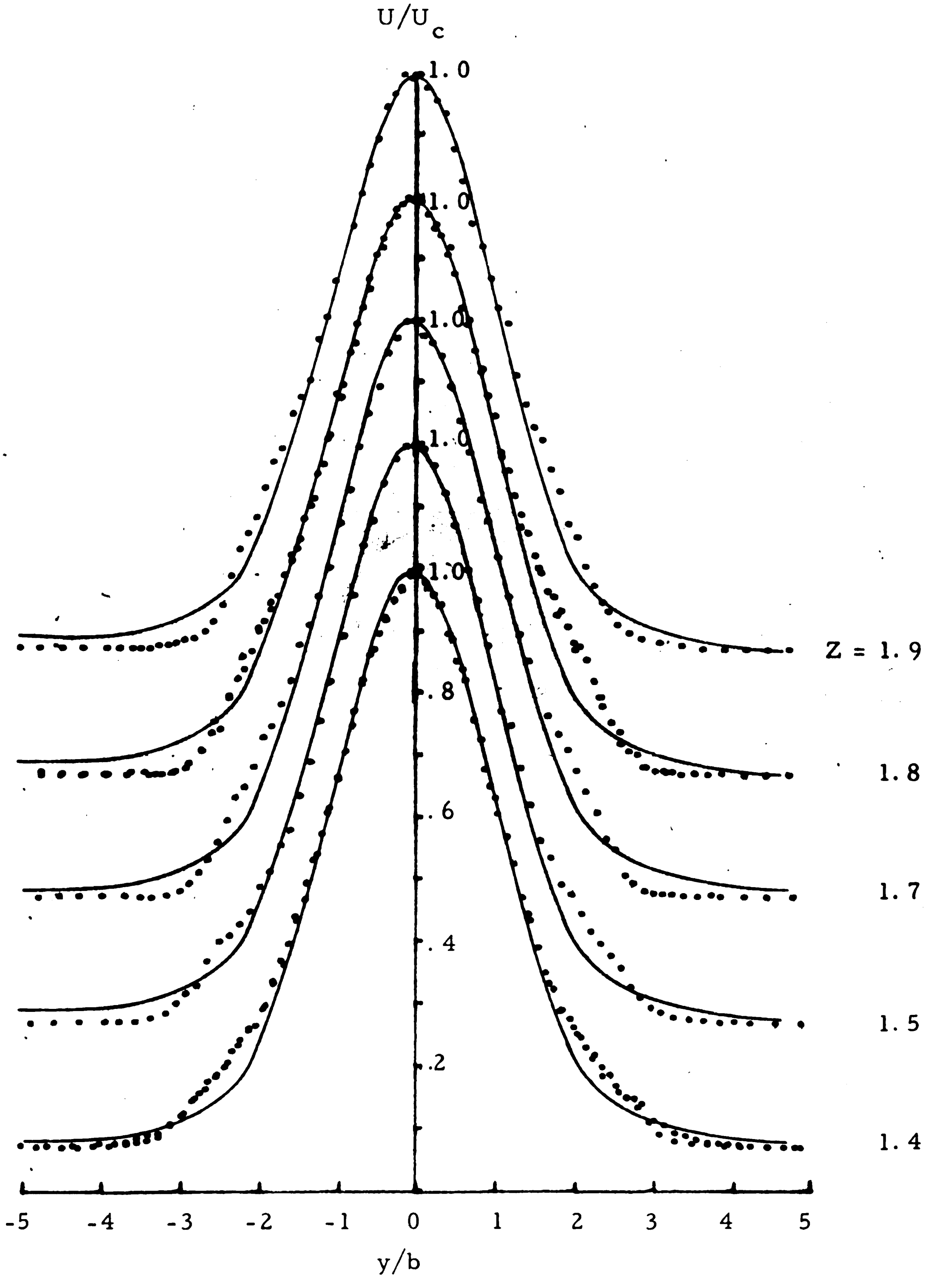

Figure 35b. Dimensionless mean velocity distributions at X=15 (Z= 1.4, 1.5, 1.7, 1.8, 1.9)

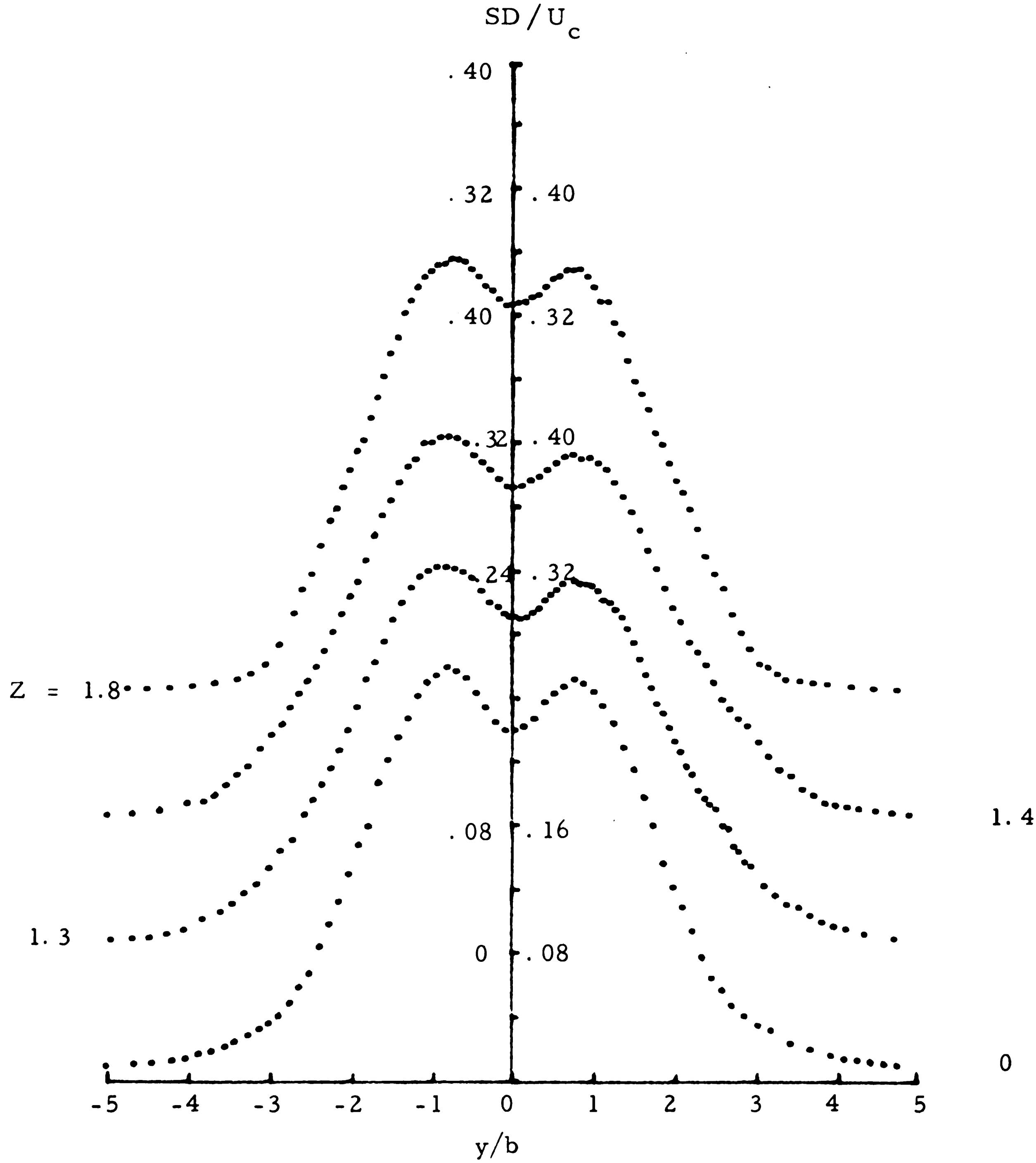

Figure 36. Dimensionless turbulence intensity distributions at X=15 (Z= 0, 1.3, 1.4, 1.8)

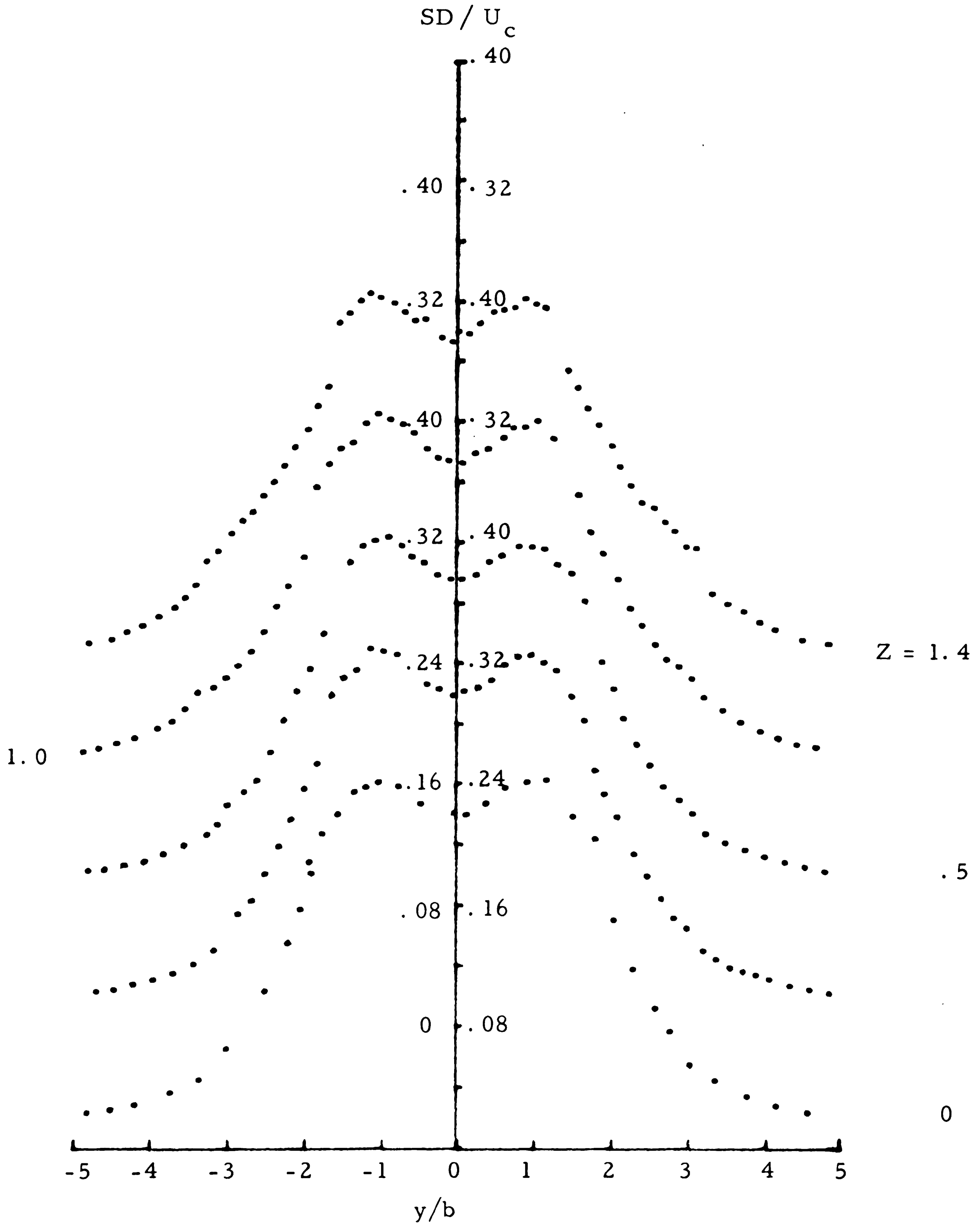

Figure 37a. Dimensionless turbulence intensity distributions at X=15 (Z= 0, .2, .5, 1.0, 1.4). Quantitatively inaccurate data; see Chapter 3.

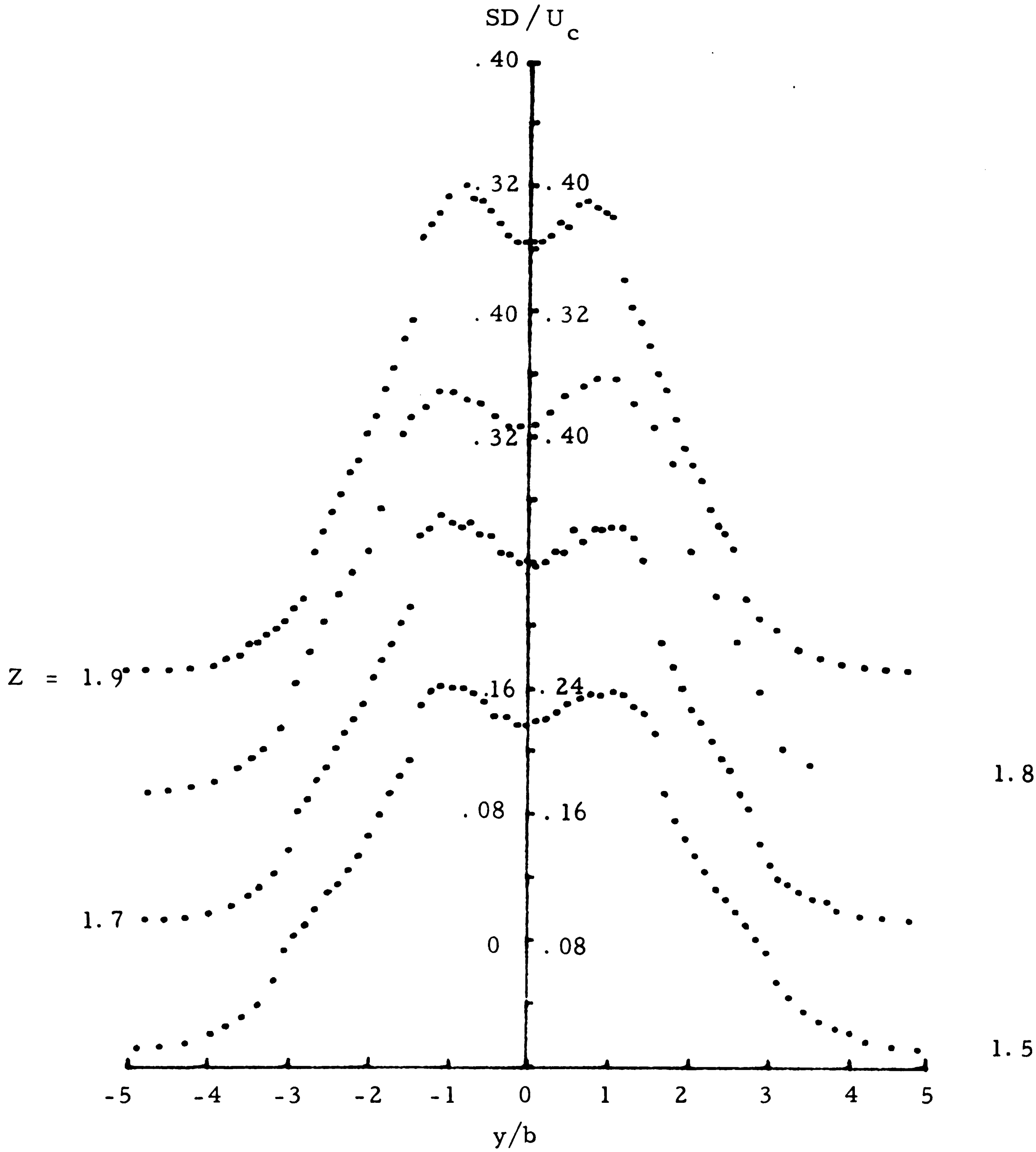

Figure 37b. Dimensionless turbulence intensity distributions at X=15 (Z= 1.5, 1.7, 1.8, 1.9). Quantitatively inaccurate data; see Chapter 3.

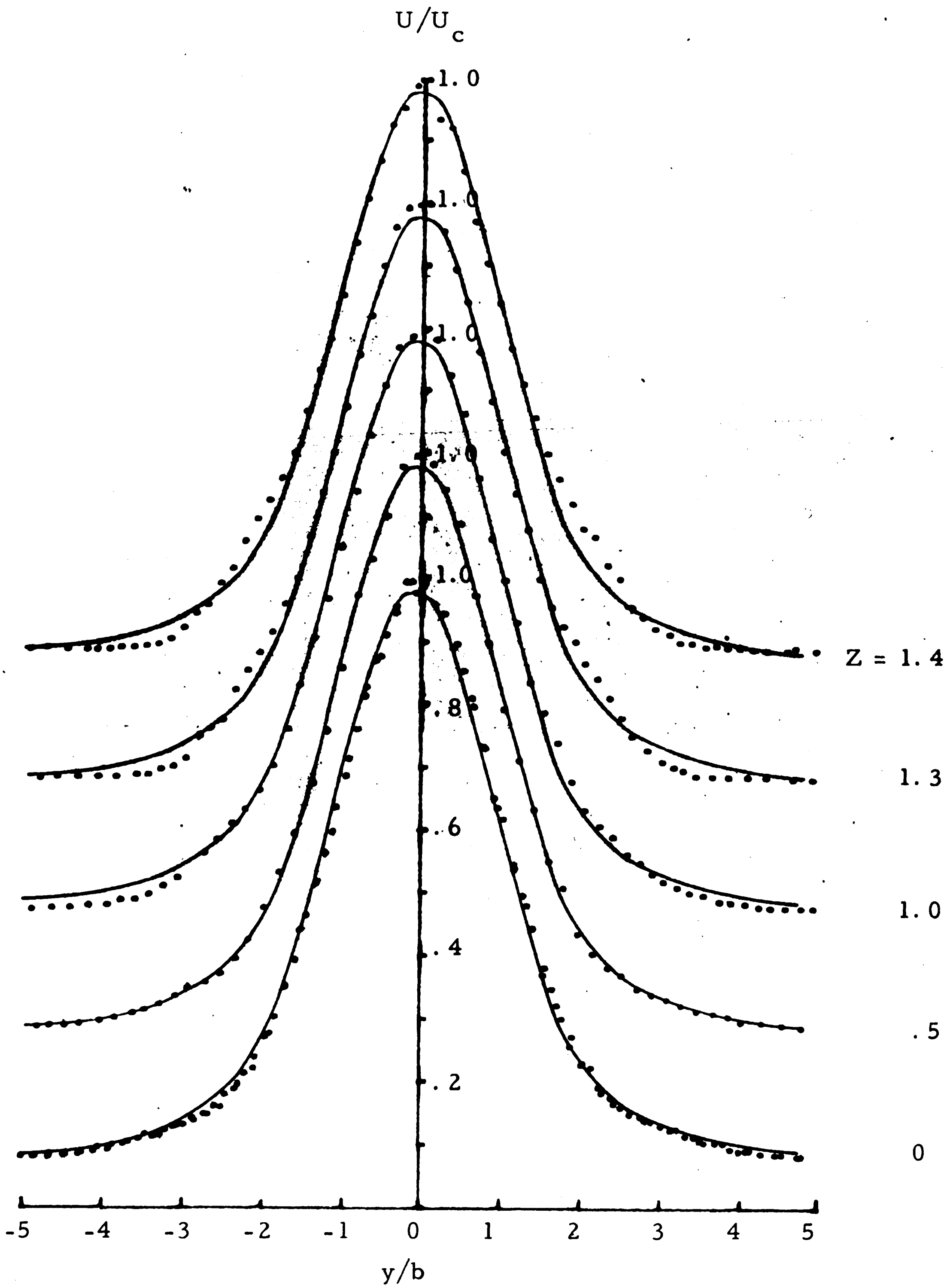

Figure 38a. Dimensionless mean velocity distributions at X=20 (Z= 0, 0. 5, 1. 0, 1. 3, 1. 4)

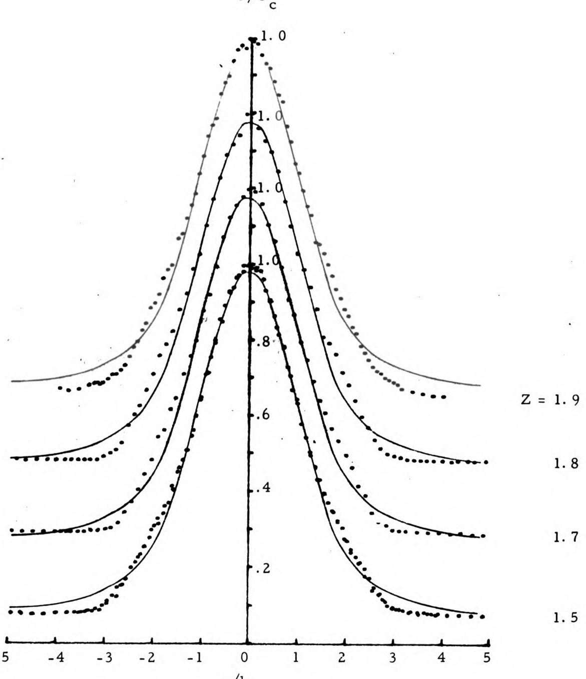

Figure 38b. Dimensionless mean velocity distributions at X=20 (Z= 1.5, 1.7, 1.8, 1.9)

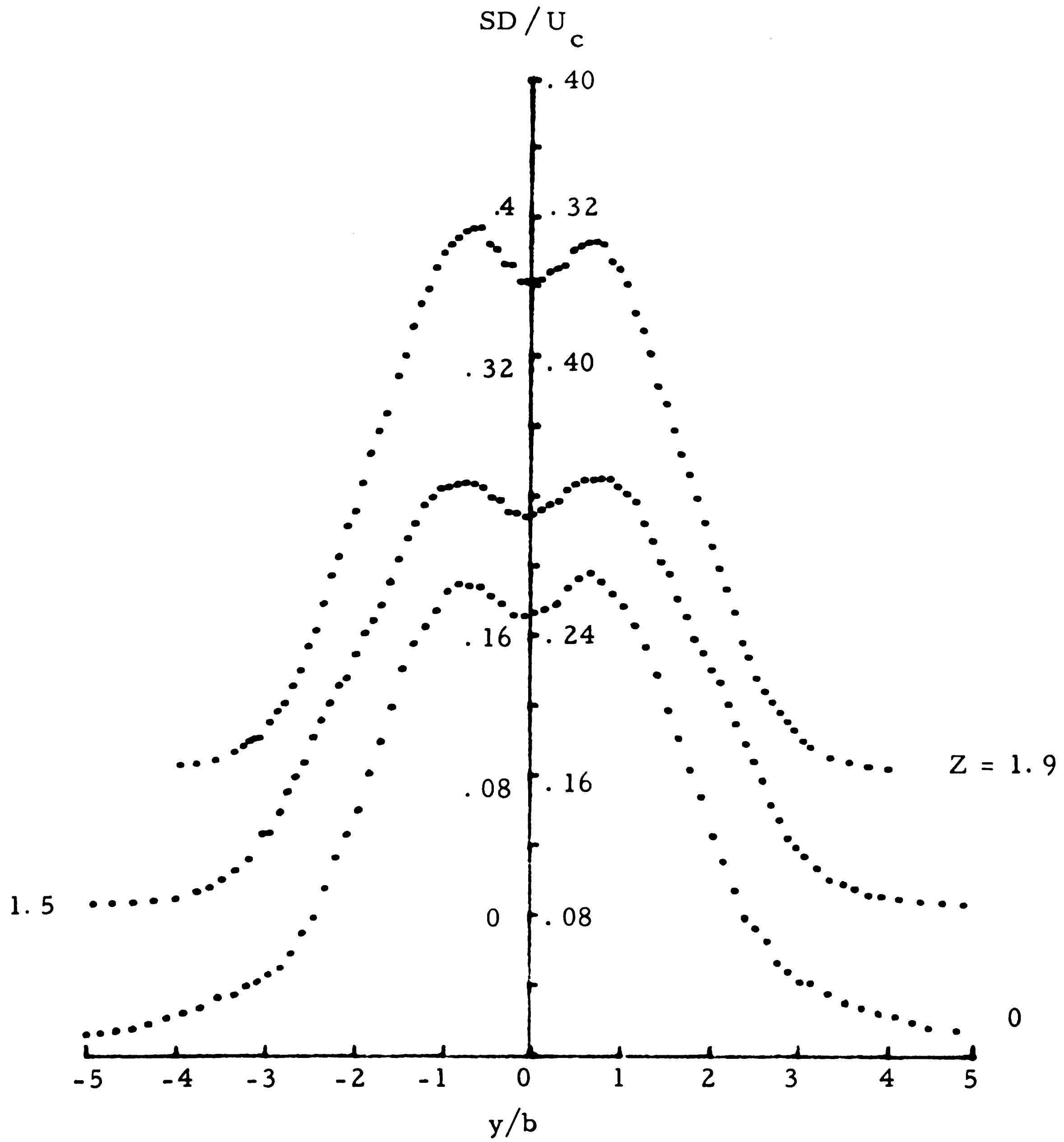

Figure 39. Dimensionless turbulence intensity distributions at X=20 (Z= 0, 1.5, 1.9)

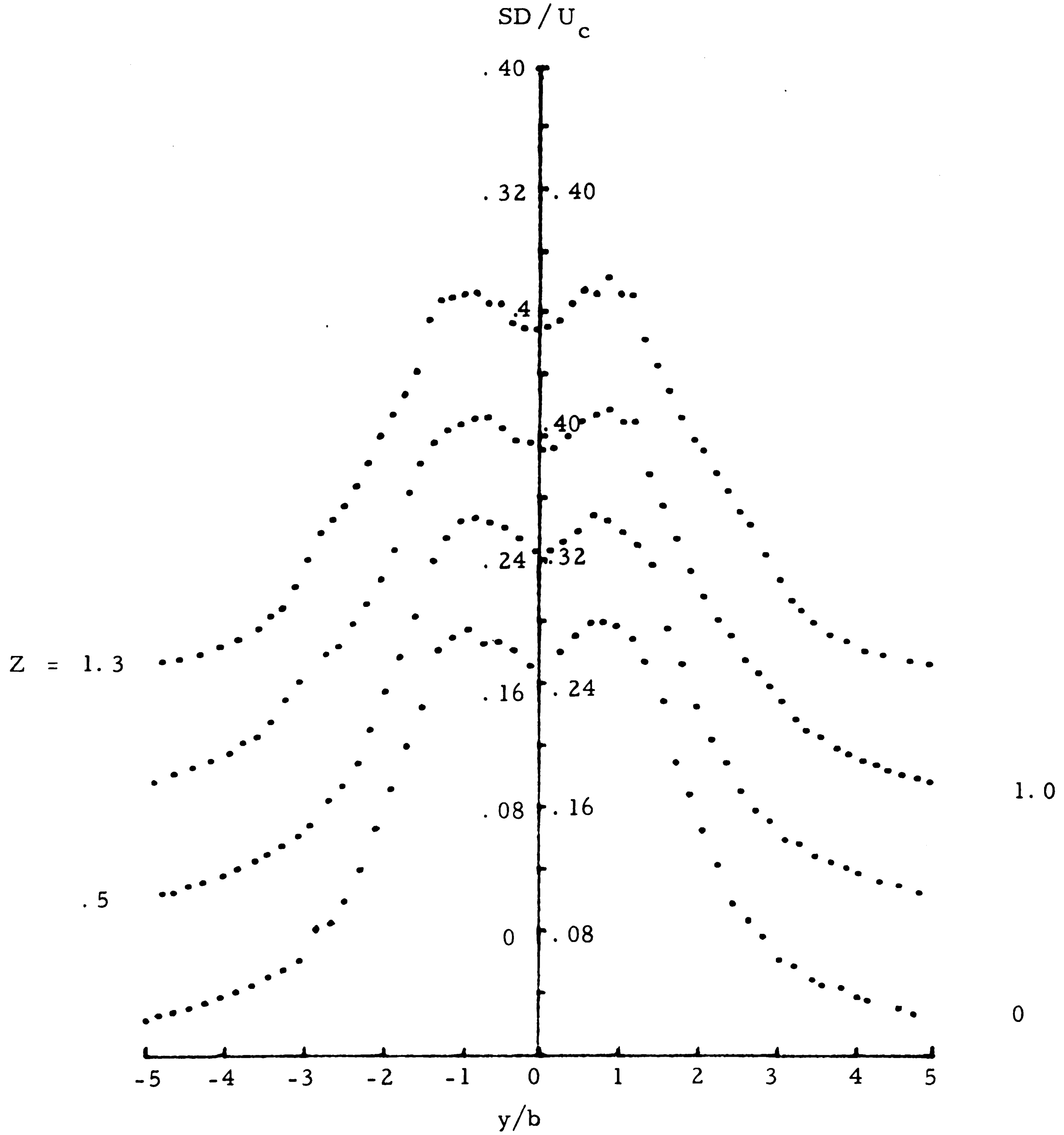

Figure 40a. Dimensionless turbulence intensity distributions at X=20 (Z= 0, .5, 1.0, 1.3). Quantitatively inaccurate data; see Chapter 3.

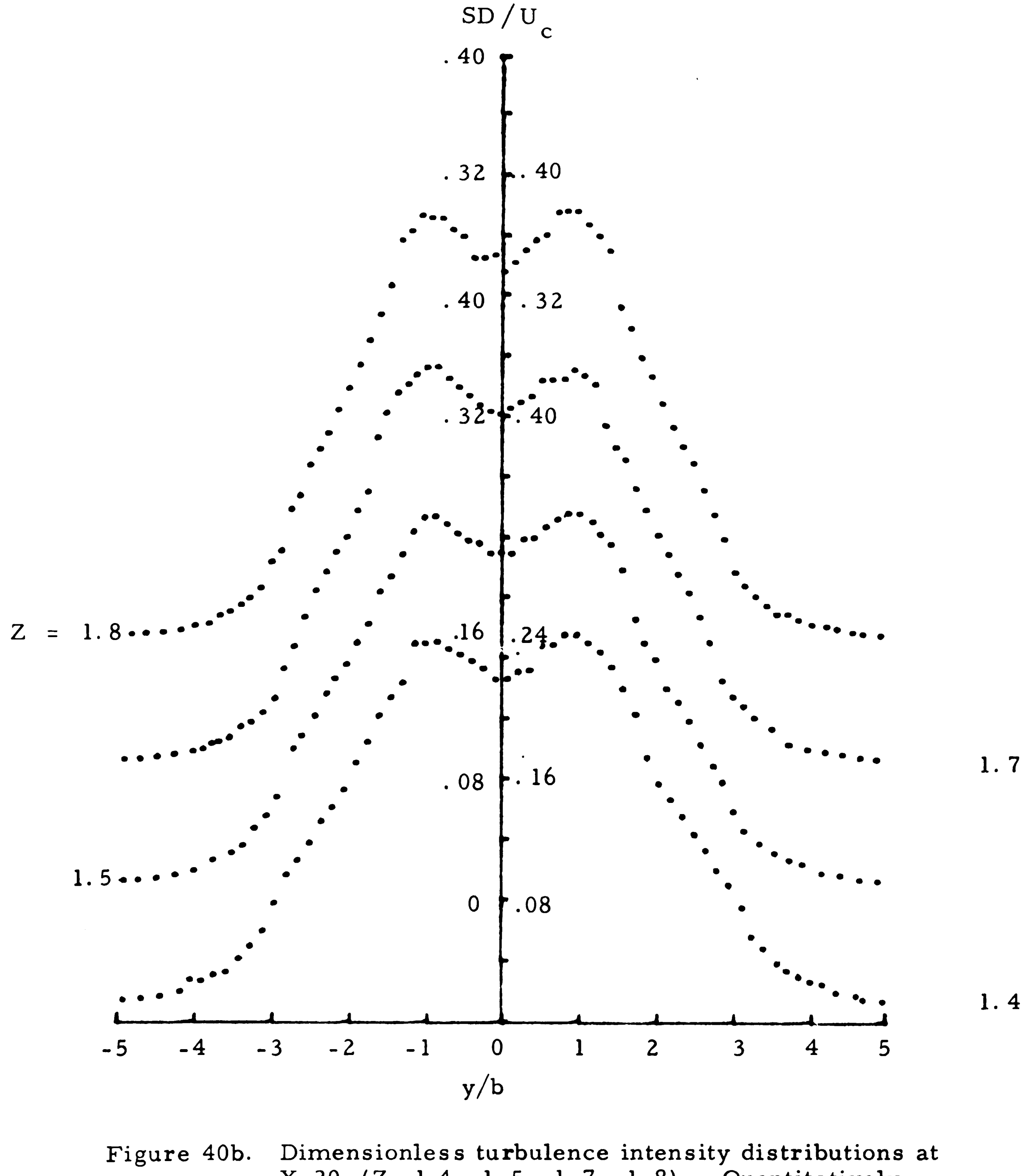

Figure 40b. Dimensionless turbulence intensity distributions at X=20 (Z= 1.4, 1. 5, 1. 7, 1. 8). Quantitatively inaccurate data; see Chapter 3.

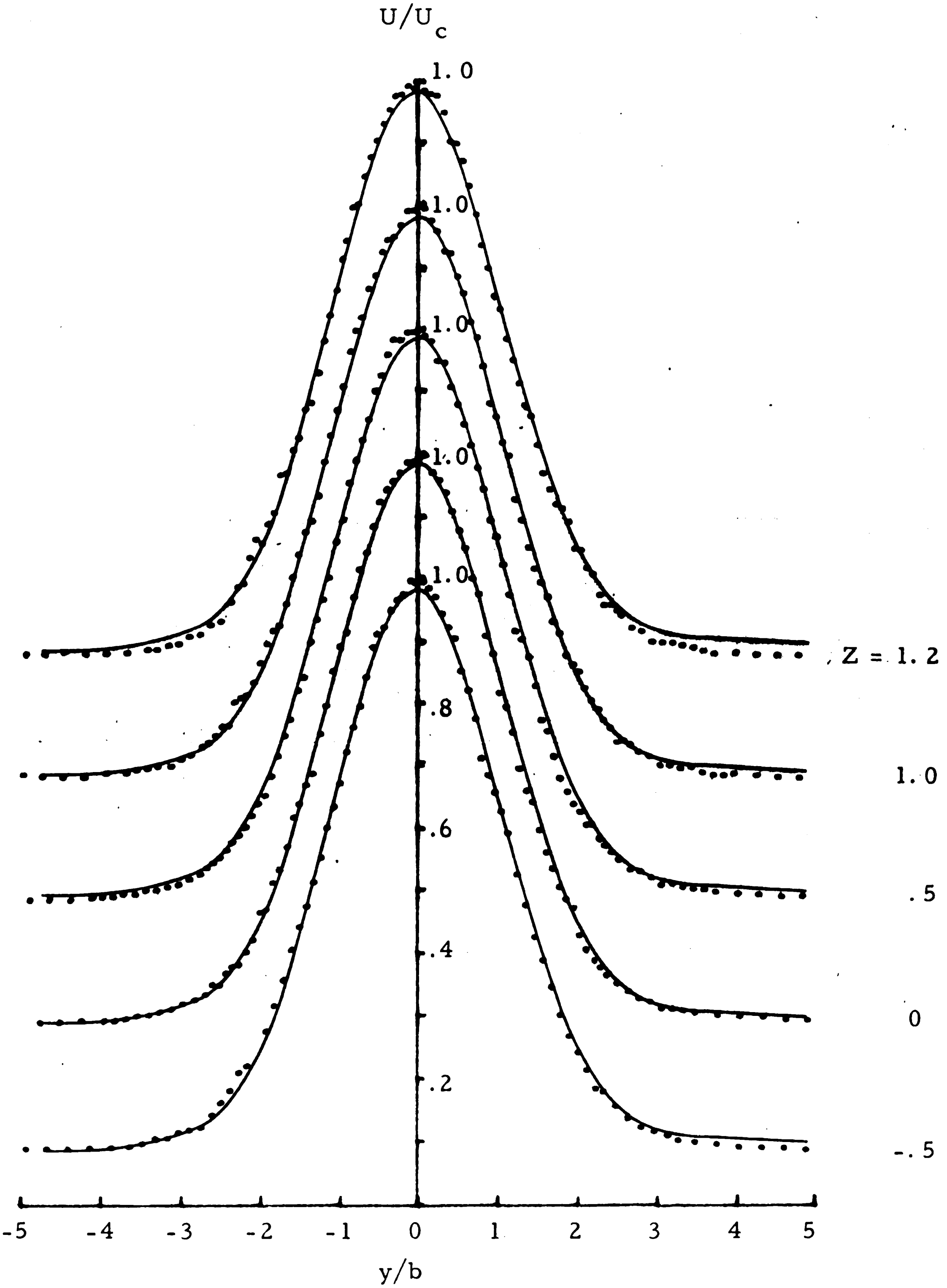

Figure 41a. Dimensionless mean velocity distributions at X=40 (Z= -.5, 0, .5, 1.0, 1.2)

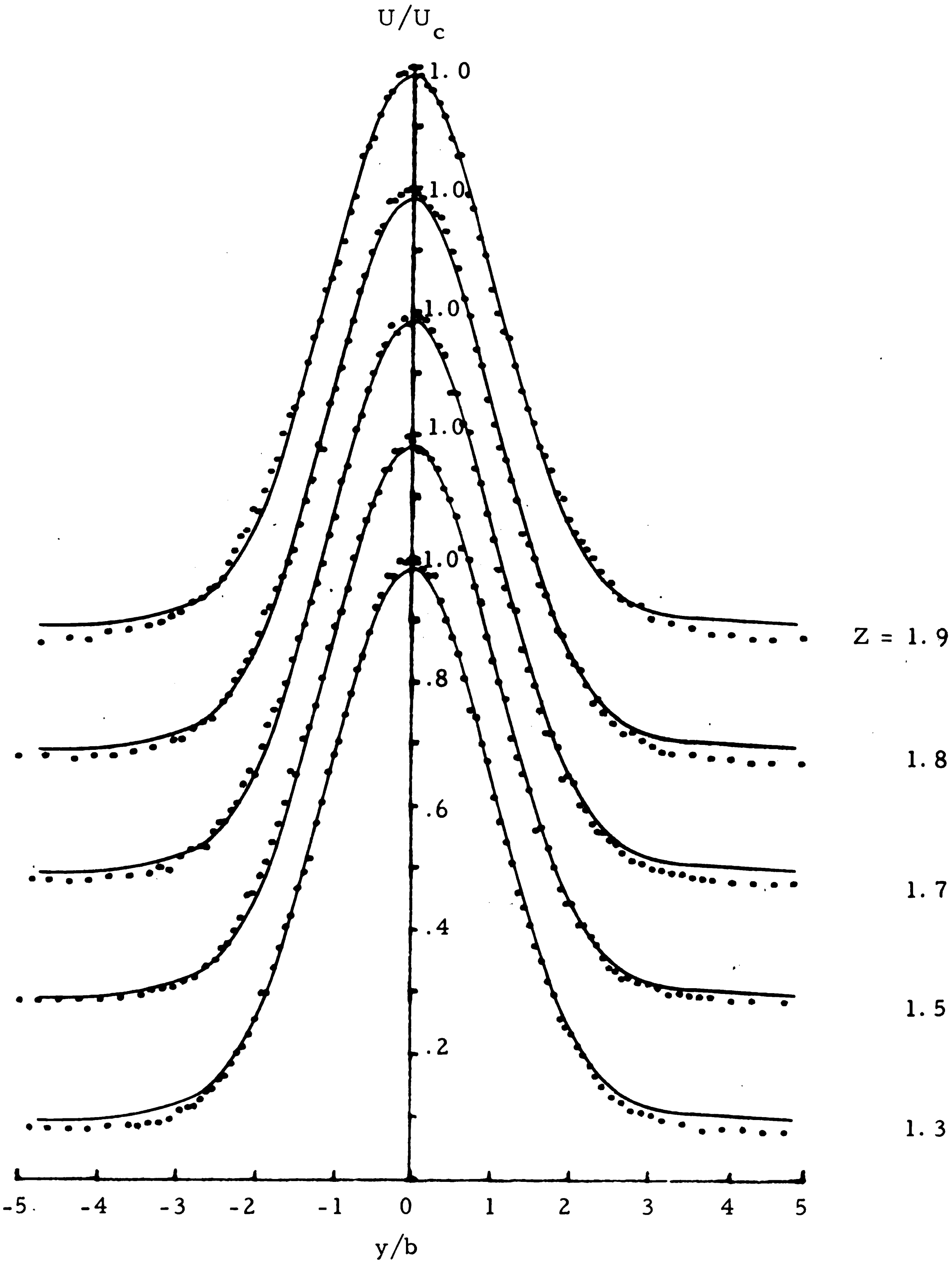

Figure 41b. Dimensionless mean velocity distributions at X=40 (Z= 1.3, 1.5, 1.7, 1.8, 1.9)

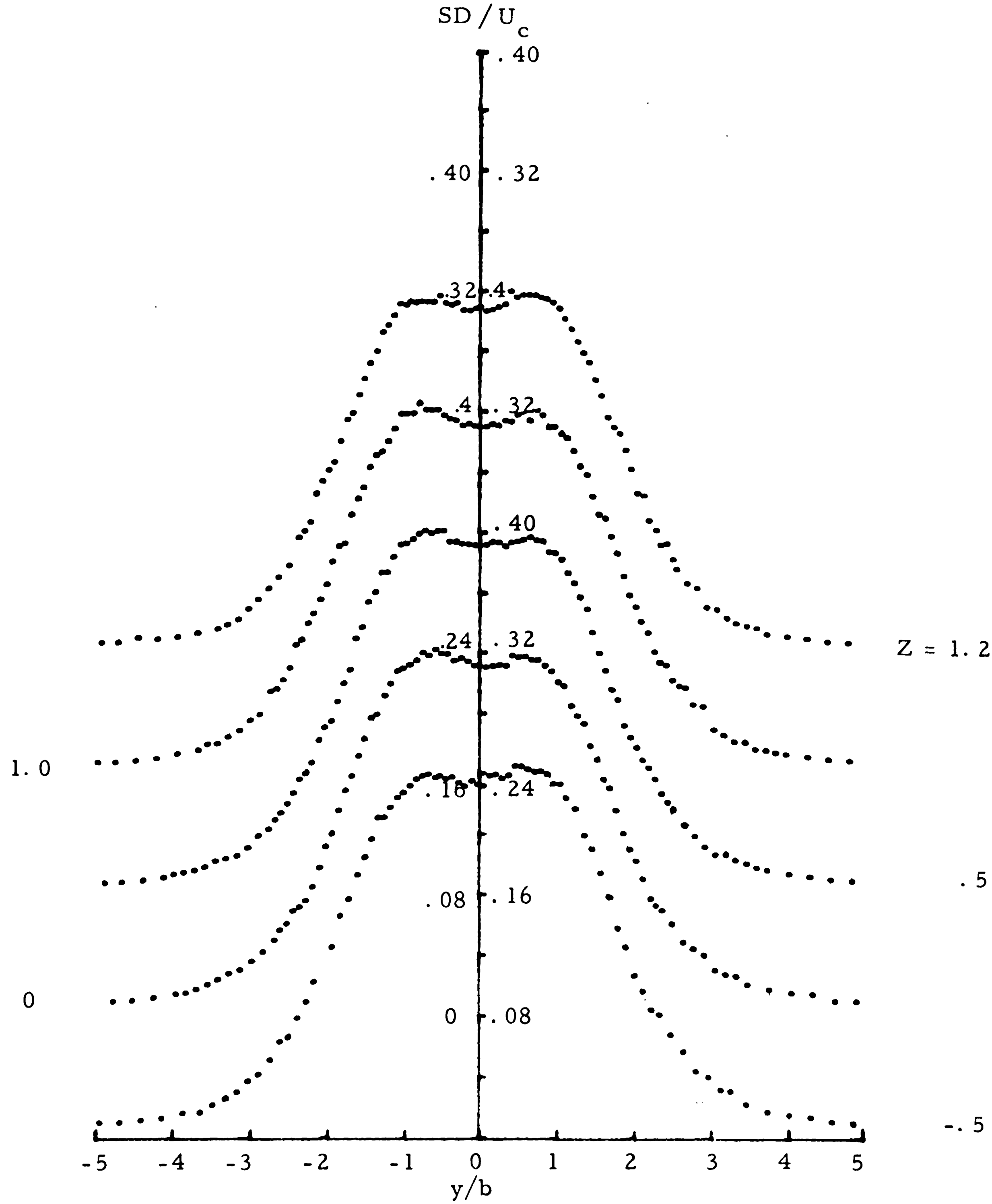

Figure 42a. Dimensionless turbulence intensity distributions at X=40 (Z= -.5, 0, .5, 1.0, 1.2)

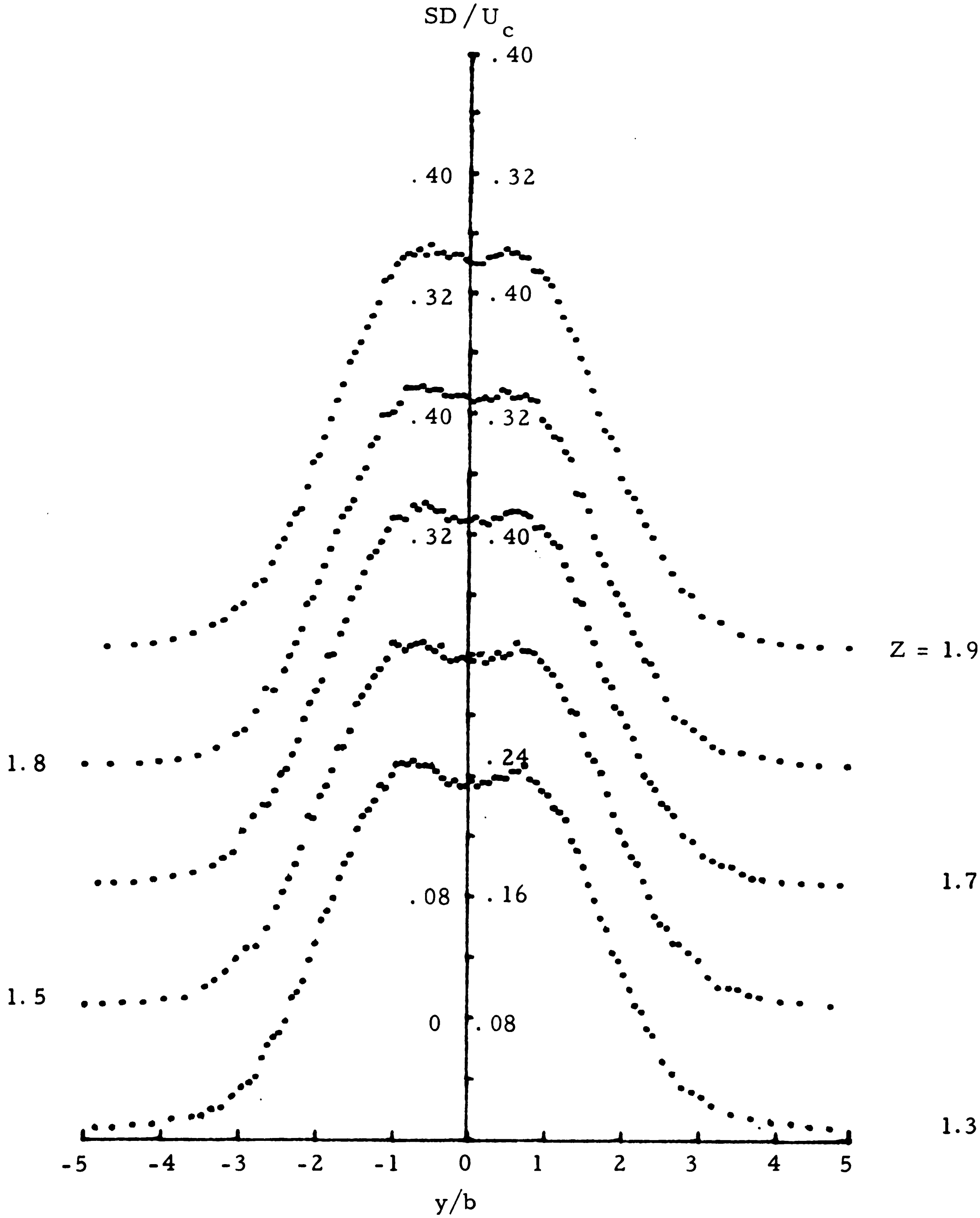

Figure 42b. Dimensionless turbulence intensity distributions at X=40 (Z= 1.3, 1.5, 1.7, 1.8, 1.9)

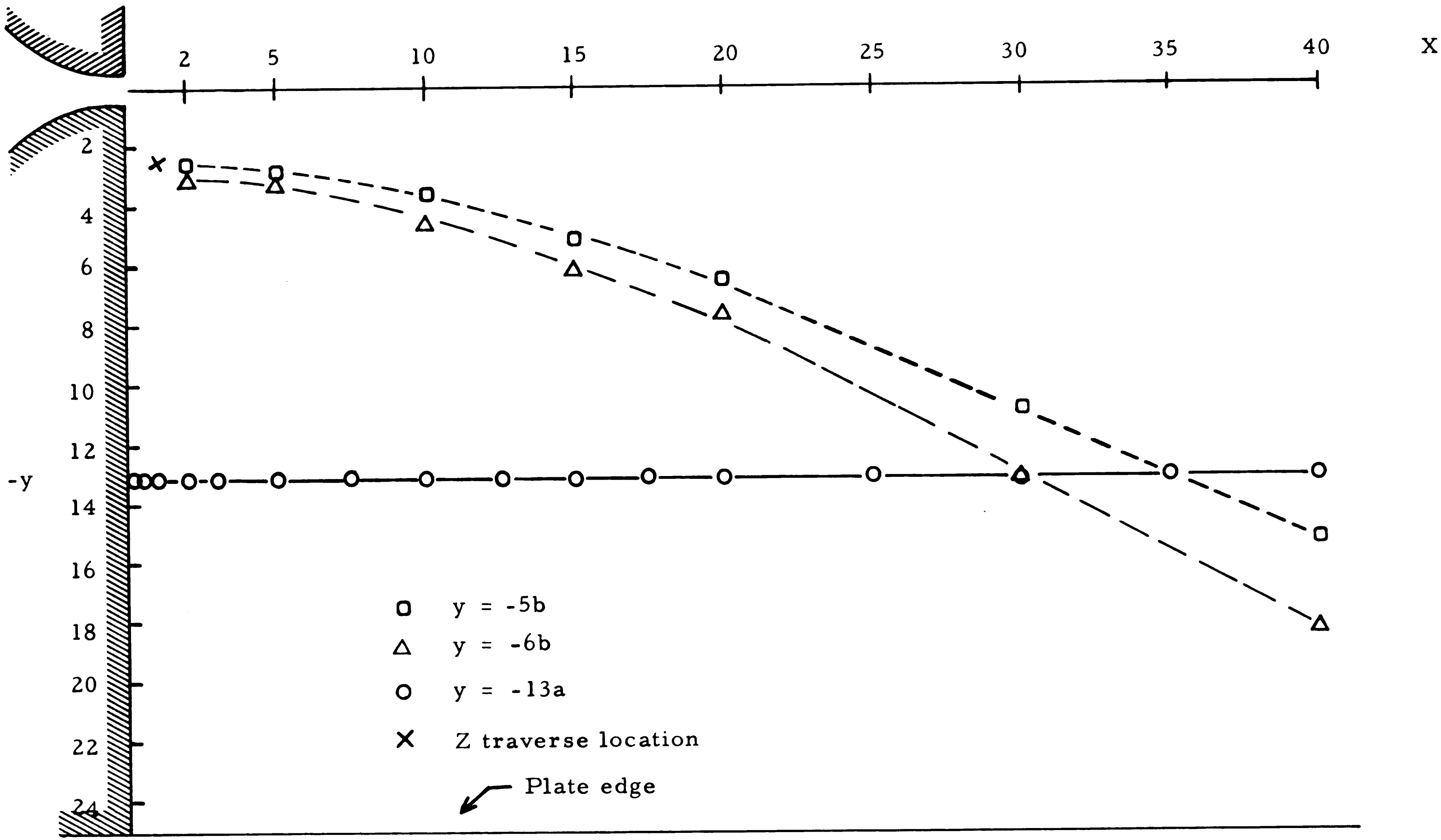

Figure 43. Location of X traverse entrainment measurements

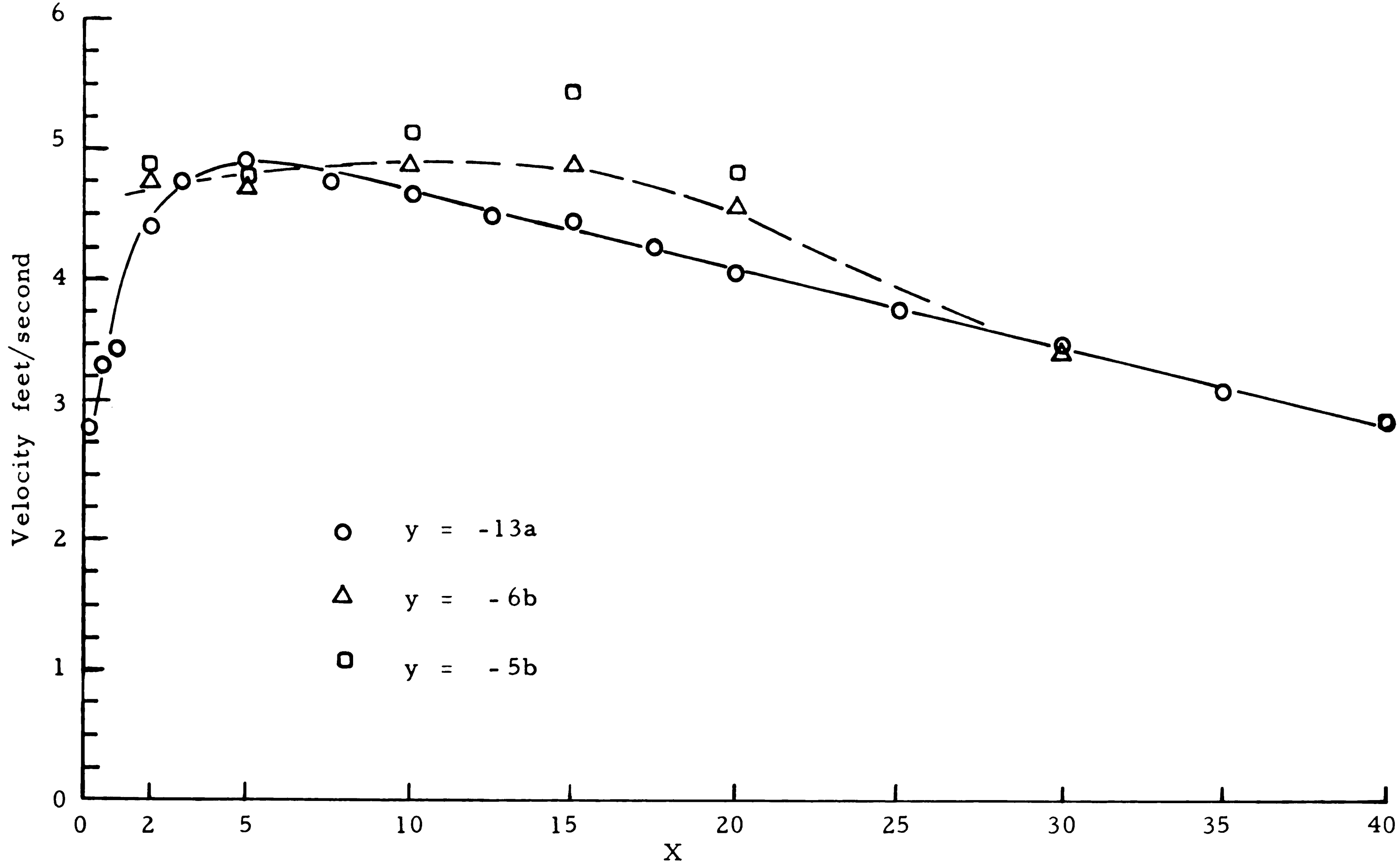

Figure 44. X traverse entrainment mean velocity distributions

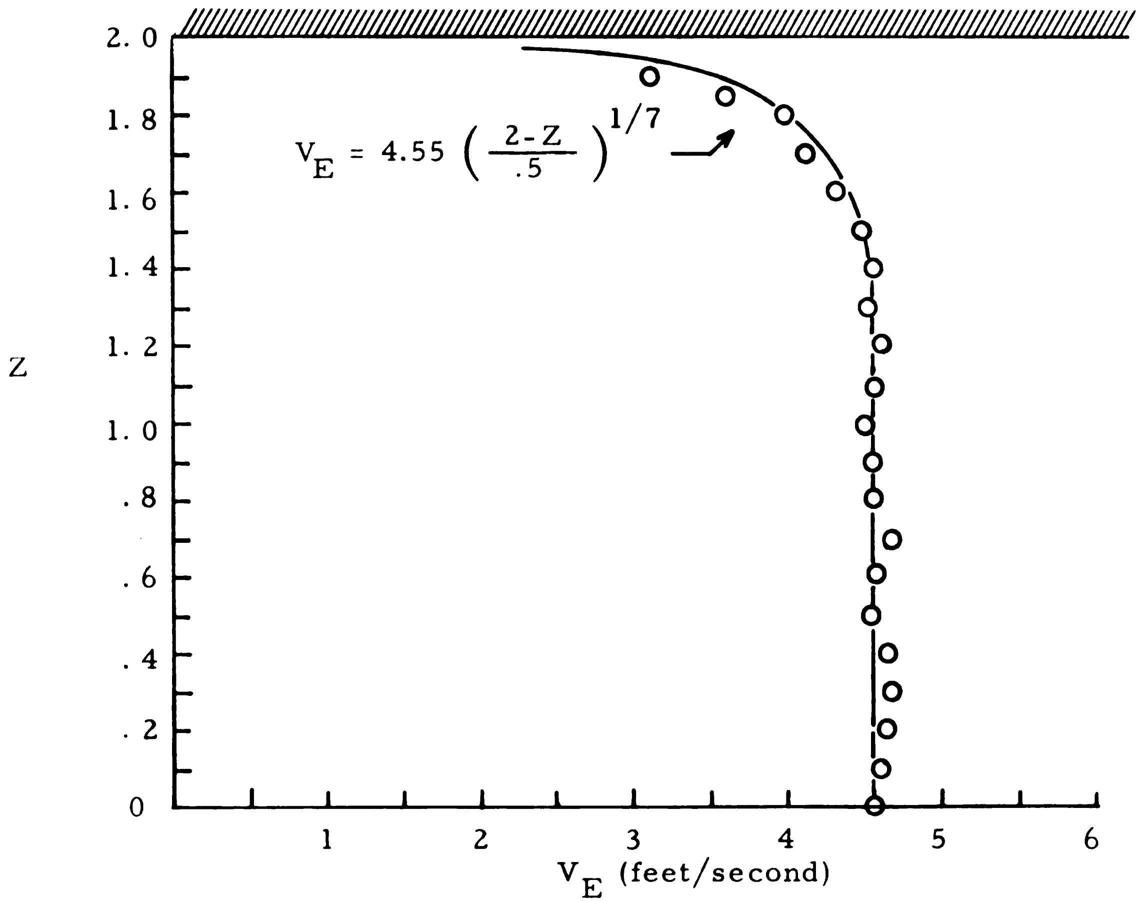

Figure 45. Z traverse entrainment mean velocity distribution.

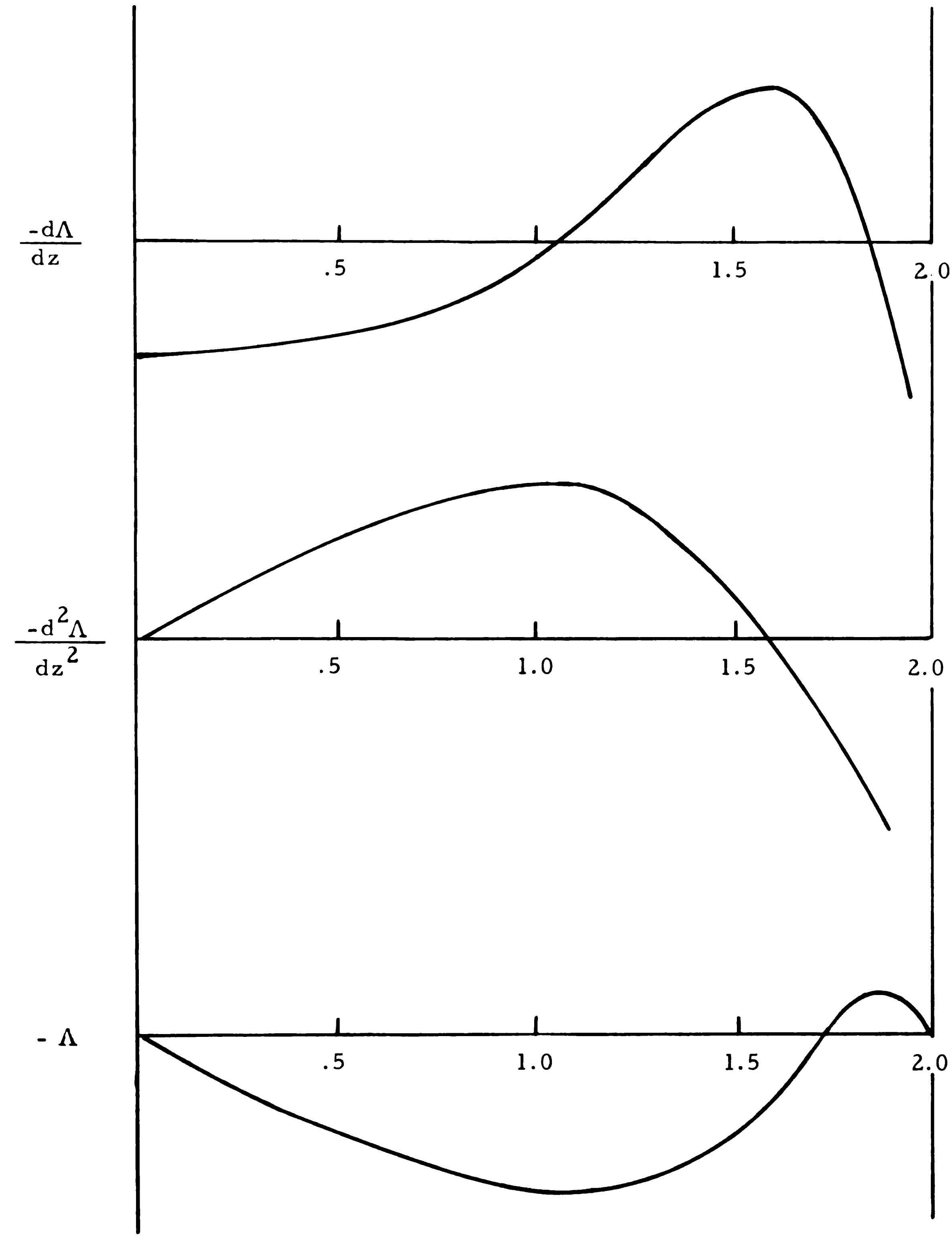

Figure 46b. Schematic representation of $-d\Lambda / dz$ at X=20

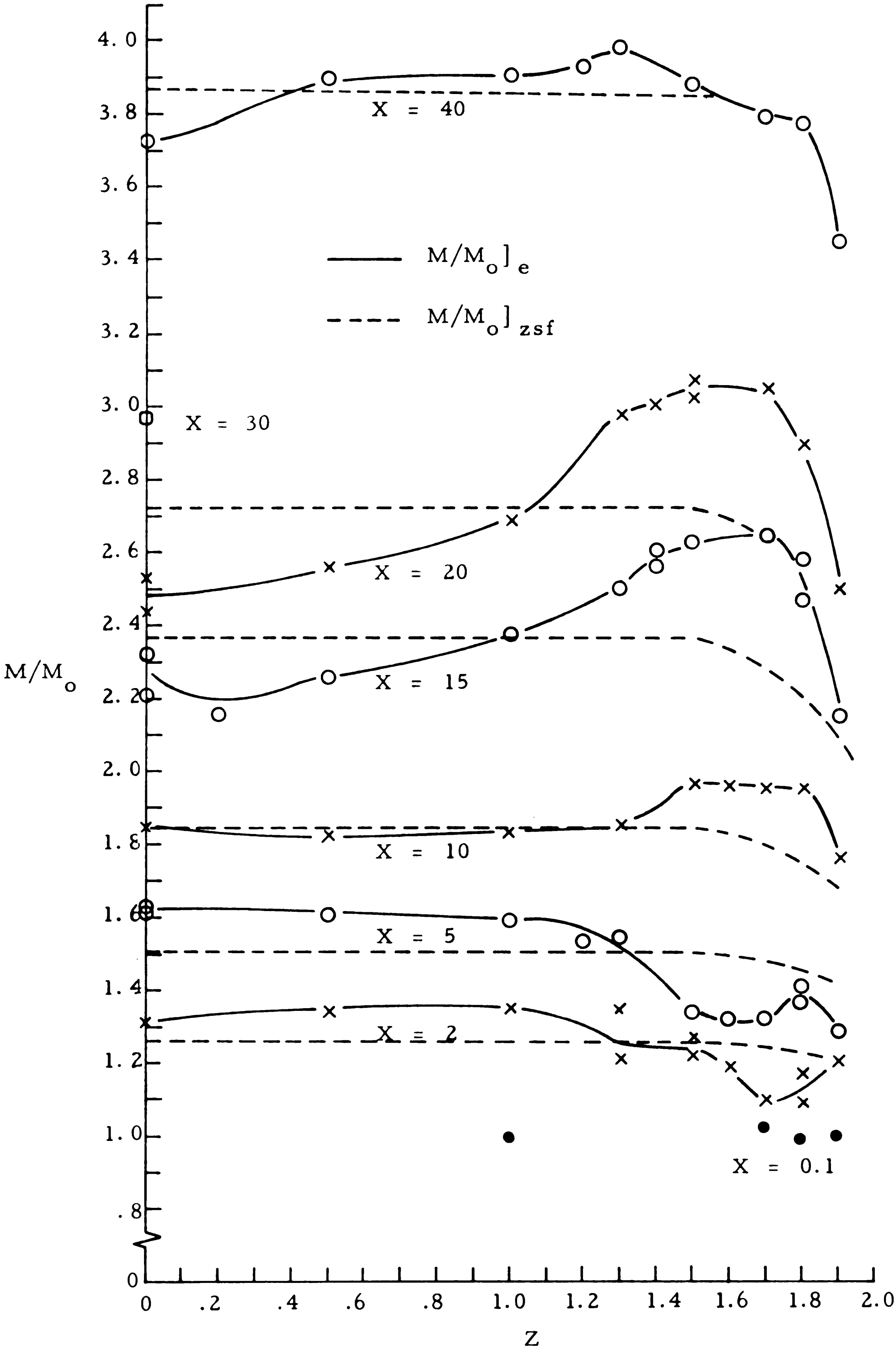

Figure 47. Mass flux ratios

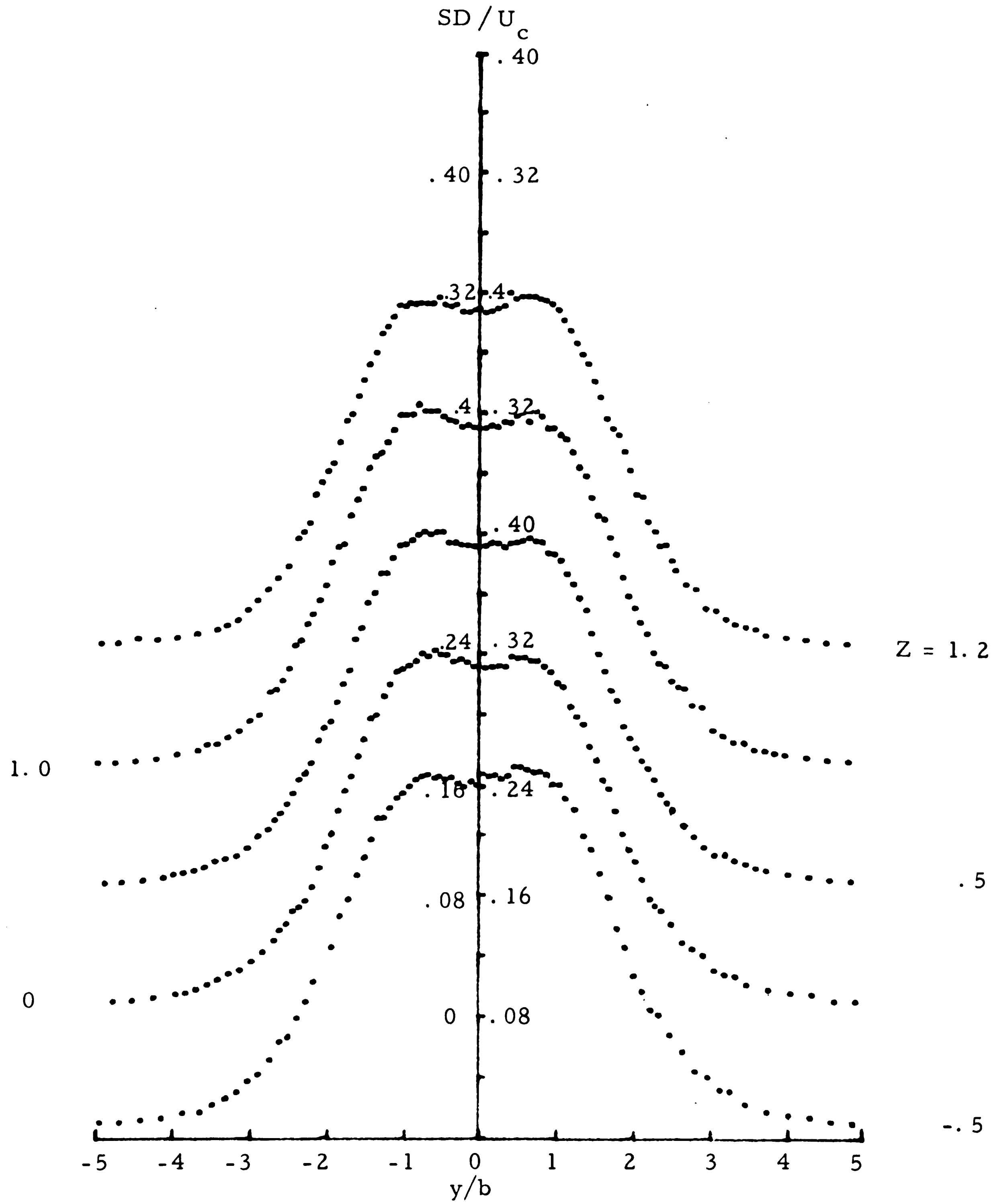

Figure 42a. Dimensionless turbulence intensity distributions at X=40 (Z= -.5, 0, . 5, 1.0, 1.2)

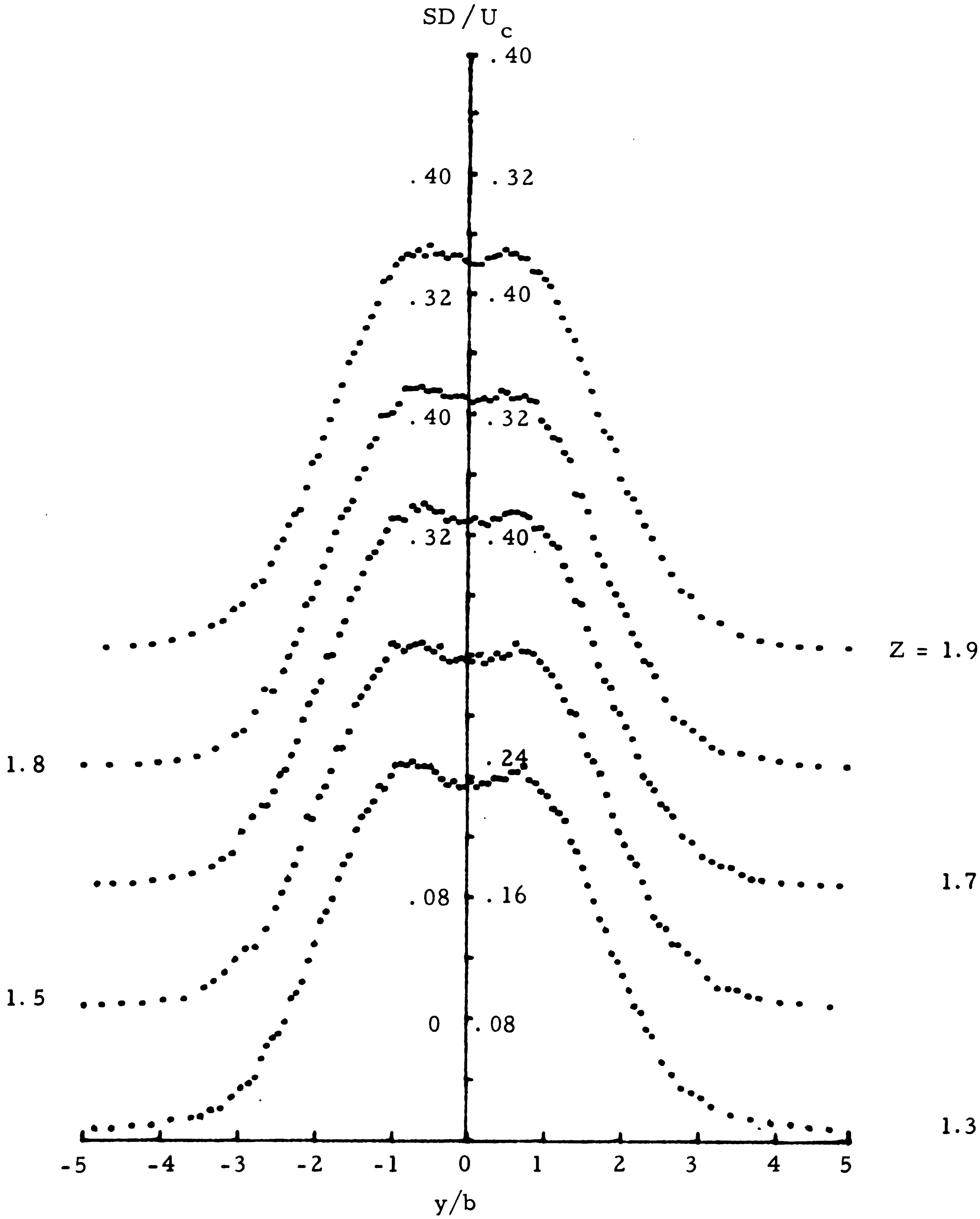

Figure 42b. Dimensionless turbulence intensity distributions at X=40 (Z= 1.3, 1.5, 1.7, 1.8, 1.9)

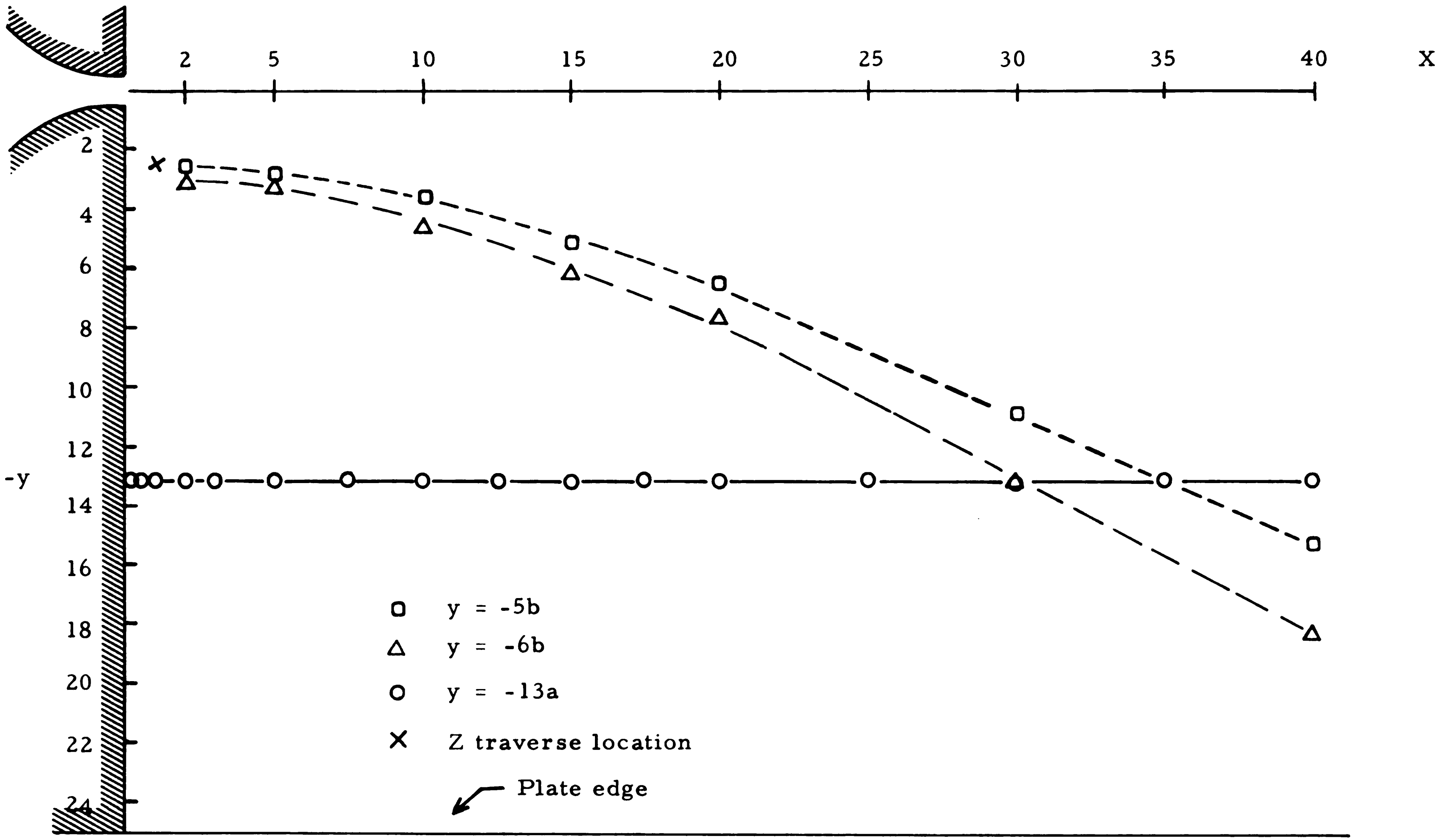

Figure 43. Location of X traverse entrainment measurements

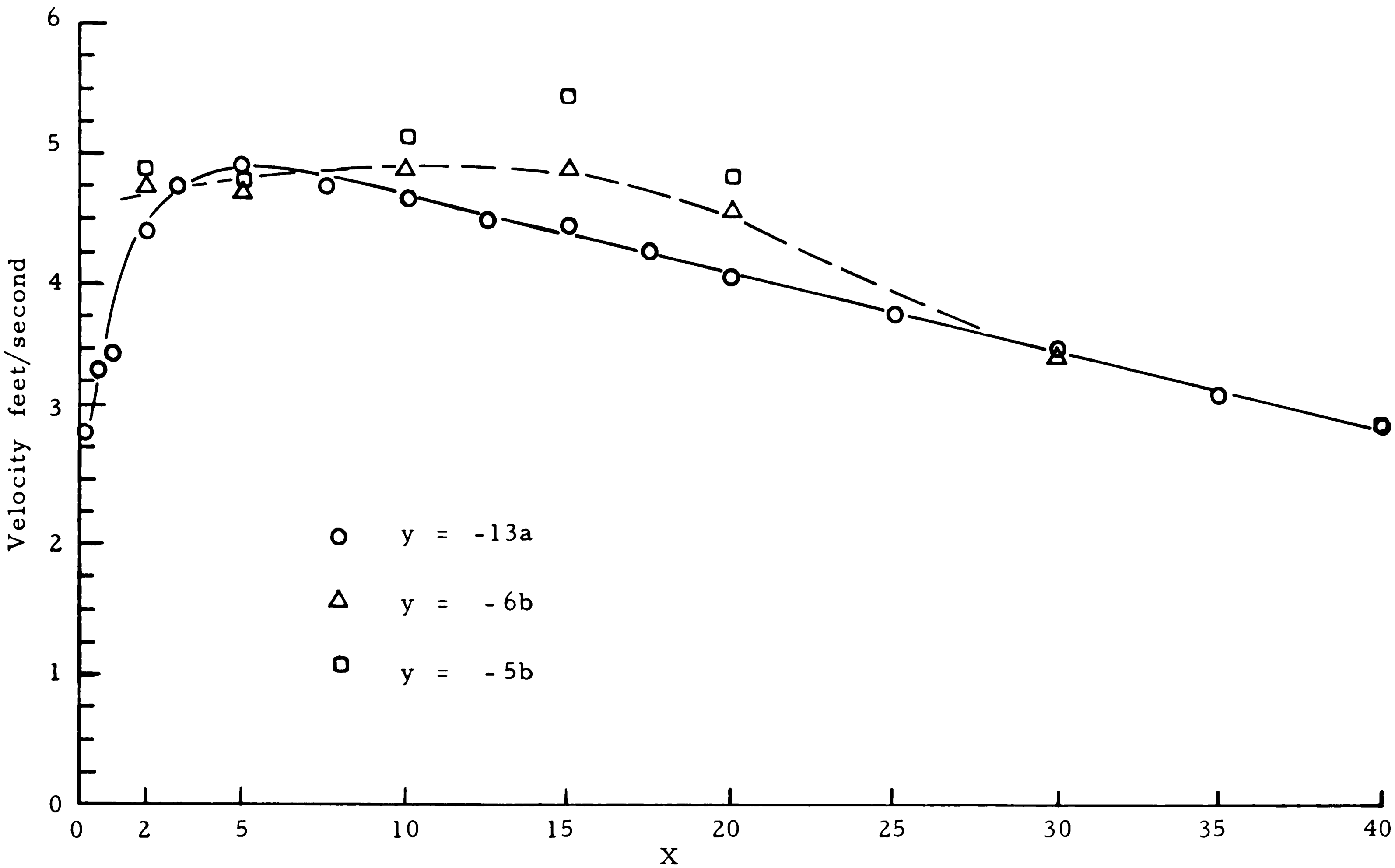

Figure 44. X traverse entrainment mean velocity distributions

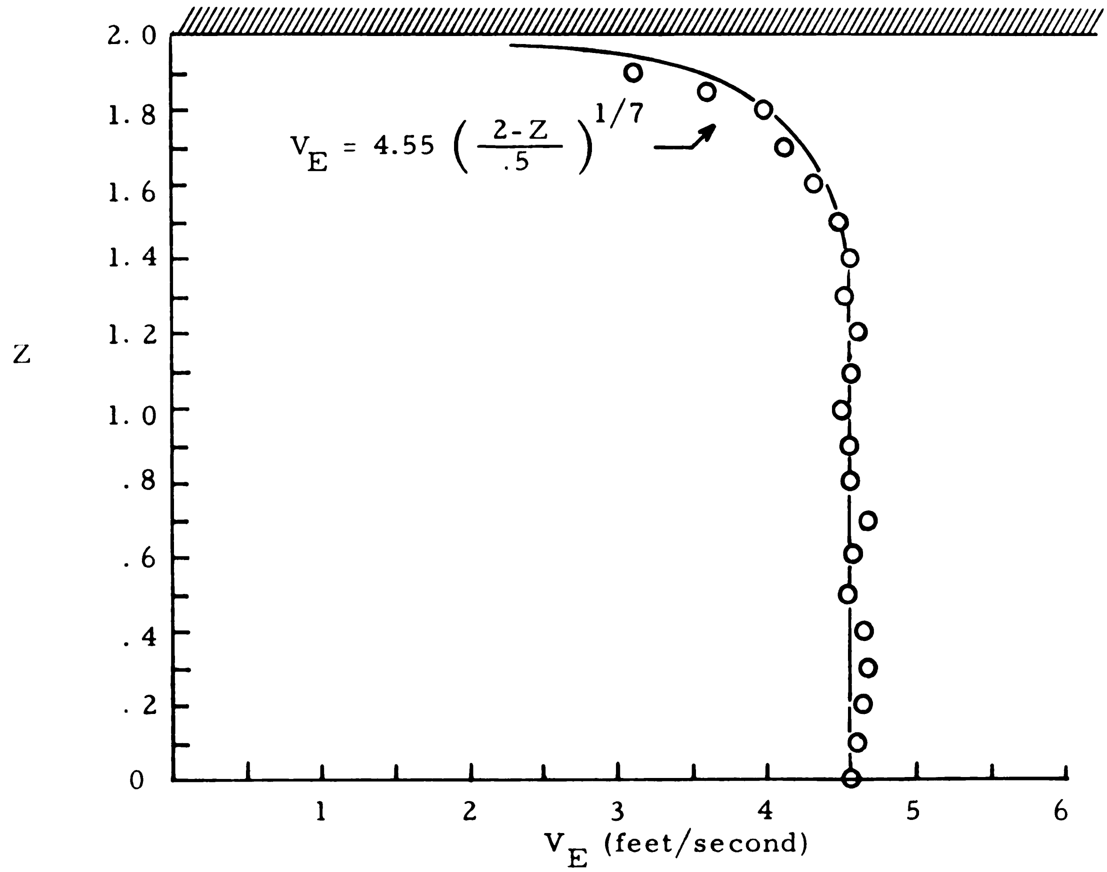

Figure 45. Z traverse entrainment mean velocity distribution.

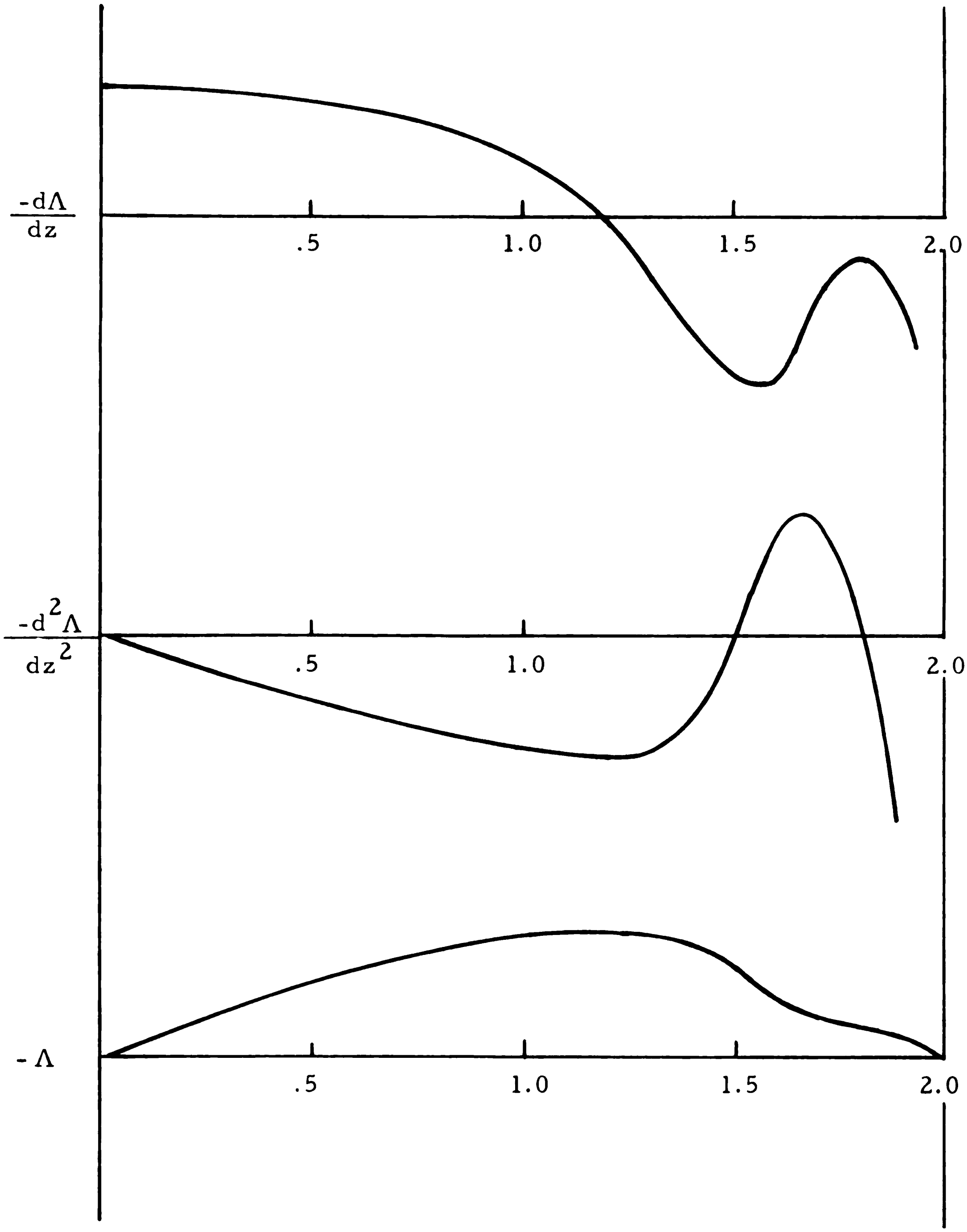

Figure 46a. Schematic representation of $-d\Lambda/dz$ at X=5

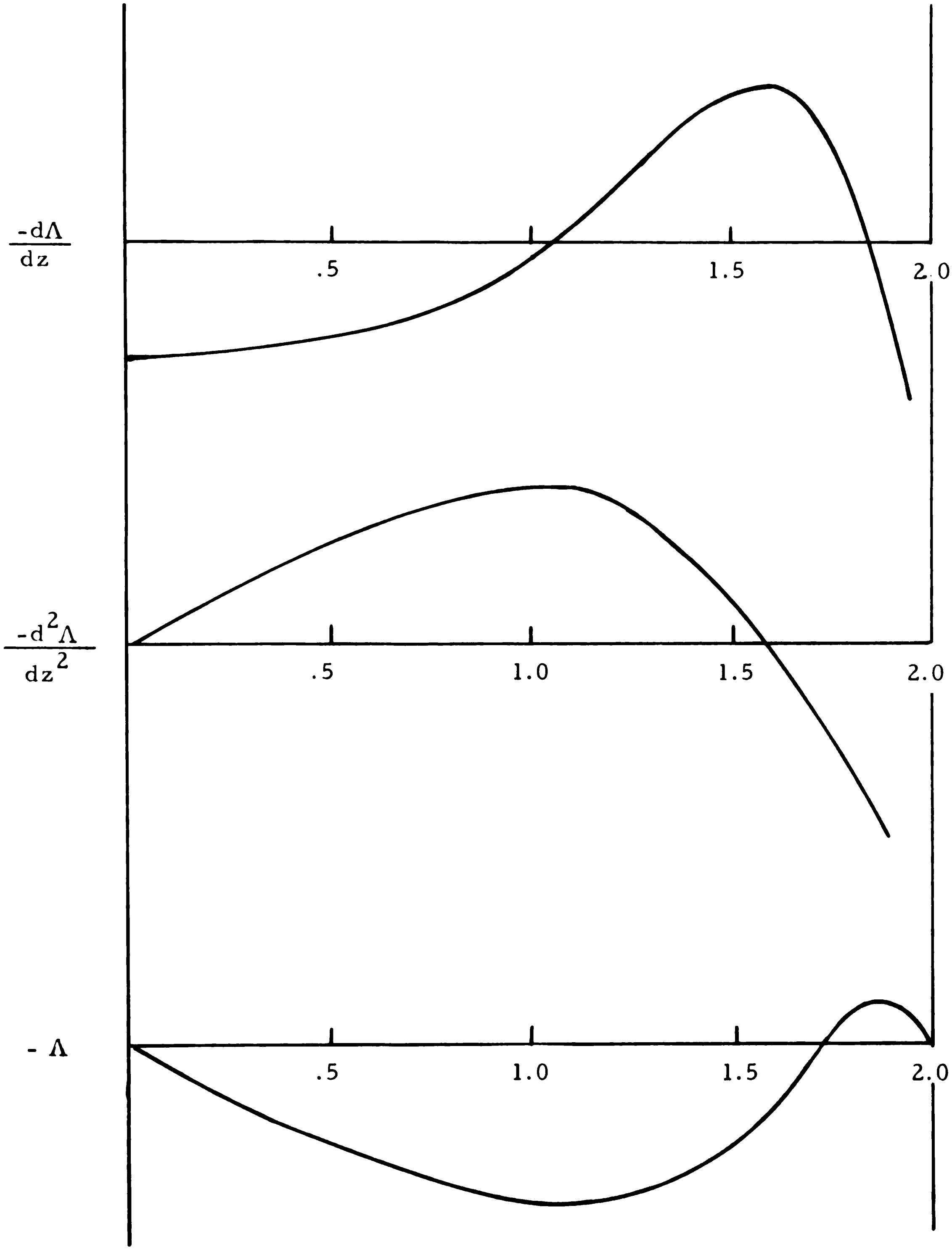

Figure 46b. Schematic representation of $-d\Lambda/dz$ at X=20

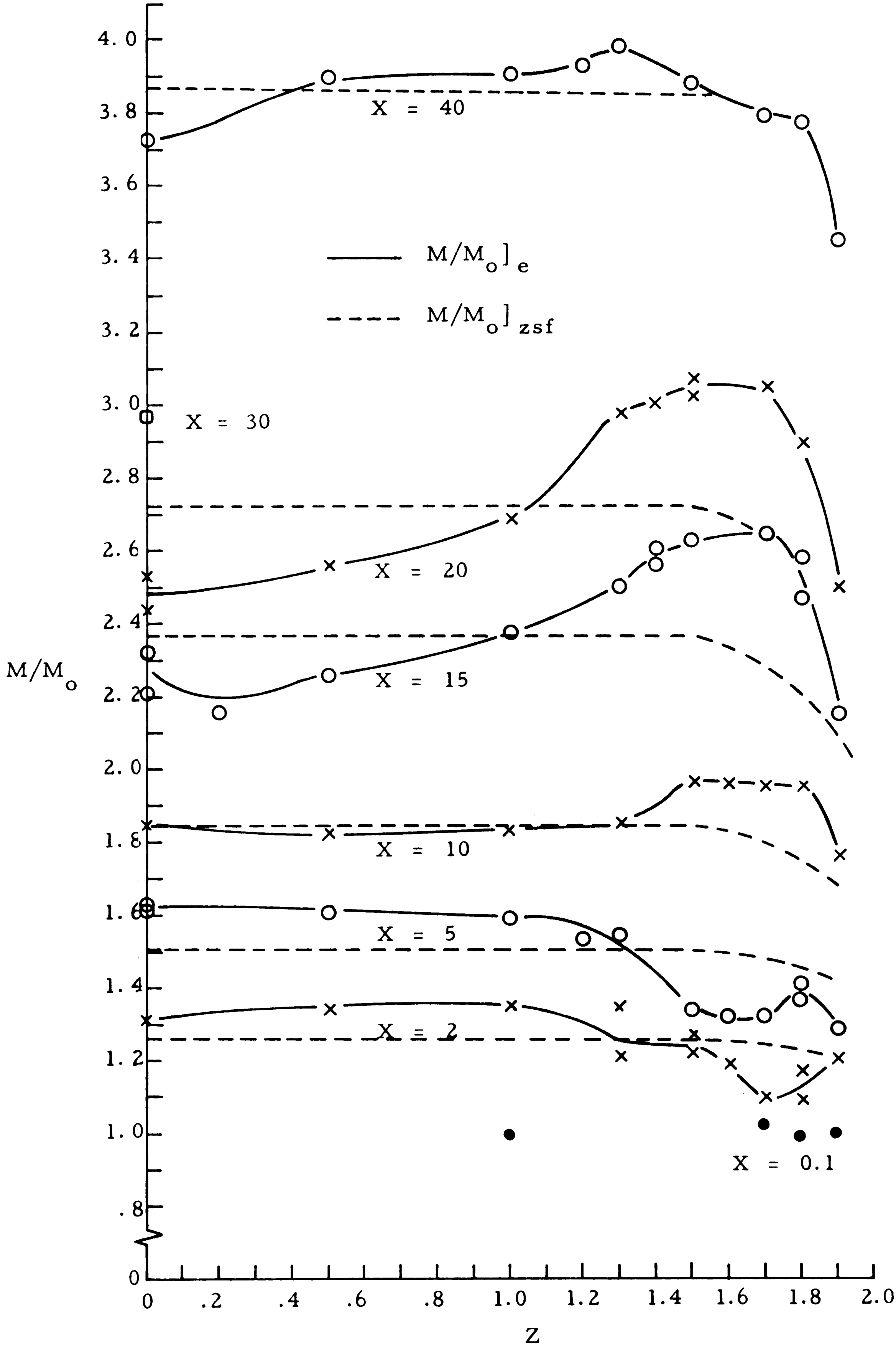

Figure 47. Mass flux ratios

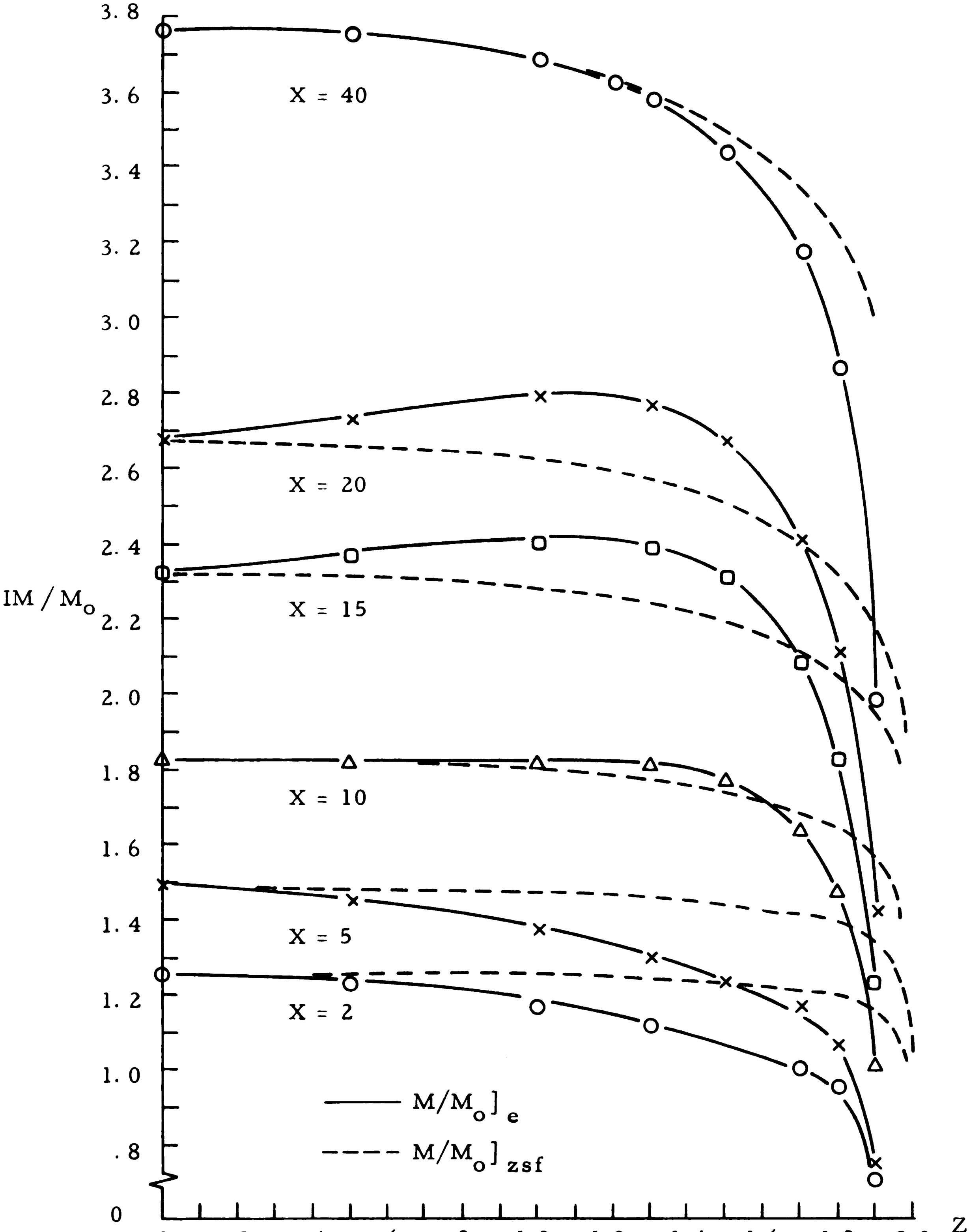

Figure 48. Integrated mass flux ratios

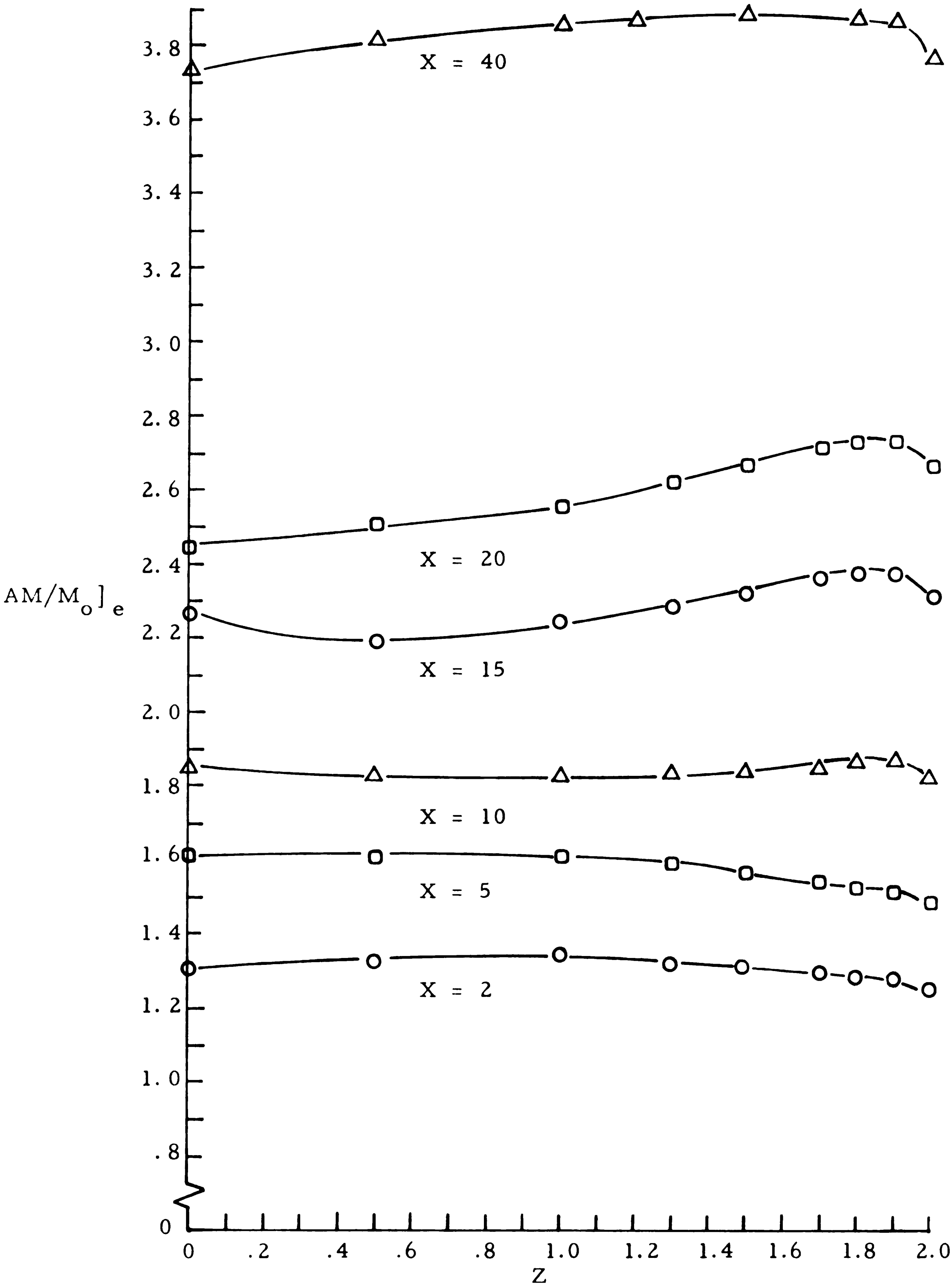

Figure 49. Average mass flux ratios

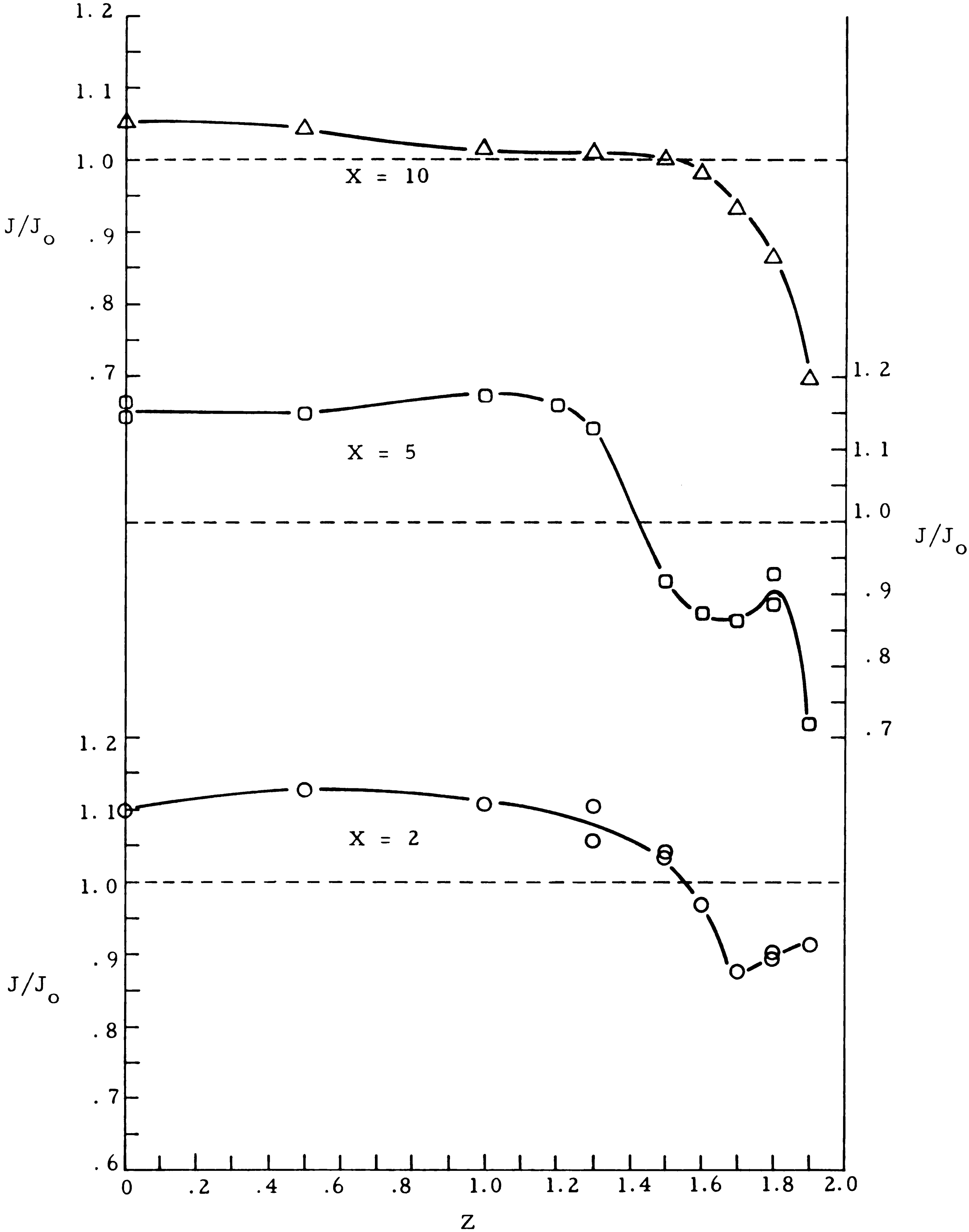

Figure 50a. Momentum flux ratios (X = 2, 5, 10)

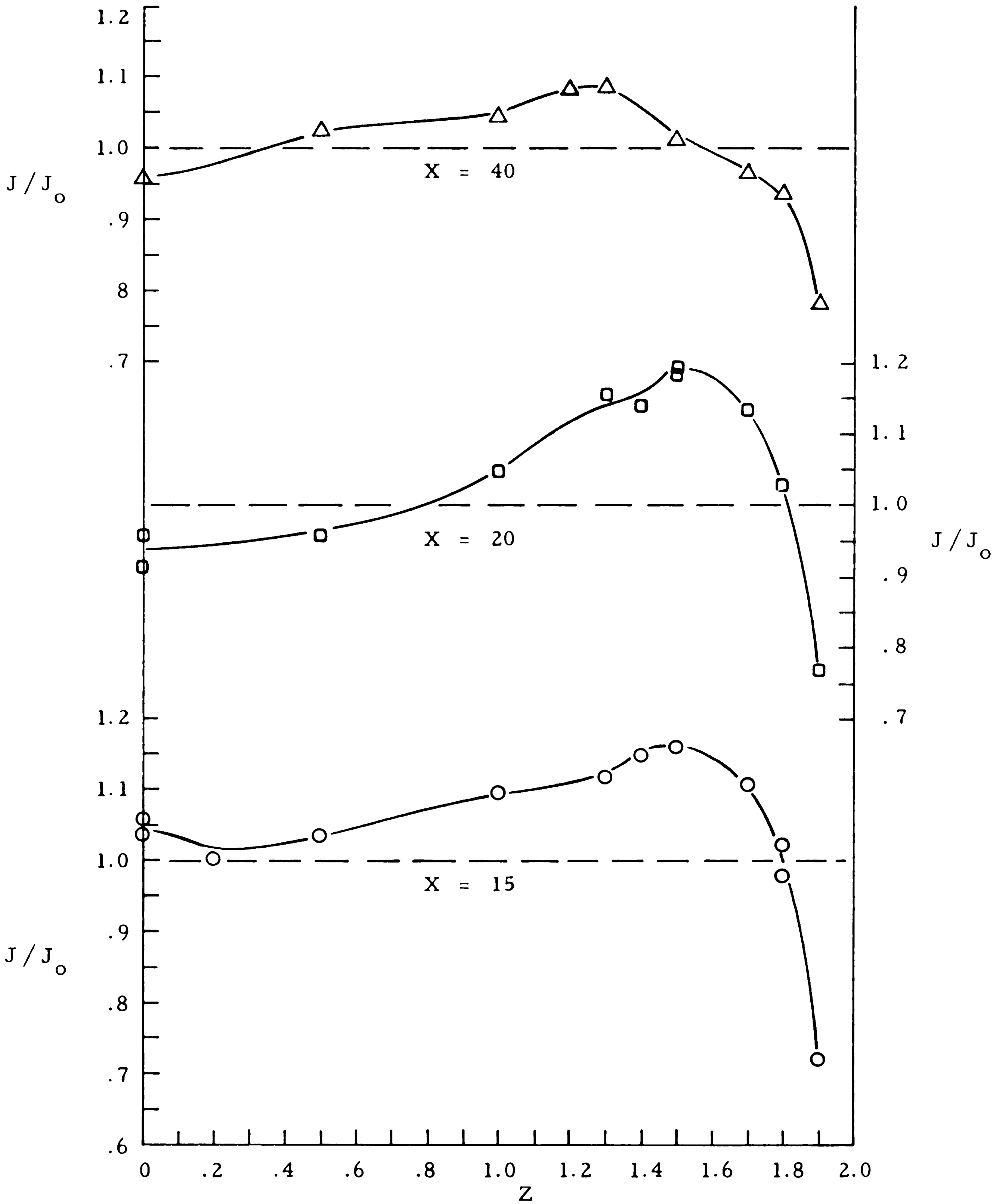

Figure 50b. Momentum flux ratios (X=15, 20, 40)

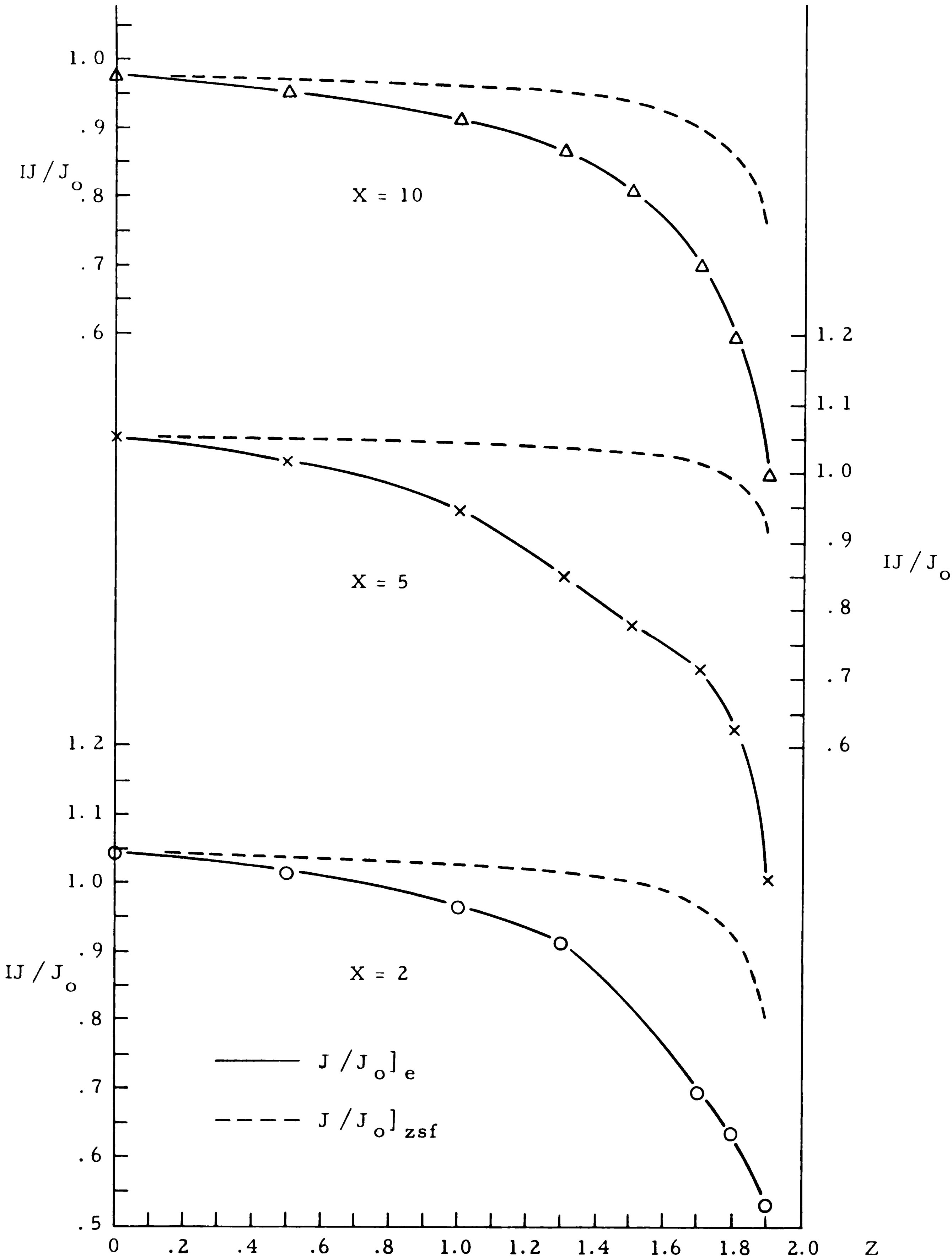

Figure 51a. Integrated momentum flux ratios (X=2, 5, 10)

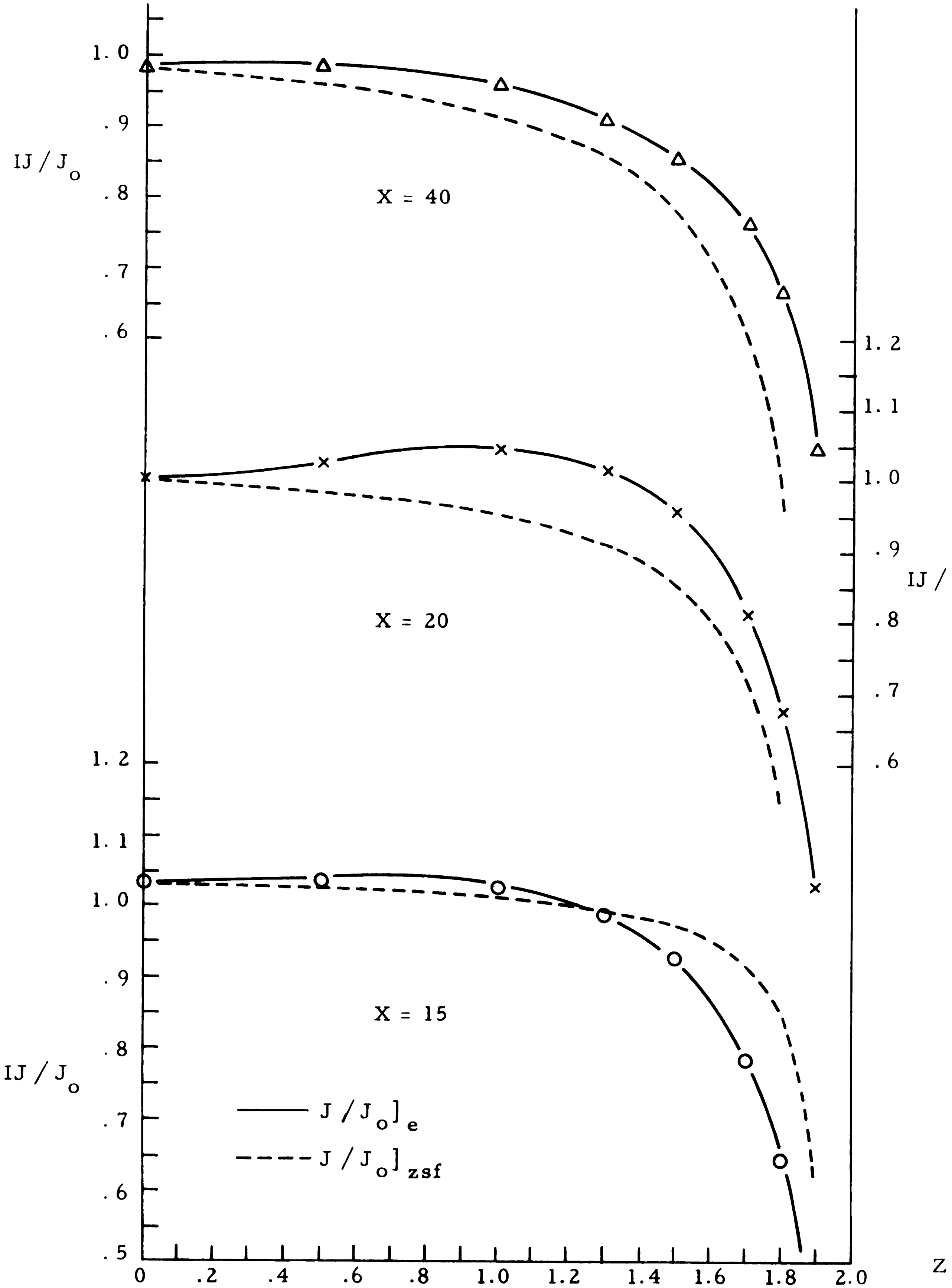

Figure 51b. Integrated momentum flux ratios (X=15, 20, 40)

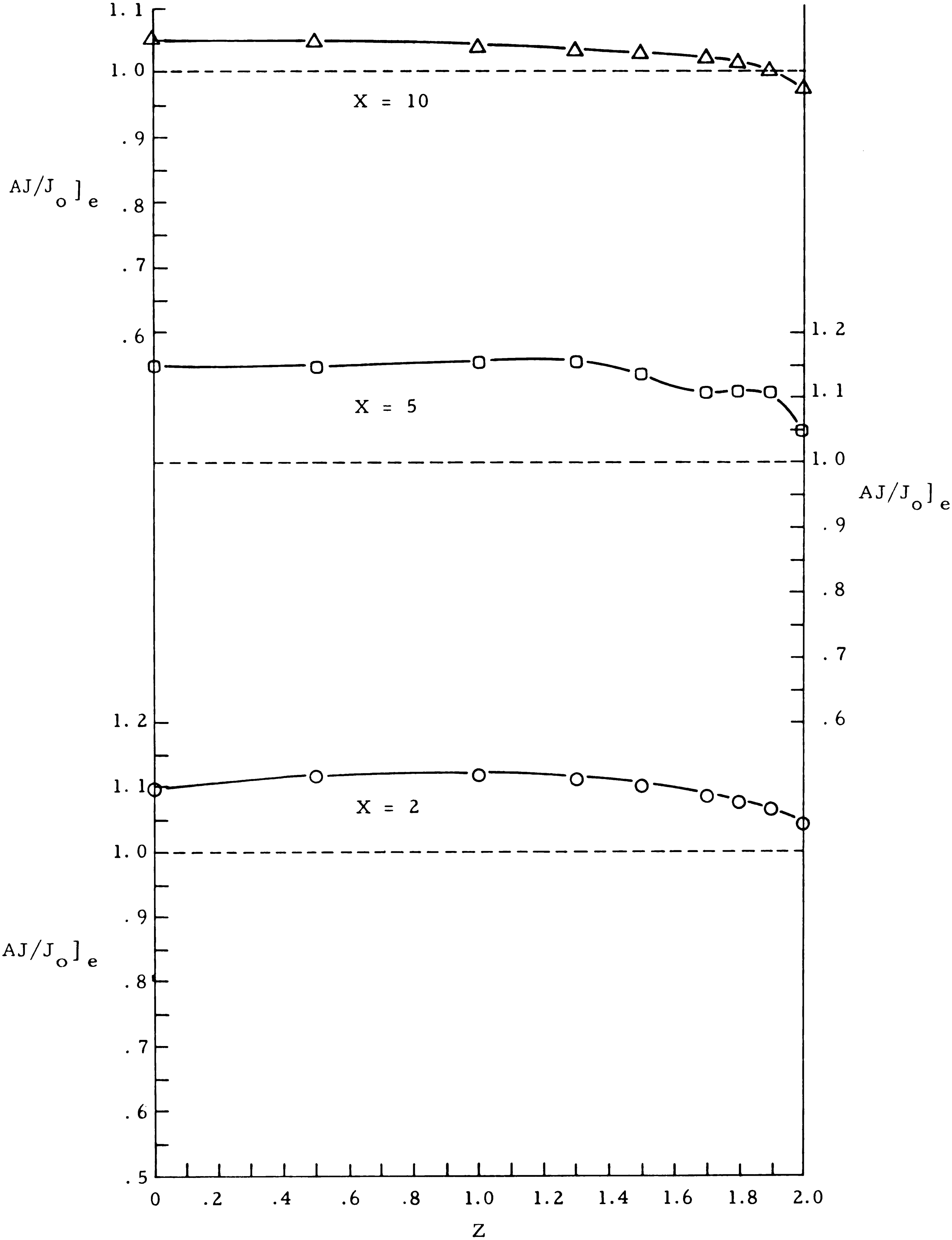

Figure 52a. Average momentum flux ratios (X , 2, 5, 10)

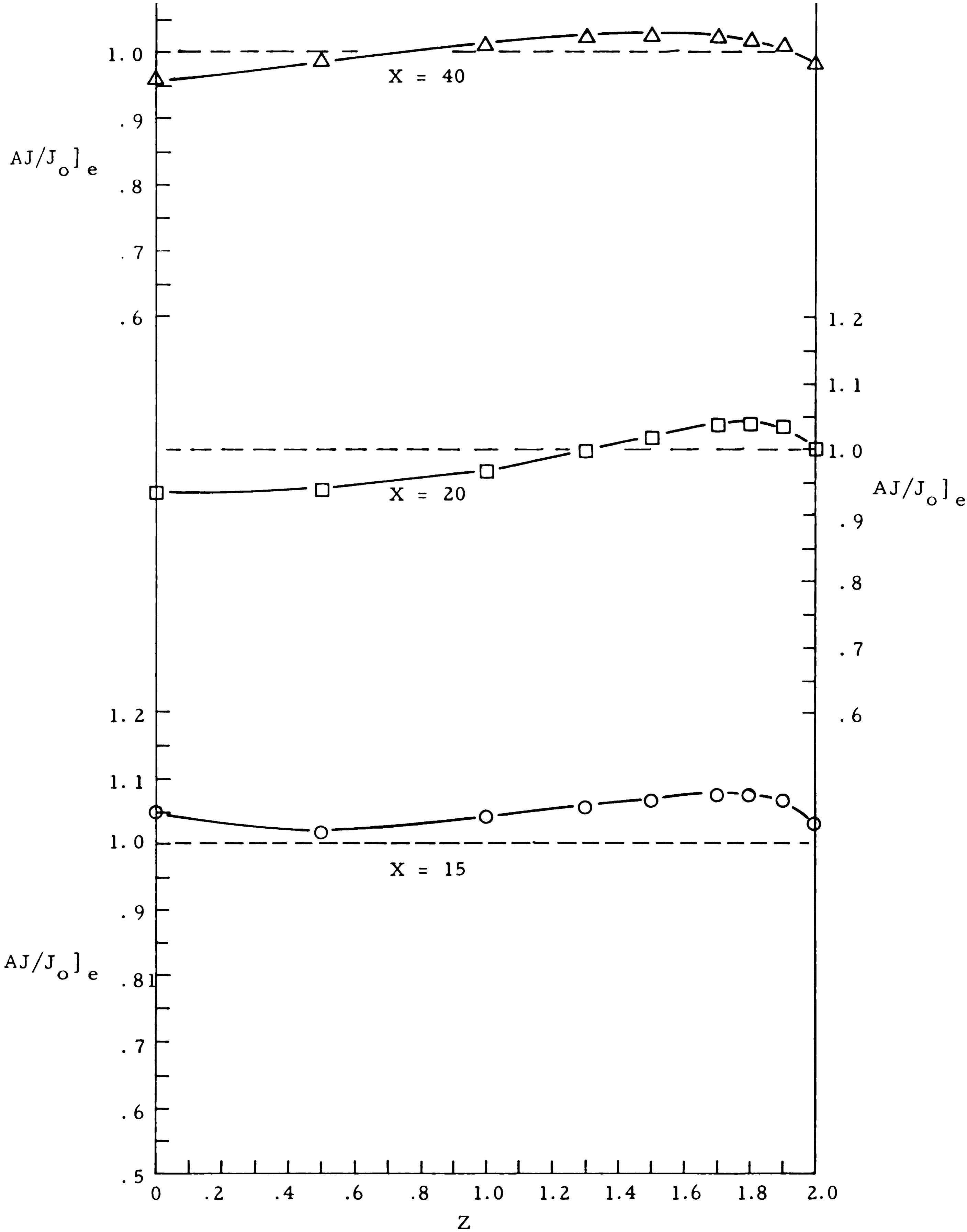

Figure 52b. Average momentum flux ratios (X=15, 20, 40)

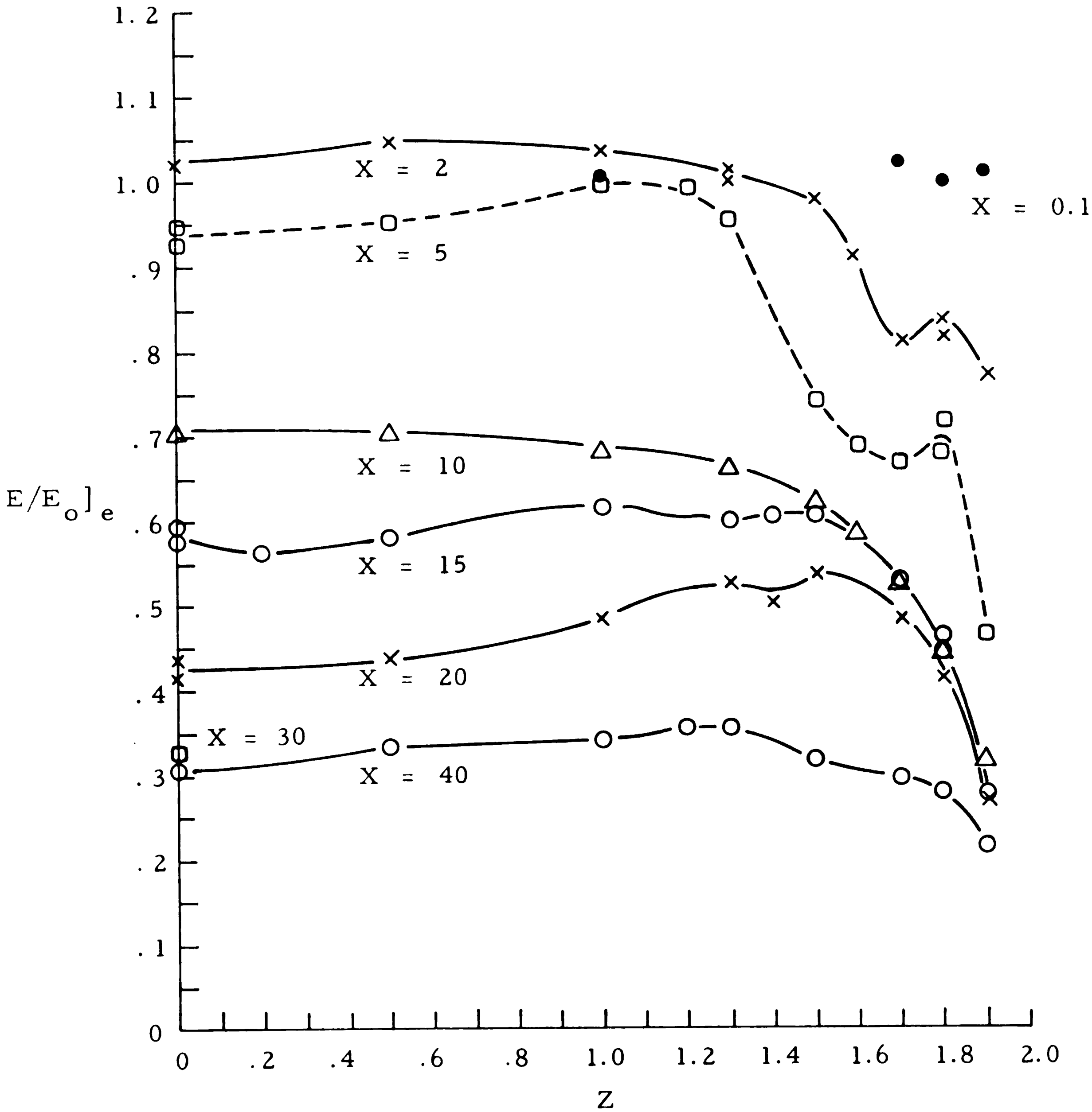

Figure 53. Energy flux ratios

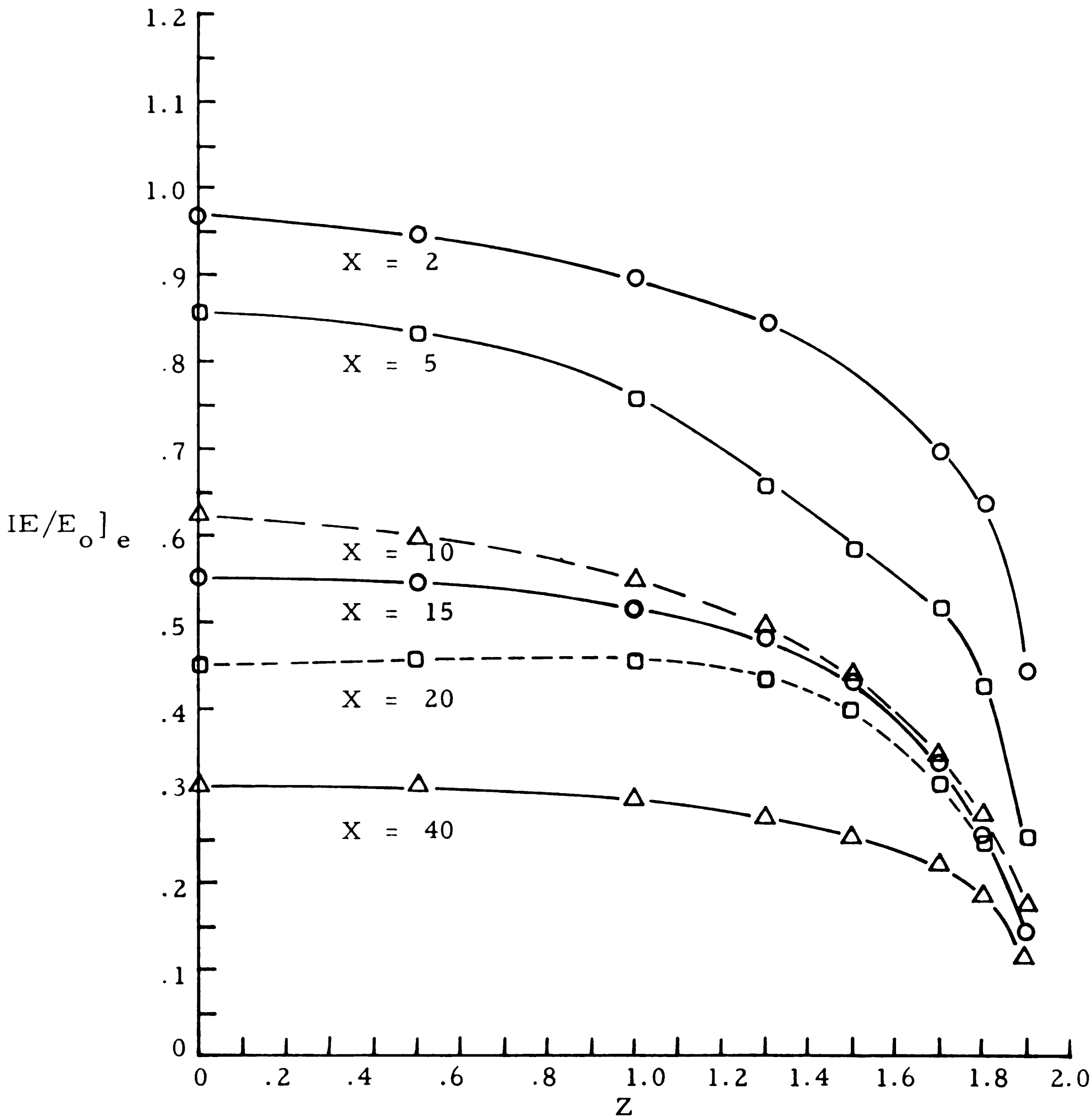

Figure 54. Integrated energy flux ratios

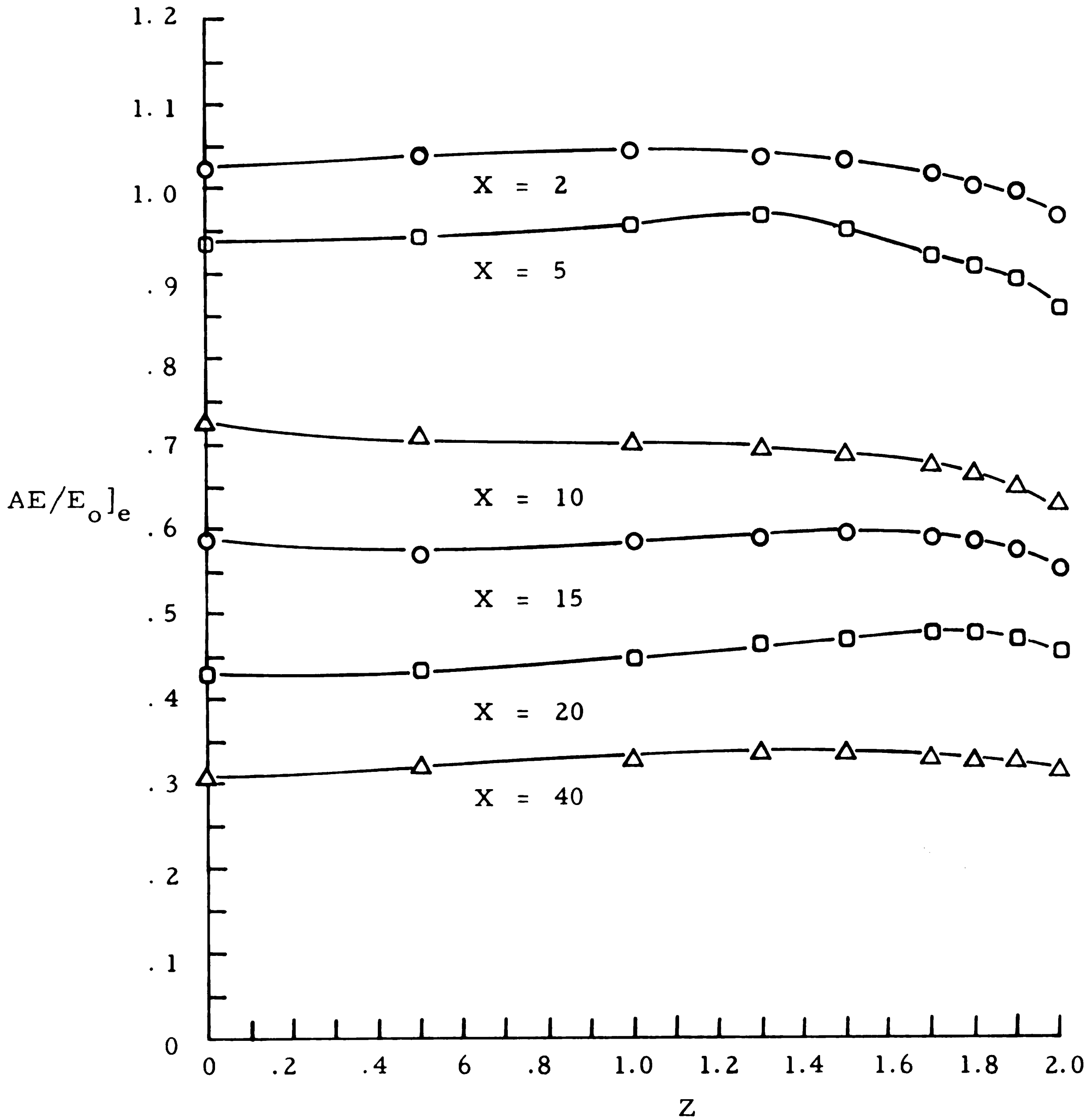

Figure 55. Average energy flux ratios

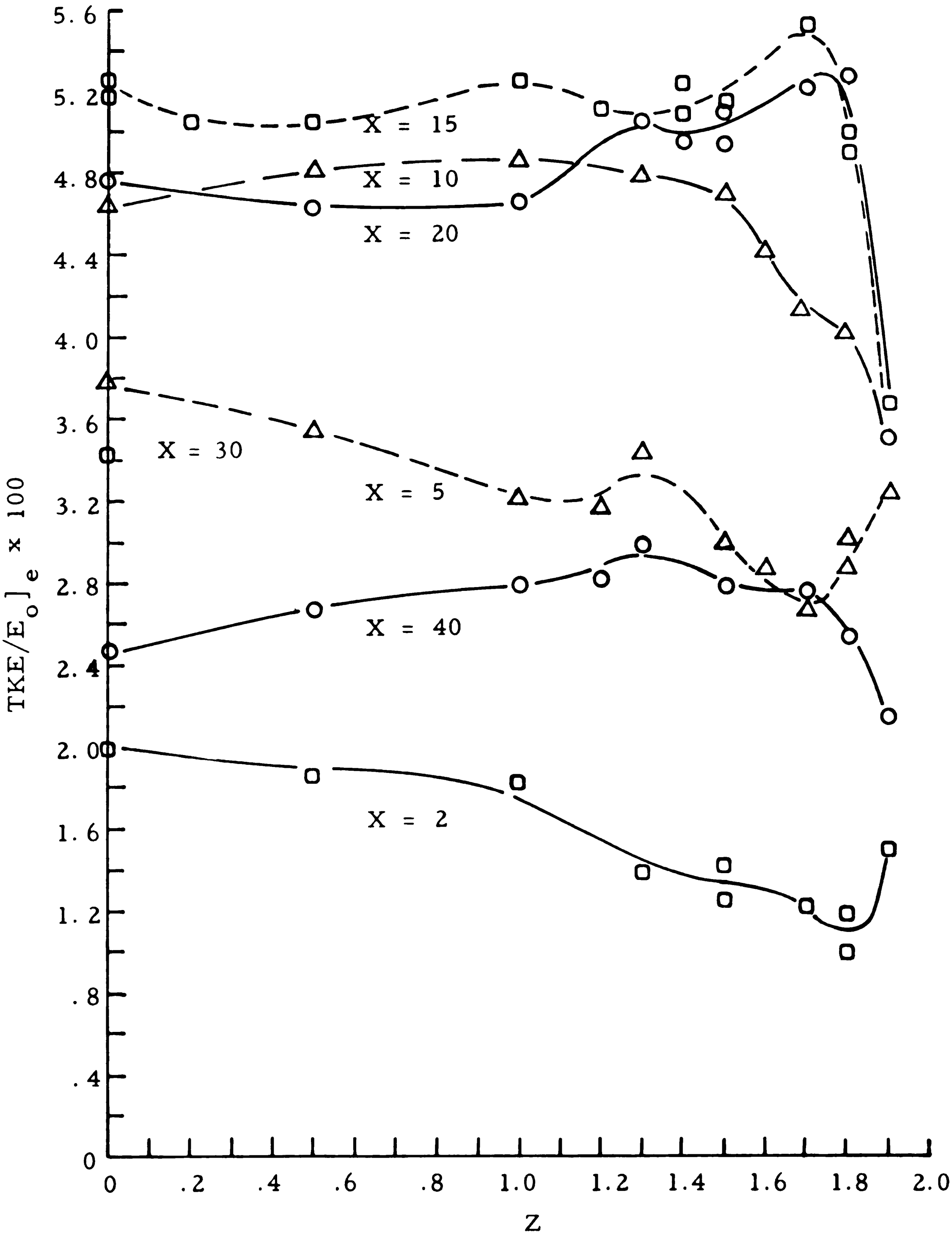

Figure 56. Turbulence kinetic energy flux ratios

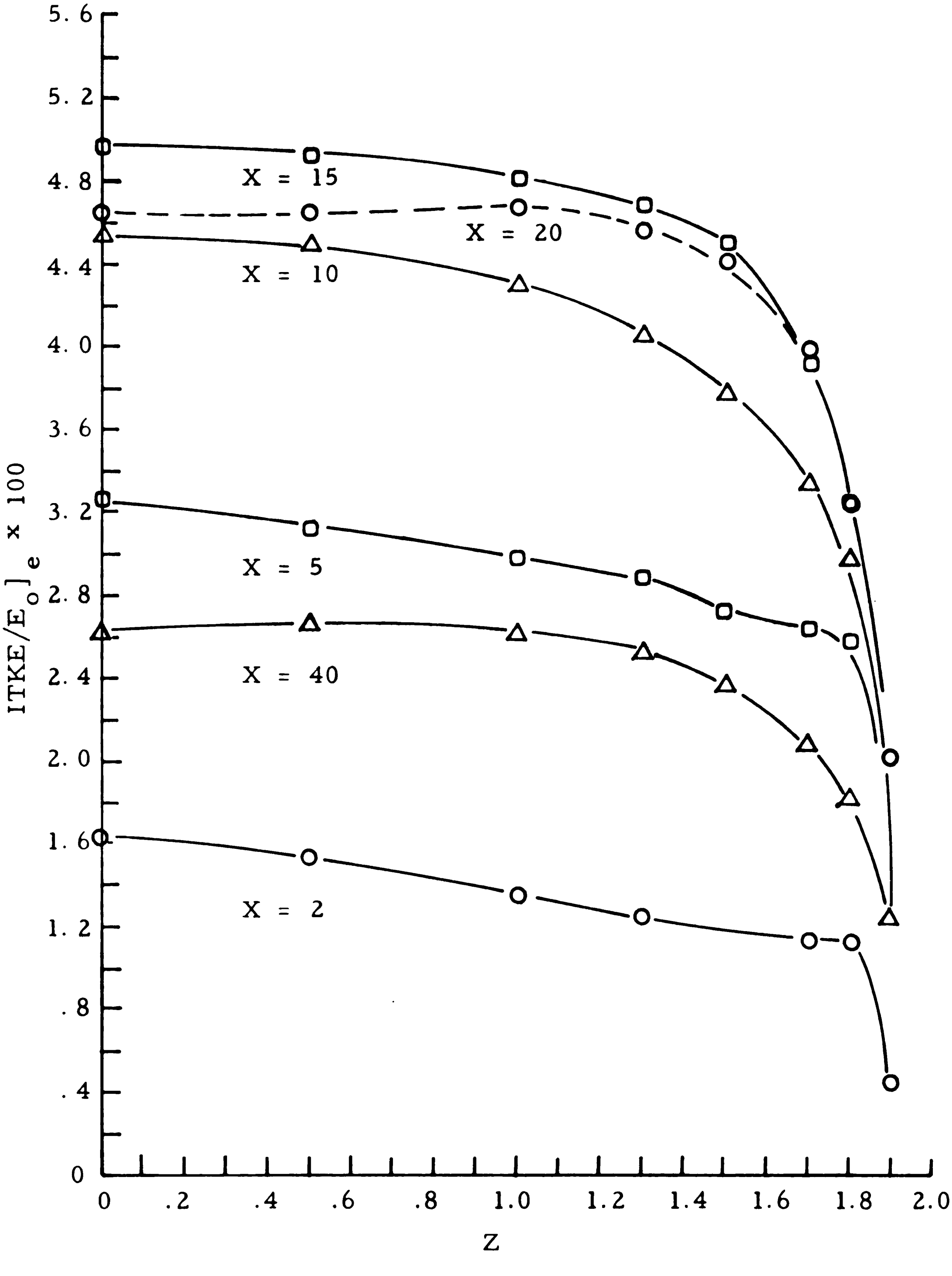

Figure 57. Integrated turbulence kinetic energy flux ratios

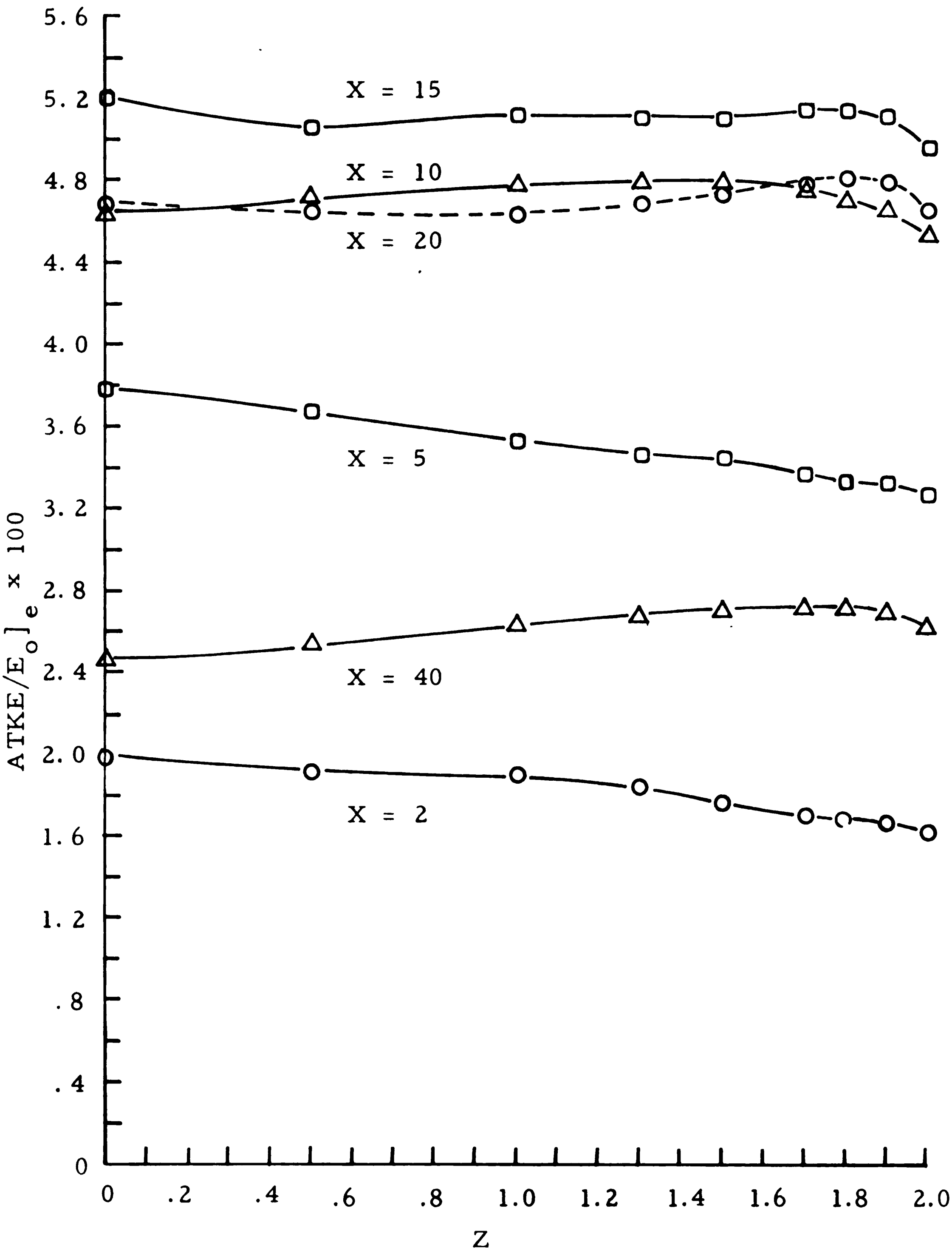

Figure 58. Average turbulence kinetic energy flux ratios

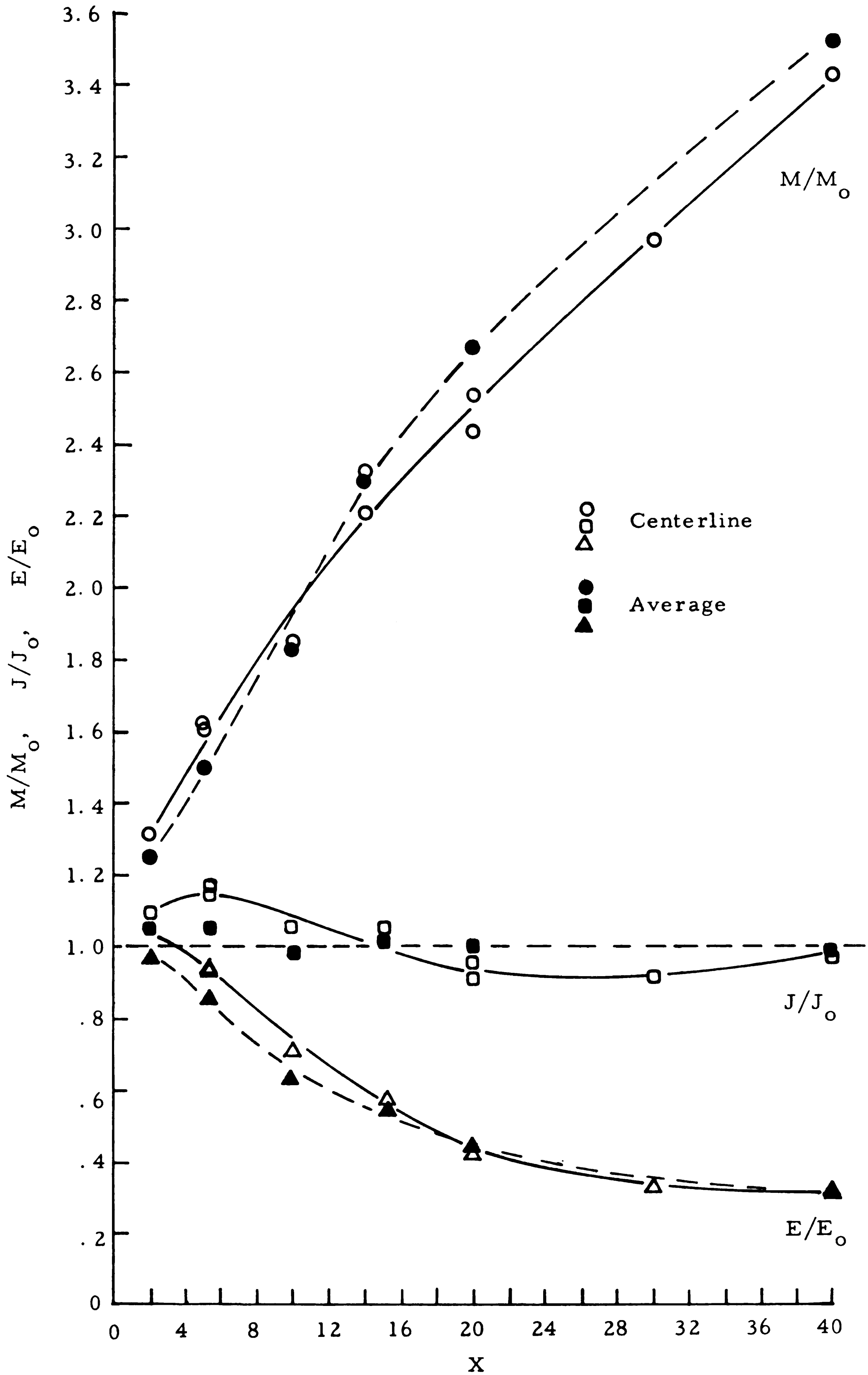

Figure 59. Average and midplane flux ratios

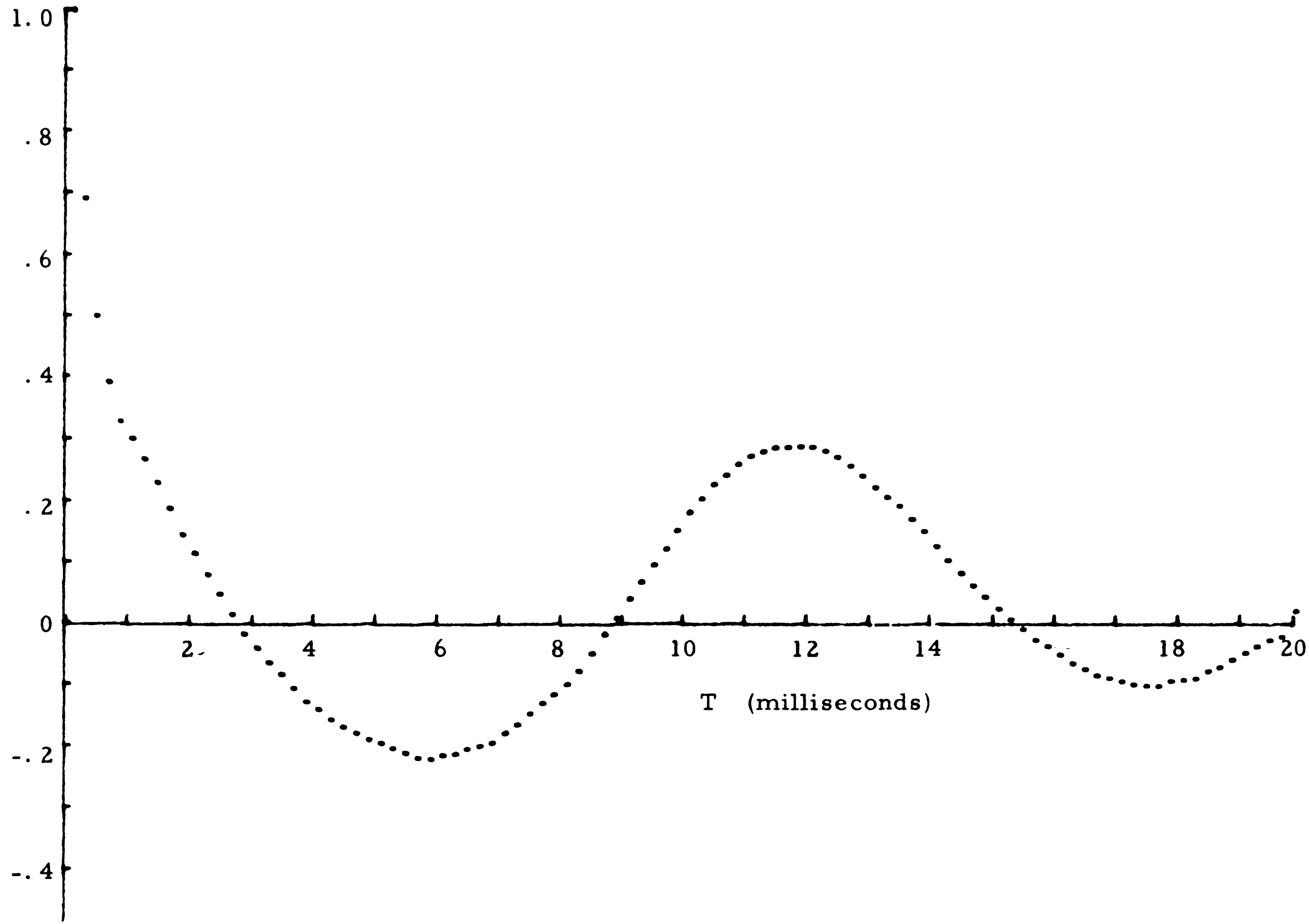

Figure 60. Vorticity meter correlation function at
X = 2, Y = -.5, Z = 1.6

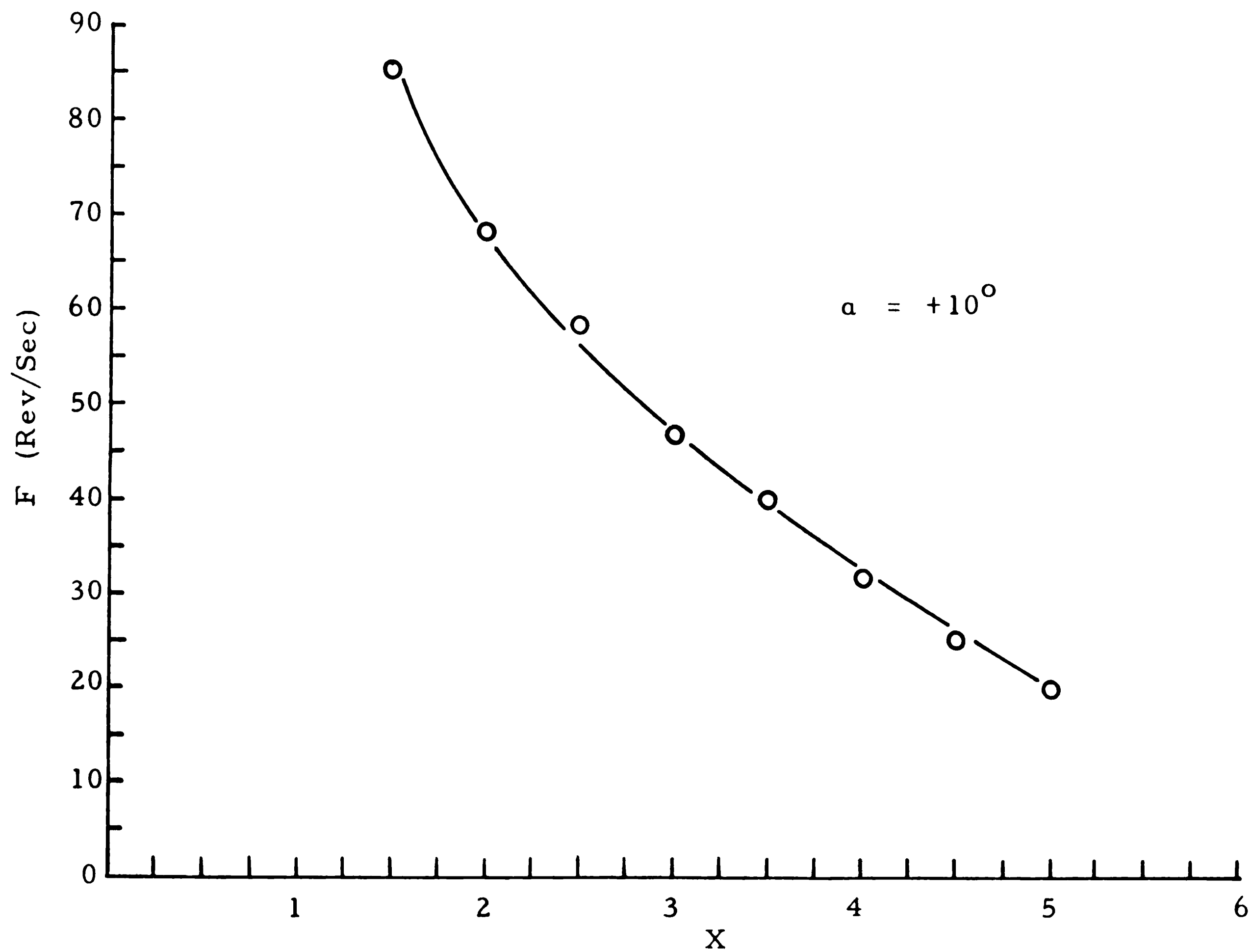

Figure 61a. Vorticity meter response to a wing tip vortex -- X traverse

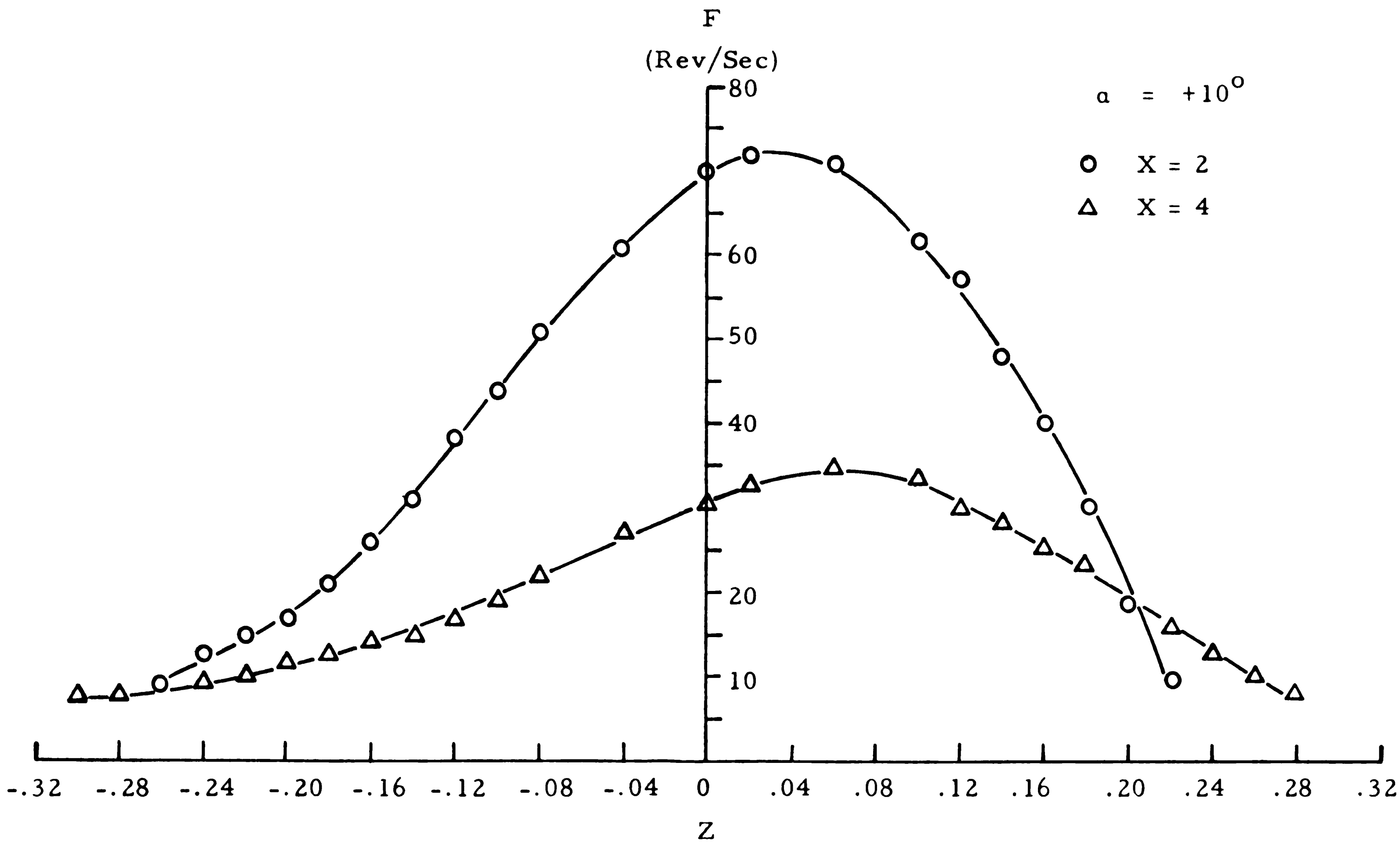

Figure 61b. Vorticity meter response to a wing tip vortex -- Z traverse

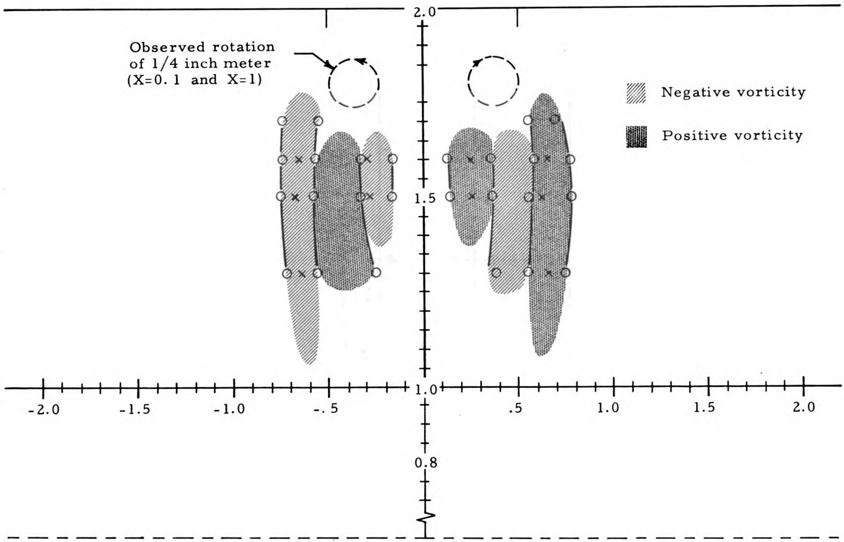

Figure 62. Vorticity zone contours at X = 1

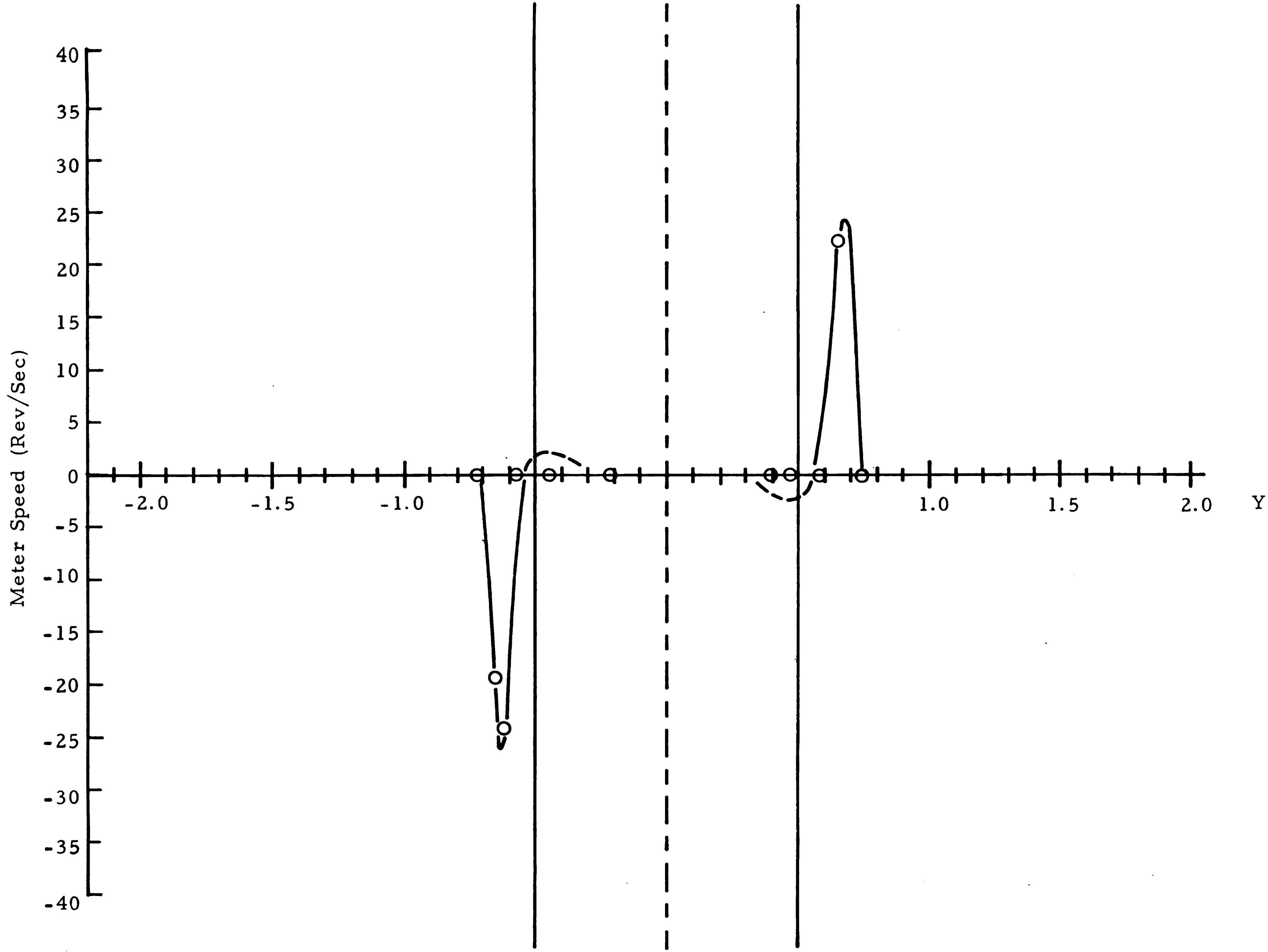

Figure 63a. Vorticity meter speed at X=1, Z=1.3

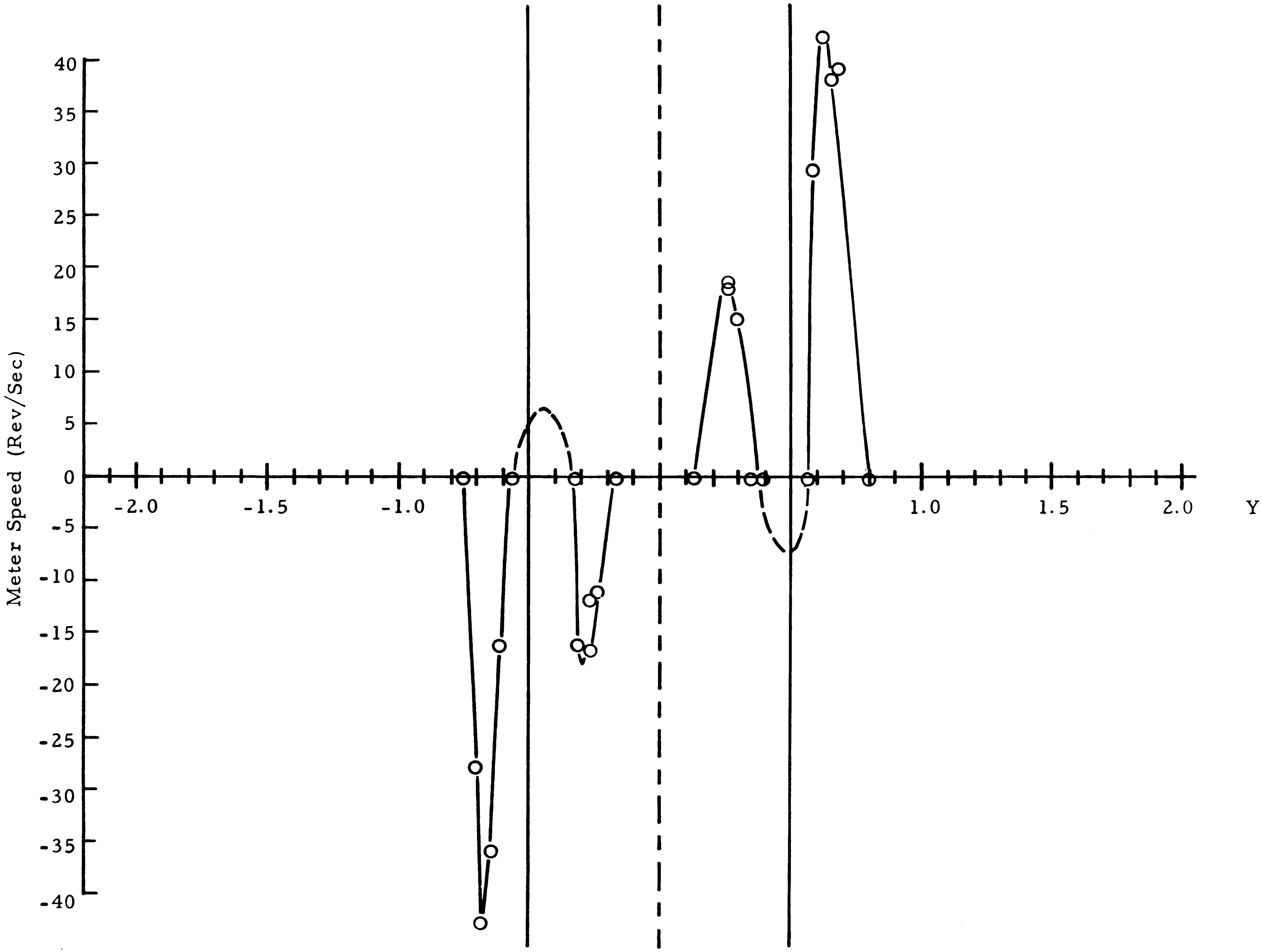

Figure 63b. Vorticity meter speed at X=1, Z=1.5

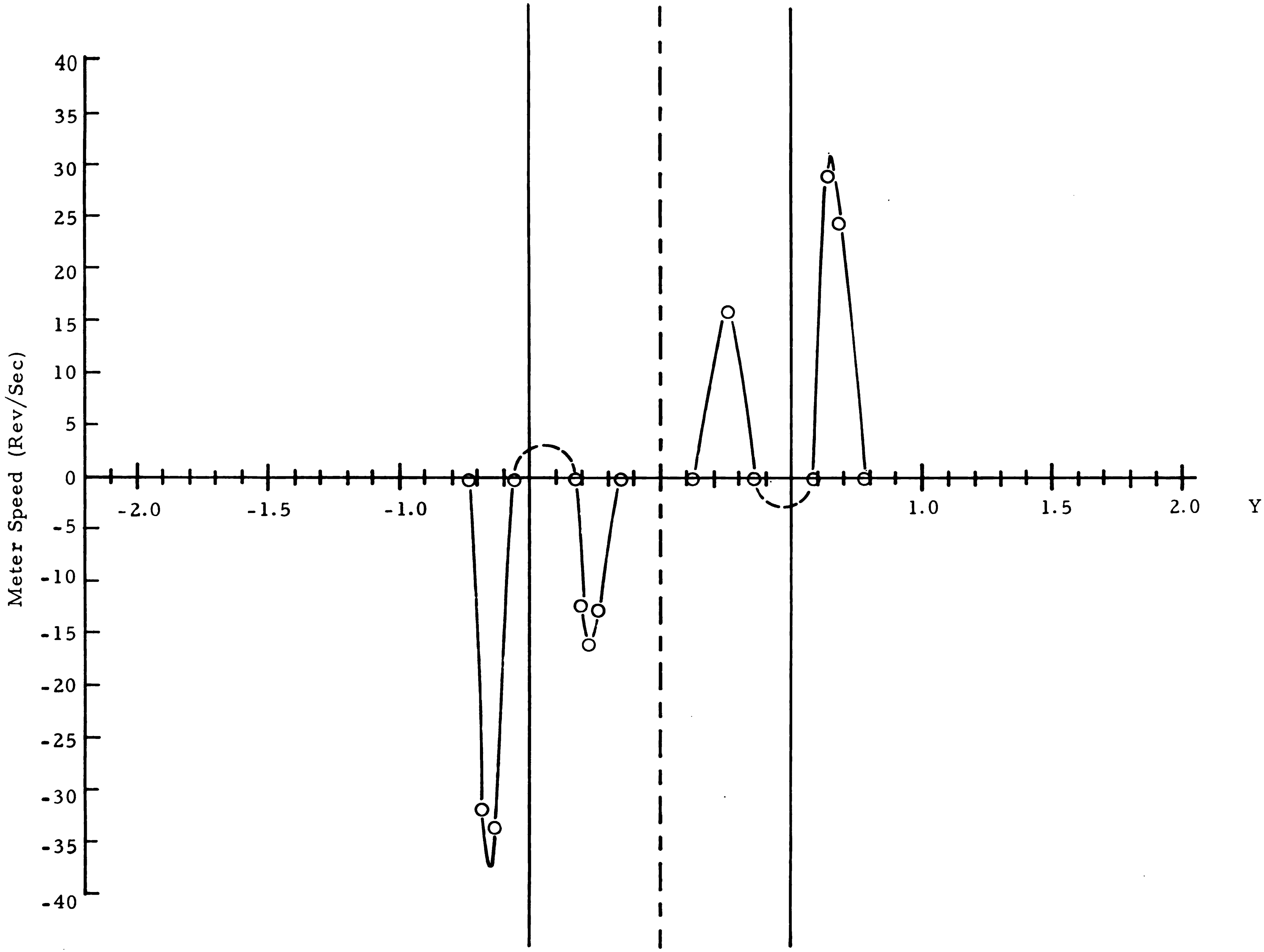

Figure 63c. Vorticity meter speed at X=1, Z=1.6

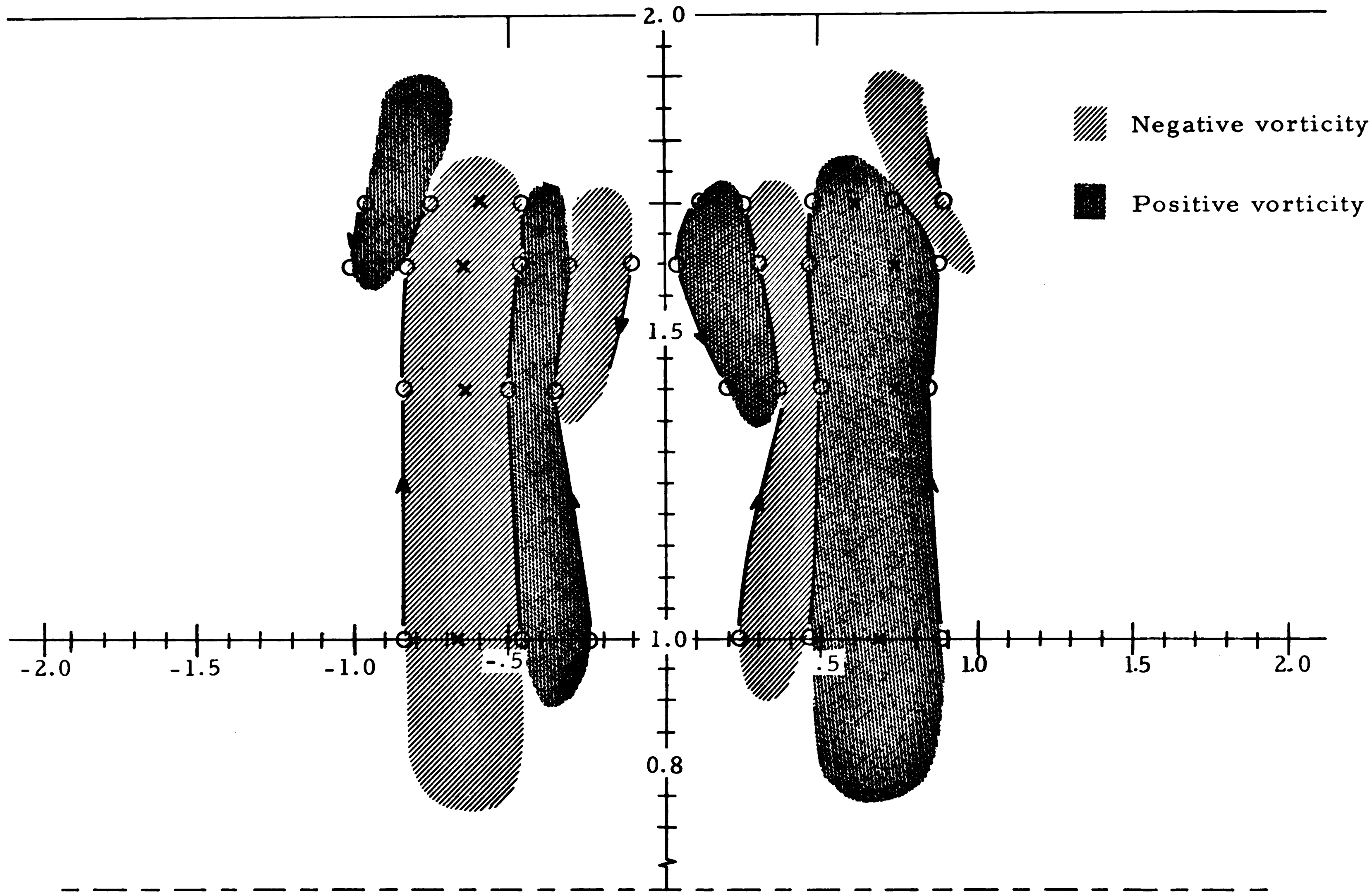

Figure 64. Vorticity zone contours at X=2

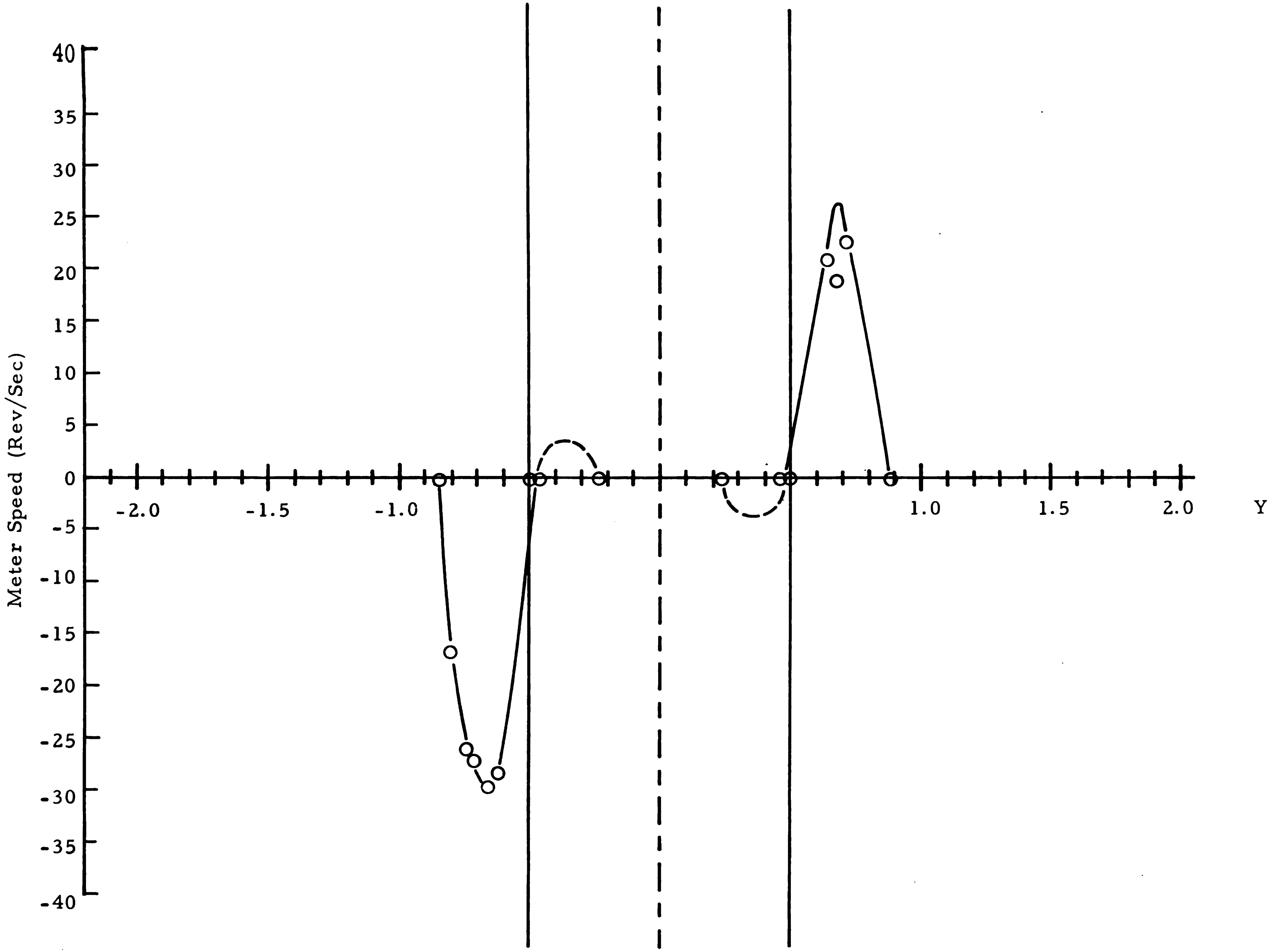

Figure 65a. Vorticity meter speed at X=2, Z=1.0

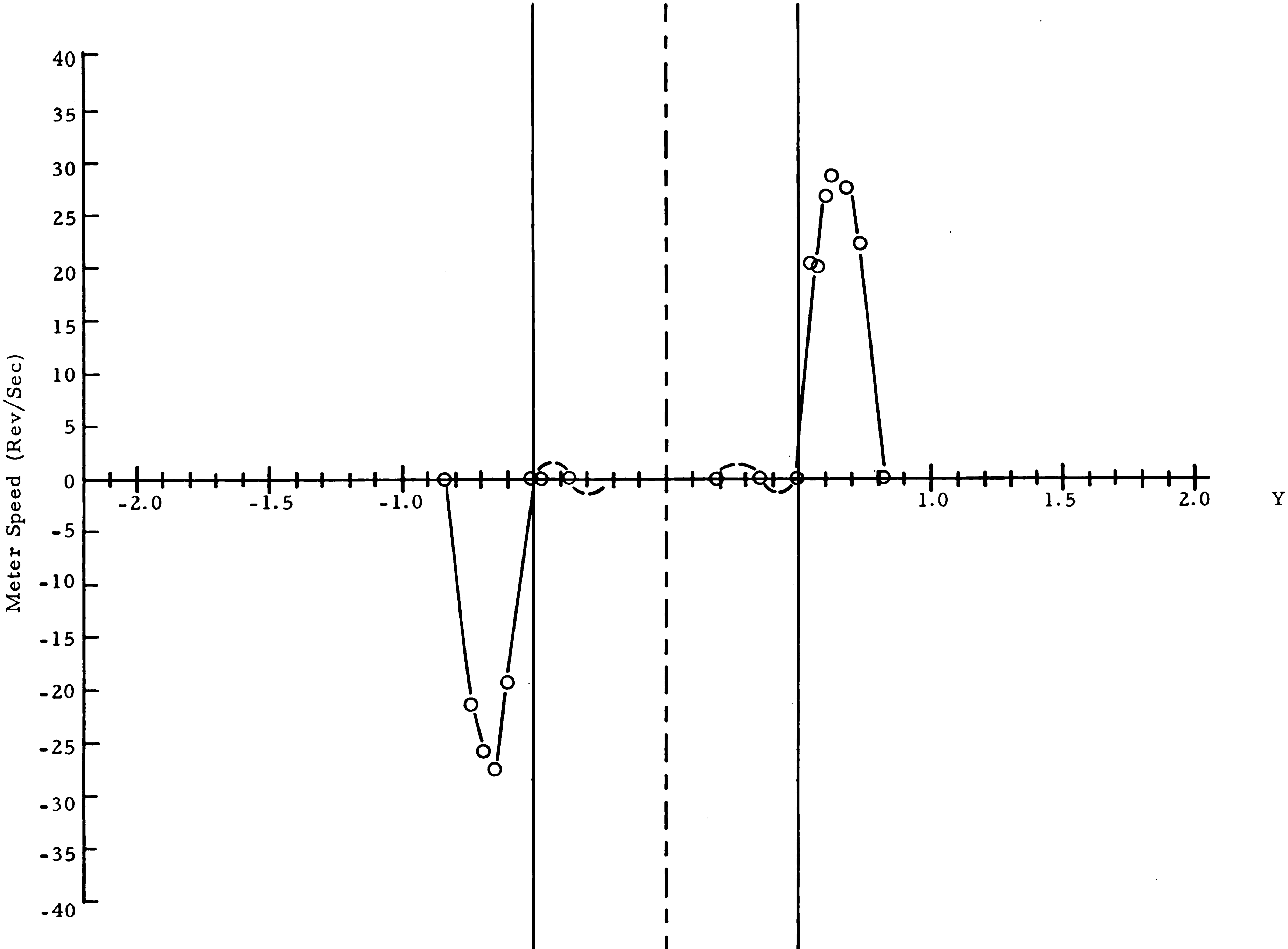

Figure 65b. Vorticity meter speed at X=2, Z=1.4

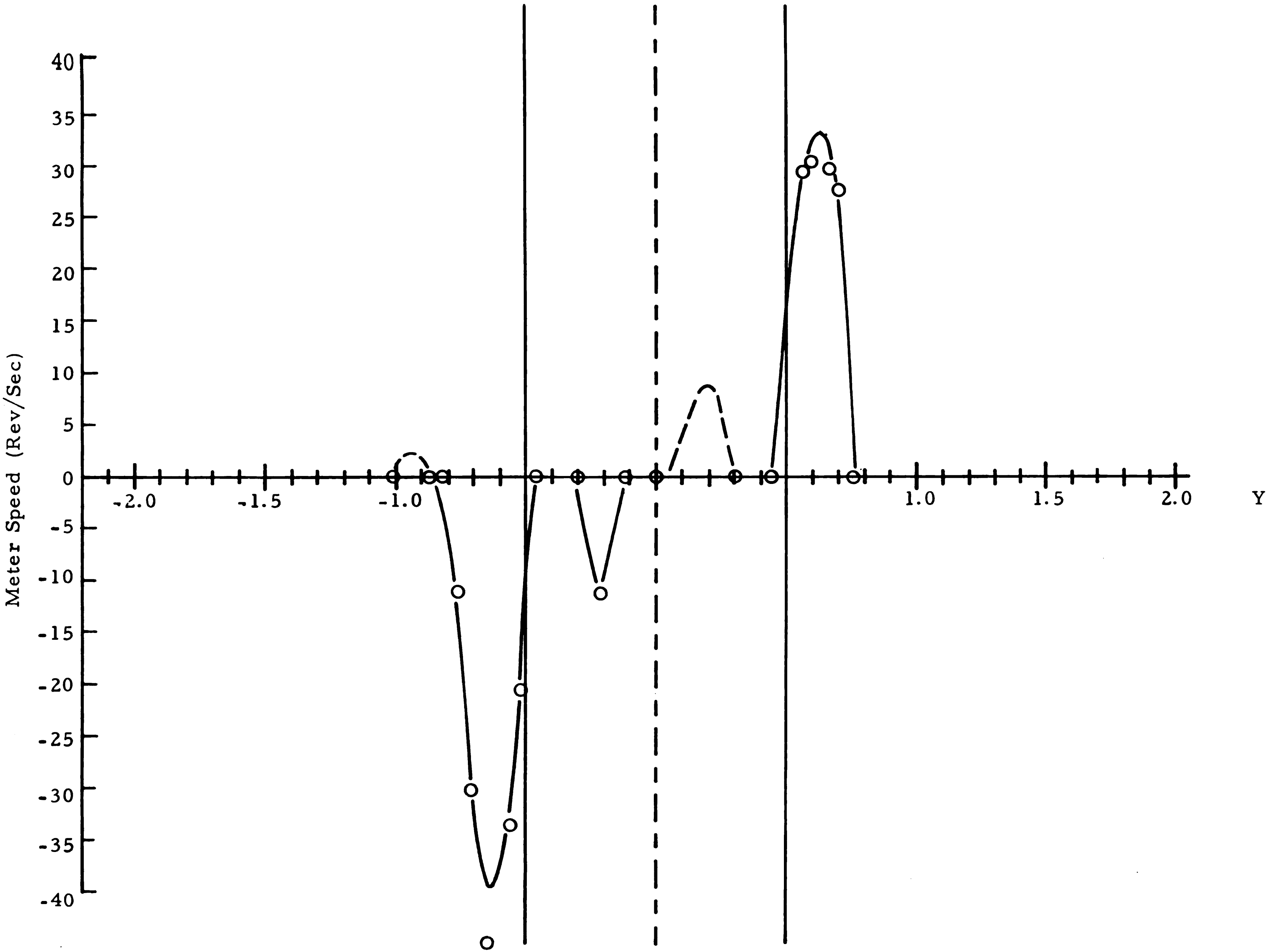

Figure 65c. Vorticity meter speed at X=2, Z=1.6

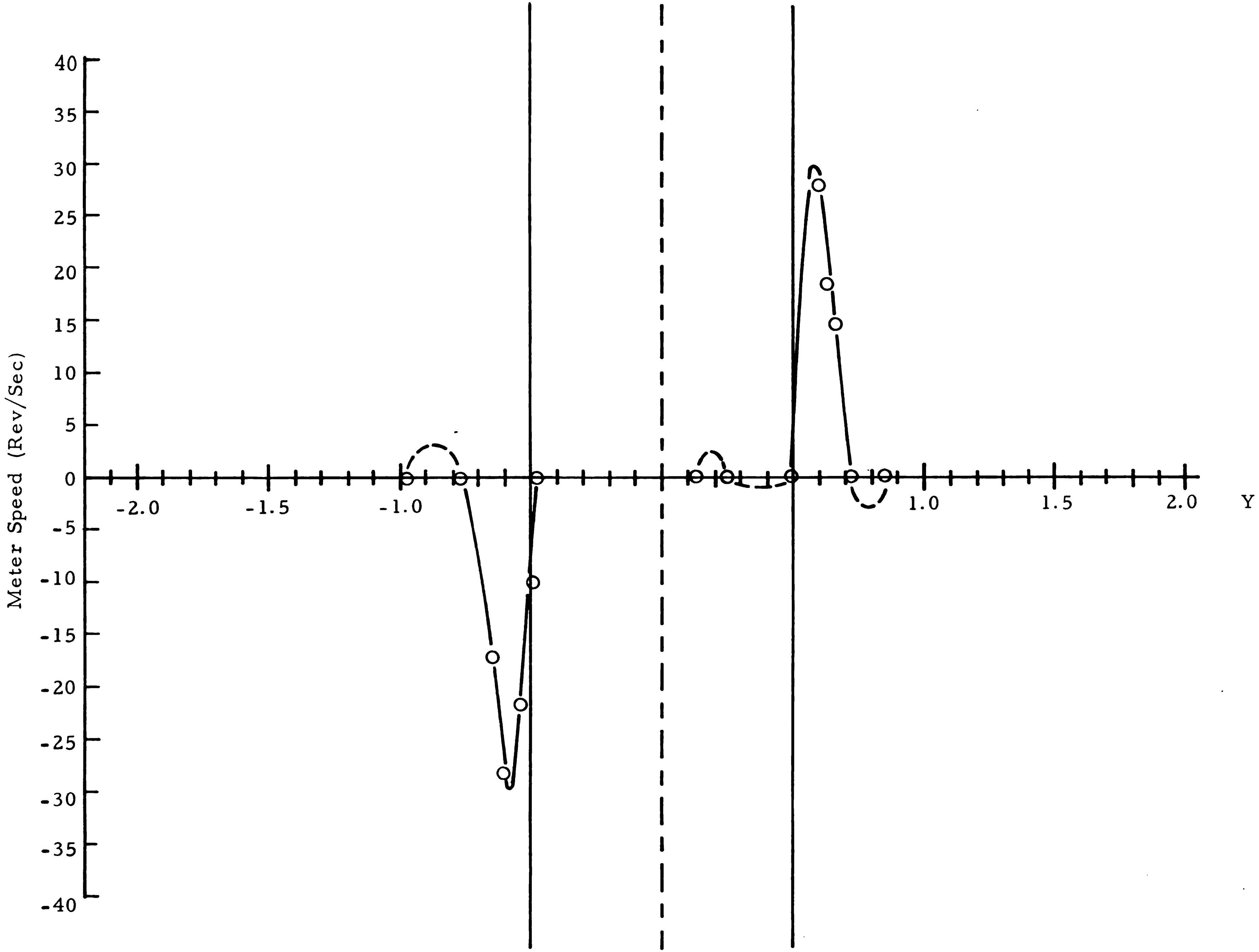

Figure 65d. Vorticity meter speed at X-2, Z=1.7

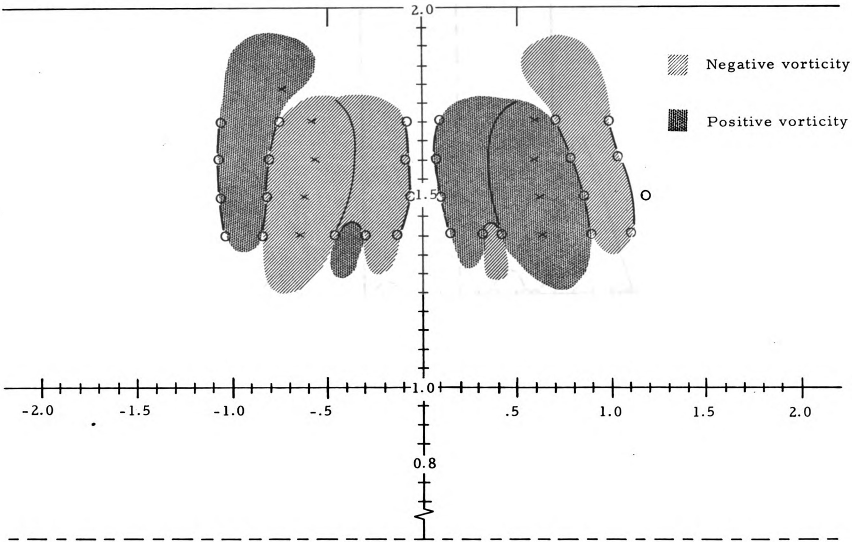

Figure 66. Vorticity zone contours at X = 3

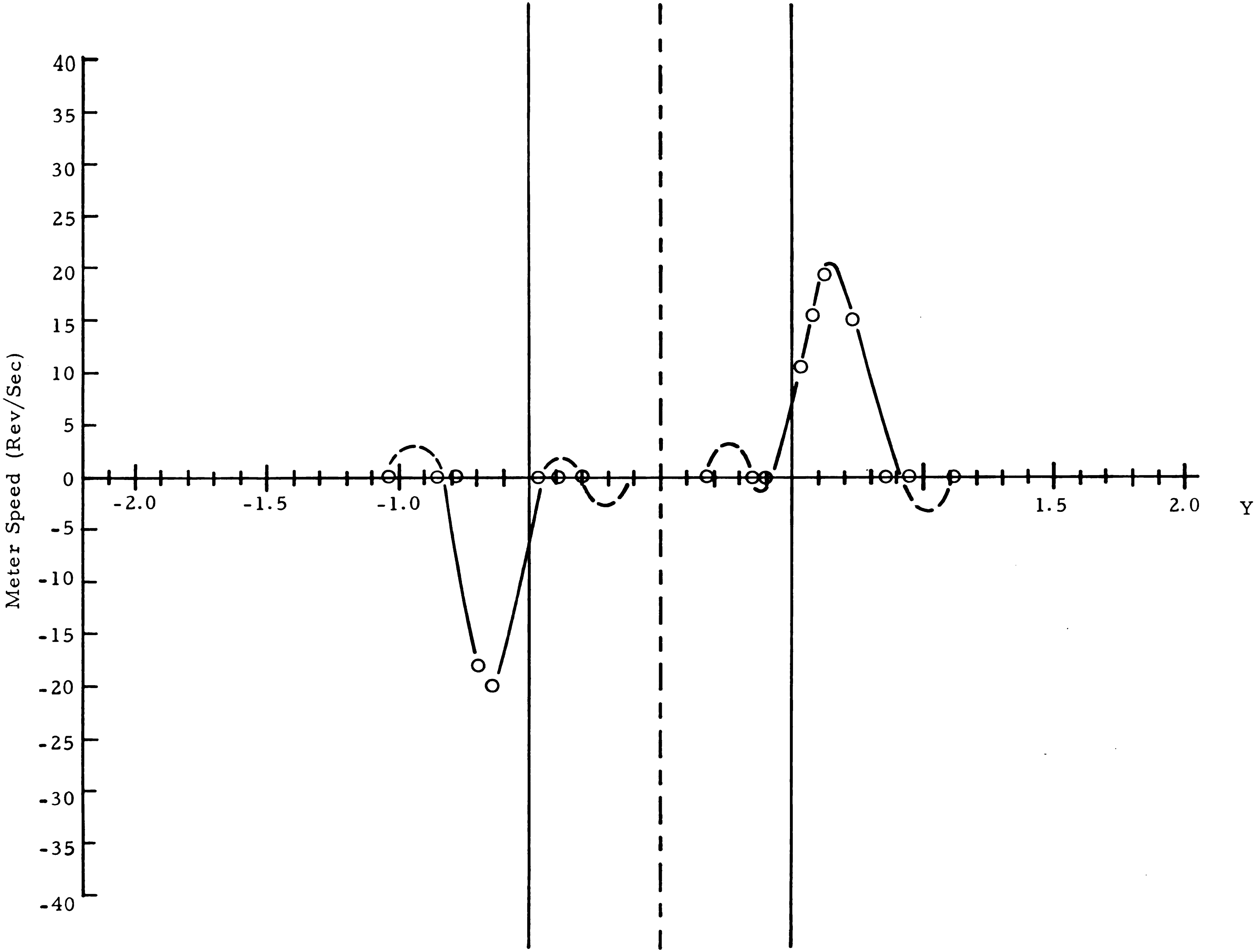

Figure 67a. Vorticity meter speed at X=3, Z=1.4

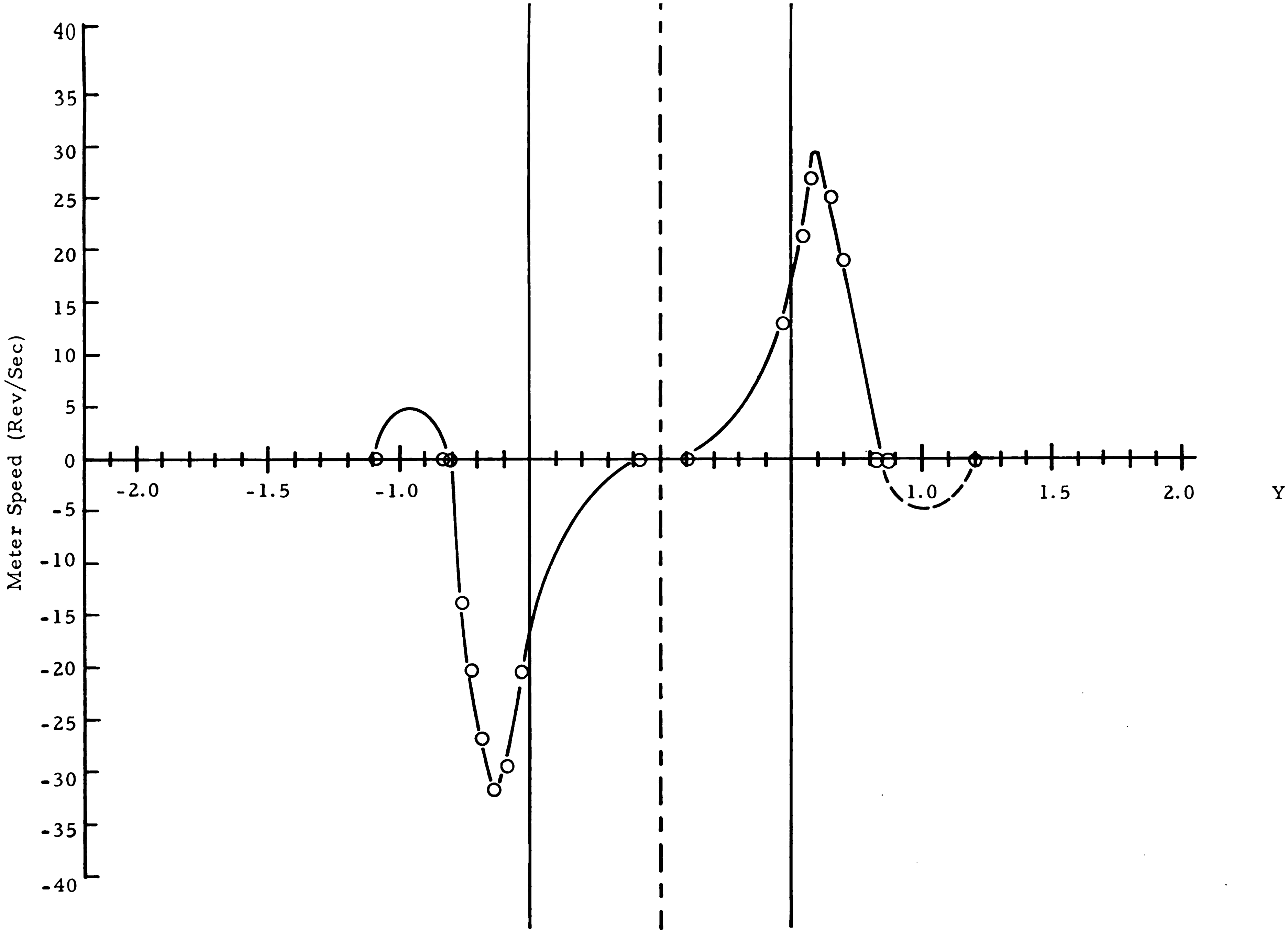

Figure 67b. Vorticity meter speed at X=3, Z=1.5

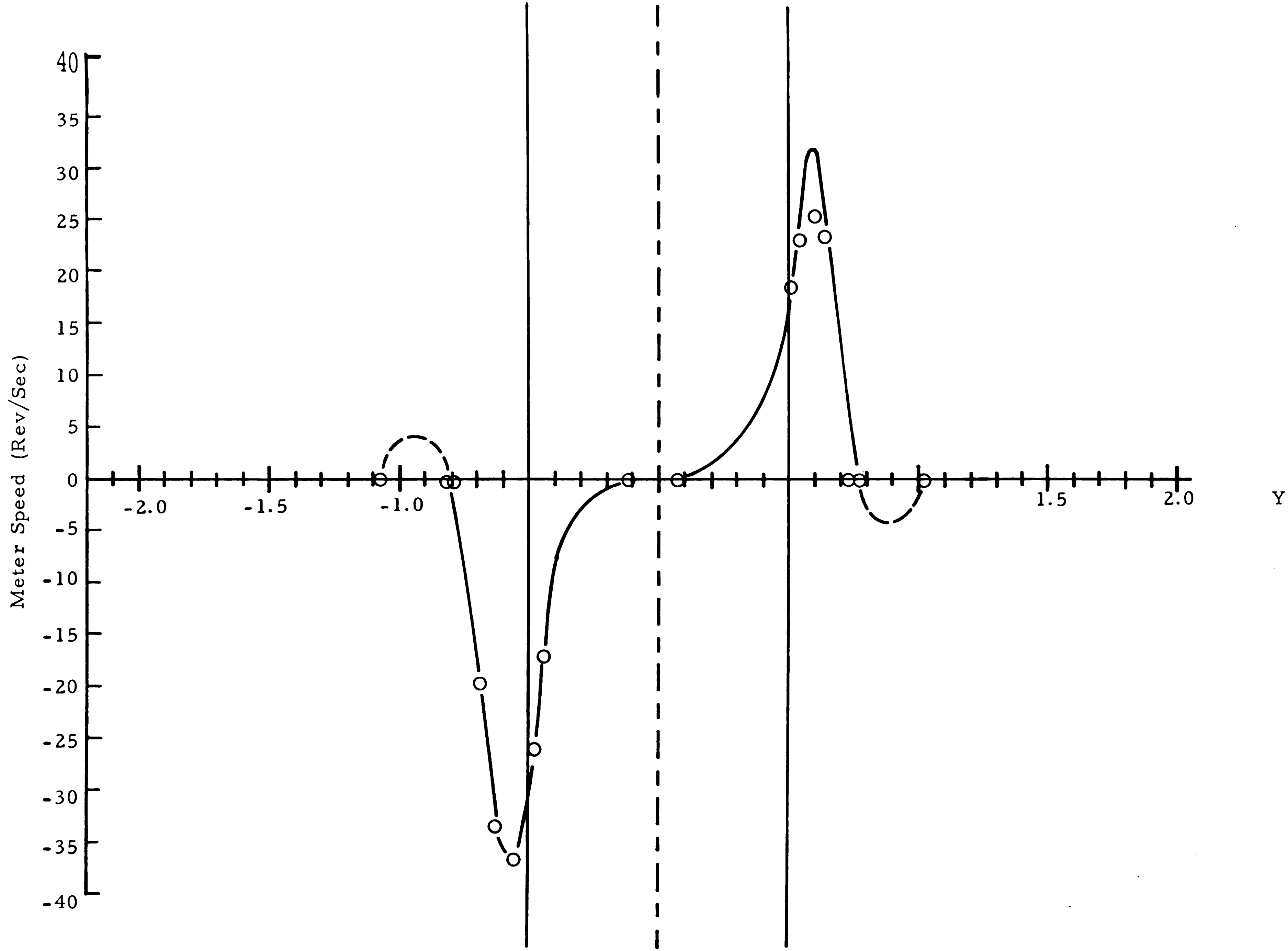

Figure 67c. Vorticity meter speed at X=3, Z=1.6

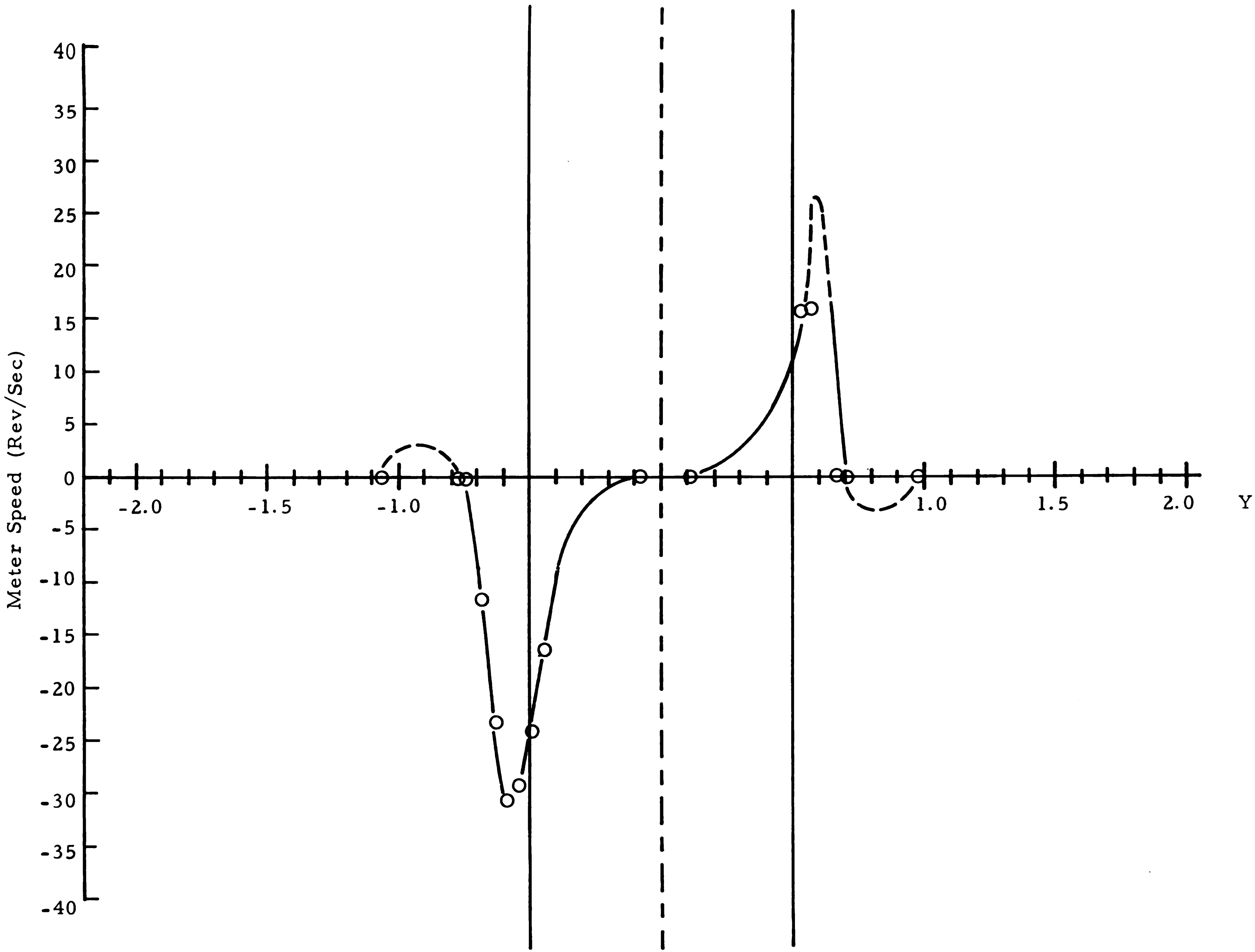

Figure 67d. Vorticity meter speed at X=3, Z=1.7

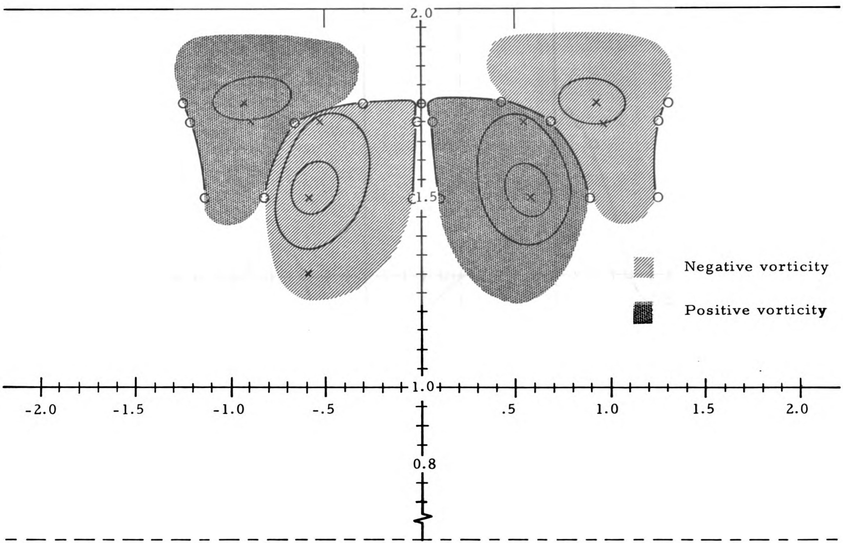

Figure 68. Vorticity zone contours at X = 4

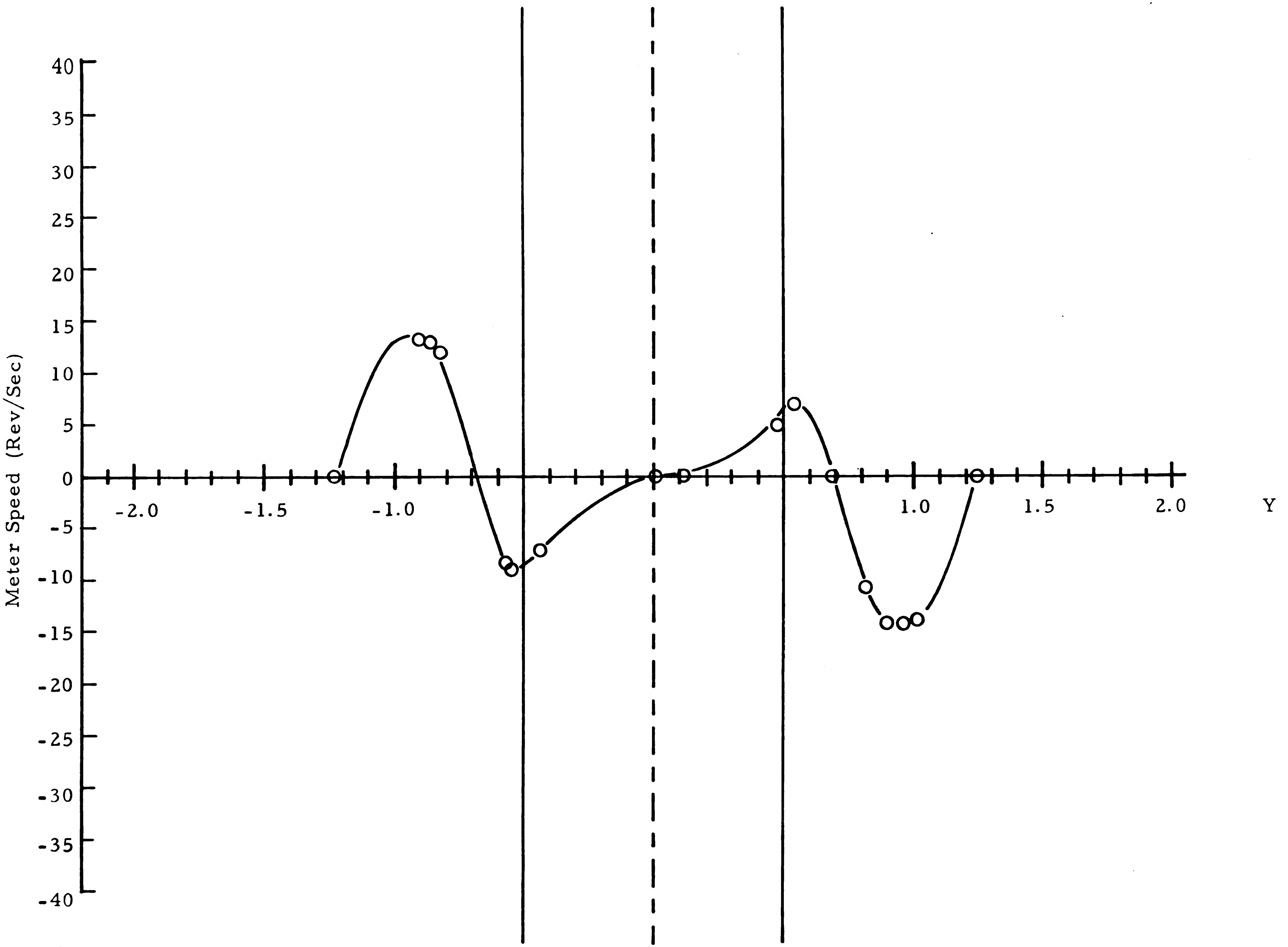

Figure 69b. Vorticity meter speed at X=4, Z=1.7

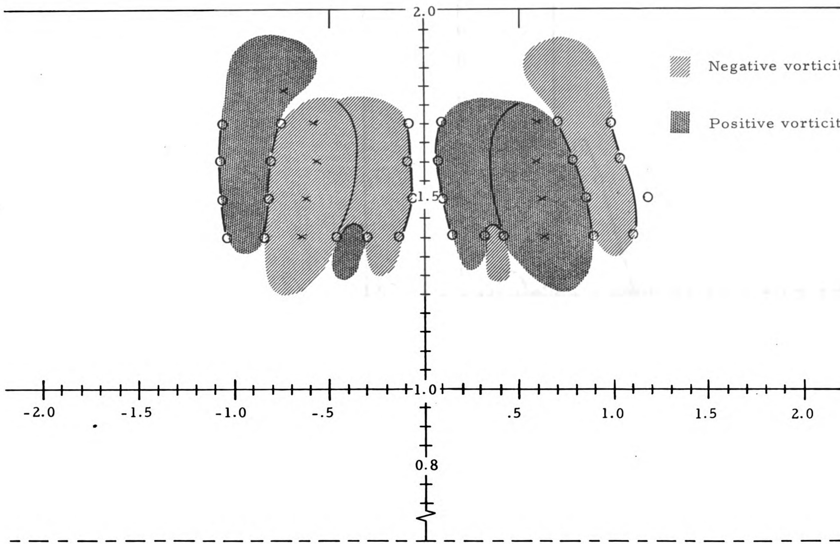

Figure 66. Vorticity zone contours at X = 3

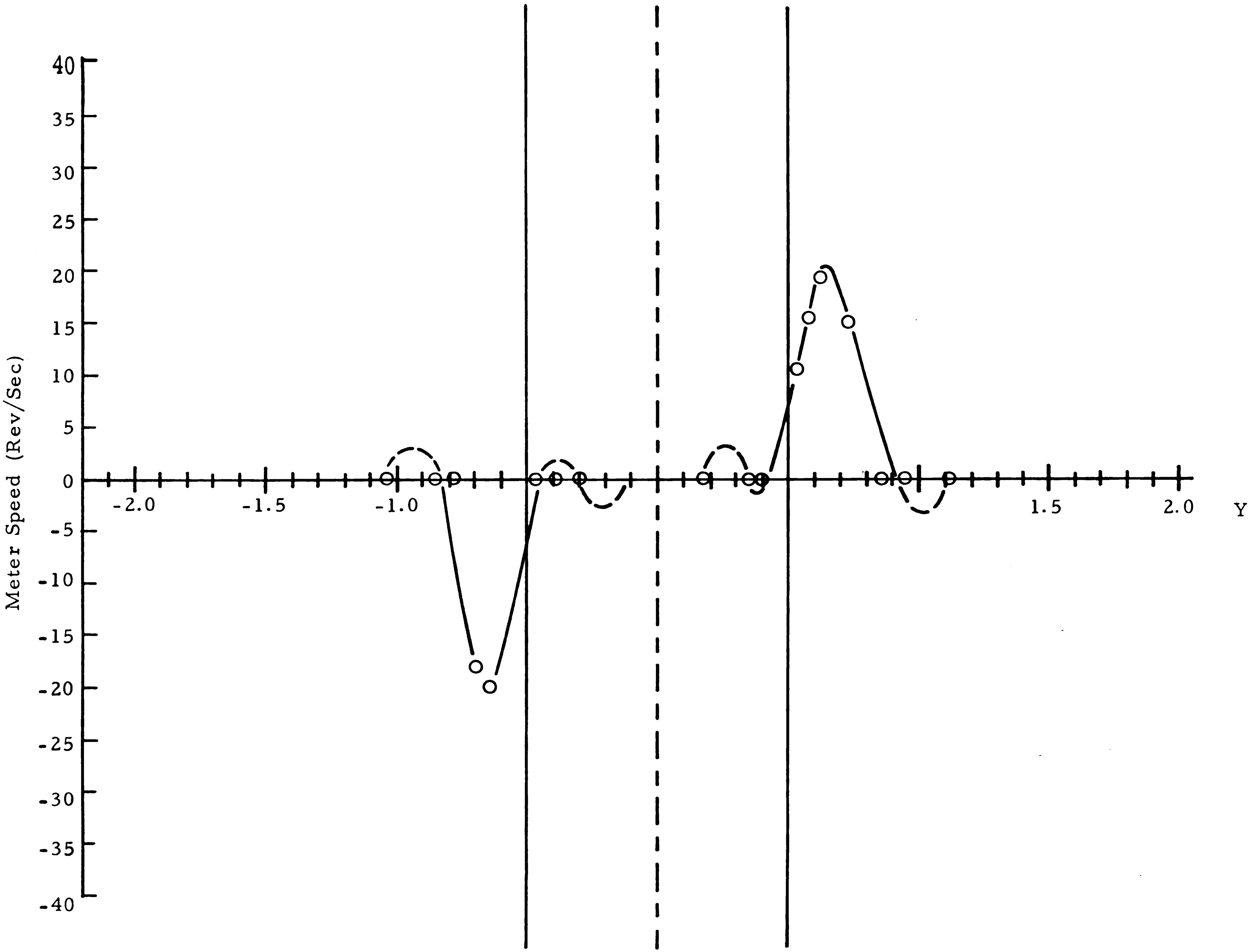

Figure 67a. Vorticity meter speed at X=3, Z=1.4

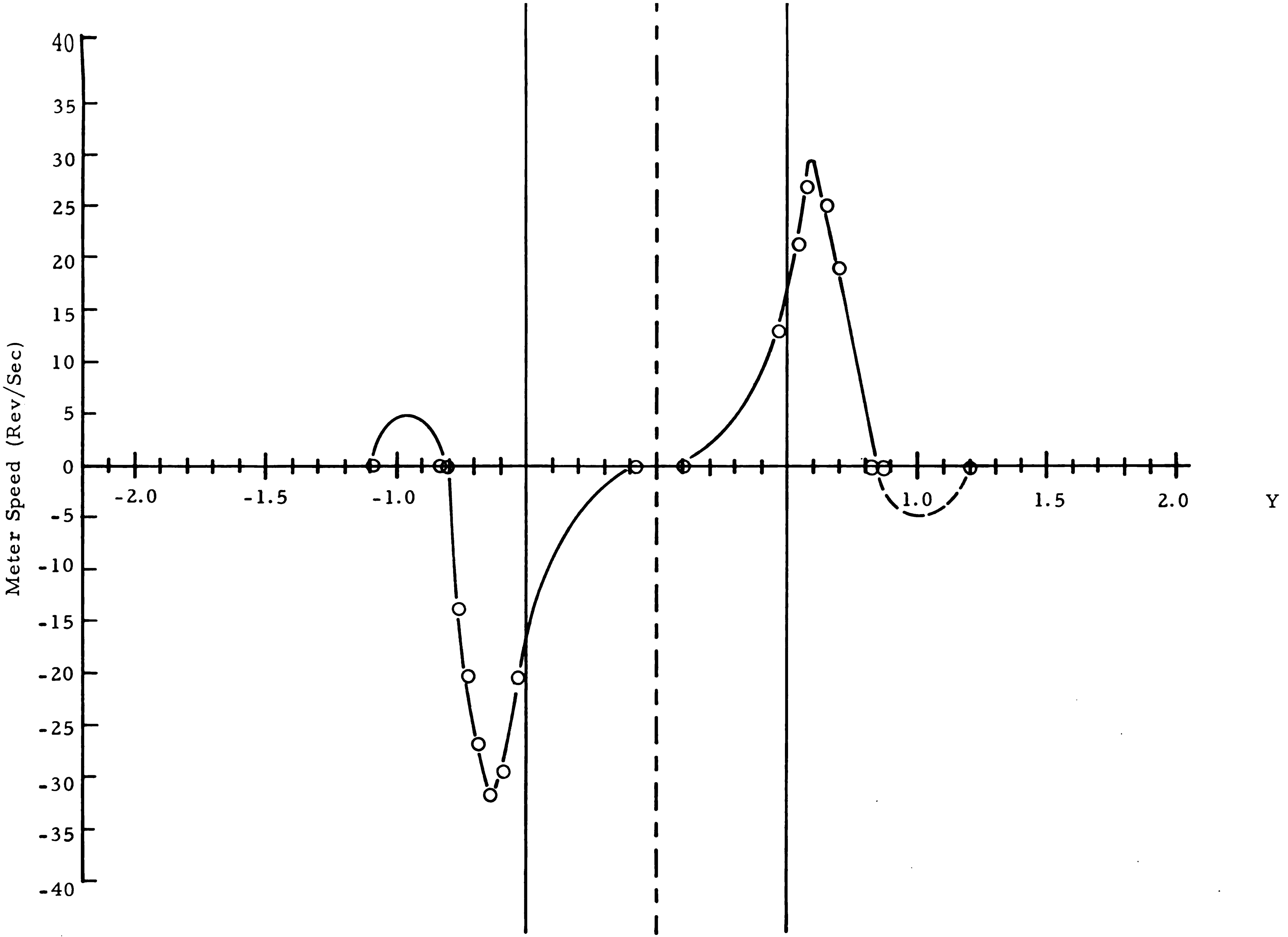

Figure 67b. Vorticity meter speed at X=3, Z=1.5

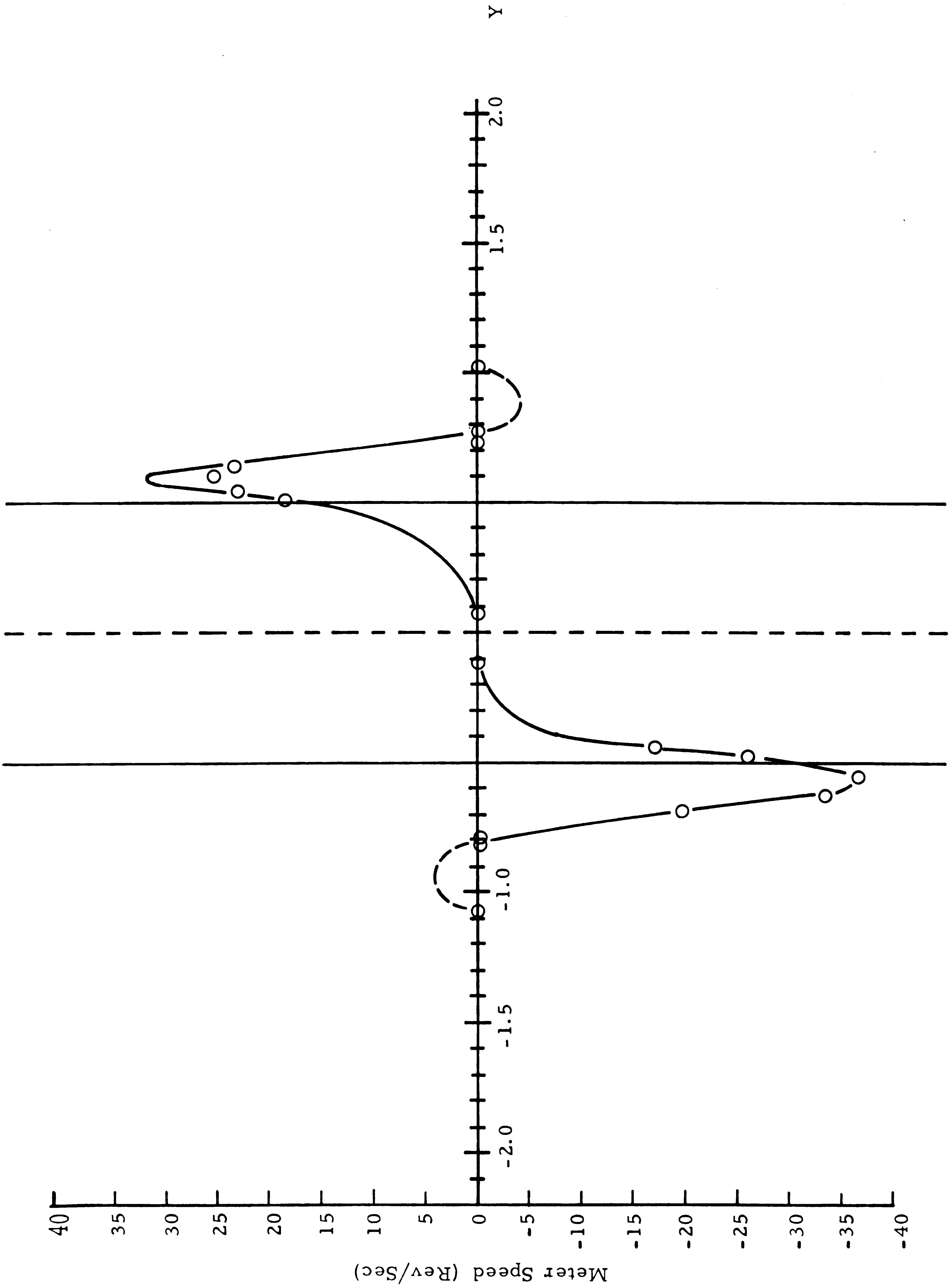

Figure 67c. Vorticity meter speed at X=3, Z=1.6

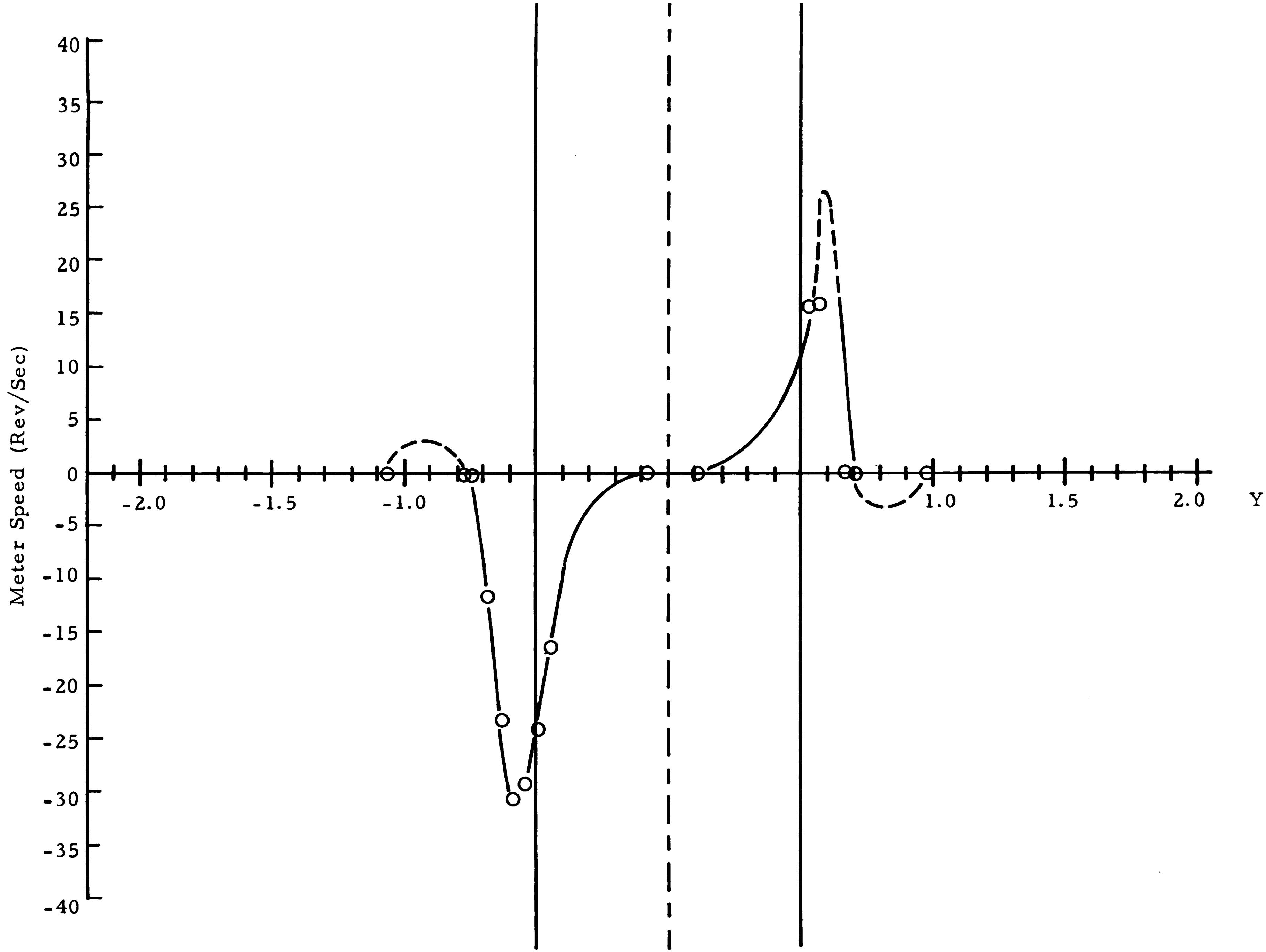

Figure 67d. Vorticity meter speed at X=3, Z=1.7

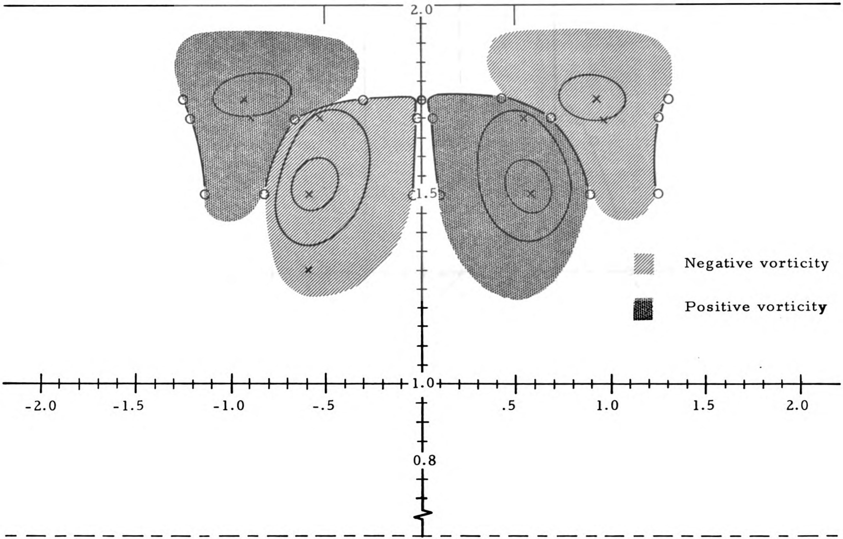

Figure 68. Vorticity zone contours at X = 4

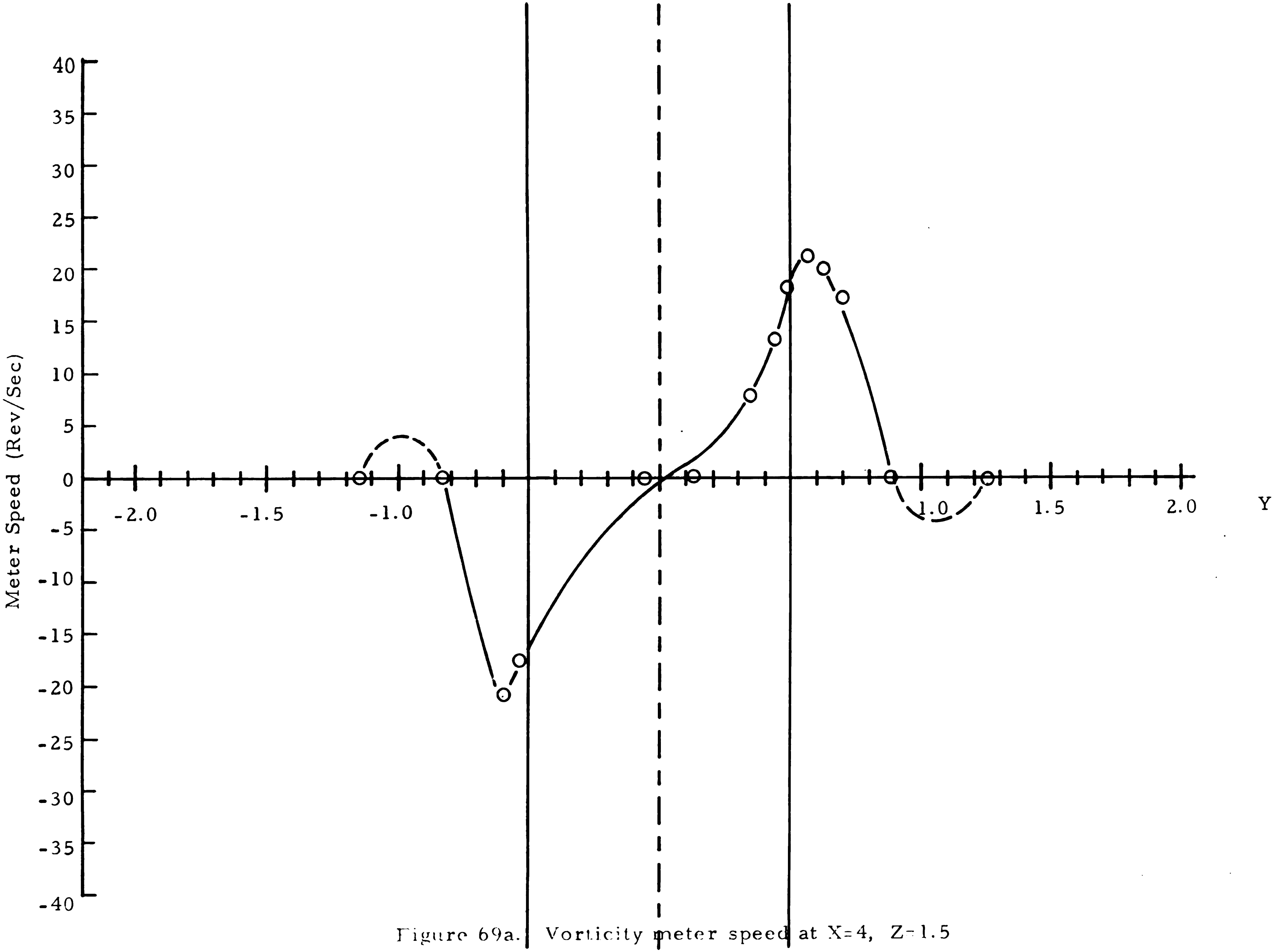

Figure 69a. Vorticity meter speed at X=4, Z=1.5

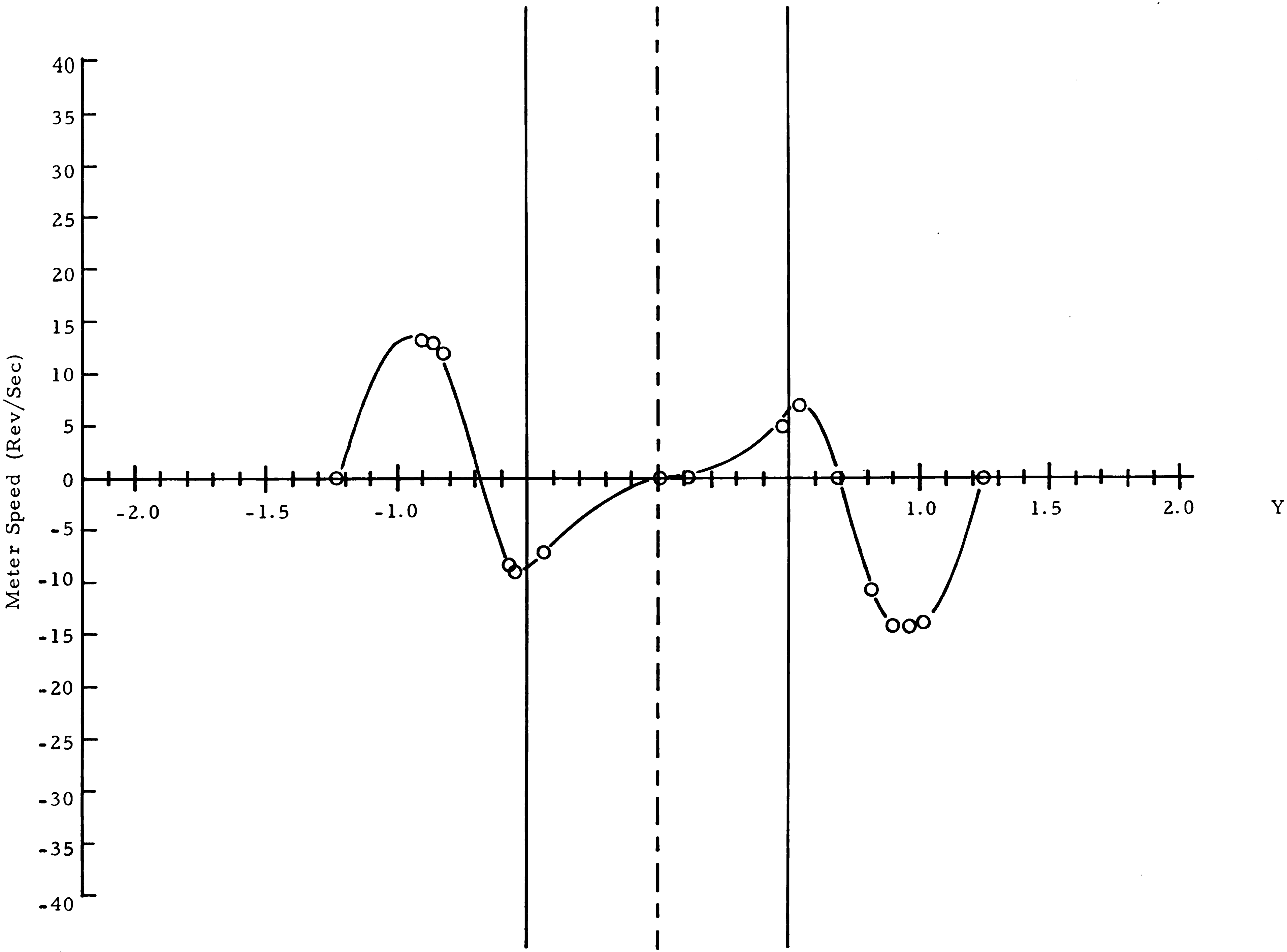

Figure 69b. Vorticity meter speed at X=4, Z=1.7

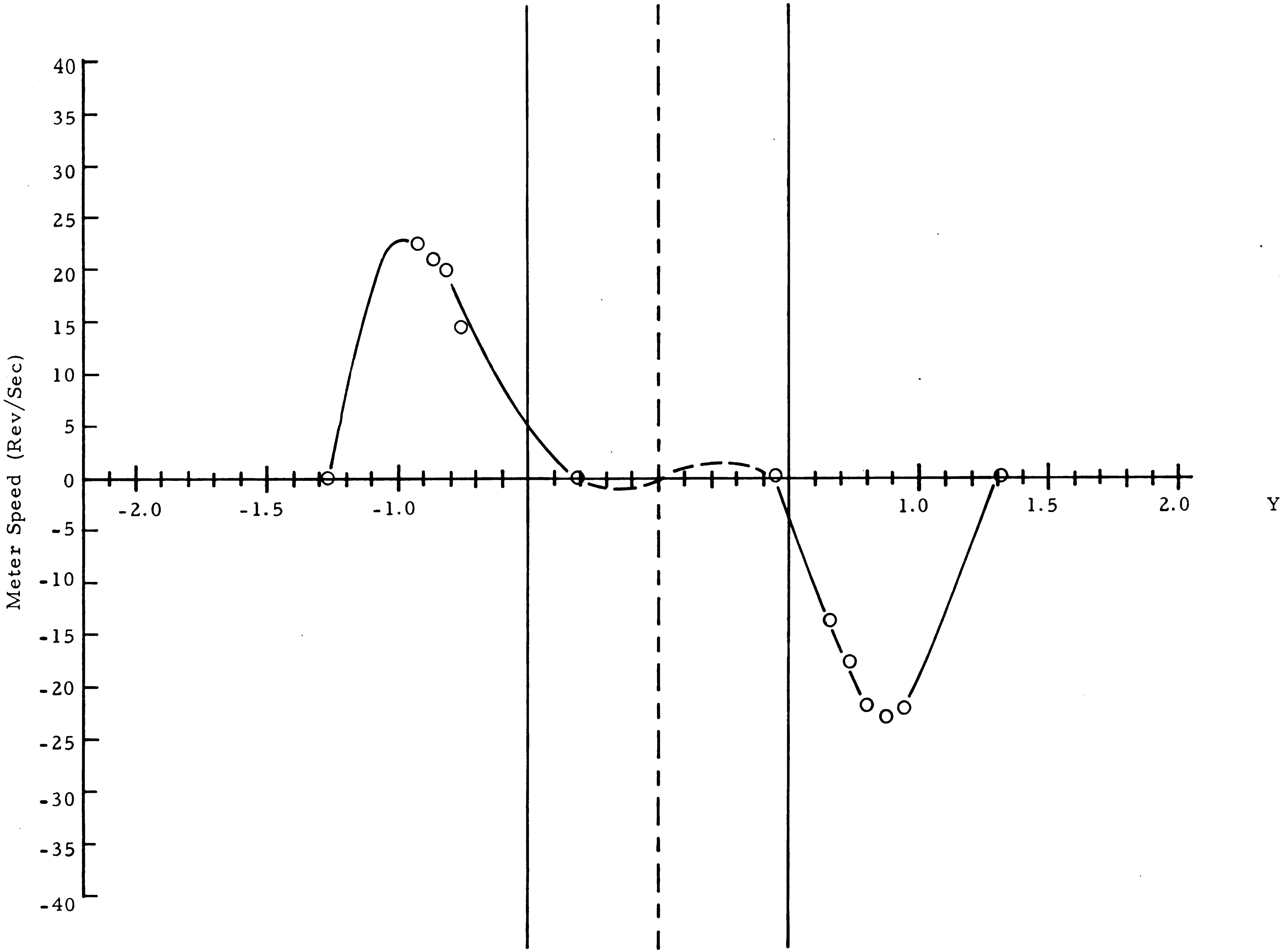

Figure 69c. Vorticity meter speed at X=4, Z=1.75

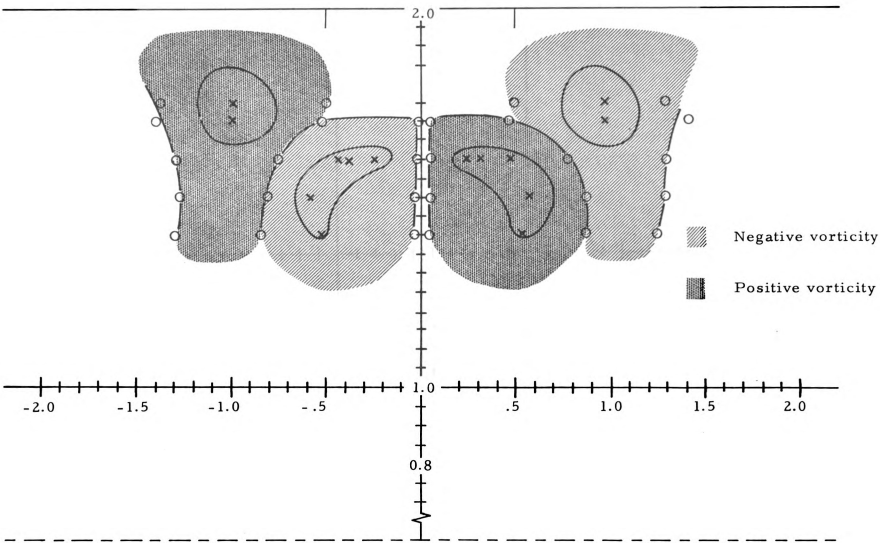

Figure 70. Vorticity zone contours at X = 5

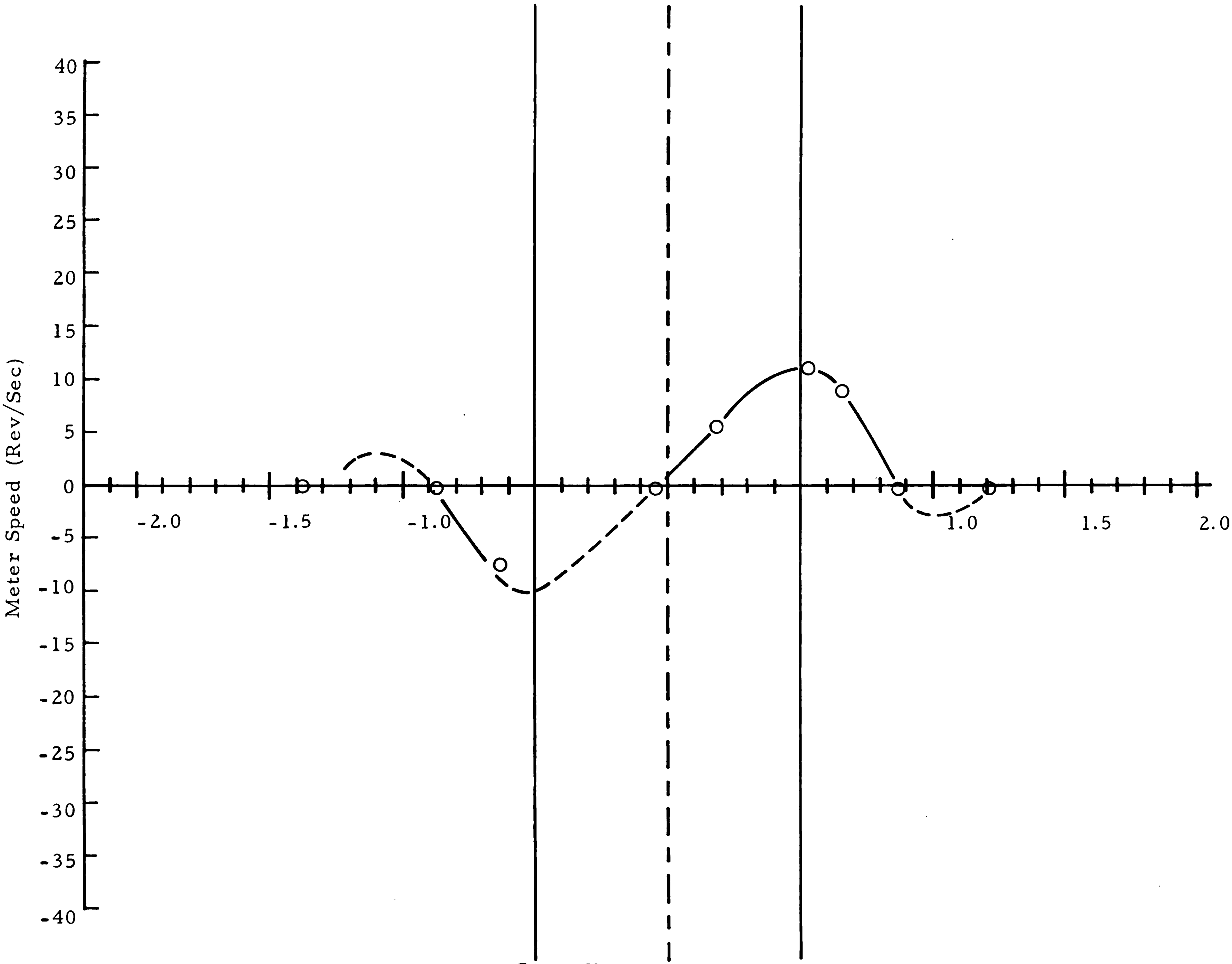

Figure 71a. Vorticity meter speed at X=5, Z=1.4

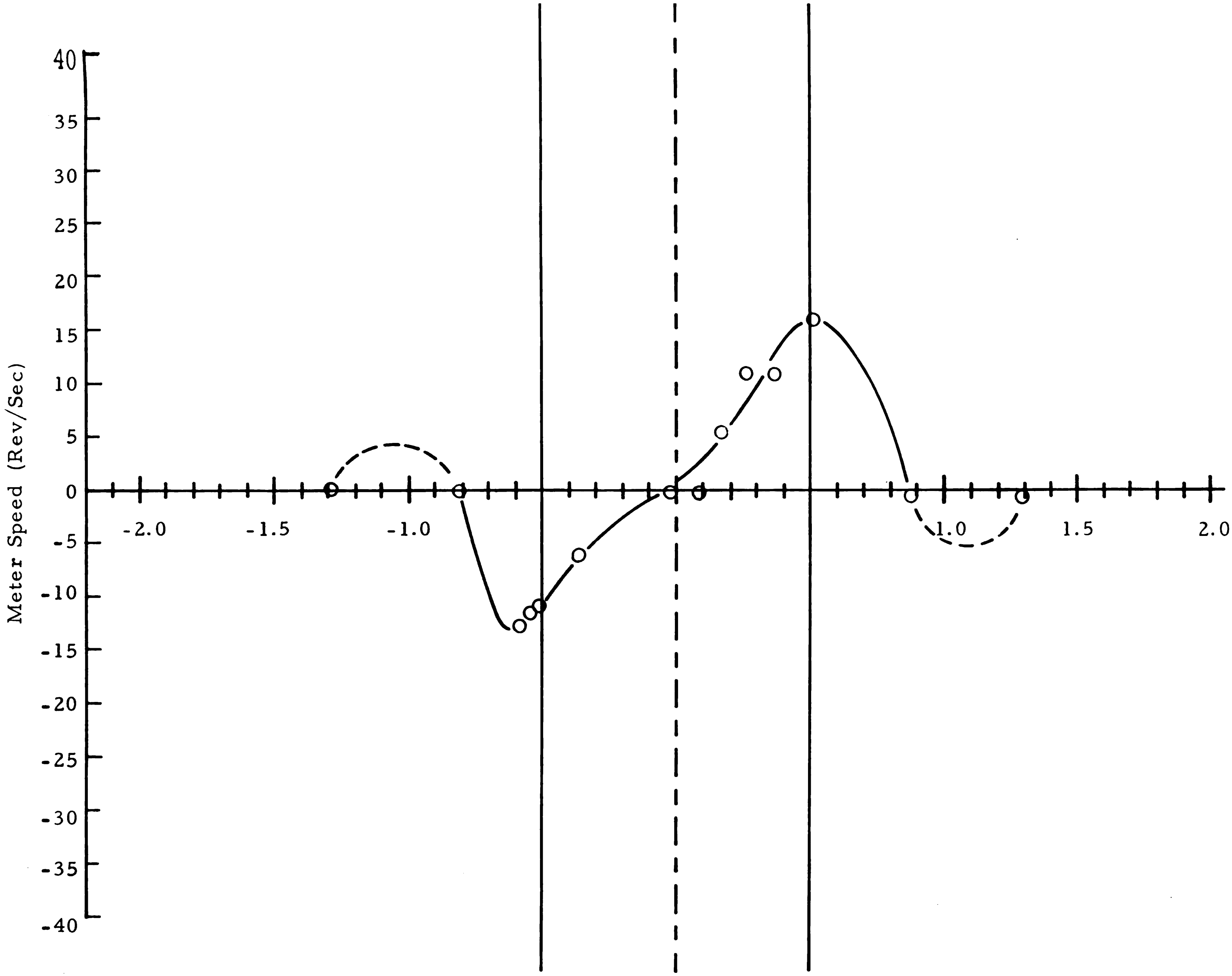

Figure 71b. Vorticity meter speed at X=5, Z=1.5

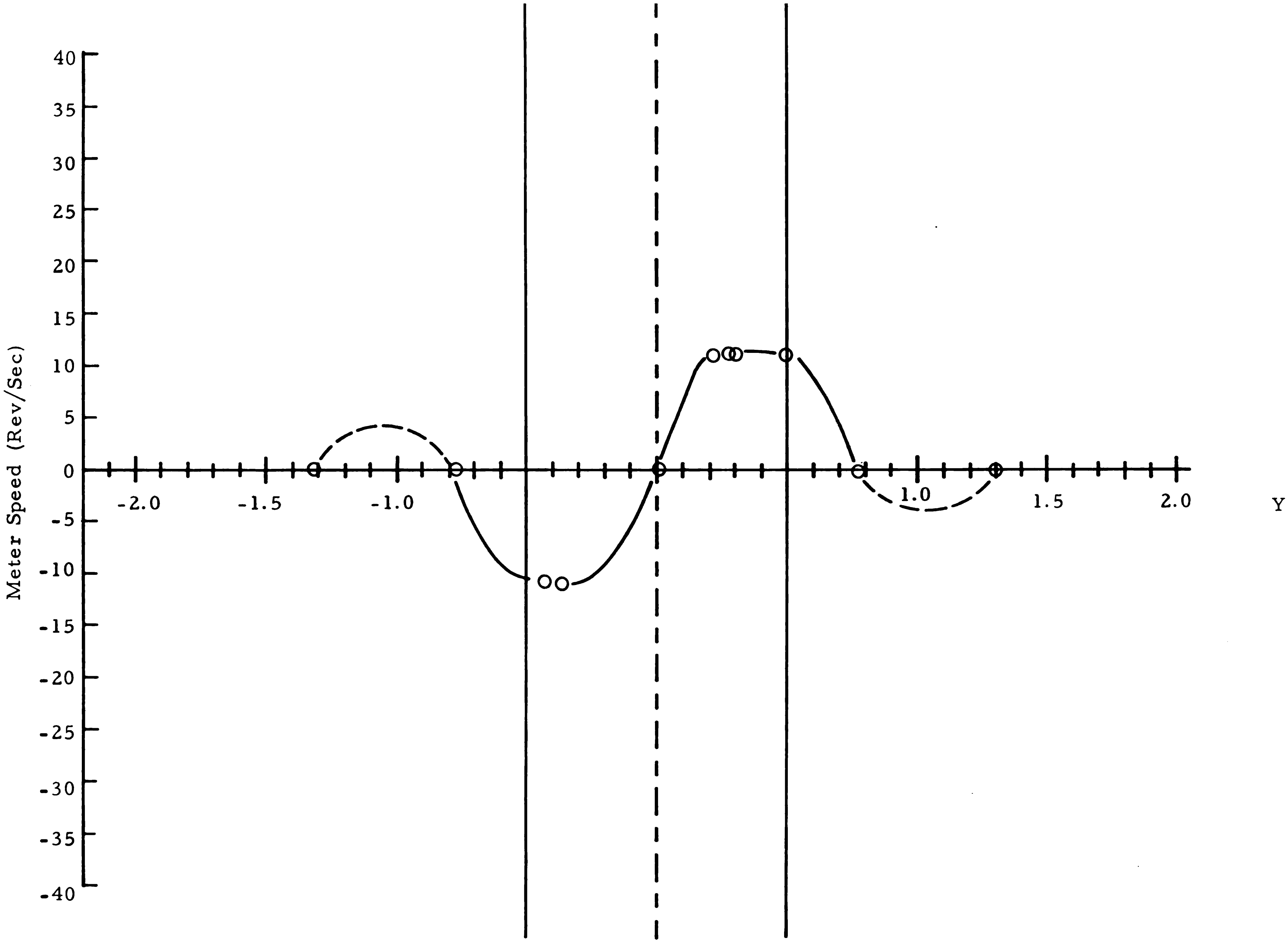

Figure 71c. Vorticity meter speed at X=5, Z=1.6

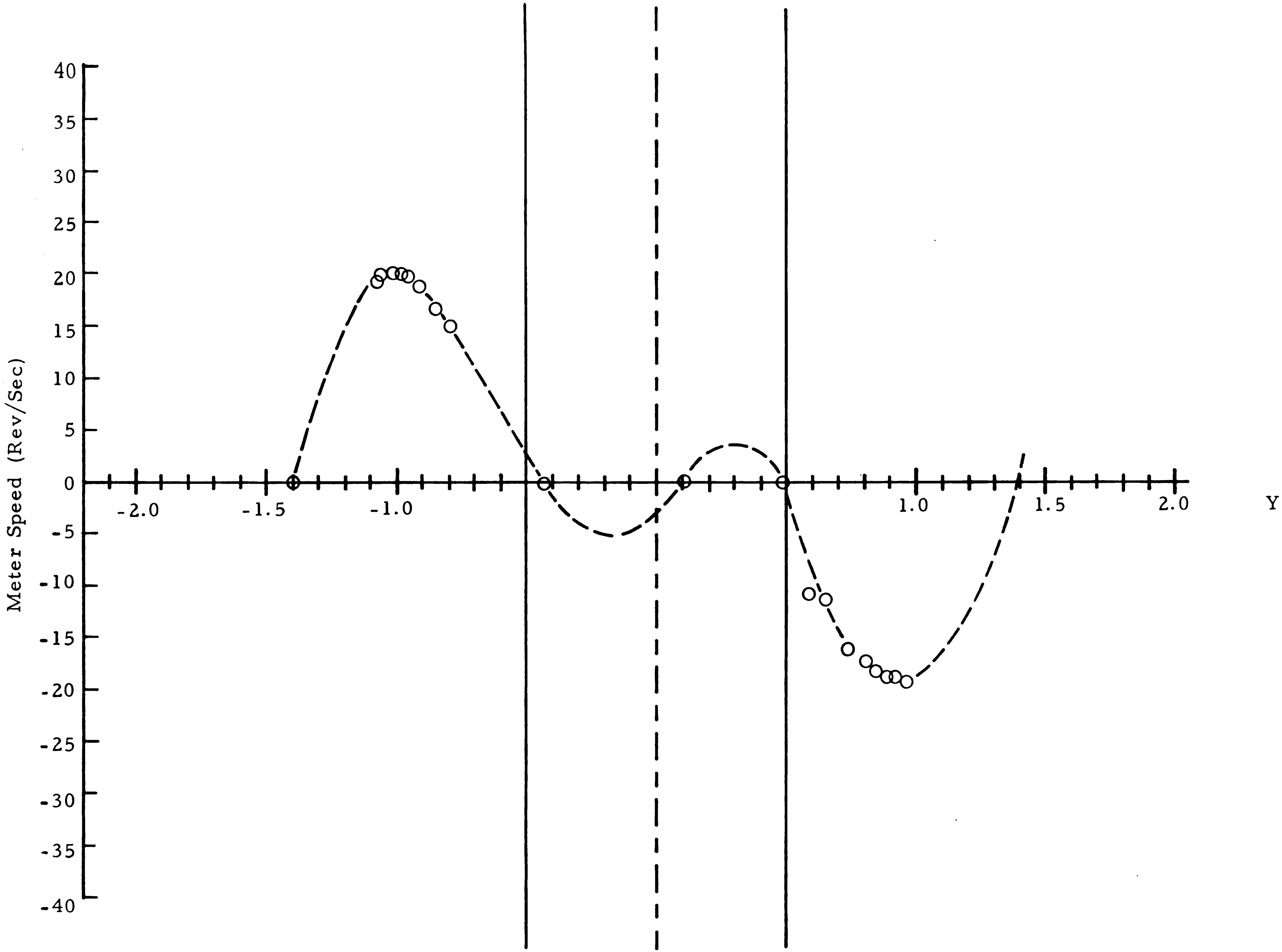

Figure 71d. Vorticity meter speed at X=5, Z=1.7

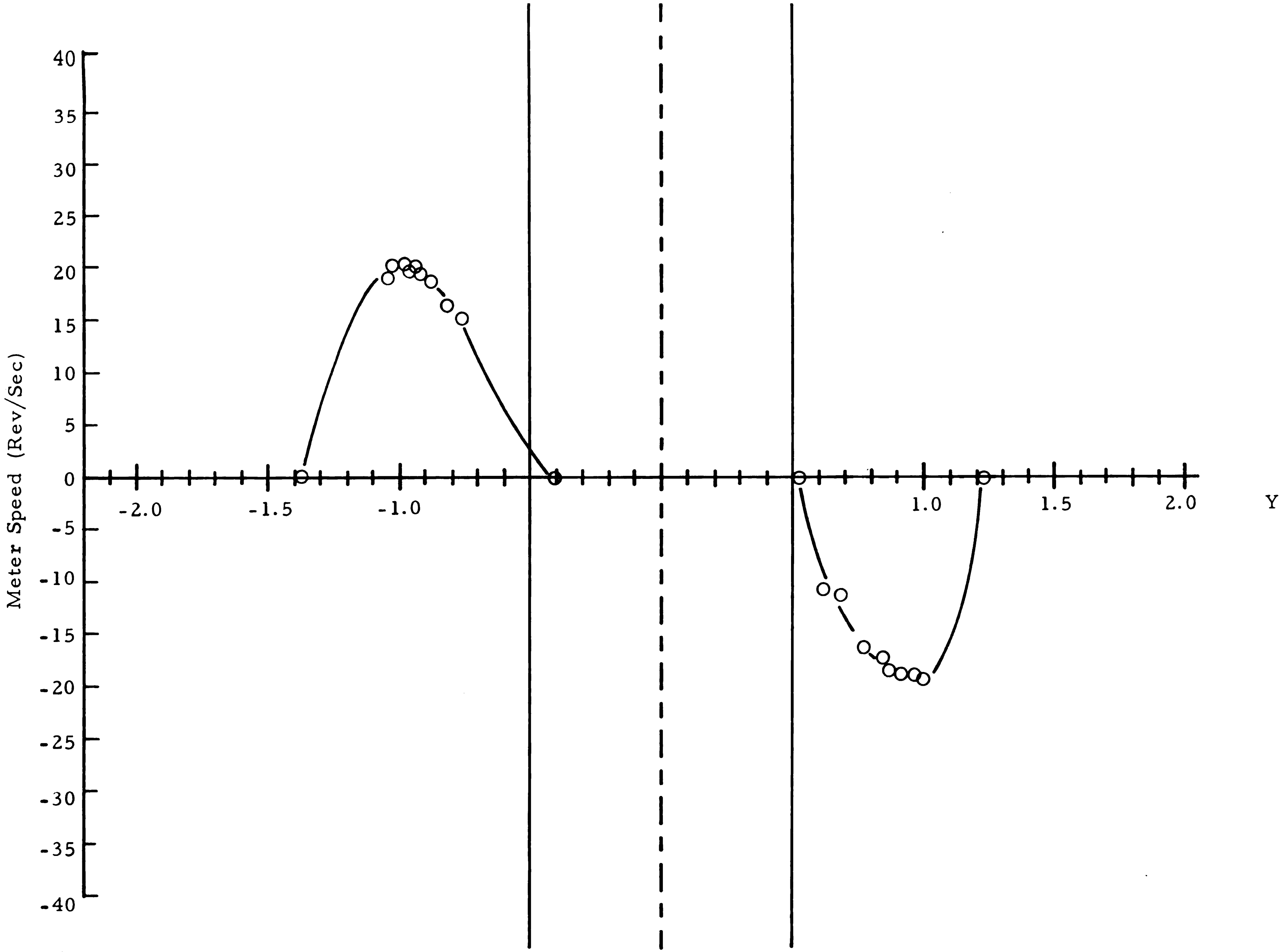

Figure 71e. Vorticity meter speed at X=5, Z=1.75

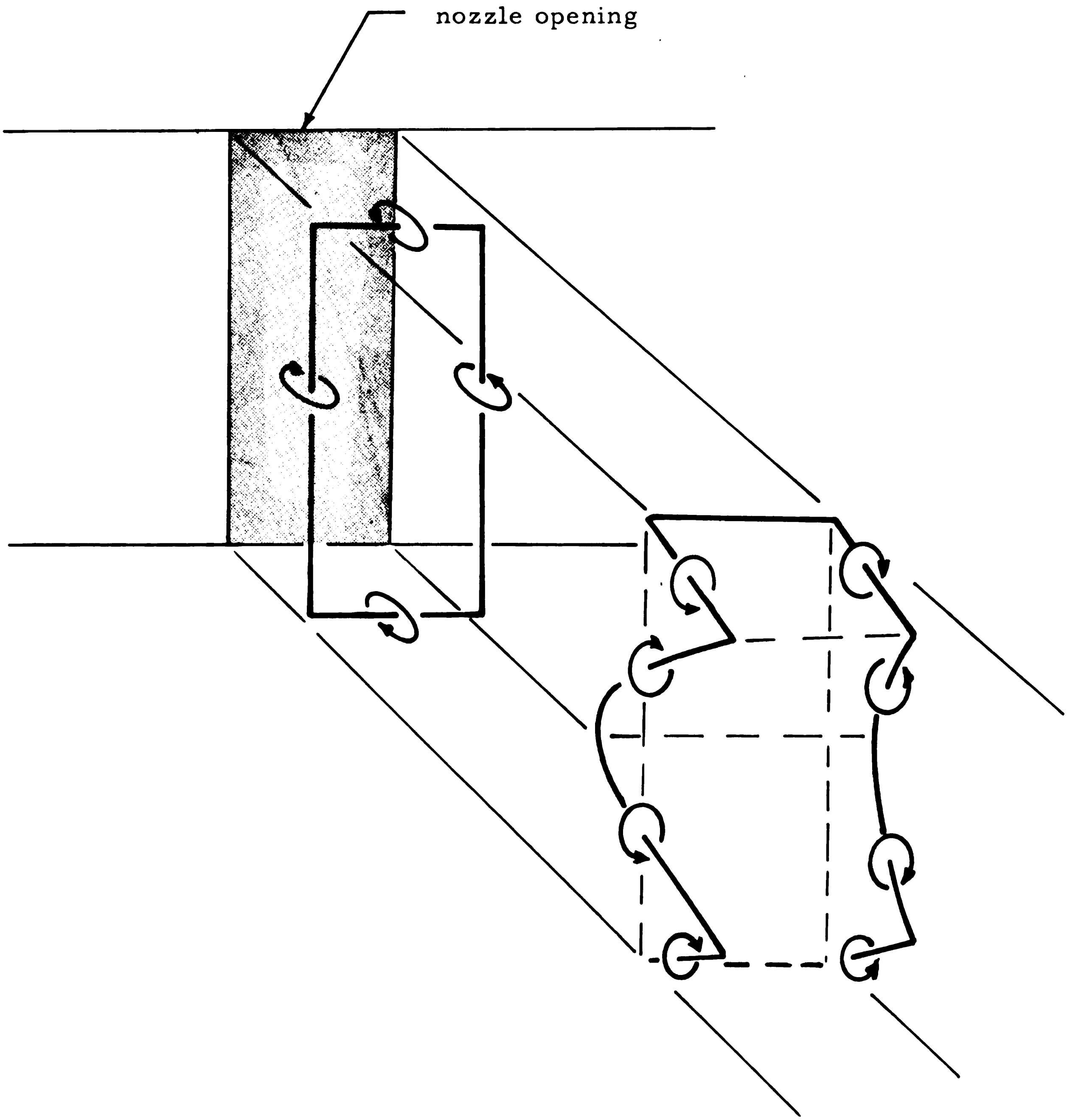

Figure 72. The extended vortex stretching model

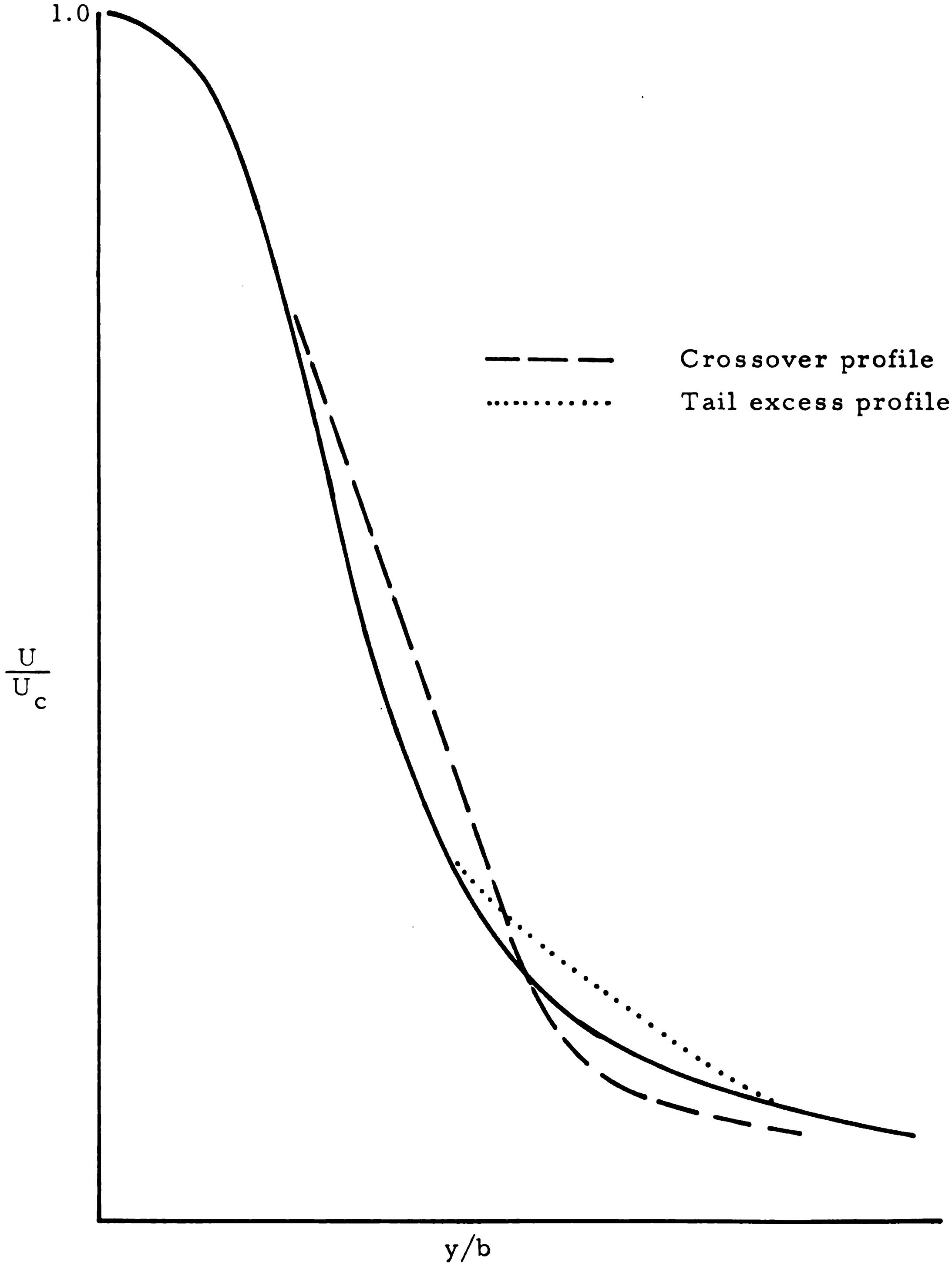

Figure 73. Non-similar velocity profile shapes

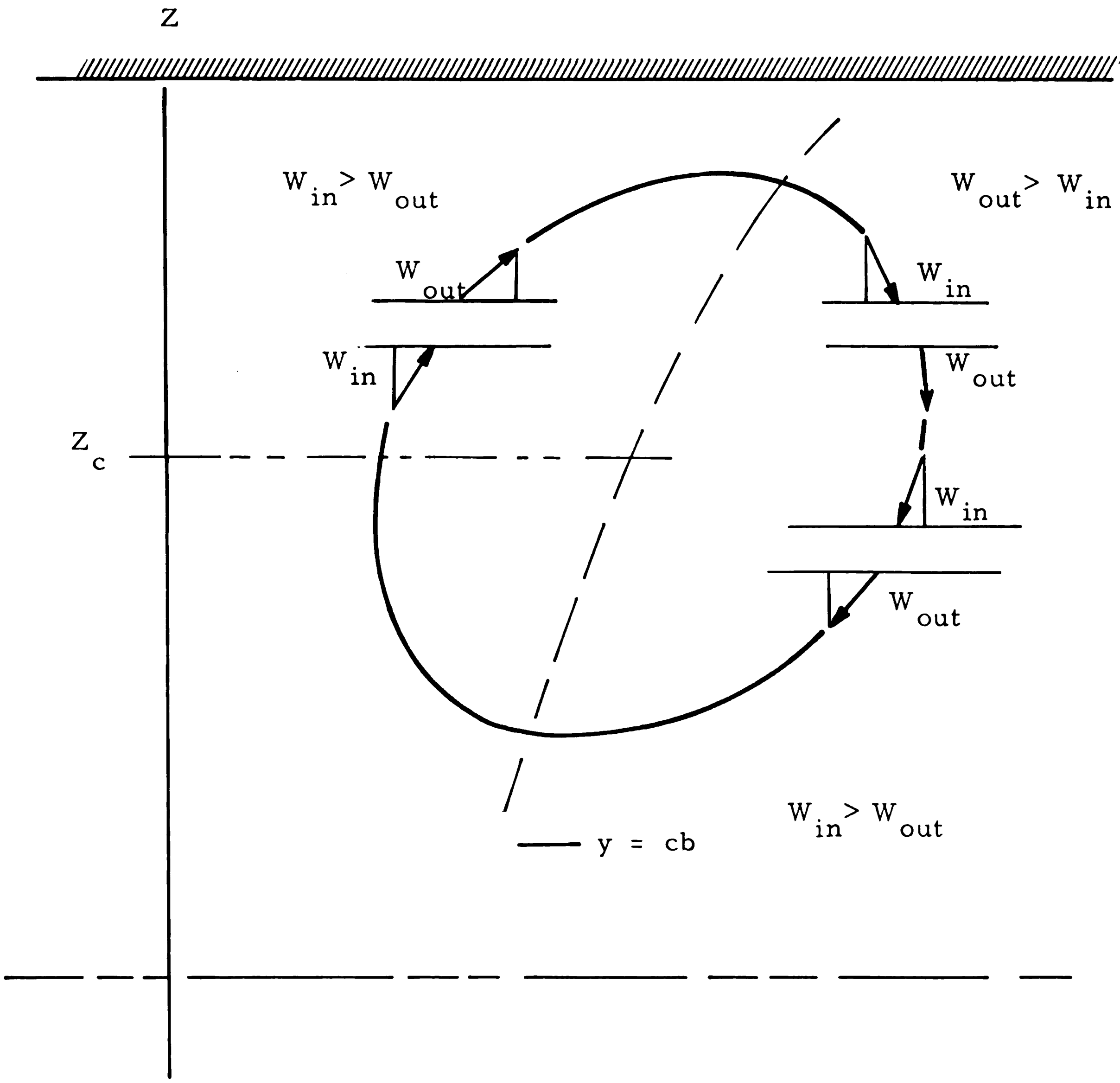

Figure 74. Influence of secondary flow on velocity profile shape